UNIVERSITÀ DEGLI STUDI DI PAVIA
DOTTORATO DI RICERCA IN FISICA – XXI CICLO

Peering into X-ray sky with Swift/BAT and XMM-Newton

Giovanni Novara

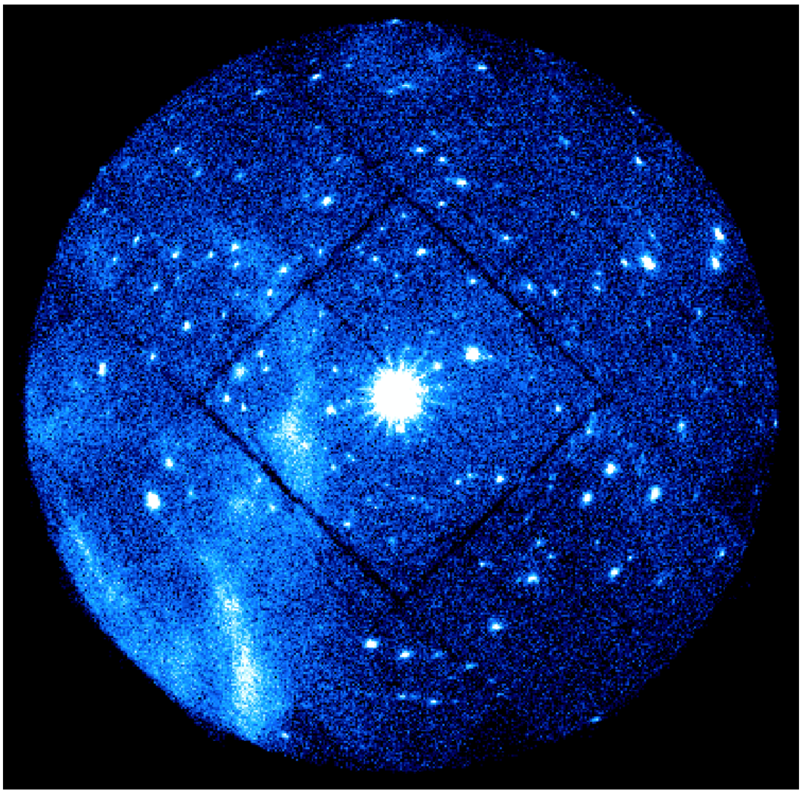

Supervisor: Prof. Andrea De Luca

Tesi per il conseguimento del titolo

Università degli
Studi di Pavia

Dipartimento di Fisica
Nucleare e Teorica

Istituto Nazionale di
Astrofisica

DOTTORATO DI RICERCA IN FISICA – XXI CICLO

Peering into X-ray sky with Swift/BAT and XMM-Newton

dissertation submitted by

Giovanni Novara

to obtain the degree of

DOTTORE DI RICERCA IN FISICA

Supervisor: Prof. Andrea De Luca
Università degli Studi di Pavia, DFNT
INAF-IASF, Istituto Nazionale di Astrofisica
IUSS, Istituto Universitario di Studi Superiore
INFN, Istituto Nazionale di Fisica Nucleare
Referee: Dr. Diego Götz
CEA-Service d'Astrophysique

Cover: XMM-Newton EPIC/MOS image of the 1E1207.4-5209 field in the energy range 0.3-8 keV

Full title: Peering into X-ray sky with Swift/Burst Alert Telescope and X-ray Multi mirror Mission-Newton

Giovanni Novara
PhD thesis – University of Pavia
Printed in Pavia, Italy, November 2008
ISBN 978-88-95767-24-6

Contents

Structure of the thesis

- Chapter 1 gives a short overview of X–ray emission mechanisms and describes the main classes of X-ray sources that may be detected in typical "serendipitous" observations. The classes of sources that may actually be detected depends both on the galactic latitude and (in the soft X-ray band) on the hydrogen column density (N_H). The use of *XMM–Newton* (for soft X–ray) and *Swift*/BAT (for the hard X–ray) data gives a unique opportunity to sample and to study both galactic and extra-galactic X–ray source population.

- In Chapter 2 a short overview of the *XMM–Newton* mission is described with a particular attention on the mirrors performance. Detailed informations of the *EPIC* instruments technical characteristics and their operating modes are presented.

- Chapter 3 is devoted to a deep serendipitous survey at intermediate galactic latitude, performed with *XMM–Newton.* The radio quiet neutron star 1E1207.4−5209 has been the target of several *XMM–Newton* observations, for a total of $\sim$ 450 ks. The source is located at intermediate galactic latitude ($b \sim 10°$). Interestingly, in such a direction both galactic and extra-galactic X-ray sources may be observed. The aim of the study presented in this Chapter is to investigate the properties of both the intermediate-latitude galactic and extra-galactic X–ray source populations in the 1E1207.4−5209 field. A systematic analysis of the whole *XMM–Newton* data set is carried out to generate a catalogue of serendipitous X–ray sources detected with high confidence, and to extract information on such sources' flux, spectrum, and time variability. Moreover, we performed a complete, multi-band (*UBVRI*), deep optical follow-up study of the field with the *Wide Field Imager* (*WFI*) at the ESO/MPG 2.2m telescope (La Silla) to search for candidate optical counterparts of the X–ray sources, in order to obtain a classification for them.

- In Chapter 4 an overview of the *Swift* mission is given. A detailed description of the BAT technical performance and its operating modes are presented. The unique combination of a huge field of view, high sensitivity in the and good angular resolution makes BAT a potentially powerful tool to study the hard X–ray sky. BAT Survey data are immediately released in the public Swift data archive. However, such a large database of serendipitous observations has remained almost unused by the astronomical community because of technical difficulties involved in data analysis. A concise description of the other two instruments on board *Swift*, the X–ray Telescope (XRT) and the Ultraviolet/Optical Telescope (UVOT), is also reported.

- Chapter 5 describe with full details a complete pipeline that we developed in order to analyze *Swift*/BAT survey data. Such a pipeline is optimized for the study of the bright variable sources (Senziani et al., 2007). Extensive tests on the capabilities and reliability of the pipeline are also presented, together with first astrophysical applications.

- In Chapter 6 we describe in detail a series of new software tools that we designed and developed in order to analyze *Swift*/BAT survey data. Such tools are devoted to the study of faint hard X–ray sources, requiring integration of very long exposure times.

- In Chapter 7 we describe detailed tests that we performed to verify the reliability of the results of the software tools devoted to the study of faint X–ray sources. Results of a study of different calibration sources are given.

- Chapter 8 gives results of a first astrophysical application of our software tools for the study of faint sources. Follow-up observations of the sample of six blazars detected as high energy γ-ray sources by the AGILE mission are presented. After an overview of the classification of Active Galactic Nuclei (§ 8.1) and about the blazar characteristics (§ 8.1.2), the study of our six targets' hard X–ray emission using BAT data spanning ~ 3.5 years is presented.

- In Appendix A we give details of the procedure we developed and used to convert the measured BAT count rate for a generic X–ray source into a flux in physical units ($\mathrm{ph \cdot cm^{-2} \cdot s^{-1}}$).

Chapter 1

An overview on the X–ray astronomy

1.1 The serendipitous science

Astronomical observations, thanks to technological improvements of space observatories in the last 40 years, have shown that all classes of celestial sources emit in the X–ray energy range, see e.g. § 1.4. Typically, the instruments' observing strategy is based on pointed observations of a main specific target which is kept at the center of the field of view for an integration time long enough to yield a photon statistics adequate for the scientific analysis. If the instrument provides a good angular resolution (very important to avoid source confusion) over a wide field of view, it will be possible to explore the sky around the main target with the aim to find other ”serendipitous” sources. Since the study of serendipitous sources comes at no cost, the "serendipitous" science has been attracting increasing attention. currently, there are three operative soft X–ray missions characterized by instruments suitable for detecting serendipitous sources: the ESA satellite *XMM–Newton*, the *Chandra* X–ray Observatory and the X-ray telescope (XRT) on board *Swift*, both NASA satellites.

In particular, thanks to their excellent sensitivity, good image quality over a wide field of view ($30'$) and wide energy range (0.2-12 keV), the *EPIC* cameras on board *XMM–Newton* allow to perform X–ray surveys of serendipitous sources with unprecedented sensitivity (for details see § 2). These characteristics, coupled with $6''$ angular resolution, allow to resolve very faint (X–ray flux limit of $\sim 10^{-14}$-10^{-15} erg cm^{-2} s^{-1}) sources making it possible to study different populations through the exploitation of the EPIC public database.

In the hard X–ray energy range, the Burst Alert Telescope (BAT) on board *Swift* mission (see § 4) is entirely devoted to serendipitous science. BAT is a coded mask gamma–ray burst (GRB) monitor (§ 4.2) and, while waiting for new GRBs detections, collects spectral and imaging information in the hard X–ray band ("survey data", see § 4.2.2), covering each day 50-80% of the sky.

The unique combination of high sensitivity in the 15-150 keV energy range ($\sim$ 100 mCrab in 30 s, on-axis) and good angular resolution (point source location accuracy of 1-3 arcmin) over a huge field of view (2 sr, partially-coded) makes BAT a powerful tool to study the hard X–ray serendipitous objects in the sky.

In this thesis, I pursued two different "serendipitous" science goals. On one side, I took advantage of a series of X-ray observations, totaling $\sim$ 450 ks scheduled time, devoted to the study of the radio quiet neutron star 1E1207.4-5209 to built one of the deepest X–ray survey obtained at intermediate galactic latitude ($|b| \simeq 10°$).The detailed analysis of the *XMM–Newton* observations yielded an impressive lists of serendipitous, partly galactic, partly extragalactic, background sources which were then studied in the optical down to $V \simeq 24.5$ through observations with the *Wide Field Imager* (*WFI*) of the ESO/MPG 2.2m telescope.

On the other side, I developed a new software in `MATLAB` (see Chapter 6 with the aim to optimize the detection of faint sources in the hard energy range. Thanks to the mosaic technique, our new tools can exploit the complete BAT data archive in order to analyze at once observations centered on a given source target and observations in which the source is a serendipitous object in the BAT field of view (see Chapter 7).

Moreover, focusing on the study of bright, hard X–ray sources I have contributed to the preparation of a pipeline to monitor the behaviour of variable X–ray sources characterized by fluxes $\gtrsim$ 50 mCrab(see Chapter 5).

1.2 Introdution

X–ray astronomy allows to study celestial sources emitting radiation between $\sim$ 0.1 and few hundreds of keV. The X–ray emission can be produced by two dominant physical processes, thermal emission from hot gas (plasma), with temperature between 10^6 and 10^8 K (thermal processes), and non–thermal emission from relativistic electrons (non-thermal processes). The spectral shape of the emission produced by the two processes is different, thus making the source spectral analysis the first method to investigate the nature of an unknown X–ray source. Standard spectral analysis is instrumental to asses the source flux (in erg $\mathrm{cm^{-2}s^{-1}}$) as well as the presence of spectral features, thus possibly the source distance through the redhsift measurement. Moreover, spectral fit optimization, with one or more components can shed light on the emission regions as well as on the different emission mechanisms possibly at work in different regions. Although all models are just phenomenological descriptions of the data, they can suggest if the X–ray emission is predominantly thermal or non-thermal.

This section is organized as follows: the X–ray emission processes are described in § 1.3 with a particular attention to thermal bremsstrahlung and blackbody radiation, in § 1.3.1 and § 1.3.2 respectively, as well as to non-thermal processes, in § 1.3.3. An overview on the X–ray serendipitous sources detected in our survey is given in § 1.4.

1.3 The X–ray emission mechanisms

1.3.1 Thermal bremsstrahlung

If the particles that collide are of the same kind, the time derivative of dipole momentum $q(\vec{v_1}+\vec{v_2})$ and the mechanical momentum $1/2(\vec{v_1}+\vec{v_2})$ are proportional. Since in a two body collision the latter is conserved, a single species plasma does not radiate by bremsstrahlung.

A hot gas of low enough density that can be described as transparent to its own radiation at temperature above 10^5 K is ionized and consists of two different types of particles, the positive ions and the negative electrons. The thermal energy is shared among these different particles and is transferred from one particle to another through collisions. Radiation due to the acceleration of a charge in the Coulomb field of another charge is called *bremsstrahlung* . Electrons in thermal equilibrium have a well determined distribution of velocities (Maxwell–Boltzmann) and the radiation from such electron–ion collisions is a continuum whose shape is a function of the temperature while its intensity is given by (Vietri, 2006):

$$I(\nu,T) = \frac{32\pi\ e^6}{3m_e c^3}\left(\frac{2\pi}{3km_e}\right)^{\frac{1}{2}} T^{-\frac{1}{2}} Z_i^2 n_e n_i e^{-\frac{h\nu}{kT}} g \tag{1.1}$$

where k is the Boltzmann's constant, n_e and n_i the electron and ion density respectively, g is the Gaunt factor and Z_i is the charge of positive ions. It is interesting to note that for $T \to 0$ $I(\nu,T) \to 0$ because the dominant term is $e^{-\frac{h\nu}{kT}}$, thus a colder gas will emit less.

At temperature $T < 10^8$ K, the plasma chemical elements heavier than the hydrogen are not fully ionized and the atomic transition become important for elements with atomic number $Z > 8$. In particular, at $T \leq 10^7$ K the line emission from excited ions dominates the continuum one. The emission dependence on temperature can be described as follows (Charles & Seward, 1995):

- at temperature below $\sim 10^6$ K, most of the energy is radiated as ultraviolet lines
- a $T \sim 2{\times}10^6$ K half of the energy is emitted as soft X–rays ($0.1 < E < 5$ keV)
- at temperature $\sim 1{\times}10^7$ K all the energy is radiated as X–rays, half in lines and half as thermal bremsstrahlung
- at $T \sim 5{\times}10^7$ K all of the energy is radiated in the X–ray continuum.

Thus, by measuring X–ray spectra, the shape of the continuum and the presence of lines, one can recognize a hot gas emission. The strength and energies of the lines can also reveal the composition of the gas.

A large class of sources both galactic and extragalactic can be described by thermal emission from hot plasma. For instance, the majority of *active coronae* of stars in the H–R diagram emits X–ray radiation with luminosity L_X between 10^{26} and 10^{34} erg s^{-1}. Also the mechanism of accretion of matter that is transferred onto a compact object, such as white dwarfs (WDs), neutron stars (NSs) or black holes candidate (BHs), from a companion source in a *binary system* generates hot plasma with high X–ray luminosity in the range 10^{33}–10^{38} ergs^{-1}. Both single *galaxies* and *cluster of galaxies* radiate in the X–ray domain a large fraction of their energy output, the first with X–ray luminosity between 10^{38} and 10^{42} erg s^{-1}, the latter owing to the presence of inter-galactic medium at temperature $T \sim 10^8$ K.

1.3.2 Blackbody radiation

If an object at temperature T emits exactly the same wavelength and intensities of the absorbed radiation which would be present in an environment at equilibrium at temperature T, it is called “black body”. Thus a blackbody is defined as an object in thermal equilibrium with respect to an environment at temperature T that does not reflect or scatter radiation shining upon it, but absorbs and re-emits the radiation completely (Karttunen et al., 2003). When the blackbody is at temperature of million of Kelvin, these properties make it an ideal source of thermal soft X–ray radiation.

The spectrum radiated is defined by a continuum with peak emission at an energy dependent only on the temperature, T. At At higher temperature corresponds more energetic photons. The shape of the spectrum is given by (Charles & Seward, 1995):

$$I(\nu, T) = \frac{2h\nu^3/c^3}{e^{(h\nu/kT)} - 1} \tag{1.2}$$

where h is the Plank's constant, c is the speed of light and k is the Boltzmann's constant. At optical wavelengths, stars radiate as blackbodies with temperature from $\sim$ 2,500 K to $\sim$ 40,000 K. Although strongly modified by stellar atmosphere, the spectra retain the overall gross shape imposed by the blackbody emission process. A recently formed neutron star is expected to have a very hot surface. The surface blackbody emission in the X–ray energy range from neutron star has been observed, this can suggest that the surface temperature can reach one million degrees or higher.

1.3.3 Synchrotron radiation and Compton effects

When a fast and relativistic electron with mass m_e and energy $\gamma m_e c^2$ ($\gamma \gg 1$) traverses a region containing a magnetic field constant in module and direction

$\vec{B}=B_0\hat{z}$, changes direction because the field exerts a force perpendicular to the direction of motion. The electron acceleration is given by the following equation (Vietri, 2006):

$$\frac{d\vec{v}_\perp}{dt} = \frac{q\vec{v}_\perp}{\gamma mc} \wedge \vec{B} \tag{1.3}$$

which describes a rotating motion with Larmor's frequency:

$$\omega_c = \frac{qB_0}{\gamma mc} \tag{1.4}$$

From the (1.4) it is clear that the acceleration of the electron allows to emit a radiation with a frequency depending on the electron energy, on the magnetic field strength and on the direction of the motion relative to the magnetic field. This is called *synchrotron radiation.* In an astrophysical setting, the magnetic field can be somewhat aligned but particle velocities are expected to be isotropic, so the observed spectrum depends only on B_0 and the energy spectrum of the electrons. The radiated power for relativistic particles is given by (Vietri, 2006):

$$P = -\frac{2q^2}{3c^3}a^\mu a_\mu = \frac{2q^2}{3c^3}\vec{a}\cdot\vec{a} \tag{1.5}$$

Since $a_\perp$, in the relativistic limit, is equal to $\gamma^2 a_\perp$, and $a_{||}$ is negligible because in a motion in magnetic field the acceleration is always perpendicular to the velocity ($a_\perp=\omega_c v_\perp$), the (1.5) becomes (Vietri, 2006):

$$P = \frac{2q^2}{3c^3}\gamma^4\omega_c^2 v_\perp^2 = \frac{2q^4\gamma^2 B_0^2}{3m^2c^5}v^2 sen^2\theta \tag{1.6}$$

were θ is the angle between the velocity and the magnetic field.

The non-thermal emission can be produced by WDs and NSs since their magnetic field are quite strong , 10^7 G and 10^{11-12} G respectively, such fields are intense enough to accelerate the charged particles at relativistic speed trough the magnetosphere.

Of course, X–ray sources cannot always be understood on the basis of a single emission process. If NS and WD temperatures are high enough ($T \geq 10^6$ K), their surfaces can emit X–ray radiation with thermal spectra while their magnetosphere will accelerate particles which will produce non-tehrmal radiation.

The *Compton emission* is due to the interaction between photons and electrons with energy and momentum.

In classical physics, the Thomson diffusion is the main diffusion process. In this case the photons energies are the same before and after the collision process with the electrons (*coherent* or *elastic scattering*) and no energy is transferred between photons and electrons. When the electrons recoil is present, there is the exchange of energy both from photons to electrons and vice versa (*Compton effect* and *inverse Compton effect* respectively). The most interesting process takes place when a relativistic electron ($\gamma \gg 1$) collides with a photon with energy $h\nu_i$, in the laboratory reference system. In the electron reference system, the photon energy is:

$$h\nu_i^{'} = h\nu_i\gamma(1 - \beta\ cos\theta) \tag{1.7}$$

where β=v/c and θ is the angle between the photon and electron directions. After the diffusion, in the electron reference system, assuming $h\nu_i^{'} \ll m_e c^2$ the final photon energy is:

$$h\nu_f^{'} \approx\ h\nu_i^{'} \left(1 - \frac{h\nu_i^{'}}{m_e c^2}(1 - cos\Theta)\right) \tag{1.8}$$

where Θ is the deflection angle; in this reference system the photon energy is not changed. On the contrary, in the laboratory reference system the photon energy is:

$$h\nu_f^{'} = h\nu_i^{'}\gamma(1 + \beta\ cos\theta_1) = h\nu_i\gamma^2(1 + \beta\ cos\theta_1)(1 - \beta\ cos\theta) \tag{1.9}$$

In the case of collisions with relativistic electrons, photons can increase their energy of a γ^2 factor, making the *inverse Compton* process the most efficient mechanism to produce high energy radiation.

For both *synchrotron* and *Compton* processes, the relativistic particles energy distribution is given by:

$$I(E) = \frac{dN(E)}{dE} = AE^{-\alpha} \tag{1.10}$$

with photon index $2 \lesssim \alpha \lesssim 3$. Indeed, when a spectrum can be fitted by a power law over a reasonably large energy range, one can safely assume that a non-thermal mechanism is at work.

The central region of the Crab Nebula, where the magnetic field is ten times stronger than in other SNRs, the electrons responsible for the X–ray emission through synchrotron radiation have energy of about 10^4 GeV.

1.4 X–ray sources

Since the first all sky survey performed by the Uhuru satellite in '70s, it was apparent that X–ray sources belonged to different classes of objects from stars to AGNs. The brightest X–ray sources are distributed close to the galactic equator and tend to increase their spatial density towards the center of the Milky Way, while the less luminous ones have instead a nearly uniform distribution and are mostly extragalactic. The galactic sources are identified as stars, binary systems and supernova remnants, the extragalactic sources are identified as AGNs, single galaxy and cluster of galaxies. In this section a general overview of different classes of X–ray sources is given.

1.4.1 Stars

The study of the X–ray stellar emission allows to develop and to verify the theories formulated in the solar physics and generally to examine the physical plasma processes that have an important role also in the supernova remnants (SNRs) or in the accreting disc around a compact object (Rosner et al., 1985). After the launch of the *EINSTEIN* satellite, it was clear that X–ray emission characterizes stars of all spectral type. The emission from active stellar coronae is optically thin and the spectral distributions are spotted by emission features produced when an excited atom (Mg, Si, S, Ar, Ca, Fe) makes transition from higher to a lower level in the astrophysical plasma strongly ionized for the high temperature ($T \gtrsim 10^6$ K). In order to obtain the best fit physical parameters about the emissions lines, the metal abundances and the plasma temperature in keV, thus improving the information on the physical characteristics of an emitting plasma, the data can be described with a single or double thermal component[1] spectral model. Stars of different spectral types behave as follows (Pallavicini, 1989; Rosner et al., 1985).

- *Early–type stars.* This group includes the O and B stars. The most luminous, most massive are the O stars. Starting with more then 25 $M_\odot$ of material they burn their nuclear fuel at a prodigious rate. They live only a short time and end in a brilliant supernova explosion. These objects are strong X–ray emitters with luminosity $L_X \sim 10^{29-34}$ erg s^{-1} and, since their surface temperature reaches the $\sim 4{\times}10^4$ K, most of energy is radiated in the ultraviolet range. The luminosity and bolometric luminosity are tied by the relation $L_X \sim L_{bol}^{\alpha}$, with $6.5 \lesssim \alpha \lesssim 7$ (Cassinelli et al., 1985). The most luminous O star known in the Milky Way galaxy is HD93129A, located in the Carina nebula, characterized by a bolometric luminosity of $\sim 2{\times}10^{40}$ erg s^{-1}.

- *Type A stars.* Stars with spectral from B7 to A5, characterized by surface temperature of $\sim 9{\times}10^3$ K, have weak X–ray emission, below the 10^{27} erg s^{-1}.

- *Late type stars.* All the main sequence stars, with spectral types from F to M, have surface temperature between 7,000 K and 3,000 K. Their X–ray spectra are due to thermal bremsstrahlung from a plasma with temperature of $\sim 10^7$ K and luminosity $L_X \sim 10^{27-30}$ erg s^{-1}.

- *Type M stars.* They are prominent X–ray emitters, the L_X and L_{bol} ratio is $\sim 10^{-3}$-10^{-2}, but from the spectral type M5, the emission decreases in the X–ray energy range. dMe (dwarf Me) are characterized by highly variable emission with luminosity of $2{\times}10^{30-34}$ erg s^{-1}.

---

[1] `bremss`, `mekal` or `apec` in `XSPEC`

- *Giant and supergiant stars.* Giant stars not very bright in the X–ray energy range, if one compares the X–ray luminosity versus the optical one. In fact, their luminosity is $L_X \sim 10^{28-30}$erg s^{-1}.

- *Binary systems RS and CVn.* These binary systems, encompassing a type K0 IV/V subgiant and a main sequence star, show bright flares releasing an energy of $\sim 10^{35}$ erg, corresponding to an X–ray luminosity of 10^{30-31} erg s^{-1}.

The theoretical interpretation of the observed data is based on the physical differences between the early-type stars (O and B) and the late type ones (F-M). The X–ray luminosity of the early-type stars is tied to the bolometric one ($L_X \sim 10^7\ L_{bol}$) while the luminosity of the F-M stars is $L_X \sim v_{rot}^2$, where v_{rot} is the rotational velocity. Such different behaviour is due to different heating mechanisms at work in the stellar coronae of early type and late type stars stars:

- for early type stars, the model is based on the action of strong, massive winds ($\dot{M} \sim 10^{-5}$-$10^{-8}\ M_\odot\ ys^{-1}$) characterized by high velocity ($v \sim 10^{-3}$ km s^{-1}) and driven by the stellar radiative pressure (early type stars are completely radiative except for the central nucleus)

- for late type stars, the model is based on dynamo mechanism in a rotating star. This mechanism produces a magnetic field under the photosphere that induces convective currents.

1.4.2 X–ray pulsars and supernova remnants

The idea of neutron stars (NS) can be traced back to the early 30's, when Subrahmanyan Chandrasekhar, while investigating the physics of stellar evolution, discovered that a collapsed stellar core with a mass more than 1.4 times the solar mass $M_\odot$ cannot counteract its own gravity, once its nuclear fuel is exhausted (Chandrasekhar, 1931). This implies that a star core with $M > 1.4\ M_\odot$ would keep collapsing and eventually disappear from view. After the discovery of the neutron in 1932, Lev Landau was the first who speculated on the possible existence of a star composed entirely of neutrons (Landau, 1932). Using the Fermi-Dirac statistics and basic quantum mechanics, he was able to estimate that such a star, consisting of $\sim 10^{57}$ neutrons, would form a giant nucleus with a radius $R \sim \frac{\hbar}{m_n c}\sqrt{\frac{c\hbar}{Gm_n^2}} \sim 3{\times}10^5$ cm. Neutron stars became an astronomical reality with the discovery of pulsars (Hewish et al., 1968). Following the ideas proposed of Pacini and Gold (Pacini, 1967, 1968; Gold, 1968, 1969), the radio pulsar population, listing currently about 2,000 objects, can be interpreted as rapidly spinning, strongly magnetized isolated neutron stars radiating at the expense of their rotational energy. This useful concept allows to obtain a wealth of information on basic pulsar parameters just from measuring the pulsar's period and period derivative. The pulsars are characterized by strong magnetic field, up to $\sim 10^{14}$ G, and rotation periods from few tenths of milliseconds to few second. The rotation-powered pulsars are most widely known for their radio emission which is interpreted as a coherent process, indeed coherent curvature radiation has been proposed as the most promising mechanism (Michel, 1991). On the other hand, the optical, X–ray and gamma–ray emission observed in a subset of the pulsar family must be incoherent. Therefore, the fluxes in these energy bands are directly proportional to the densities of the radiating high-energy electrons in the acceleration regions.

The high energy radiation detected from rotation-driven pulsars has been attributed to various thermal and non-thermal emission processes.

Non-thermal emission is generated from charged relativistic particles accelerated in the pulsar magnetosphere. As the energy distribution of these particles follows a power–law distribution, the emission is also characterized by "power–law–like" spectra in broad energy bands. The emitted radiation can be observed from optical to the gamma–ray band.

It is possible to observe the extended emission from pulsar-driven synchrotron nebulae. Depending on the local conditions, such as the density of the interstellar medium and its magnetic field, these nebulae can be observed from radio through hard X–ray energies.

From the hot surface of a cooling neutron star, soft X–ray emission has been detected. In this case, a modified blackbody spectrum and smooth, low-amplitude intensity variations with the rotational period are expected, from the optical through the soft X–ray range (Greenstein & Hartke, 1983; Romani, 1987).

Thermal soft X–ray emission from the neutron star's polar caps, heated by the relativistic particles streaming back to the surface from the pulsar magnetosphere, has also been detected. (Kundt & Schaaf, 1993; Caraveo et al., 2004; De Luca et al., 2005; Manzali et al., 2007).

Young neutron stars are associated with their supernova remnants (SNRs) which represent another class of X–ray sources. At the end of a massive stellar evolution, the supernova explosions occurs and, after this cataclysmic event, the ejected matter at high velocity collides with the interstellar medium. The pressure of the matter compresses and heats the interstellar medium to high temperature and the hot spherical gas in expansion emits thermal radiation with X–ray luminosity of $\sim 10^{30-37}$ erg s^{-1}. The energy distribution follows a bremsstrahlung continuum spectrum with emission lines. The X–ray observations trace both the supernova remnants and the compact objects that may reside within them. Neutron stars and neutron star candidates have been found in a small fraction, $< 10\%$, of the 220 known galactic SNRs (Kaspi et al., 1999; Green, 1998). Less than half of these objects are radio pulsars, the others are radio-quiet neutron stars which are seen only in X–rays. The young radio pulsars can be divided in two groups, Crab-like (age less 1,000

y) and Vela-like (age in excess of 10,000 y) pulsars, according to somewhat different phenomenology apparently associated with the evolution of pulsar properties with age. The radio-quiet neutron stars include anomalous X–ray pulsars (AXPs), soft gamma–ray repeaters (SGRs), and quiescent neutron star candidate.

1.4.3 X–ray binary systems

A large number of binary systems made by a collapsed object (often defined as the “primary star”) and a donor companion star (the “secondary star”) were discovered and studied in the X–ray domain (King, 1995). In most cases, the efficient energy production is due to the accretion of matter (Frank et al., 1992) from the secondary star into the gravitational well of the collapsed objects. Up to 10-42% (depending on the compact object) of the rest-mass of the accreting flow can, in principle, be converted into radiation, the bulk energy of which falls in the X–ray band. The compact object can be a white dwarf (WD), a neutron star (NS) or a black hole (BH). The systems containing a NS or a BH and a massive losing-mass star, such as the early-type stars, are named *High Mass X–ray Binary* (HMXRB); if the losing-mass star is a late-type star (K, M) the binary system is known as *Low Mass X–Ray Binary* (LMXRB). The efficiency of the accretion is high and can yield X–ray luminosity of $\sim 10^{38}$ erg s^{-1}. If the compact object is a WD, the binary system is known as Cataclysmic Variable, its luminosity is $L_X \sim 10^{30-32}$ erg s^{-1}.

- *HMXRB*. These X–ray binary systems, distributed close to the galactic plane, where young stars are more common, are characterized by a compact object with a early-type star companion (typically an early type O-B star) of 10-40 $M_\odot$ (Ilovaisky, 1985; White, 1985; Van Paradijs, 1998). The compact object can accrete matter from the companion which loses mass in the form of stellar wind. The companion star is known to emit a strong stellar wind when its mass is greater than $\geq 10\ M_\odot$, making the compact star a bright X–ray source. In this configuration, the optical luminosity of the companion star dominates the total emission from the system and the rate of mass transfer is determined by the strength and the speed of the wind as well as by the orbital separation. Typically, it is possible to distinguish two HMXRB classes:

    1. persistent sources:

        - the secondary star is very luminous and massive and has a very strong stellar wind ($v_w \sim 10^3$ km s^{-1}) with a mass loss rate of $\dot{M} \sim 10^{-6}$-$10^{-4}\ M_\odot$ yr^{-1}
        - the accretion of matter onto the compact object occurs for gravitational capture of the companion stellar wind (Henrichs, 1983; Frank et al., 1992; King, 1995)

    - Periodic variations in the light curve are observed when the companion star occults the primary object
    - if the compact object is a NS, intense X–ray pulsations could be seen. The strong magnetic field drives the accreting matter onto the magnetic poles and, owing to the "lighthouse" effect, the observer can detect pulsations (~ 1 s) and the NS rotational velocity.
  2. transient sources:
    - the companion source is a main sequence star, typically a B-type star with prominent optical emission lines
    - the accretion of matter onto the compact object is episodic because either the stellar wind is equatorial or the companion orbit is eccentric

- *LMXRB*. These X–ray binary systems, with a higher density towards the galactic center where older stars are dominant, are formed by a compact object with a late-type star companion with $M \lesssim 1\ M_{\odot}$ (White, 1985; Van Paradijs, 1998). Also in this case, two LMXRB classes are reported:

  1. persistent systems:
    - typically the companion star is a cold A-type star, not very luminous, without significant stellar wind (Henrichs, 1983; Frank et al., 1992; King, 1995)
    - the mass transfer on the compact object is characterized by an accretion disc and occurs mainly through Roche-lobe overflow (Petterson, 1978)
    - the source light-curve exhibit erratic variations probably due to the geometric structure of the disc characterized by a bulge which, if the inclination is appropriate, can occasionally eclipse the compact object
    - X–ray flux variability is typical of the systems with a NS
  2. transient systems:
    - the physical characteristics are very similar to those of the persistent systems, but the mass transfer is more variable. The systems alternate periods of quiescence to periods of activity in which the accretion onto the compact object increases and the X–ray luminosity is $\gtrsim 10^{33}$ erg s^{-1}.

1.4.4 Galaxies and cluster of galaxies

Thanks to the *EINSTEIN* satellite, it was possible to observe that galaxies of all morphological types are X–ray sources, with soft X–ray luminosity between 10^{38} and 10^{42} erg s^{-1}. Spiral and elliptical galaxies exhibit a different behaviour:

1. *Spiral galaxies* In the spiral galaxies, the majority of the X–ray emission is due to bright point sources, such as accreting binary systems, supernova remnants and stars. In fact, the X–ray/optical flux ratio, measured from these galaxies, is bigger than the value expected for a normal star population. Furthermore, the dominant class of X–ray sources seems to vary as a function of the galaxy type. In late-type galaxies, with well developed spiral arms, the population I is dominating, while in early-type galaxies with a prevalent central bulge, globular clusters stars of older population play a major role. The X–ray luminosity profile follows the disc optical one but in the internal regions, underlining the existence of a prevalent young stellar component in the external parts of the galaxies. On the contrary, the excess in central regions may point to the presence of a brighter source population. Thermal emission from the galactic disk interstellar medium, heated by supernova remnants, is an additional source of X–ray emission. Spiral galaxies total X–ray luminosities are in the range 10^{38-41} ers s^{-1} and appear to be proportional to the B band emission. Indeed, for all morphological types, the ratio L_X/L_B values are centered around 10^{-7}.

2. *Elliptical galaxies* Halos of very hot gas characterize elliptical and S0 galaxies. Elliptical galaxies X–ray luminosity are included between 10^{39-42} erg s^{-1} except for galaxies dominant the clusters for which the luminosity is 10^{43} erg s^{-1}. This kind of X–ray emission can reach radius of 70 kpc. The halo heating is due to stellar motion, supernova explosions and the gravitational drop of gas in the potential central hole; if the gravity is prevalent, it allows to limit the hot gas in its emission volume, instead, if the heating due to supernova explosion is prevalent, the limit must be granted by the combination of radiative cooling and interstellar medium pressure.

The largest aggregations of matter that can be detected as visible entities are not the galaxies. The large-scale structure of the universe has been determined by measuring the distribution and motion of galaxies in the space. Although on the largest scale the arrangement of matter in the universe is uniform, the galaxy distribution is not random on the intermediate level where galaxies are found in gravitationally bound aggregates referred to as “groups” and “clusters”. Clusters are defined as increases in the galaxy surface density and Abell’s criteria (Abell, 1958) allow to identify them:

1. a cluster contains at least 50 galaxies in the magnitudes range between m_3 and $m_3 + 2$, where m_3 is the magnitude of the third brightest galaxy

2. these galaxies have to be located in a region with a radius of $\sim$ 1.7 arcmin/z, where z is the estimated cluster redshift

3. the estimated cluster redshift is in the range 0.02-0.2

From the X–ray emission point of view, galaxy clusters have the following properties:

- they are the most common extragalactic X–ray sources
- their X–ray luminosity is in the rage 10^{43-45} erg s^{-1},thus making them the second brightest source class after the quasars
- they are extended sources
- their spectra don't show absorption in the low energy
- their X–ray emission is constant

Such properties suggest that the X–ray emission has a diffuse origin due to the presence of high temperature intergalactic gas rather than to single source contributions. The spectra analysis can provide insights on the X–ray emission mechanism:

- the majority of the observed X–ray radiation is due to thermal bremsstrahlung from an hydrostatic equilibrium plasma with temperatures as high as ($T = 2\times10^{7-8}$ K); if the gas is contaminated by heavy elements, emission lines can be observed
- a small fraction of the emission is of non-thermal origin and is due to the inverse Compton process whereby relativistic electrons upgrade low energy photons into X–ray ones.

The morphological characteristics of galaxy clusters can be used to classify them on the basis of observational parameters such as the overall luminosity distribution or the presence of a main central galaxy. Irregular clusters are characterized by emissions peaks due to single galaxies while regular clusters are characterized by a central emission with a smooth shape. In the latter case it is possible to distinguish clusters dominated by the central galaxy emission from the others.

1.4.5 Active galactic nuclei

Active galactic nuclei (AGNs) are extragalactic sources with high absolute luminosity in all energy ranges (from radio to gamma-ray. They are associated to the central regions of galaxies, although for more distant objects the host galaxy is much too faint to be detectable. Their emission is dominated by non-stellar processes because their luminosity, comparable to that of billions of stars, comes from regions $< 1\ pc^3$. The observed X–ray luminosity ranges from 10^{41} to 10^{48} erg s^{-1}, typically "normal" AGNs have luminosities in the range 10^{42-45} erg s^{-1}. The central engine is probably accretion into a black hole with mass values ranging in the interval $\sim 10^{7-9}\ M_\odot$. Although various classes of AGNs have been recognized, all different phenomenologies can be explained in the framework the unified astrophysical model (Urry & Padovani, 1995; Antonucci & Miller, 1985) on the basis of different orientations between the objects' jets and the line of sight. The main AGN classes are as follows:

- *Quasar* are the more distant and most luminous sources in which the X–ray luminosity of the central bulge ($\sim 10^{45-47}$ erg s^{-1}) dominates the whole galaxy. It is possible to further distinguish two subclasses, the quasar with high radio emission (radio loud) and the quasar characterized by a low radio emission (radio quiet).

- *Seyfert galaxies* are spiral galaxies with very bright nuclei. Their X–ray luminosity is $L_X \sim 10^{43-45}$ erg s^{-1}. Seyfert galaxies are divided in two classes that can be easily recognized owing to differences in the emission lines in their optical spectrum. The Seyfert 1 galaxies show a blue continuum with large allowed lines and narrow forbidden ones, while the Seyfert 2 spectrum is characterized only by narrow forbidden features. The nucleus is encircled by a ring of dust which is responsible for the occultation of the radiation from the nucleus itself and from the dust clouds (broad line region) around the center bulge, responsible of the broad emission lines. The difference between Seyfert 1 and Seyfert 2 galaxies is due only to their orientation with respect to the direction of the observer line of sight.

- *Blazars* they are very variable on all time scales and are characterized by a high degree of polarization. They are AGNs with the jet facing almost exactly the observer.

Chapter 2

The *XMM–Newton* satellite

2.1 The mission

The *XMM–Newton* (X–ray Multi-mirror Mission) is a “cornerstone” project in the ESA programme for space science. This satellite launched on December 10th, 1999 carries three Wolter type-1 X–ray telescopes, with different X–ray detectors, and a 30 cm optical/UV telescope with a microchannel-plate pre-amplified CCD detector in its focal plane. The three types of science instruments are: *European Photon Imaging Camera* (*EPIC*), three CCD cameras for X–ray imaging (Jansen et al., 2001), moderate resolution spectroscopy, and X–ray photometry, *Reflection Grating Spectrometer* (*RGS*), two spectrometers for high–resolution X–ray spectroscopy and spectro–photometry (den Herder et al., 2001), *Optical Monitor* (*OM*), the instrument for optical/UV imaging and grism spectroscopy (Figure 2.1). *XMM–Newton* offers the possibility to perform the simultaneous studies of the sky sources in the two different electromagnetic windows X and optical/UV.

The most important characteristics of *XMM–Newton* can be summarize in this way:

- *Simultaneous operation of all science instruments.*
  All six *XMM–Newton* science instruments operate simultaneous and independently (exposures of the individual instruments do not necessarily start and end at the same time).

- *High sensitivity.*
  X–ray telescopes have the largest effective area of focusing telescope ever (Table 2.1). The total mirror geometric effective area at 1.5 keV energy is $\sim$ 1,550 cm^2 for each telescope, with 4650 cm^2 in total.

- *Good angular resolution.*
  The achieved poin–spread function (PSF) has a full width at half maximum (*FWHM*) on the order of $6''$ and a *HEW*, at which 50% of the total energy are encircled, of $\sim 15''$ (Table 2.1).

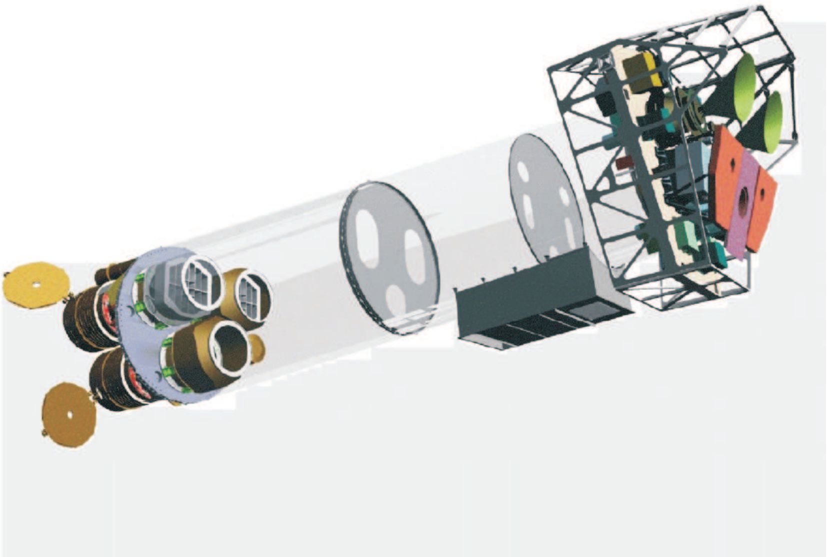

Figure 2.1: *The* XMM–Newton *payload. The mirrors modules, two of which are equipped with* RGS*, are visible at the lower left. At the right end, the focal X–ray instruments are shown: the* EPIC MOS *cameras with their radiators (green), the radiator of the* pn *camera (violet). The* OM *telescope (orange) is obscured by the lower mirror module.*

- *Moderate and high spectral resolution.*
  The *EPIC* CCD cameras have moderate spectral resolution (with a resolving power $E/\Delta E$ of $\sim$ 20–50), the *RGS* spectrometers offer much higher spectral resolution, with a resolving power in the energy range of 200–800.

- *Simultaneous X and optical/UV observations.*
  Observations with co–aligned *OM* opticla/UV telescope render possible the monitoring and identification of optical/UV counterparts of X–ray sources.

- *Long continous target visibility.*
  The highly elliptical orbit offers continuous target visibility of up to $\sim$ 40 hours, with a minimum height for science observations of 46,000 km.

2.2 The *XMM–Newton* mirrors

XMM–Newton's three X–rat telescopes are co–aligned with an accuracy of better than $\sim 1'$. The 44% of the incoming light focused by the multi-shell grazing incidence mirrors is directed onto the camera at the prime focus, while

Table 2.1: *Comparison of* XMM–Newton EPIC *characteristics with the most recent X–ray telescopes.*

Satellite	FWHM (”)	HEW$^{(a)}$ (”)	Energy range (keV)	A_{eff} a 1 keV (cm^2)
XMM–Newton (EPIC)	6	15	0.15-15	4650
Chandra	0.2	0.5	0.1-10	800
ROSAT	3.5	7	0.1-2.4	400
ASCA	73	174	0.5-10	350

$^{(a)}$ radius within the 50% of the energy.

Table 2.2. *Mirror module characteristics.*

Mirror module parameter	Value
Focal length	7.5 m
Mirror diameter and thickness outermost	700 mm (1.07 mm)
Mirror diameter and thickness innermost	306 mm (0.47 mm)
Mirror length	600 mm
Packing distance	1-5 mm
Number of mirrors	58
Reflective surface	Gold (250 nm layer)
Mirror module mass	420 kg

the 40% of the radiation is dispersed by a grating array onto a linear strip of CCDs (RGS). The remaining light is absorbed by the support structures of the RGS. The mirror module is a grazing incident telescope (Wolter type-1, Aschenbach et al. (2000)) which is designed to operate in the X–ray energy range of 0.1-12 keV with a focal length of 7.5 metres and with a resolution of 16 arcsec. The mirror module consists of 58 nested mirror shells bonded at one end on a spider and their supporting structure, the most important characteristics are shown in the Table 2.2.

Each mirror is shaped to a paraboloid surface in front and an hyperboloid surface at the rear for double reflection of the grazing X–rays. The 58 mirror shells are mounted in a co-focal and coaxial configuration and are glued at their entrance plane to the 16 spokes of a spider (spoke wheel) made out of Inconel; this material was chosen for its thermal expansion close to that of the electrolytic nickel of mirrors. To minimize the mechanical deformations of the mirrors and therefore the optical degradation, the flatness of the mounting interface between the spider and the MIS (Mirror Interface Structure), which is a surface with an inner diameter of 740 mm an the outer diameter of 770 mm, needs to be better than 5 μm. The X–ray mirrors are thin monolithic gold-coated nickel shells and their manufacturing is based on a replication process, which transfer a gold layer deposited on the highly polished master mandrel to the electrolytic nickel shell which is electroformed on the gold layer.

2.2.1 The image quality

The first critical parameter determining the quality of a X–ray mirror module is its ability to focus photons. The core of its on–axis point–spread function (PSF) is sharp and varies little over a wide energy range (0.1-4 keV). Above 4 keV, the PSF becomes only slightly more energy dependent. The values for the full width at half maximum (*FWHM*) and half energy width (*HEW*) of the PSF are listed in Table 2.3. For on-axis sources, high energy photons are reflected and focused predominately by the inner shells of the telescopes. The inner shells apparently give better focus than the average of the shells, hence the fractional encircled energy increases with increasing photon energy. Above 12 keV, the effective area, A_e is very small, which makes simulations and calibrations of the PSF at such high energies unreliable.

The PSF of the X–ray telescopes depends on the source off-axis angle and azimuth, i.e., its distance from the centre of the field of view. The effect is that the PSF at large off-axis angles is elongated due to the off-axis aberration (astigmatism).

The angular resolution, and the corresponding image quality, is basically determined by the PSF of the mirror modules. This is due to the fact that the *MOS* and *pn* cameras have pixels with size of 40 and 150 μm, respectively. For the focal length of the X–ray telescope (see Table 2.2), this corresponds to $1.1''$ ($4.1''$) on the sky. Given the *FWHM* of the PSF of $\sim 6''$, the Nyquist theorem is thus fulfilled for the *MOS* cameras and the images are fully sampled. The pixel size of the *pn* camera slightly undersamples the core of the PSF.

2.2.2 X–ray effective area

The second important characteristic of the mirror performance is their effective area, A_e, which reflects the ability of the mirrors to collect radiation at different photon energies. The definition of effective area is: $A_e = A_{geom} {*} QE_T(E)$ where A_{geom} is the mirrors geometric area and $QE_T(E)$ is the detection probability of a photon with energy E, assumed the focalization mirrors efficiency and the FoV cameras detection probability (*quantum efficiency*). The *quantum efficiency* of both *EPIC* CCD chips is a function of photon energy. As shown in the Figure 2.2, can be seen that the *XMM–Newton* mirrors are most efficient in the energy range from 0.1 to 12 keV, with a maximum at above 1.5 keV and a pronounced edge near 2 keV (the Au M edge). The effective areas of the *MOS* cameras are lower than that of the *pn*, because only part of the incoming radiation falls onto these detectors, which are partially obscured by the RGS. Not only the shape of the X–ray PSF, but also the effective area of the mirrors is a function of off-axis angle within the mirrors' $30'$ FoV. With the increasing off-axis angle, less of the photons entering the telescopes actually reach the focal plane. This effect is called "vignetting".

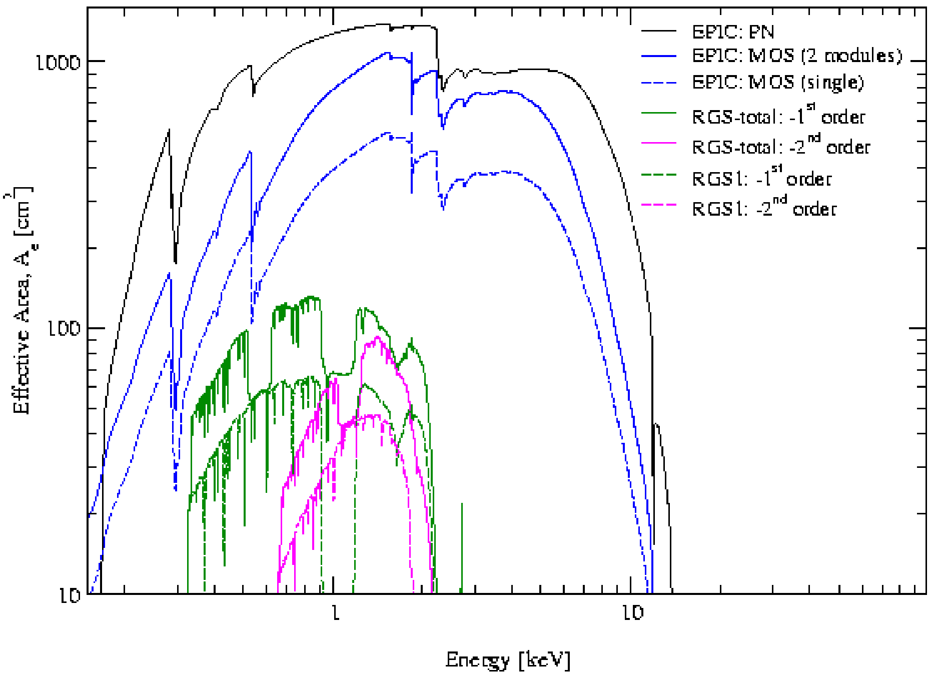

Figure 2.2: *The net effective area of all* XMM–Newton *X–ray telescopes, combined with the response characteristics of the focal instruments,* EPIC *and* RGS*.*

2.3 European Photon Imaging Camera (EPIC)

In two of the focal planes of two *XMM–Newton* X–ray telescopes are located the *EPIC MOS* (Metal Oxide Semi–conductor) CCD arrays (Turner et al., 2001), in the third a different CCD camera called *EPIC pn* (Strüder et al., 2001) is present. In a nutshell, the *EPIC* cameras offer the possibility to perform extremely sensitive imaging observations over a field of view of $30'$ with the main characteristics reported § refmission and in the Table 2.3.

All *EPIC* CCDs (Jansen et al., 2001) operate in photon counting mode with a fixed, mode dependent frame read-out frequency, producing event list attributing (among others) to each photon the x and y position, its arrival time and energy. This allows for simultaneous imaging and non–dispersive spectroscopy due to the intrinsic energy resolution of the pixels.

The *MOS* chip arrays consist of 7 individual identical, front-illuminated chips (Figure 2.3, left). The individual CCDs are not co-planar, but offset with respect to each other, following closely the slight curvature of the focal surface of the Wolter telescopes. The *MOS* chip has a frame store region which serves as a data buffer for storage before they are readout through the readout nodes, while the rest of the chip is obtaining the next exposure. The core of the *pn* camera is a single silicon wafer with 12 CCD chips integrated (Figure 2.3, right) and back-illuminated, which affects the detector *quantum efficiencies* decisively.. The two types of *EPIC* cameras are fundamental different, not only hold for the geometry of the *MOS* chip array and the *pn* chip one but for other properties as well their readout times.

The *pn* type camera can be operated with very high time resolution down to 0.03 ms in the timing mode and 7 μs in the burst mode. This is possible because the readout of the *pn* chip is much faster than that of the *MOS* cameras, each *pn* pixel column has its own readout node.

2.3.1 EPIC operating modes

The *EPIC* cameras allow several modes of data acquisition. In the case of *MOS* the outer ring of 6 CCDs remain in standard imaging mode while the central |MOS CCD can be operated separately; thus all CCDs are gathering data at all times, independent of the choice of operating mode. The *pn* camera CCDs can be operated in common modes in all quadrants for full frame, extended full frame and large window mode, or just with one single CCD for small window, timing and burst mode.

- *Full frame and extended full frame mode (only* pn*)*: all pixels of all CCDs are readout and thus the full FoV is covered.

- *Partial window mode*

    1. *MOS*: the central CCD of both *MOS* cameras can be operated in a different mode of science data acquisition, reading out only part of

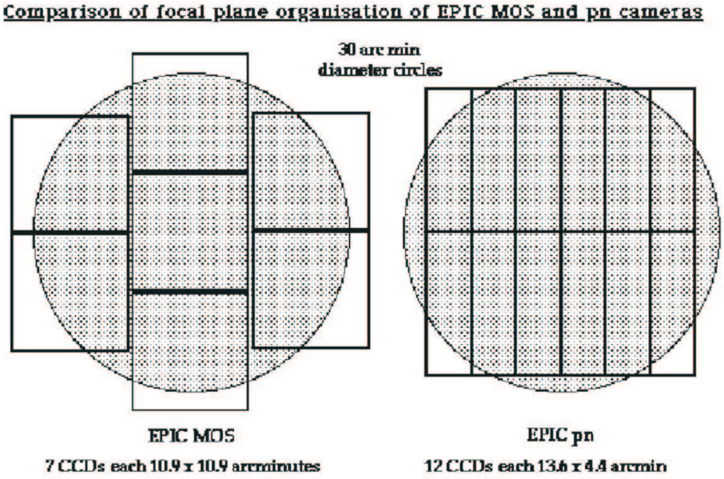

Figure 2.3: *A sketch of the field of view of two types og* EPIC *cameras,* MOS *(left),* pn *(right). The circle describes a 30′ diameter area.*

CCD chip.

2. *pn*: in large window mode only half of the area in all 12 CCDs is read out, whereas in small window mode only a part of CCD number four is used to collect data.

- *Timing mode*

  1. *MOS +pn*: the imaging is made only in one dimension, along the column RAWX axis. Along the row direction, data from a predefined area on one CCD chip are collapsed into a one-dimensional row to be read out at high speed. Since the two *MOS* cameras orientation differ by 90°, the "imaging" directions in the two *MOS* are perpendicular to each other.
  2. *pn* only: the "burst" mode offers very high time resolution, but has a very low duty cycle of 3%.

Table 2.3: *The most important* EPIC *characteristics.*

Camera	*MOS*	*pn*
Sensibility(b)	$\sim 10^{-14}$	$\sim 10^{-14}$
FoV	$30'$	$30'$
PSF (FWHM)	$5''$	$6''$
PSF (HEW)	$14''$	$15''$
Timing resolution	1.5 ms	0.03 ms
Spectral resolution (1 keV)	$\sim$ 70 eV	$\sim$ 80 eV

(b) after 10 ksec, in the 0.15-15 keV energy range and in erg $\mathrm{cm^{-2}s^{-1}}$ unit.

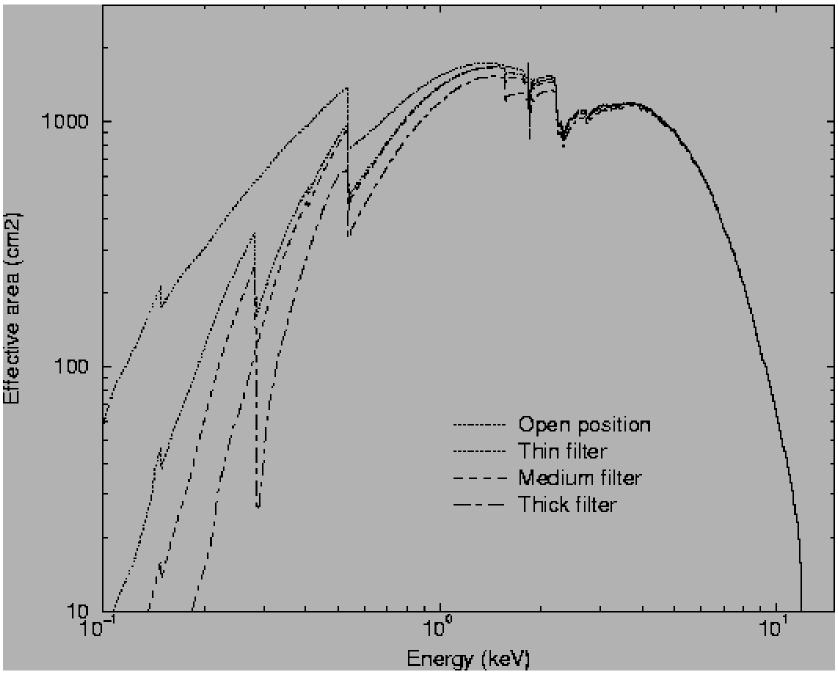

Figure 2.4: *The net effective area of the* pn *camera for each of the filters.*

2.3.2 EPIC filters and effective area

The last factor influencing the *EPIC* effective area, specifically in the low energy, is the choice of the optical blocking filter. These filters are used, because the *EPIC* CCDs are not only sensitive to X–ray photons, but also to IR, visible and UV light. Therefore, if an astronomical target has high optical to X–ray flux ratio, there is a possibility that the X–ray signal becomes contaminated by those photons. To prevent this, the *EPIC* cameras include aluminised optical blocking filters, and also an internal "offset table" to subtract the constant level of optical light or other systematic shifts of the zero level of charge measurements. Each *EPIC* camera is therefore equipped with a set of three separated filters, *thick*, *medium* and *thin*. It is necessary for the observer to select the filter which maximizes the scientific return, by choosing the optimum optical blocking required for the target of interest. Here a small description of the blocking filters:

- *Thick filter*: this filter should be used if the expected visible brightness of the target would degrade the energy scale and resolution of *EPIC*. It should be able to suppress efficiently the optical contamination for all point source targets up to magnitude (m_v) of 1-4 (*MOS*) or magnitude of 0-3 (*pn*). The range depends on the spectral type, with only extremely red or blue colours causing the change to 3 magnitudes fainter level.
- *Medium filter*: the optical blocking is expected to be about 10^3 less efficient than the thick filter, so it is expected that this filter will be useful

for preventing optical contamination from point sources as bright as magnitude of 8-10.

- *Thin filter*: the optical blocking is expected to be about 10^5 less efficient than the thick filter, so its use will be limited to point sources with optical brightness about 14 magnitudes fainter than the corresponding thick filter limitations.

The impact of the different filters on the soft X–ray response of both types of *EPIC pn* camera is shown in Figure 2.4.

2.3.3 EPIC background

The *EPIC* background can be divided into two parts: a cosmic X–ray background (CXB), and an instrumental background. The latter component may be further divided into a detector noise component, which becomes important at low energies (below 200 eV) and a second component which is due to the interaction of particles with the structure surrounding the detectors and the detectors themselves. This component is characterized by a flat spectrum and is particulary important at high energies (above a few keV). The particle induced background can be divided into two components: an external flaring component, characterized by strong and rapid variability, which is often totally absent and a second more stable internal component. The flaring component is currently attributed to soft protons, which are presumably funneled towards the detectors by the X–ray mirrors. The stable component is due to the interaction of high–energy particles (energy larger than some 100 MeV) with the structure surrounding the detectors. The component shows only small intensity variations in time which are typically observed on long time scales. The spectra are quite flat and present a number of spectral features due to fluorescence from the detectors and the structure surrounding them. Al-K and Si-K lines are clearly visible in the *MOS* spectrum. In the case of the *pn* Al-K and an intense complex due to Cu-K, Ni-K and Z-K lines around 8 keV is visible. The intensity of the quiescence component has been measured for both *MOS* and *pn* cameras during closed filter observations.

EPIC external flaring background

This component is produced by protons with energies less than a few 100 keV which are funneled towards the detectors by X–ray mirrors. When the soft proton cloud impacts against the *EPIC* instruments, the background lightcurve shows a rapid and strong variability. The spectra of soft proton flares are variable and no clear correlation is found between intensity and spectral shape. The current understanding is that soft protons are most likely organized in clouds populating the Earth's magnetosphere. The number of such clouds encountered by *XMM–Newton* in its orbit depends upon many factors, such as the altitude of the satellite, its position respect to the magnetosphere, and the amount of solar activity.

Chapter 3

A deep *XMM–Newton* serendipitous survey of a middle–latitude area

3.1 Introduction

Since the launch of *XMM–Newton* in 1999, the radio quiet neutron star 1E12 07.4-5209 in the supernova remnant (SNR) PKS 1209−51 has been the target of several observations, for a total of $\sim$ 450 ks scheduled time. Therefore, observations of this field make up one of the deepest X–ray surveys obtained at intermediate galactic latitude ($|b| \simeq 10°$). This gives the unique opportunity to sample, in the same survey, both the galactic and extra–galactic X–ray source population. Thanks to the wide energy range, high throughput, and good spectral resolution of the *European Photon Imaging Camera* (*EPIC*) (Turner et al., 2001), this data set allows us to investigate with high sensitivity both the distant population of quasi-stellar objects (QSOs), active galactic nuclei (AGNs), and normal galaxies, and the galactic population of stars and X–ray binaries (XRBs).

The two longest *XMM–Newton* observations, performed in August 2002 and corresponding to a total of $\sim$ 260 ks of net integration time, were used to study the pulsations and the absorption features of the neutron star 1E1207.4−5209 (Bignami et al., 2003; De Luca et al., 2004). As a by–product, we used the data of the two *Metal Oxide Semi-conductor* (*MOS*) cameras to investigate the population of the faint *serendipitous* sources detected in the field. This yielded to the detection of 196 serendipitous X–ray sources (Novara et al., 2006), which were characterised by a very interesting log$N$–log$S$ distribution. On one hand, in the 0.5–2 keV energy range it shows an excess with respect to both the Galactic Plane and the high–latitude distributions, which suggests a mixed population composed of both galactic and extra–galactic sources. On the other hand, in the 2–10 keV energy band the log$N$–log$S$ distribution is comparable to that derived at high galactic latitudes, thus suggesting that it is dominated by extra–galactic sources. The cross–match of the serendipitous X–ray sources with the version 2.3 of the *Guide Star Catalogue* (*GSC 2.3*) (Lasker et al. 2008) provided a candidate optical counterpart for about half of them, down to limiting magnitudes $B_J \sim 22.5$ and $F \sim 20$. For the 24 brightest sources it was possible to obtain a spectral characterisation and an optical identification was proposed for $\sim 80\%$ of them. Finally, the detailed spectral investigation of one of the brightest sources, characterised by a highly absorbed spectrum and an evident Fe emission line, and its optical identification with the galaxy ESO 217-G29, led to classify it as a new Seyfert–2 galaxy. These results prompted us to extend our analysis to the whole sample of the *XMM–Newton* observations of the 1E1207.4−5209 field. In addition to the observations published in Bignami et al. (2003) and De Luca et al. (2004), we thus have considered also the first observation of the field, performed in December 2001 (Mereghetti et al., 2002), and the sequence of the seven observations, performed during a 40 day window between June and July 2005 (Woods et al., 2007). In this way we have almost doubled the total integration time and significantly increased the count statistics. We used this enlarged data set to refine the study of the serendipitous X–ray source population. To this aim, we have also taken advantage of the improvements of the *XMM–Newton* data processing pipeline, which now minimises the number of spurious detections and provides a better source positioning. Moreover, we have performed dedicated follow-up optical observations with the *Wide Field Imager* (*WFI*) of the ESO/MPG 2.2m telescope, down to $V \simeq 24.5$, i.e. with a factor 10 of improvement in the flux limit compared to the *GSC 2.3* used in Novara et al. (2006).

This section is organised as follows: the X–ray observations and data reduction are described in § 3.2, while the serendipitous source catalogue and the analysis of its bright sub-sample are presented and discussed in § 3.3 and § 3.4, respectively. The optical observations and data analysis are described in § 3.5 and the cross–correlations of the X–ray and optical catalogues is described in § 3.6. The optical/X–ray classification of the brightest sources, as well as of the peculiar Seyfert–2 galaxy, are discussed in § 3.7.

3.2 X-Ray observations and data processing

3.2.1 Observations

1E1207.4−5209 was observed with *XMM–Newton* in ten different pointings from 2001 December 23 to 2005 July 31, for a net exposure time of ~ 346 ks. All the three *EPIC* focal plane cameras (Turner et al., 2001; Strüder et al., 2001) were active during these pointings: the two *MOS* cameras were operated in standard *Full Frame* mode, in order to cover the whole $30'$ field–

of–view; the *pn* camera was operated in *Small Window* mode, where only the on–target CCD is read–out, in order to time–tag the individual photons and provide accurate arrival time information. Since the interest is focused on the serendipitous X–ray sources only, the following analysis considers only data taken with the *MOS* cameras.

In Table 3.1 we report the *good time intervals* (*GTI*) of the two *MOS* cameras for each of the ten observations, i.e. the “effective” exposure times after the soft–proton rejection. In the seven 2005 observations the CCD number 6 of the *MOS* 1 camera was not active, since it was switched off in March 2005 due to a micrometeorite impact [1]. For the second and the third observations of Table 3.1 both *MOS* cameras were used with the thin filter, while the medium filter was used for all the other observations.

3.2.2 Data processing

For each pointing we obtained two data sets (i.e. one for each *MOS* camera) which we processed independently through the standard *XMM–Newton Science Analysis Software* (*SAS*) v.7.1.0. In the first step, the *XMM–Newton SAS* tasks `emproc` was used to linearize the *MOS* event files. In the second step, event files were cleaned up for the effects of soft protons flares. We filtered out time intervals affected by high instrument background induced by flares of soft protons (with energies less than a few hundred keV) hitting the detector surface. In order to avoid contributions from genuine X–ray sources variability, we selected only the single and double events (PATTERN$\leq$4) with energies greater than 10 keV and in the peripheral CCDs (CCD = 2-7). Then, we set a count–rate threshold for good time intervals (GTI) at 0.22 cts s^{-1}. By selecting only events within GTIs we finally obtained two “clean” event lists for each *MOS* data set, whose “effective” exposure times are reported in Table 3.1.

3.2.3 Source detection

The *EPIC* images of the 1E1207.4−5209 field show the presence of several faint X–ray sources. Therefore, we have used a source detection algorithm in order to produce a catalogue of the serendipitous X–ray sources in the field.

In order to increase the *signal–to–noise (S/N)* ratio of our detections and to reach fainter X–ray flux limits, we used the *SAS* task `merge` to merge, for each of the ten pointings, the clean linearised event lists of the two *MOS* cameras. As seen from Table 3.1, we have divided the data set in two time windows: the first spanning from 2001 December 23 to 2002 August 06 (three observations), the second spanning from 2005 June 22 to 2005 July 31 (seven observations). We have decided to run the source detection on each of these two observation subsets separately, in order to search for long term source variability (§ 3.4.2). Although it would be interesting to look also for variability

---

[1] http://xmm.vilspa.esa.es/external/xmm_news/items/MOS1-CCD6/index.shtml

Table 3.1: *Log of the* XMM–Newton *observations of the 1E1207.4−5209 field with the net good time interval for the two* EPIC/MOS *cameras.*

Observation ID	*XMM–Newton* revolution	Date (UT)	GTI (ks) MOS1	GTI (ks) MOS2
0113050501	374	2001-12-23T18:59:41	24.3	25.2
0155960301	486	2002-08-04T07:25:09	105.3	105.8
0155960501	487	2002-08-06T07:17:29	100.7	102.0
0304531501	1014	2005-06-22T12:10:05	15.1	15.1
0304531601	1020	2005-07-05T00:44:58	18.3	17.9
0304531701	1023	2005-07-10T06:43:47	7.1	9.3
0304531801	1023	2005-07-11T02:00:45	56.6	54.5
0304531901	1024	2005-07-12T11:08:22	3.5	3.2
0304532001	1026	2005-07-17T00:18:21	12.7	10.7
0304532101	1033	2005-07-31T14:03:09	2.5	2.1

on shorter time scales, we have not run the source detection for each of the ten observations in Table 3.1. Indeed, with the only exceptions of the 2002 observations and the fourth observation of the 2005 data set, all observations have a by far too short integration time to allow for a statistically significant time variability analysis. Therefore, we merged the cleaned event files of the 2001/2002 and 2005 observation subsets separately to obtain, for each of them, three total images in three selected energy bands: the two standard coarse soft/hard energy bands 0.5–2 keV and 2–10 keV, and the total energy band 0.3–8 keV.

In order to perform the source detection, for each image we need a corresponding exposure map, to account for spatial quantum efficiency *(QE)* variations, mirror vignetting, and effective field of view. Unfortunately, it is not possible to obtain a correct exposure map from an image based on the merged event file. Therefore we had to produce the required exposure maps with a different procedure.

For each observation we used the cleaned event file to produce *MOS1* and *MOS2* images in the three selected energy bands and, then, the corresponding exposure maps. Since different observations correspond to different pointings, which have different aspect solutions, we corrected, for each of the three energy bands, the coordinates measured on the *MOS* exposure maps through a relative coordinate transformation. To this aim, for each of the two time windows we selected the image with the longest exposure time and took it as reference to register all *MOS* exposure maps; we used the *IRAF* task `wregister` to compute the frame coordinate transformation and apply the exposure map registration. At the end, for each energy band we merged the exposure maps of each observation and *MOS* camera, thus obtaining the total exposure map corresponding to the total image previously extracted from the merged event file. Finally, we applied the same procedure also to the ten observations together, in order to maximize the S/N ratio.

At this point, we run the source detection on the three sets of merged data. We give below details about the procedure used to run the source detection, for each energy band, in each of the three sets of observations: the 2001/2002 and the 2005 subsets defined in Table 3.1 and the whole observation set.

1. For each observation set, and for each energy band, we have run the *SAS* task `eboxdetect` in *local mode* to create a preliminary source list. Sources have been identified by applying the standard *minimum detection likelihood* criterion, i.e. we have validated only candidate sources with detection likelihood -*ln* $P \geq 8.5$ (Novara et al., 2006), where P is the probability of a spurious detection due to a Poissonian random fluctuation of the background. This corresponds to a probability $P = 2{\times}10^{-4}$ that the source count number in a given energy band originate from a background fluctuation. This implies a contamination of at most 1 spurious source per energy band.

2. Then, we have run the task `esplinemap` to remove all the validated sources from the original image and to create a background map by fitting the so called *cheesed image* with a cubic spline.

3. For each observation set, and for each energy band, we have run again the task `eboxdetect` in *map mode*, using as a reference the calculated background map. For each set, we have added the likelihood values from each individual energy band and we have transformed them to *equivalent single band* detection likelihoods, and a threshold value of 8.5 was applied to accept or reject a detected source.

Unfortunately, even using the maximum number of spline nodes (20), the fit performed in step 2 (see above) is not sufficiently flexible to model the local variations of the background, due to the presence of the bright SNR G296.5+10.0. Therefore, it was necessary to correct each background map *pixel by pixel*, measuring the counts both in the *cheesed image* and in the background map itself by applying the correction algorithm described in Baldi et al. (2002). All sources have been checked against the corrected background maps and all their parameters calculated again. Finally, for each energy band, the revised source list has been filtered to include, again, only sources with corrected detection likelihood -*ln* $P > 8.5$.

3.2.4 Source list

At the end of the source detection process we have thus produced, for each of the three observation sets, a master list including only sources with detection likelihood -*ln* $P > 8.5$ in *at least* one of the three energy bands and manually screened to reject residual false detections. For each source, the master list provides various parameters like, e.g. the detector and sky coordinates, the effective exposure time and, for each of the three energy bands (soft/hard/total), the total counts, count–rate and errors, the *S/N* ratio, and the detection likelihood. The master list does not include quantitative information on the source extension, which can be used for a preliminary morphological classification (point–like or extended). This is because the significant distortion of the PSF at large off–axis angles (where most serendipitous sources are detected), together with the coarse spatial resolution of the *MOS* cameras ($1''.1$/pixel), would make the determination of the source extension uncertain. In order to estimate a sky coordinate uncertainty for all the detected sources, we have recomputed their positions using the task `emldetect`, which performs maximum likelihood fits to the source spatial count distribution. In this case, we have fixed the threshold values of the equivalent single band detection likelihood (parameter *mlmin*) to 30, in order to select only high–confidence sources. Our master lists contain a total of 132 sources for the 2001/2002 observation subset, 107 sources for the 2005 subset, and 144 sources for the whole observation set. Although we have performed the source detection using the same tasks, the master list presented in Novara et al. (2006) contained 196 sources for the 2002 observations only. The difference between the number of sources in the two lists is mainly due to the improvement of the task `eboxdetect` in the *SAS* v.7.1.0, which was used to perform the source detection. The task now allows for a more accurate analysis in regions of diffuse emission, thus minimising the detection of spurious sources. Moreover, in the new procedure the sources have to fulfil tighter selection criteria in order to be qualified as real.

In the same sky region the *Incremental Second XMM–Newton Serendipitous Source Catalogue* (*2XMMi*, Watson et al. (2008)) reports 344 sources[2]. We attribute this discrepancy mainly to the difference in the threshold value of the *detection likelihood* used in our procedure and in the procedure used to produce *2XMMi*. In our case, this value is set at 8.5 for the *likemin* parameter of the *SAS* task `eboxdetect` and 30 for the *mlmin* parameter of the *SAS* task `emldetect`; on the other hand, in the case of *2XMMi* the corresponding values are 5 and 6[3]. This means that we applied much tighter criteria to the source selection, thus rejecting several low–confidence or spurious sources which instead are included in *2XMMi*. This is proven by Figure 3.1, which compares the sources detected by our procedure and those reported in *2XMMi*. It clearly shows that most of the additional *2XMMi* sources are either very faint or in sky areas where the source detection is very difficult, since they are at the edge of the *field–of–view* or in the region of diffuse X–ray emission due to the SNR. Therefore there is a high probability that a large fraction of these sources are spurious.

---

[2] http://xmmssc-www.star.le.ac.uk/Catalogue/xcat_public_2XMMi.html

[3] http://xmmssc-www.star.le.ac.uk/Catalogue/UserGuide_xmmcat.html

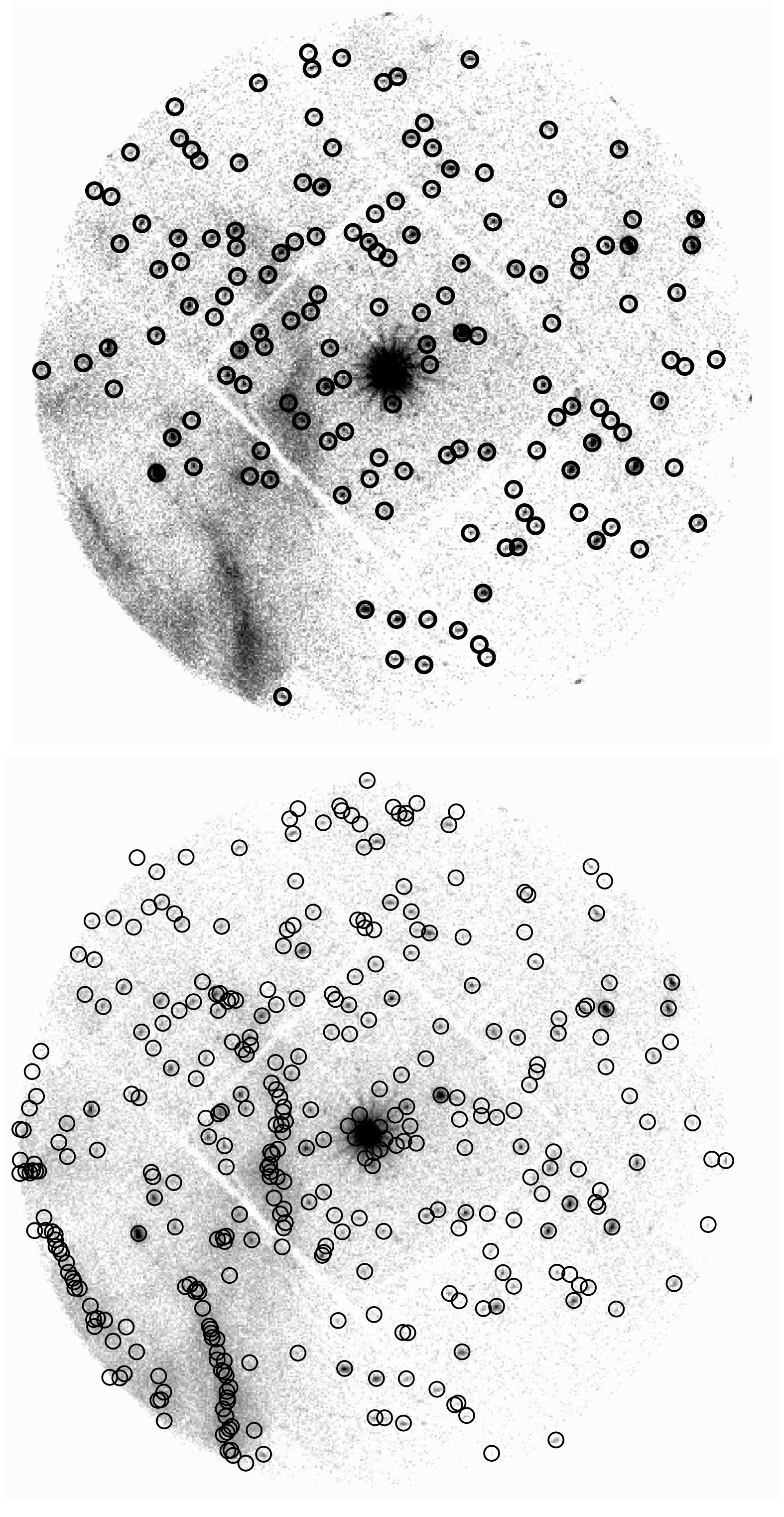

Figure 3.1: *Top: distribution of the 144 X–ray detected sources over the* EPIC *image of 1E1207.4−5209 in the energy range 0.3–8 keV. Bottom: distribution in the same sky region of the 344 sources reported by 2XMMi.*

Table 3.2: *Number of X–ray sources detected in each energy band and relative fraction for the three observation sets defined in § 3.2.3.*

Band (keV)	0.5–2	2–10	0.3–8	Total
Set	N(%)	N(%)	N(%)	N
1	101 (76.5)	68 (51.5)	123 (93)	132
2	84 (78.5)	42 (39)	97 (90.6)	107
3	114 (72)	87 (60)	135 (94)	144

3.2.5 Source statistics

In order to perform a detailed statistical analysis we have also computed, for all the observation sets, the number of sources detected in each of three energy bands. We summarize these numbers in Table 3.2, where we also report their relative fraction with respect to the total number of sources detected in at least one energy band. We note that almost all sources are detected in the energy band 0.3–8 keV, with a good fraction of them also detected in the soft energy band (0.5–2 keV). The number of sources detected in each energy band is different across the three observation sets, which is an effect of the uneven effective exposure times. This is evident in the case of the 2005 observation subset (see Table 3.1).

3.3 The serendipitous X–ray source catalogue

3.3.1 Catalogue description

We have used the source master list obtained from the whole observation set to build a detailed catalogue of serendipitous X–ray sources detected in the 1E1207.4−5209 field. The complete serendipitous source catalogue is made available in electronic form through the *Vizier* database server. Each source was assigned a unique identifier using the recommended *XMM–Newton* designations for serendipitous sources. The catalogue information include most of the entries already included in the master list, i.e. sky coordinates and associated uncertainty, effective exposure time, total counts, count–rate and errors, S/N ratio, and detection likelihood. In addition, we have provided information on the source spectral parameters and the computed fluxes in the soft/hard/total energy bands.

Since for most sources the measured counts are too few to produce significant X–ray spectra, we have used the *Hardness Ratio* (*HR*) to provide qualitative spectral information. The *HR* has been computed from the measured count–rate (*CR*) in the hard (2–10 keV) and soft (0.5–2 keV) energy bands and defined according to the equation:

$$HR = \frac{CR(2-10) - CR(0.5-2)}{CR(2-10) + CR(0.5-2)} \tag{3.1}$$

where $CR(2-10)$ and $CR(0.5-2)$ are the count–rates in the hard and soft energy bands, respectively. The source flux in the soft/hard/total energy bands has been computed from the measured count–rates. Following the procedure used by Baldi et al. (2002), the *count–rate–to–flux* conversion factors (*CF*) have been computed for each of the *MOS* cameras individually using their updated response matrices, combined with the effective exposure times of each pointing. As a model spectrum we have assumed an absorbed power-law, with photon index $\Gamma = 1.7$, i.e. a typical AGN spectrum, and a hydrogen column density $N_H = 1.3\times10^{21}$ cm^{-2}, i.e. value measured in the direction of 1E1207.4−5209.

In the following sub-sections, we report basic statistics on the more important catalogue entries, like the source *S/N* ratio, the total *CR*, and the *HR*, relative to the whole observation set. In the last sub-section we also present the log$N$–log$S$ distribution built from the sources in our new serendipitous catalogue.

3.3.2 S/N ratio distribution

The histogram of the source *signal–to–noise* (*S/N*) ratio distribution is shown in Figure 3.2 in the soft, hard, and total energy bands. In the 0.3–8 keV energy band the distribution peaks at *S/N* = 4–6 (Figure 3.2, top). However, thanks to the large effective integration time and to the increased count statistics, a large fraction ($\sim$ 40%) of sources is also detected with *S/N* $\geq$ 10. Very few sources are detected with *S/N* $\geq$ 20. In the hard energy band (2–10 keV), sources are generally detected with a quite low *S/N* ratio, with the peak of the distribution (Figure 3.2, middle) at 4 and with only $\sim$ 20% of the sources detected with *S/N* $\geq$ 10. On the other hand, sources are detected with the best *S/N* ratio in the soft energy band (0.5–2 keV), with the distribution (Figure 3.2, bottom) peaking at 6–8, and with a much larger fraction of sources ($\sim$ 35%) detected with *S/N*$\geq$10. This is most likely ascribed to the better sensitivity of the *MOS* cameras at low energies.

In Figure 3.3 we show, as a reference, the correlation between the source detection likelihood $-lnP$ and the source *S/N* ratio in the 0.3–8 keV energy band. As expected, the detection likelihood increases with the *S/N* ratio, without any large scatter or change of slope at the two extremes of the distribution.

3.3.3 Count–rate distribution

The histograms of the source *count–rate* (*CR*) distribution for the two coarse soft (0.5–2 keV) and hard (2–10 keV) energy bands are shown in Figure 3.4. Since the number of sources detected per *CR* bin decreases below the peak *CR*, it is clear that the sample becomes incomplete for lower *CR* values. Therefore, we have assumed the *CR* peak values as the completeness limits in both energy

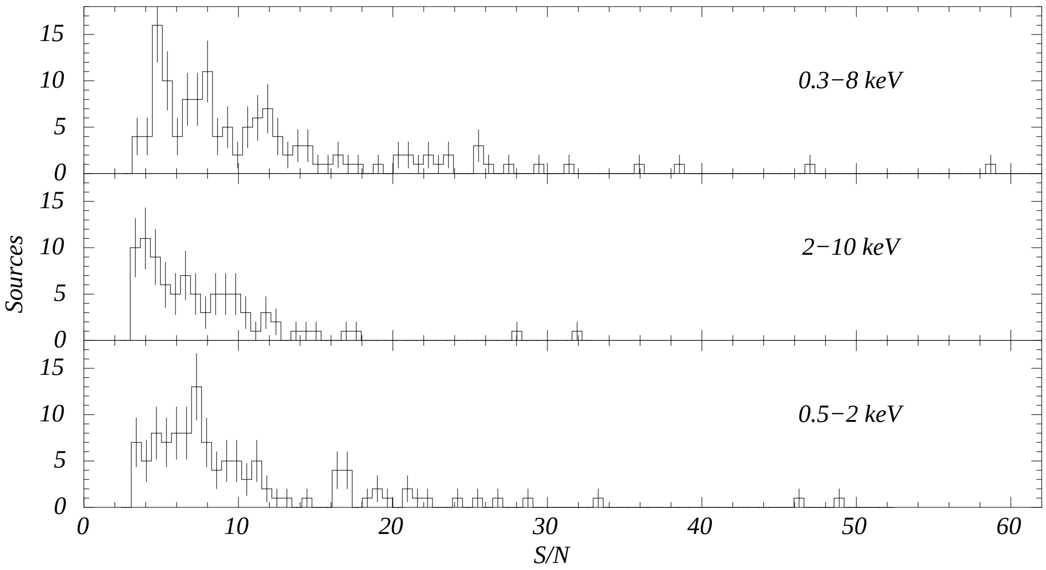

Figure 3.2: *Histogram of the S/N ratio distribution in the energy bands 0.3–8 keV, 2–10 keV, and 0.5–2 keV (top to bottom) for the serendipitous X–ray sources.*

bands. Indicative average CR limits are 6.31 cts s^{-1} ($logCR$ = -3.2) and 2.81 cts s^{-1} ($logCR$ = -3.55) in the soft and hard energy bands, respectively. As seen from the histograms, in either of the two energy bands only a few X–ray sources have a relatively high count–rate (logCR $\geq$ -3), and thus lower statistical errors. For this reason, only for them the count–rate variations measured over the 2001/2002 and 2005 observation subsets can be considered indicative of a statistically significant long term variability (§ 3.4.2).

3.3.4 Hardness ratio distribution

The histogram of the HR distribution is shown in Figure 3.5. Most of the sources have -0.5$\leq$ HR $\leq$0 and a large fraction has $HR \sim -1$. This suggests that a significant fraction of the X–ray source population is characterised by rather soft spectra, with no detection in the 2–10 keV energy band. On the other hand, the histogram shows that only few sources have very hard spectra ($HR \simeq 1$). To obtain further information on the source nature, we have compared their measured HR with the value estimated by assuming an absorbed power–law spectrum with photon index Γ = 1.7 (see § 3.3.1) and 5 different values of the hydrogen column density (see Figure 3.5). For comparison, the results are shown as vertical segments on the top of the histogram in Figure 3.5. Sources with HR $\leq$ -0.3 correspond to values of N_H lower than, or comparable to, that measured in the direction of 1E1207.4$-$5209 (1.3$\times$10^{21}cm^{-2}) and, thus, are almost certainly galactic and likely identified as nearby stars. Sources with HR $\geq$ -0.3 correspond to larger values of N_H, which suggest

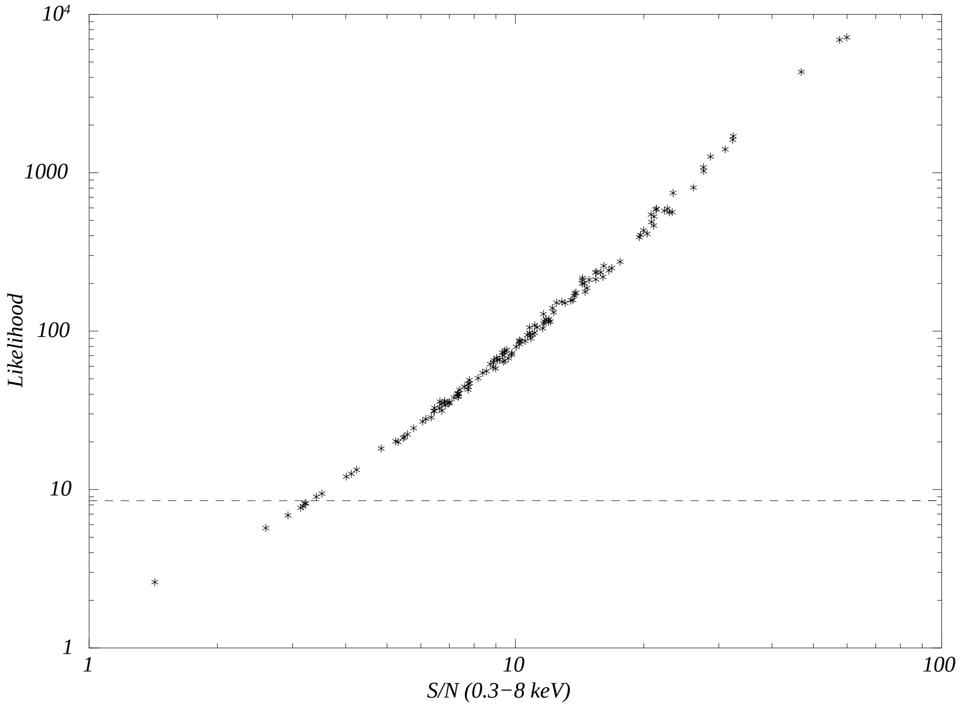

Figure 3.3: *Correlation between the detection likelihood and the S/N ratio, both computed in the 0.3–8 keV energy band, for the serendipitous sources. The dashed line corresponds to the detection likelihood threshold ($-lnP = 8.5$) in the 0.3–8 keV band. Sources below this line are included because they are above the detection threshold in at least one of the other two energy bands (see § 3.2.4).*

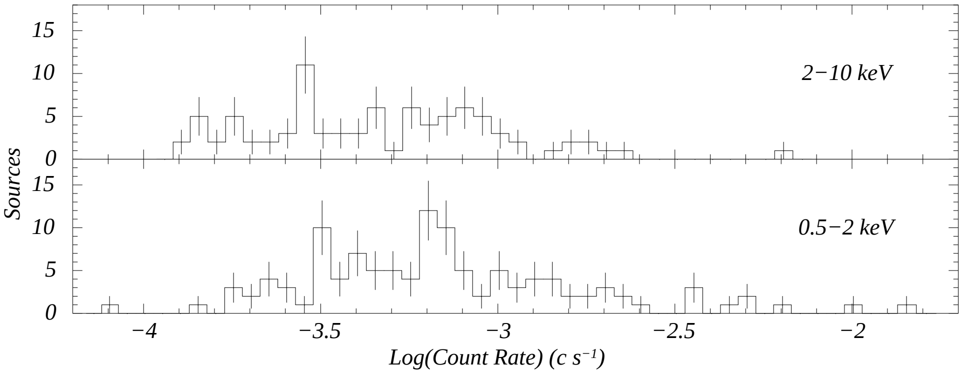

Figure 3.4: *Histogram of the source count–rate distribution in the 0.5–2 keV and 2–10 keV energy bands (bottom and top, respectively).*

that they are either distant galactic accreting X–ray binary systems, or extra–galactic sources with intrinsic absorption. The latter scenario is not surprising, since the 1E1207.4−5209 field is at an intermediate galactic latitude ($|b| \simeq 10°$) and, therefore, it is expected to contain both galactic and extra–galactic X–ray sources.

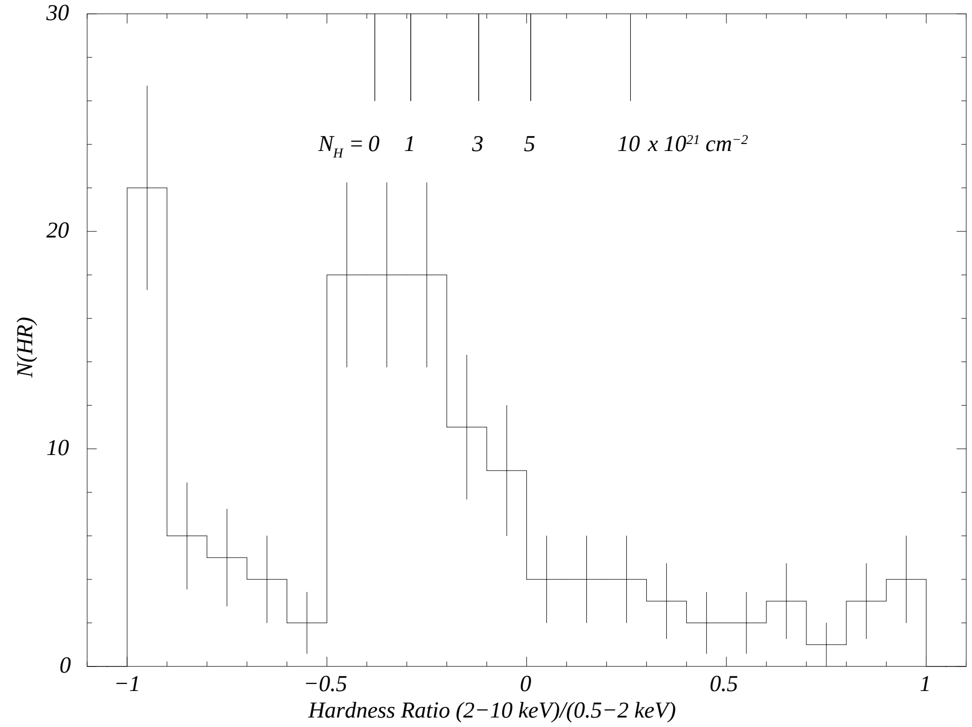

Figure 3.5: *Histogram of the HR distribution for the serendipitous X–ray sources detected in the 1E1207.4−5209 field. The vertical bars on the top of the graphic indicate the expected HR computed for a power–law spectrum with photon index* Γ *=1.7 and* N_H *= 0, 1, 3, 5, 10 (in units of* $\times 10^{21} cm^{-2}$*).*

3.3.5 Flux limit and sky coverage

The actual sky coverage in the various energy ranges was calculated based on the procedure described in Baldi et al. (2002), which agrees with the standard method used in the *XMM–Newton Serendipitous Survey* (Carrera et al., 2007; Mateos et al., 2008). For each energy band we used the exposure maps of each of the two *MOS* cameras and the background map of the merged image have been used, as derived in § 3.2.3, to compute the flux limit map of the whole observation set. This gives, for each position on the sky covered by the *MOS* observations, the flux that a source must have in order to be detected with a minimum probability $P = 2\times10^{-4}$ (Baldi et al., 2002; Novara et al., 2006). We used the flux limit maps to derive the total sky coverage shown in the

Figure 3.6. It shows that our survey covers a total sky area of $\simeq 0.15$ deg^2, and that this maximum value is reached at X–ray fluxes of $2 \simeq 1 \times 10^{-15}$ and 8×10^{-15} erg cm^{-2} s^{-1} for the energy ranges 0.5-2 and 2-10 keV, respectively; at half of the previous values the corresponding sky coverage is ~ 0.1 deg^2.

3.3.6 LogN–logS distribution

We based on the procedure used by Baldi et al. (2002) to calculate the log$N$–log$S$ distribution of the detected sources, therefore we refer to their paper for further details. Figure 3.7 shows the cumulative log$N$–log$S$ distribution built from our serendipitous X–ray sources, relative to the soft (0.5–2 keV) and hard (2–10 keV) energy bands. In the soft band the flux limit is $\sim 1{\times}10^{-15}$ erg cm^{-2} s^{-1}, corresponding to a maximum angular density of ~ 1300 sources deg^{-2}; in the hard energy band the corresponding values are $\sim 3{\times}10^{-15}$ erg cm^{-2} s^{-1} and ~ 700 sources deg^{-2}. Both the soft and hard distributions feature an evident change of slope at $S \sim 4{\times}10^{-15}$ and $S \sim 2{\times}10^{-14}$ erg cm^{-2}s^{-1}, respectively. We note that a similar turn–over was already observed by Ebisawa et al. (2005) in the *Chandra* observation of the galactic plane, and also in the latest results of the *XMM–Newton Serendipitous Survey* (Carrera et al., 2007; Mateos et al., 2008), even if in this latter case the fluxe breaks are at $S \sim 1{\times}10^{-14}$ erg cm^{-2}s^{-1} in both energy bands. In comparison with the results reported by Mateos et al. (2008), we obtain a comparable flux limit in the soft energy band, while in the hard band we obtain a much lower limit; moreover, in both energy ranges our cumulative sky density of sources at the flux limit is higher, since they obtain ~ 600 and ~ 300 sources deg^{-2} in the soft and hard energy ranges, respectively. We note that we used a unique power–law slope $\Gamma = 1.7$ to calculate our *CFs* in the two energy ranges, while Mateos et al. (2008) used slope values 1.9 and 1.6 below and above 2 keV, respectively. However, they showed that slope differences within 0.3 can imply changes up to $\sim 9\%$ in the hard band and of only 1–2% in the soft band; therefore we assume that this model difference does not affect our results.

For comparison, in Figure 3.7 we have superimposed to our data the lower and upper limits of the log$N$–log$S$ measured by Baldi et al. (2002) at high galactic latitude ($|b| > 27°$): they obtained the upper limit log$N$–log$S$ by applying the same detection threshold ($P_{\rm th} = 2 \times 10^{-4}$) but a larger extraction radius, while the lower limit log$N$–log$S$ was obtained with the same extraction radius but a more constraining threshold value ($P_{\rm th} = 2 \cdot 10^{-5}$). Moreover, in the same figure we have also reported the log$N$–log$S$ distributions, as well as the 90% confidence limits, measured by *Chandra* in the galactic plane (Ebisawa et al., 2005).

In the soft energy band our log$N$–log$S$ distribution is well above the high–latitude upper limit over the full flux range. This means that in our serendipitous survey we detected a large sample of galactic sources which are missed not only at higher latitudes but also in the Galactic plane, due to the high amount of interstellar absorpiton. However, we note that the observed count excess decreases at low X–ray fluxes, below the flux break at $\sim 4\times10^{-15}$ erg cm^{-2} s^{-1}. As explained in § 3.2.4, this discrepancy is due to the tighter criteria that we adopted to validate the detection of serendipitous sources, together with the improved *SAS* detection algorithm which minimises the number of spurious sources detected inside regions of diffuse emission, like the SNR G296.5+10.0. This results in a lower number of sources detected in the soft energy band, which is now 114 with respect to the 135 reported in Novara et al. (2006). Indeed, we have identified the missing sources with the faintest ones reported in Novara et al. (2006), which explains the reduced number of sources at the low flux end of the new log$N$–log$S$ distribution. Our log$N$–log$S$ distribution is also well above the Galactic Plane log$N$–log$S$ distribution (the red points), which means that we detected a significant fraction of extra–galactic sources which are missed at low galactic latitude.

In the hard energy band, the distribution of our sources is very near to the distribution observed in the Galactic Plane. In comparison with the high latitude limits, our distribution shows a slight excess in the flux range 1–2×10^{-15} erg cm^{-2} s^{-1}; it is possible that this effect is due to a fraction of Galactic sources which are missed at higher latitudes. On the other hand, the faintes end of our distribution is below the high latitude lower limit. We attribute this result to the tight criteria that we used to validate the detected source, which implies the rejection of the faintest objects.

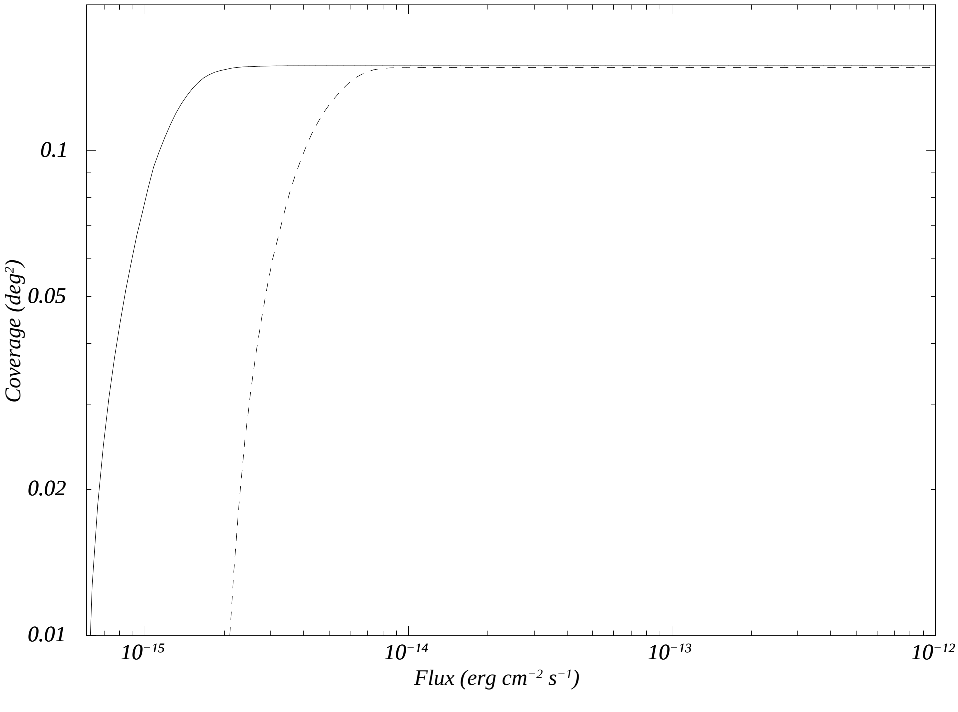

Figure 3.6: *Sky coverage of the* XMM–Newton *observations, in the soft energy range 0.5–2 keV (solid line) and in the hard energy range 2–10 keV (dashed line).*

3.4 The bright source sample

3.4.1 Spectral analysis

Although the *HR* provides a qualitative information on the source X–ray spectra, it is clearly not sufficient if one aims at obtaining a robust spectral classification. As we mentioned in Novara et al. (2006), at least 500 total *MOS* counts (i.e. *MOS1* + *MOS2* events) over the whole detector energy range are required to discriminate thermal X–ray spectra from non–thermal ones. Following this criterion, the 40 brightest sources are selected (Figure 3.8) in our new serendipitous source catalogue, which total > 500 counts. This bright source sample obviously includes the 24 brightest sources similarly selected in Novara et al. (2006). For each of the two *MOS* cameras we have extracted the source event list using extraction radii of $20''$–$35''$. We have selected background regions near the source positions, with a radius three times that used for the source extraction. We have rebinned all spectra extracted from the event lists in order to have a minimum of 30 counts per energy bin, which is required to precisely apply the χ^2 minimization fitting technique.

For each of the two *MOS* spectra we generated *ad hoc* response matrices and ancillary files using the *SAS* tasks `rmfgen` and `arfgen`. We took into account the different size of the source and background extraction areas and renormalized the background count–rate, then we fitted simultaneously the two spectra of each source forcing common parameters and allowing only for a cross–normalization factor, to account for the different instrument efficiency. To this aim we considered four spectral models: *power–law*, *bremsstrahlung*, *black–body*, and *mekal*. In all cases, the hydrogen column density N_H was left as a free parameter. For each emission model we calculated the 90% confidence level error on both the N_H and on the spectral parameters, i.e. the plasma temperature or the photon–index. As seen from Table 3.5, we have found that 14 sources were best fitted by a *power–law* model (Figure 3.9), 2 by a *bremsstrahlung* model, and 3 by a *mekal* model (Figure 3.10). For 16 of the remaining 20 sources, at least two different models provided an acceptable fit with a comparable value of the χ^2_ν. For 5 sources it was not possible to obtain acceptable results with single–component spectral model. This is, e.g. the case of source #239 (XMMU J121029.0−522148), the proposed Seyfert–2 galaxy identified in Novara et al. (2006), which is characterised by a complex spectral model discussed in § 3.4.3.

3.4.2 Time variability

In order to investigate possible long term variability we have selected from our bright source sample 33 X–ray sources we have detected in both the 2001/2002 and 2005 observation subsets (see Table 3.1) and in the 0.3–8 keV energy band, chosen as a reference. For each source we have computed the count–rate variation ΔCR between the two observation subsets. Figure 3.11 (top) shows

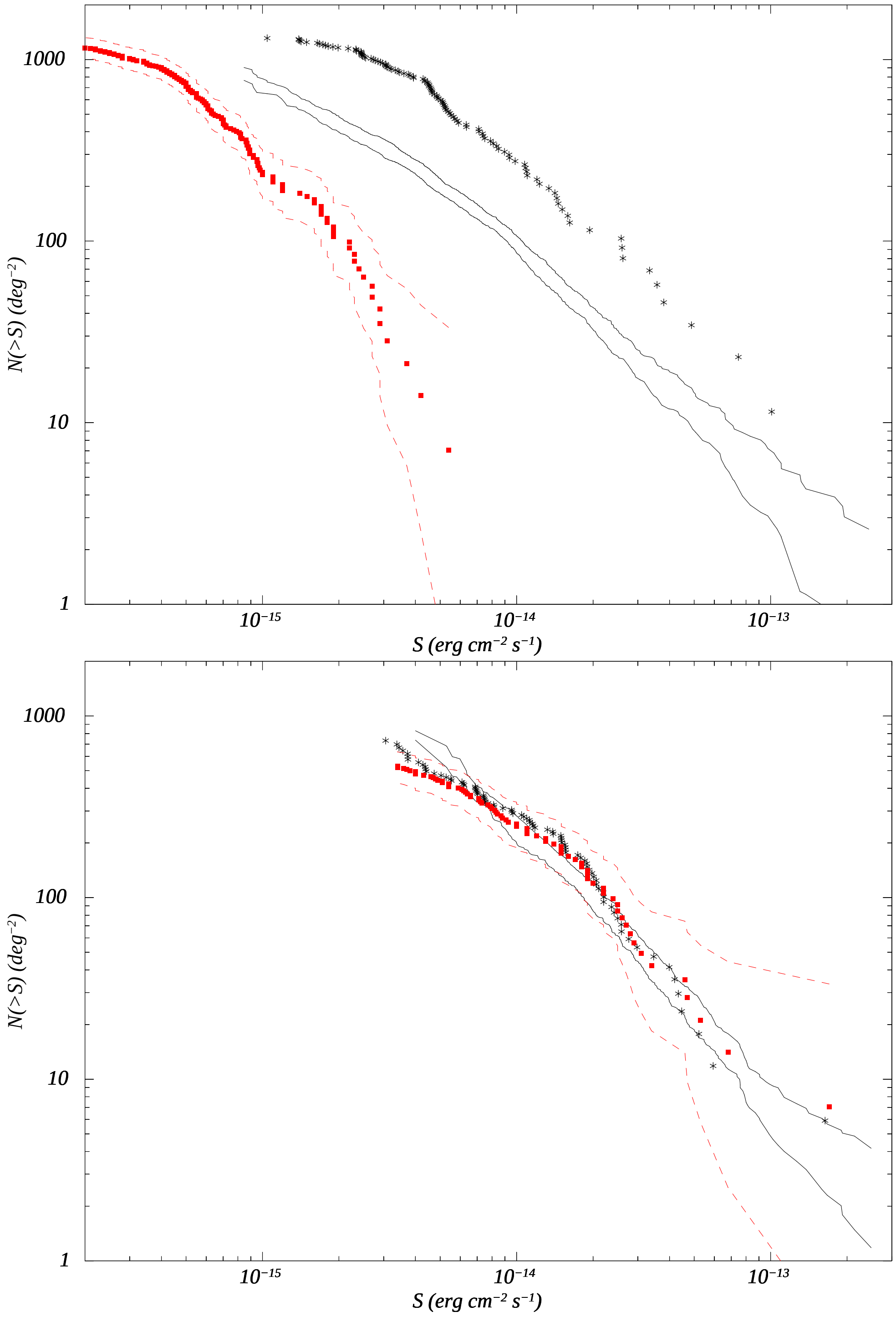

Figure 3.7: *Cumulative logN–logS distributions (asterisks) of the serendipitous sources detected in the 1E1207.4−5209 field in the soft (0.5–2 keV, top) and hard (2–10 keV, bottom) energy ranges. The black solid lines trace the upper and lower limits obtained by Baldi et al. (2002) in the same energy ranges but at higher galactic latitudes; the red filled squares and the red dashed lines represent, respectively, the distributions and the limits measured by Chandra in the Galactic Plane (Ebisawa et al., 2005).*

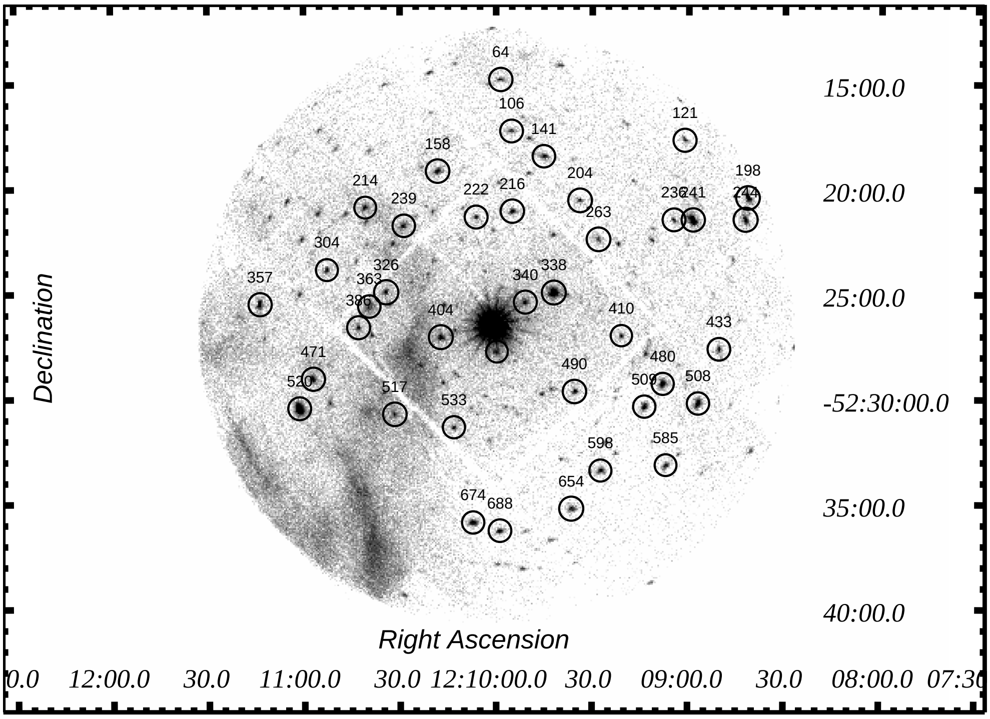

Figure 3.8: *Processed* XMM–NewtonEPIC/MOS *0.3–8 keV band image of the 1E1207.4−5209 field with the position of the 40 brightest serendipitous sources over plotted. Sources are labelled according to the numbering used in Table 3.5. Circles are drawn only to highlight the X–ray source positions and their size do not correspond to their actual positional errors.*

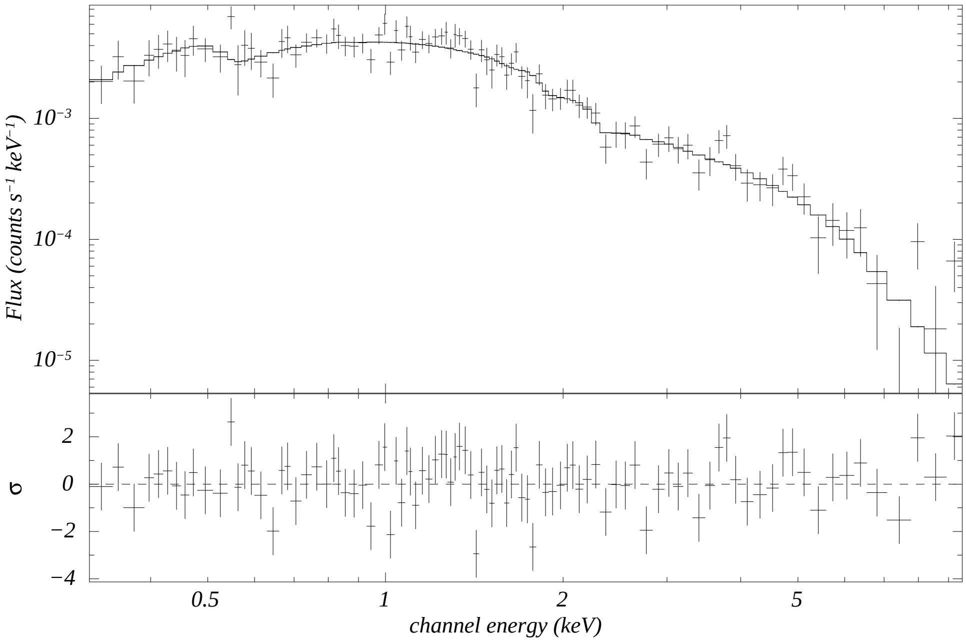

Figure 3.9: *Unbinned non–thermal spectrum of source #338 (XMMU J120942.1−522458) with the best–fit power–law model. The source is classified as an AGN (see § 3.7.2)*

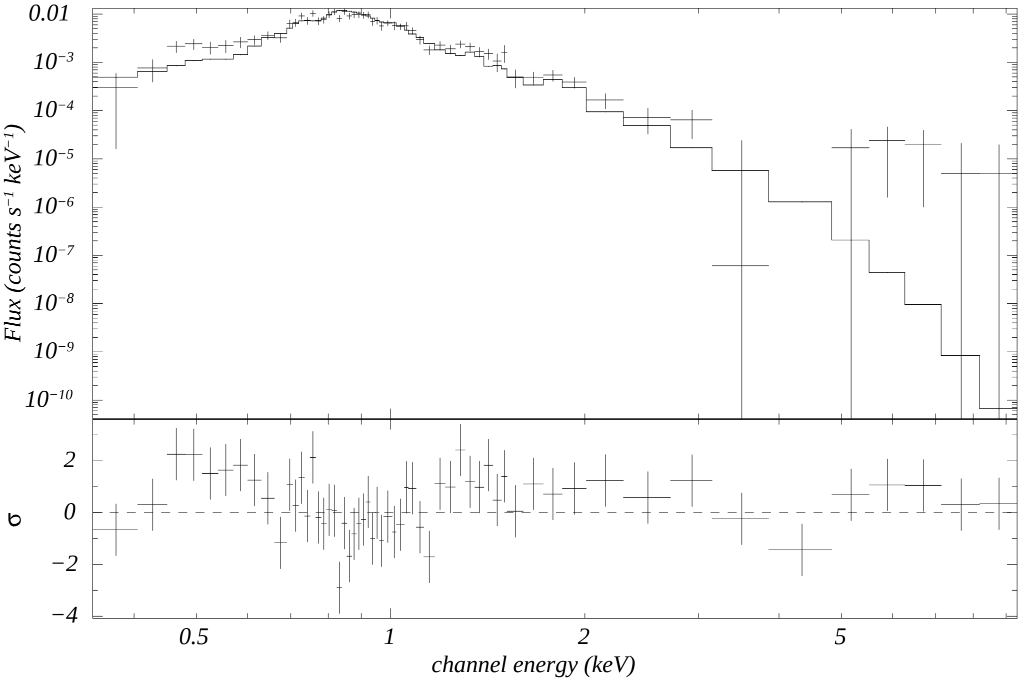

Figure 3.10: *Unbinned thermal spectrum of source #241 (XMMU J120858.8−522129) with the best–fit thermal mekal model. The source is classified as a star.*

the relative *CR* variation with respect to the first observation subset plotted as a function of the source *S/N*. As seen, a few sources show a non-zero long term variability which is mostly within 30% but can be up to $\sim 200\%$. Figure 3.11 (bottom) shows the absolute *CR* variation $|\Delta CR|$ divided by its associated error $\delta(\Delta CR)$ plotted as a function of the source *S/N*. As seen, 10 X–ray sources show evidence of variability at more than 3-σ. For 6 of them, i.e. source #326 (XMMU J121034.6−522457), #404 (XMMU J121017.5−522706), #410 (XMMU J120921.0−522700), #471 (XMMU J121057.3−522905), #480 (XMMU J120908.1−522918), and #520 (XMMU J121101.5−523030), the variability is at the $\gtrsim$ 5-σ level. Thus it is possible to regard these sources as likely transients whose nature is discussed in § 3.7. Among them, source #326 (XMMU J121034.6−522457) features the strongest variability ($\sim$ 200%, $\approx$7-σ), followed by source #410 (XMMU J120921.0−522700) whose variability is of $\sim$ 100% but is significant only at the $\sim$ 5-σ level. On the other hand, sources #480 (XMMU J120908.1−522918) and #520 (XMMU J121101.5−523030) feature a variability of only $\sim$ 15%–25%, although detected with the highest significance ($\approx$10-σ). This is obviously due to the fact that both sources were detected with the highest *S/N* ratio ($\geq$ 30).

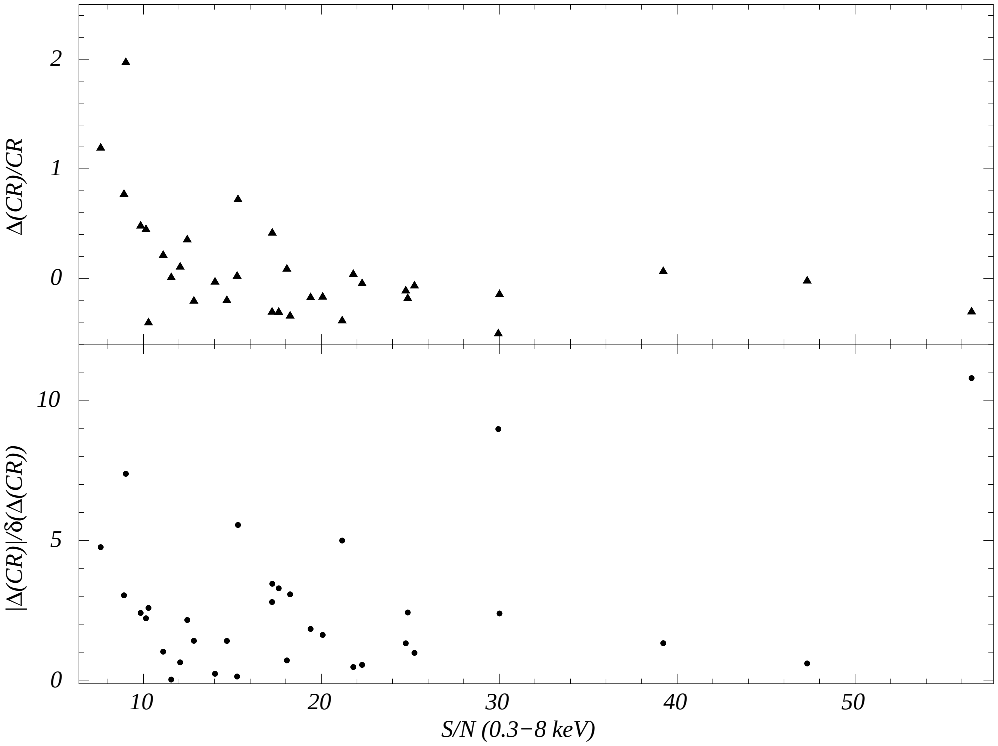

Figure 3.11: *Top: relative CR variation with respect to the first observation subset plotted as a function of the source S/N ratio (filled triangles). Bottom: absolute CR variation $|\Delta CR|$ divided by its associated error $\delta(\Delta CR)$ plotted as a function of the source S/N ratio (filled circles).*

At the same time, for all sources in our bright sample, we have searched for variability on a shorter time scale through a light–curve analysis with optimised time binning (1, 5, or 10 ks), and using as a reference only CR measurements relative to the observations with the largest exposure times, i.e. the second and the third observation of the 2002 data–set and the fourth observation of the 2005 data–set (Table 3.1). Of the 6 X–ray sources with $\geq$ 5-σ possible long term variability, our light–curve analysis does not show evidence of short term variability while it confirms the long term one for all sources but not for source #520 (XMMU J121101.5$-$523030). This result is not surprising since this source is the one with the lowest relative variation ($\sim$ 25%, see Figure 3.11 (top)), which is thus more difficult to recognise if spread on a shorter time scale. None of the remaining 4 X–ray sources with possible ($\sim$ 3–5-σ) long term variability shows any evidence of short term variability.

For the persistent sources (long term variability $\leq$ 3-σ), we confirm flux variability on time–scales of a few hundred seconds for source #158 (XMMU J121018.4$-$521911) and of $\sim$ 10 ks for source #338 (XMMU J120942.1$-$522458), which correspond to source #72 and #183 of Novara et al. (2006), respectively. For the remaining sources, we have not found evidence of significant variability on any time scale.

Finally, we have also looked for possible periodic time variability. Unfortunately, in this case the low count statistics prevented the detection of any periodic signal at a reasonable significance level, therefore our search was unfruitful.

3.4.3 The Seyfert-2 galaxy ESO 217-G29

Source #239 (XMMU J121029.0$-$522148) was originally identified as a new Seyfert galaxy in Novara et al. (2006) (source #127), due to its X–ray spectrum and to its positional coincidence with the galaxy ESO 217-G29, a bright (R = 14.93) barred spiral with a spectroscopic redshift of 0.032 (Visvanathan & van den Bergh, 1992) also detected in the *Digitised Sky Survey* images. From the merged image (see § 3.2.3) we have now obtained a total of 821 counts in the energy range 0.3–8 keV for source #239, corresponding to a 38% larger statistics with respect to that of the data set used in Novara et al. (2006). For this reason, we have repeated the source spectral analysis in order to achieve a more accurate characterisation of the X–ray spectrum. The spectrum of the source between 1 and 12 keV is complex and cannot be fitted by a single-component model. We thus used the AGN unification model of Antonucci (1993) and Mushotzky et al. (1993)

$$S = A_G[A_{SP}(R_W) + A_T(PL + R_C + GL)]^4$$

where A_G is the galactic absorption (1.28×10^{21} cm^{-2}), A_{SP} is the absorption related to the AGN host galaxy, R_W is the warm and optically thin reflec-

---

[4] `wabs*(zwabs*powerlaw + zwabs*(powerlaw + pexrav + zgauss))` in `XSPEC`

tion component, A_T is the absorption acting on the nuclear emission associated to the torus of dust around the AGN nucleus, PL is the primary power–law modelling the nuclear component, R_C is the cold and optically thick reflection component, and GL is the Gaussian component that models the Fe line at 6.4 keV. For the A_{SP}, A_T, R_C, and GL components the redshift value is fixed at $z = 0.032$ (Visvanathan & van den Bergh, 1992).

For both the *MOS*1 and *MOS*2 spectra we performed the spectral fitting both fixing the redshift z to the literature value of 0.032 and leaving it as a free parameter. In the first case (Figure 3.12), the fit yields a $\chi^2_\nu = 0.77$ (33 d.o.f.) but it does not satisfactorily account for the Fe line since the fitted centroid energy of the line is 6.2 keV instead of 6 keV, as actually measured in the unfitted spectrum. Furthermore, the fitted line is not significant with respect to the model continuum. The fit yields an absorption associated to the dust torus (A_T) of $\sim 71.91\times10^{22}$ cm^{-2}, slightly lower than the value reported in Novara et al. (2006). In the second case (Figure 3.13), the fit also yields a χ^2_ν = 0.77 (32 d.o.f) with a best-fit redshift value $z = 0.042^{+0.038}_{-0.032}$ which is between the value reported in Novara et al. (2006) ($z = 0.057$) and the literature one of 0.032. The fit with the free z better accounts for the Fe line whose fitted profile is now significant at the 90% confidence level, with a fitted centroid energy of $\sim$ 6.0 keV. The intrinsic absorption associated to the dust torus (A_T) is $\sim$ 72.16×10^{22} cm^{-2}, very similar to the previous case. All best-fit parameters for the two cases are summarised in the Table 3.3. The 2–10 keV unabsorbed flux (calculated with `XSPEC`) of the primary nuclear component is $6.59^{+2.13}_{-1.23}\times10^{-13}$ erg cm^{-2} s^{-1} and the X–ray luminosity, computed for a redshift of 0.032, is $2.75^{+0.89}_{-0.51}\times10^{42}$ erg s^{-1}.

3.5 Optical observations

3.5.1 Observation description

In order to search for the optical counterparts of the X-ray sources, we have performed follow–up observations (Figure 3.14) with the *WFI* mounted at the 2.2 m ESO/MPG telescope at the La Silla observatory (Chile). The *WFI* is a wide field mosaic camera, composed of eight 2048×4096 pixel CCDs, with a scale of $0''.238$/pixel and a full field of view of $33'\times32'.7$ which well matches the one of the *EPIC*/*MOS* cameras. Observations in the U, B, V, R, and I filters were performed in Service Mode between March 2005 and April 2006 (see Table 3.4). Unfortunately, scheduling problems prevented observations to be executed during the same run. To compensate for the inter chip gaps, pointings were split in sequences of five dithered exposures with shifts of $35''$ and $21''$ in right ascension and declination, respectively. The target field was always observed close to the zenith and with nearly always under sub-arcsecond seeing conditions, as measured by the La Silla DIMM seeing monitor.

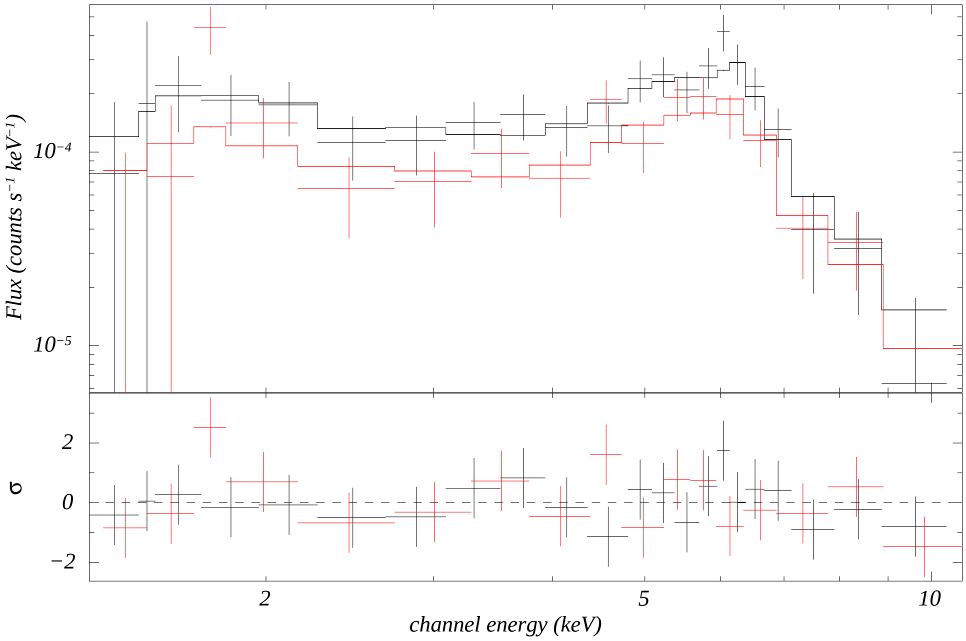

Figure 3.12: *(upper panel) The 1.2–12 keV unbinned spectrum of source #239 (XMMU J121029.0−522148) identified with the Seyfert-2 galaxy ESO 217-G29. The fit was performed using the AGN unification model of Antonucci (1993) and Mushotzky et al. (1993) with a fixed redshift of* $z = 0.032$*. Spectral fits were computed for both the* MOS*1 and* MOS*2 data (black and red, respectively). (lower panel) Data–model residuals are shown in units of* σ*.*

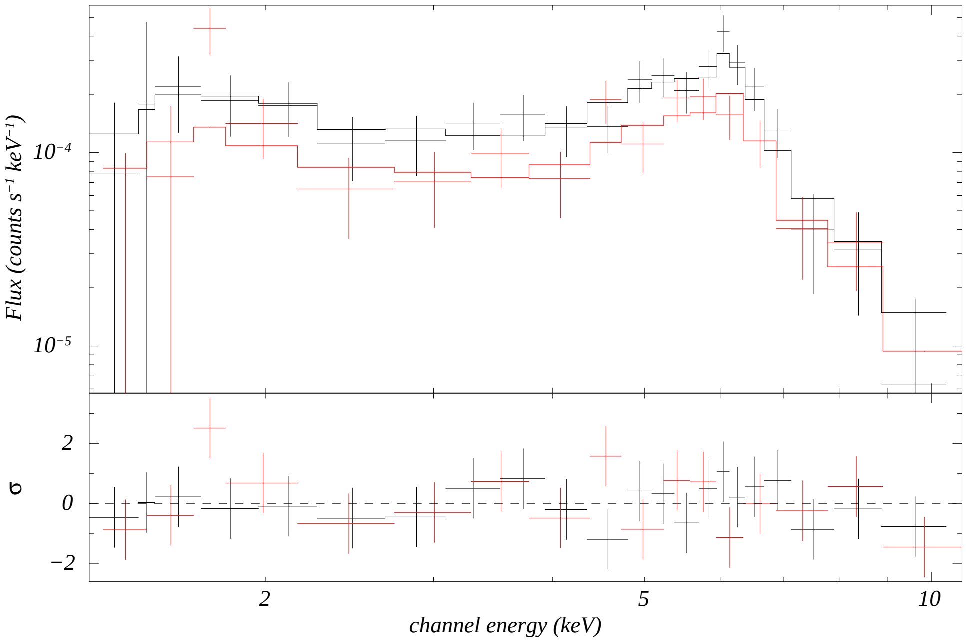

Figure 3.13: *Same as Figure 3.12 but with the best-fit redshift value of* $z = 0.042$.

Table 3.3: *Best–fit parameters for source #239 (XMMU J121029.0−522148), for the optical redshift* $z = 0.032$ *and for its best–fit value* $z = 0.057$.

Component	Parameter	z=0.032 (fix)	z=0.042
A_{SP}	$\mathrm{N}^{a}_{\mathrm{H1}}$	$2.27^{+1.12}_{-0.88}$	$2.27^{+1.12}_{-0.82}$
R_W	Γ	1.9 (fixed)	1.9 (fixed)
	Flux @ 1 keV^{b}	$8.84^{+3.25}_{-2.65}$	$8.63^{+1.58}_{-1.87}$
A_T	$\mathrm{N}^{a}_{\mathrm{H2}}$	$71.91^{+16.18}_{-15.24}$	$72.16^{+20.92}_{-15.20}$
PL	Γ	1.9 (fixed)	1.9 (fixed)
	Flux @ 1 keV^{c}	$2.28^{+1.17}_{-0.79}$	$2.20^{+0.71}_{-0.41}$
R_C	Γ	1.9 (fixed)	1.9 (fixed)
	Flux @ 1 keV^{c}	$2.28^{+1.17}_{-0.79}$	$2.20^{+0.71}_{-0.41}$
GL	E_{line}(keV)	6.4 (fixed)	6.4 (fixed)
	I^{d}_{line}	$1.02^{+1.32}_{-1.02}$	$1.31^{+1.45}_{-1.26}$
	EQW (eV)	126^{+164}_{-126}	164^{+181}_{-158}
d.o.f.		33	32
χ^2_ν		0.77	0.77

^{a} 10^{22} cm^{-2}
^{b} 10^{-6} ph cm^{-2} s^{-1} keV^{-1}
^{c} 10^{-4} ph cm^{-2} s^{-1} keV^{-1}
^{d} 10^{-6} ph cm^{-2} s^{-1}

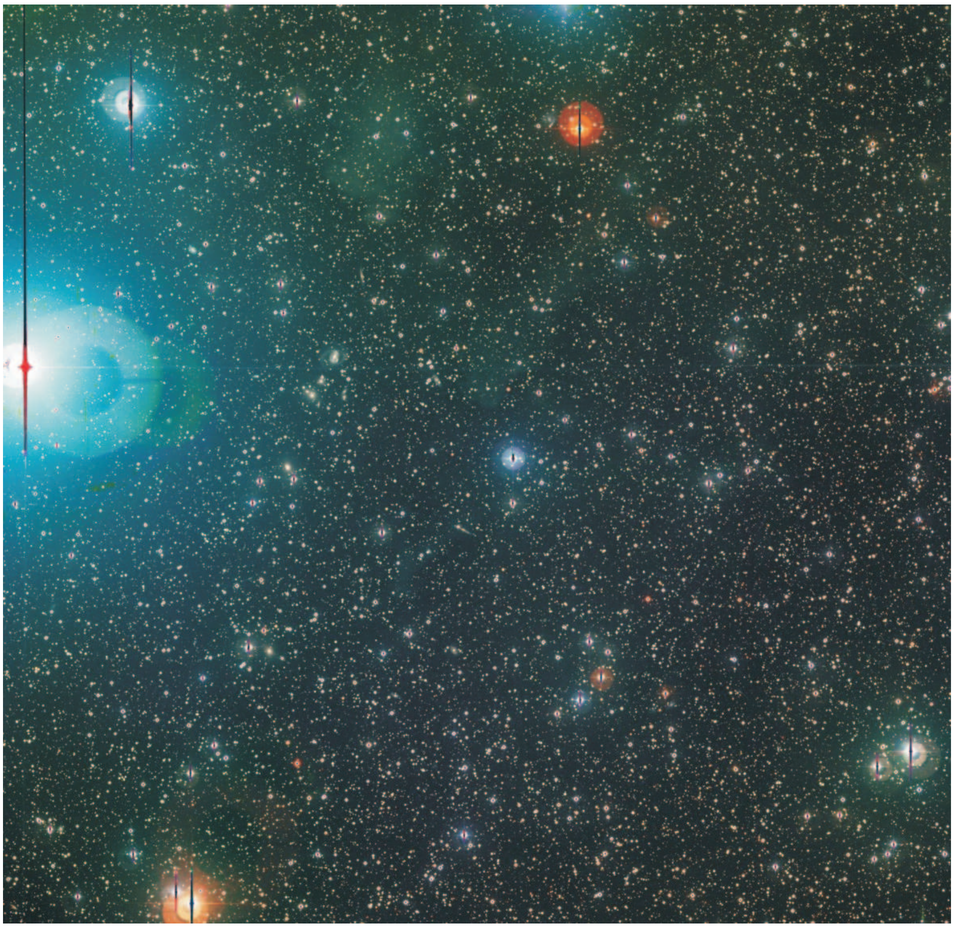

Figure 3.14: *Composite VRI image of the 1E1207.4−5209 field ($34' \times 34'$) taken with the WFI at the ESO/MPG 2.2 m telescope. North to the top, east to the left. The effects of the very bright star ρ Cen are clearly visible on the image, with the presence of reflections and bright ghosts.*

Table 3.4: *Summary of the observations performed by of the ESO/MPG 2.2m telescope.*

Date	Filter	Time (s)	Airmass	Seeing
10 Mar 2005	R	2888.75	1.09	0.99
	I	1999.73	1.15	1.09
01 May 2005	V	2559.09	1.11	0.52
02 May 2005	I	269.42	1.10	0.69
25 Feb 2006	I	1999.59	1.09	0.86
25 Apr 2006	B	1999.59	1.09	0.68
	U	2499.59	1.11	0.61

3.5.2 Data reduction and calibration

The data reduction of the *WFI* data was performed with the *THELI* pipeline (Erben et al., 2005) which was also used for the reduction of the *WFI* data of La Palombara et al. (2006). Since we have followed the same procedures, we refer to the paper of La Palombara et al. (2006) for a more detailed description of the data reduction. Briefly, for each band the individual images were de–biased, flat–fielded, and corrected for the fringing. After the chip-by-chip astrometric calibration computed using well-suited reference stars selected from the *USNO-B1.0* catalogue (average rms $\sim 0''.3$), single frames were co–added using a weighted mean to reject cosmic ray hits. A flux–renormalisation to the same relative photometric zero-point was applied using the exposure maps produced by the pipeline to account to the uneven exposure produced by the dithering. Since standard star observations were not acquired for all nights and for all bands, we have used default *WFI* zero-points[5] for the photometric calibration, namely 21.96, 24.53, 24.12, 24.43 and 23.37 (in Vega magnitudes) for the U, B, V, R, and I filters, respectively. A deeper image was then constructed by registering the individual co–added images in the single bands, which was used as a reference for the source detection.

3.5.3 Source detection

The source extraction was performed on the final co–added single band images by running the *SExtractor* software (Bertin & Arnouts, 1996). The source detection was performed after masking the region around the very bright star ρ Cen, a B3V star ($V = 3.9$) that was saturated on all *WFI* images (Figure 3.14). This was done to avoid including spurious detections produced by the saturation spikes and to filter out objects whose photometry is polluted by the bright star halo. The masking was applied on the weighted images and, due to the different brightness of the star in the different bands and to the different integration time, the size of the masked region was tailored on each image. The extracted catalogues were checked against the images and

---

[5] http://www.ls.eso.org/lasilla/sciops/2p2/E2p2M/WFI

the counterparts were visually inspected, to make sure that the spurious detections were minimal (less than $\sim 1\%$). Single band optical catalogues were then matched using a matching radius of 0.2 arcsec, i.e. equal to the rms of astrometric solution, to produce the final *WFI* colour catalogue. The catalogue includes a total of 64910 sources with at least a detection in one of the five bands (*UBVRI*). Of these, only 15201 have been detected in all bands. For each filter, the limiting magnitude of the colour catalogue was defined as the magnitude of the object fainter than the remaining 99%. This corresponds to *U*-to-*I* limiting magnitudes of 23.25, 24.72, 24.39, 23.97 and 22.72.

3.5.4 The optical/NIR catalogue

To extend the colour coverage, required for a colour–based classification of the *WFI* sources, we added near infrared (NIR) photometry information in the *J*, *H* and *K* bands by correlating the *WFI* colour catalogue with the *2MASS* catalogue (Skrutskie et al. 2006). The extracted *2MASS* source list in a $40' \times 40'$ region around the 1E1207.4−5209 position was retrieved through the *Vizier* database server and matched with the *WFI* colour catalogue using the IRAF task `tmatch`. A match radius of $0''.5$ was used to account both for the uncertainty on the *WFI* coordinates and on the $\leq 0''.2$ astrometric accuracy of *2MASS*. A total of 6996 *WFI* sources ($\sim 10\%$) have a match with a *2MASS* source and for 5032 of them we have found the full *UBVRI*-to-*JHK* photometry information. The match produced a master optical/NIR catalogue that we used as a reference for the X–ray source identification and for the colour-based object classification. For all sources with an adequate colour-coverage we used the colour-based optical classification technique described in Hatziminaoglou et al. (2002b) and tested in Hatziminaoglou et al. (2002a) and Groenewegen et al. (2002).

3.6 X–ray vs. optical/NIR catalogues

3.6.1 Catalogue cross–correlations

In order to identify candidate counterparts to the X–ray sources, we have cross-matched the new serendipitous X–ray source catalogue with the optical/NIR master catalogue. Thanks to the improved *SAS* task `emldetect`, the coordinates of the X–ray sources were measured with high accuracy. The measured errors vary between $0''.1$ and $1''.5$, depending on the source counts, with an average error of $\sim 0''.7$. These errors, however, substantially reflect the positional accuracy of the X–ray sources with respect to the detector reference frame and do not account for systematic errors. Indeed, the absolute accuracy of these coordinates with respect to the International Celestial Reference Frame (ICRF) is inevitably affected by the precision of the satellite aspect solution. In order to determine the accuracy of the tie of the measured coordinates to the ICRF, we thus have cross-matched our new X–ray catalogue with the optical/NIR master catalogue. In this way, we have found six X–ray sources which have a single, relatively bright (but not saturated) and obvious optical counterparts, and are not at the edges of the *MOS* cameras field–of–view (*FoV*). We thus computed the linear transformation between the X–ray and optical coordinates to correct the *MOS* astrometry. Since the astrometry of the *WFI* catalogue is calibrated with reference catalogues which are tied to the ICRF, we are sure that we do not introduce a bias in the procedure. Using the IRAF task `geomap` we have found that the X–ray source coordinates are affected by a (radial) systematic astrometric error of $1''.34$, corresponding to the rms of the X–ray–to–optical coordinate transformation.[6] To this, we have to add in quadrature the measured positional statistic error of each source ($0''.1$–$1''.5$). Therefore, the total uncertainty on the X–ray source position is between $1''.34$ and $2''.01$. The correction to the X-ray coordinates was then applied to all sources of new serendipitous X–ray catalogue with the IRAF task `geoxytran` using the coefficients of the computed X–ray–to–optical coordinate transformation. To account for all other sources of uncertainty, e.g. the $0''.35$ absolute (radial) accuracy of the *GSC* reference frame (Lasker et al. 2008), the distortions of the *MOS* cameras, etc., in the X–ray–to–optical cross–correlation we have conservatively assumed a more generous matching radius equal to three times the estimated absolute error on the X–ray source coordinates.

3.6.2 Sources with candidate optical counterparts

After the cross–match we have found at least one candidate counterpart for 112 out of the 144 X–ray sources in our new serendipitous catalogue (i.e. 78% of the total). However, a total of 195 candidate counterparts were found since we have obtained multiple matches for several X–ray sources. Due to the relatively deep limiting magnitudes of the *WFI* observations, this is in line with the expectations. It is possible to note that in Novara et al. (2006), where we used the shallower *GSC* catalogue (with only $\sim$ 16000 optical sources instead of the almost 65000 of the *WFI* catalogue), we found at least one candidate counterpart only for about half of the X–ray sources, even using a more conservative fixed positional uncertainty, hence a more generous cross–matching radius, of 5 arcsec. The choice of assuming a fixed positional uncertainty in Novara et al. (2006) was dictated by the fact that the *SAS* task `emldetect` was failing in providing reliable positional errors.

Due to the contamination of fore/background objects, the result of the cross–matching between the X–ray and optical catalogues is obviously affected by spurious matches. In order to estimate the number of spurious matches,

---

[6] We note that in Novara et al. (2006) the systematic astrometric error of the X–ray coordinates was 2.33 arcsec, the discrepancy being due to the different counterpart assumed for one of the six X–ray reference sources.

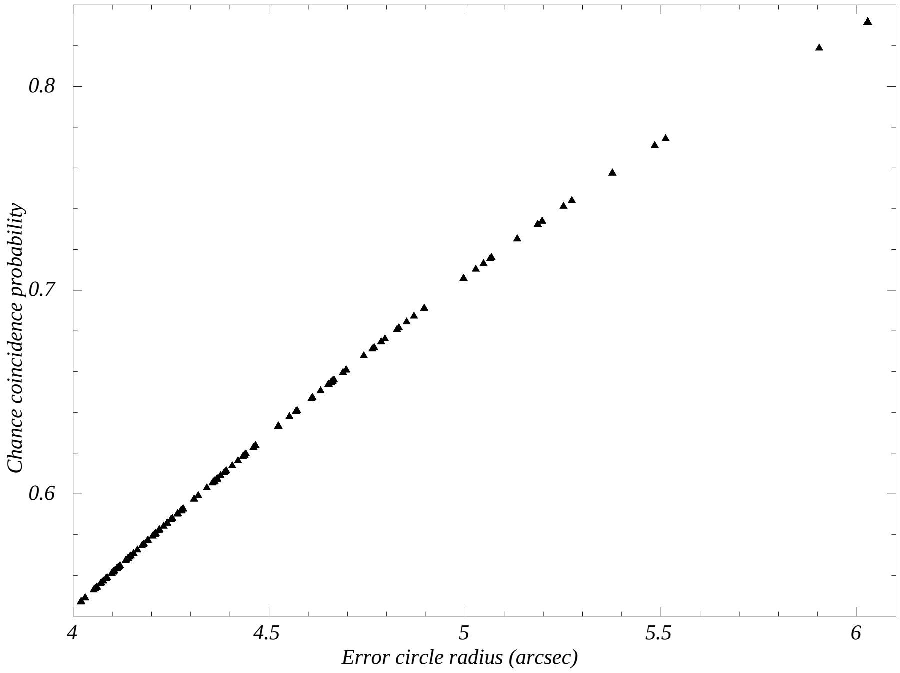

Figure 3.15: *Chance coincidence probability between an X–ray source and an optical* WFI *source as a function of the matching radius assumed equal to three times the size of the estimated absolute position uncertainty.*

we have used the relation $P = 1 - e^{-\pi r^2 \mu}$, where r is the assumed X–ray matching radius and μ is the surface density per square arcsecond of the optical sources, to compute the chance coincidence probability between an X–ray and an optical source (Severgnini et al., 2005). In our case, the *WFI* catalogue provided a total of 64910 sources distributed over an area of about 34×34 arcmin^2 (i.e. slightly larger than the detector field of view because of the frame dithering). In practice, the useful area is smaller since the $9' \times 7'.5$ region around the bright star ρ Cen was masked after the source extraction. This corresponds to a density of optical sources of $\mu = 0.016$ arcsec^{-2}, with $r = 4''$–$6''.03$. This yields a probability of chance coincidence between 55% and 83% which means that, at limiting magnitudes, contamination effects cannot be ignored. Thus, it is possible that several of the candidate counterparts are indeed spurious matches. This conclusion is circumstanced by Figure 3.15, where we show the dependence of the chance coincidence probability P on the position uncertainty.

3.6.3 Sources without candidate optical counterparts

For 32 sources in our new serendipitous X–ray source catalogue the cross–matching did not produce any candidate optical/NIR counterpart. For seven of them, #357, 380, 387, 230, 173, 181, and 124, the apparent lack of matches is ascribed to the fact that they fall within $\sim 6'$ from the position of the bright star ρ Cen, i.e. in a region which was masked before running the source detection on the *WFI* images (see § 3.5.3). For these sources we have checked the original unmasked single-band optical catalogues and we have visually inspected the *WFI* images to verify the existence of possible counterparts. For all of them we have found indeed one or more candidate optical counterparts on the *WFI* images. However, since their flux measurements are highly uncertain, they are useless for a reliable X–ray source identification. This is likely true also for flux measurements taken from, e.g. the *GSC* and *2MASS* catalogues, which were probably affected by the same problem. Thus, although we have spotted out their detection as a reference for future follow-up optical observations, these candidate counterparts are not considered in the following analysis. The remaining 25 X–ray sources ($\sim$ 20% of the total) fall well outside the masked region and are thus the only ones which actually lack a candidate optical/NIR counterpart.

3.7 X–ray source classification

3.7.1 The classification scheme

For all X–ray sources we have computed the "X–ray–to–optical" flux ratio $\frac{f_X}{f_{opt}}$. We have computed the X–ray flux by assuming the best–fit emission model and hydrogen column density or, when none of the tested models gives acceptable spectral fits or no spectral fitting is possible, an absorbed power–law spectrum with photon–index $\Gamma = 1.7$ and $N_H = 1.3\times10^{21}$ cm^{-2}, corresponding to the hydrogen column density measured in the direction of 1E1207.4$-$5209. The optical flux f_{opt} was computed from the measured magnitudes using the relations reported in Appendix B of La Palombara et al. (2006). The $\frac{f_X}{f_{opt}}$ was mostly computed using the R–band magnitude as a reference, because it was the band with the most detections. When no R–band magnitude was available for the candidate optical counterpart, we alternatively used the V, B, I, and U–band magnitudes (in this order). In order to use the $\frac{f_X}{f_{opt}}$ ratio as a diagnostic for the X–ray source classification, we have adopted the scheme proposed by La Palombara et al. (2006), where sources with a $log(\frac{f_X}{f_{opt}}) > 1$ are likely extra-galactic, while sources with $log(\frac{f_X}{f_{opt}}) <$ -1.5 are likely stars. As a general rule, in cases where two or more different spectral models provide equally acceptable fits to the X–ray spectrum, and thus cause ambiguity in the determination of the $\frac{f_X}{f_{opt}}$ ratio, we have claimed the source classification on the basis of the best agreement between the different classification indexes (see below). When no candidate optical counterpart is found within the cross–matching radius the R-band limiting magnitude ($R = 23.97$) we have adopted to estimate the lower limits on the $\frac{f_X}{f_{opt}}$ ratio.

Then we have used the combined available multi-wavelength information, i.e. the best-fitting X–ray spectra (or the *HR* for the faintest sources), the measured hydrogen column density N_H, the X–ray–to–optical flux ratio $\frac{f_X}{f_{opt}}$, and the optical/NIR colours of the candidate counterparts, to propose an optical identification and a likely classification for the 112 X–ray sources selected after the catalogue cross–matching (see § 3.6.2). For the 25 certified sources without candidate optical counterparts (see § 3.6.3) we used the lower limit on the $\frac{f_X}{f_{opt}}$ ratio to support the proposed classifications based on the source spectrum and N_H. In some cases, X–ray source variability was taken as an important classification index. We note that, due to the quite low declination of our field (∼ -52°), no coverage is provided by available large scale radio surveys, like the *NVSS* and *FIRST*, and no candidate radio source counterpart could be identified which could provide a further classification evidence.

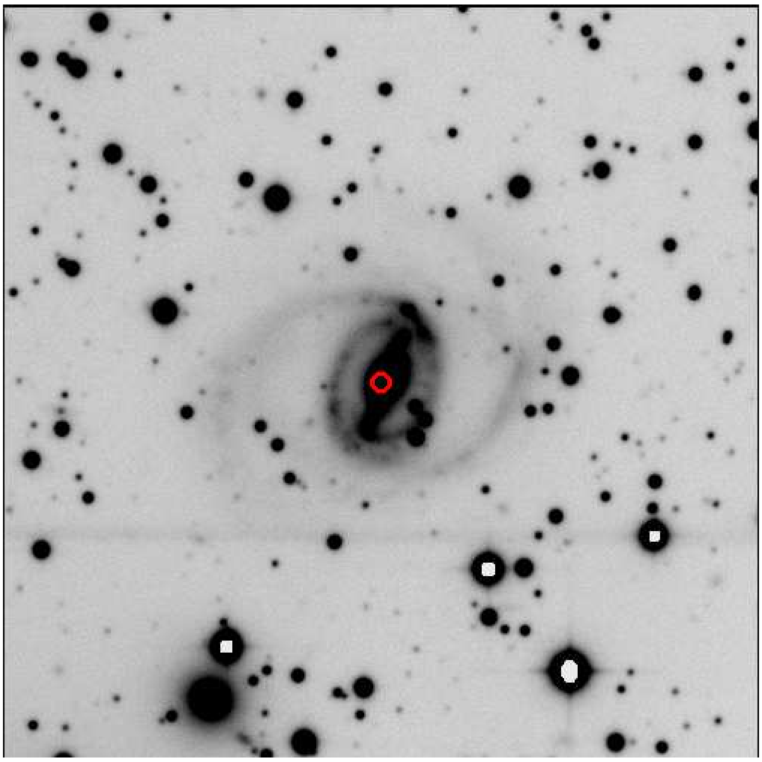

Figure 3.16: *$2' \times 2'$* R*-band image of the Seyfert-2 galaxy ESO 217-G29 taken with the WFI at the ESO/MPG 2.2m telescope. The position of the X–ray source #239 (XMMU J121029.0−522148) is marked with the red circle ($1''.38$ radius) and coincides with the ESO 217-G29 nucleus.*

3.7.2 Brightest X-ray sources

We have first evaluated the classification of the X–ray sources in our bright sub sample (see 3.4), for which the relatively accurate determination of the source spectrum and N_H represent already an important piece of evidence. In addition, for most of them the optical candidate counterparts are expected to be bright enough to be detected in nearly all the passbands, and thus to have a more reliable colour-based classification.

As mentioned in § 3.4.3, source #239 (XMMU J121029.0−522148) was already identified in Novara et al. (2006) as a Seyfer–2 galaxy, positionally coincident with the galaxy ESO 217-G29. The positional coincidence is further strengthened by our updated X–ray coordinates $\alpha_{J2000} = 12^h 10^m 29.01^s$, δ_{J2000} = -52° 21′ 48″.1 (after applying the astrometric correction, see § 3.6.1). The association of the source XMMU J121029.0−522148 with the galaxy ESO 217-G29 is evident in our *WFI* images (see Figure 3.16), which clearly resolve the galaxy structure (nucleus, bar, and spiral arms) and show that the source position is clearly coincident with the bright nucleus. Strangely enough, the cross–correlation with the *WFI* catalogue yields a candidate optical counterpart which is at 3″.37 from the nominal X–ray source position. This is an error of *SExtractor*, the software used to run the source detection on the *WFI* images, which did not correctly resolve the nucleus of the galaxy. We thus discarded the flux of the galaxy computed by *SExtractor* and we assumed an R–band magnitude of 14.93, as reported in *Simbad*. From the computed X–ray flux (see § 3.4.3) we thus derived an X–ray–to–optical flux ratio $\frac{f_X}{f_{opt}} = 0.166$, in agreement with the expectations for a low–luminosity Seyfert–2 galaxy.

In Table 3.5 we have listed all the candidate counterparts to the other 39 X–ray sources of the bright sample (see § 3.4). 32 of them ($\sim$ 82%) have at least one optical candidate counterpart. In particular, for 12 X–ray sources ($\sim$ 27%) the cross–matching produced more than one optical candidate counterpart. For each of the optical candidate counterparts (either single or multiple) we report both their magnitudes (in one reference passband) and their $\frac{f_X}{f_{opt}}$ ratios (computed for the assumed X–ray spectral model). The proposed classification, reported in Table 3.5, is considered virtually secured when best agreement is found between the different classification indexes, i.e. the X–ray source spectrum and the hydrogen column density N_H, on one side, and the colour-based classification and $\frac{f_X}{f_{opt}}$ ratio of the optical candidate counterpart, on the other one. For simplicity, we considered only two main X–ray source classes, i.e. *STELLAR* and *AGN*: in the first class we include the standard galactic sources with a soft, mainly thermal spectrum and low X–ray/optical flux ratio, while in the second class we include extra–galactic sources with a hard, likely non–thermal spectrum and high X–ray/optical flux ratio. None of our X–ray sources is associated with cluster of galaxies or with non–active galaxies. Moreover, we flagged cases where the source classification is likely, but not secured, or uncertain because of one or more inconsistencies between the different classification indexes. To this aim, we devised the following classification flags: *a* the source classification is likely but not secured by the identification of its optical counterpart, since the candidate optical counterpart is unclassified, or poorly classified, or undetected; when compelling evidence is lacking the source classification is uncertain because *b* the best–fit N_H value is too low for AGNs and too high for stars, *c* the X–ray spectrum is not in agreement either with the magnitude or with the colour-based classification of the optical candidate counterparts, *d* the source X–ray spectrum is not unambiguously determined, and/or the spectral parameters have large errors. Of course, multiple flags were assigned when different cases apply.

Following a decision-tree approach, we have thus proposed a virtually secure or likely classification for 15 of the 39 brightest X–ray sources (36% of the total). According to our classification scheme, we propose that these 15 sources are active galactic nuclei (AGNs). These sources have all a clear, or generally most likely, *power–law* X–ray spectrum, relatively high N_H, and 6 of them have an optical candidate counterpart identified with a QSO, with a consistent $\frac{f_X}{f_{opt}}$ ratio. For example, we classified source #216 (XMMU J120955.1−522105) as an AGN, without any flag, because of its *power–law* spectrum and N_H, and because its candidate optical counterparts is classified as QSO. We thus considered the classification of these 6 sources as secured. Three sources, i.e. #304 (XMMU J121052.9−522354), #326 (XMMU J121034.6−522457), and #517 (XMMU J121031.9−523046), have no optical candidate counterpart, while other sources, i.e. #520 (XMMU J121101.5−523030), #471 (XMMU J121057.3−522905), and #533 (XMMU J121013.2-523123), have a candidate optical counterpart but for it no color-based classification is possible. However, their *power–law* X–ray spectra, N_H, and the constraints on the $\frac{f_X}{f_{opt}}$ ratio, suggest that they are AGNs. Furthermore, two of them, i.e. #326 (XMMU J121034.6−522457) and #520 (XMMU J121101.5−523030), also feature a significant long term X–ray variability (see § 3.4.2), which reinforces their classification as AGNs. We thus classified these five sources as AGNs and we flagged as *a* because of the lack of a possible, or unambiguous, optical identification.

For 18 X–ray sources the proposed classifications reported in Table 3.5 (11 AGNs and 7 stars) are uncertain because of inconsistencies between the classification indexes. For instance, we classified source #158 (XMMU J121018.4−521 911) as a star since its X–ray light curve features large and short flares (see § 3.4.2) and its candidate optical counterpart is an M3 star. However, because of its somewhat large best–fit N_H, we prudently flagged its classification as *b*. Instead, source #198 (XMMU J120841.6−522026) was classified as an AGN because of its *power–law* spectrum, but it has a quite low N_H and we flagged its classification as *b*. We classified sources #410 (XMMU J120921.0−522700) and #688 (XMMU J120959.0−523618) as AGNs but we flagged these classifications as *a* since their candidate optical counterparts are unclassified. The former was also flagged as *d* since its X–ray spectrum is not unambiguously determined.

For the 6 X–ray sources for which no fit to the X–ray spectrum was possible with the tested single model component, or different model fits yield comparable χ^2 (flagged with *"uncl"* in Table 3.5) we could only suggest, at most, tentative classifications. For instance, source #263 (XMMU J120928.2−522225) might be classified as a galaxy since the colours of its nearest optical candidate counterpart are consistent with an elliptical galaxy. Similarly, source #121 (XMMU J120901.3−521741) has a candidate QSO optical counterpart and might be thus classified as an AGN. For source #386 (XMMU J121043.1−52263 8) not even the optical candidate counterpart is classified. Source #357 (XMMU J121113.8−522532) has no candidate counterpart in the optical/NIR catalogue[7]. The source #426 (XMMU J121000.0−522747) remains unclassified, due to conflicting power–law spectral model and stellar X-ray/optical flux ratio (although within its error-circle a clear galaxy can be seen in the *WFI* images).

Based on the previous analysis, we can summarize the classification of the 39 brightest sources as follows:

- 15 sources are classified: 5 of them were already classified in Novara et al. (2006), while 1 had an uncertain classification and 3 were unclassified; the remaining 6 sources are new detections
- 18 sources have an uncertain classification: 2 of them were classified in Novara et al. (2006), while 5 were uncertain and 6 unclassified; the remaining 5 sources are new detections
- 6 source are unclassified: 1 of them was unclassified also in Novara et al. (2006), while the remaining 5 sources are new detections

We note that in Novara et al. (2006), apart from the Seyfert–2 galaxy ESO 217-G29, a classification was proposed only for 7 of the remaining 23 brightest X–ray sources (30%). For these 7 sources we have revised the classification proposed in Novara et al. (2006), which is now confirmed for only 5 of them, while it is downgraded as uncertain for the other 2. Among the 6 source of Novara et al. (2006) with an uncertain classification, 1 is now fully classified, while the other 5 remain uncertain. Finally, 3 of the 10 unclassified sources are now classified, while other 6 are uncertain and only 1 remains stil unclassified.

3.7.3 Faintest X-ray sources

Finally, we have also evaluated the classification of the 104 remaining, fainter X–ray sources in our new serendipitous catalogue. Since for all of them the lower number of counts (≤ 500) does not allow to perform an accurate spectral analysis, the characterisation of the X–ray spectrum only relies on the source *HR*. As in the case of the bright sources (§ 3.7.2), the proposed X–ray source classifications is based on the source *HR* and on the X–ray–to–optical flux ratio $\frac{f_X}{f_{opt}}$, using the classification scheme devised in La Palombara et al. (2006).

---

[7] It is possible to note that this source falls in a region polluted by the halo of the bright star ρ Cen, which was masked before the source extraction (see § 3.5.3), so that no match was produced by the X–correlation (see § 3.6.3). Although a star is indeed detected in the *WFI* images, close the X-ray source position, it is saturated in almost all bands so that not even crude optical flux estimates can be obtained.

When a reliable classification of the optical/NIR candidate counterparts is found, also this information is used as a further classification evidence. Based on the *HR* distribution discussed in § 3.3.4, we have assumed that sources with an $HR <$ -0.9 have spectra corresponding to coronal emission from normal stars, while sources with $HR >$ -0.5 are either extra–galactic (normal or active galaxies or cluster of galaxies) or accreting binary systems (XRBs or CVs). Because of the typical *HR* errors, we have considered sources with intermediate values (-0.9 $< HR <$ -0.5) as borderline cases and thus we have not considered this parameter considered compelling for the new source classification. For sources affected by too large errors on the *HR*, this parameter is not considered at all. As in § 3.7.1, when no candidate counterparts were found we have assumed the $R = 23.97$ limiting magnitude of the *WFI* catalogue to compute the $\frac{f_X}{f_{opt}}$ lower limit.

Following the same decision-tree approach used to classify the brightest X–ray sources, 4 of the 25 sources with no candidate counterpart remain unclassified, while all the remaining 21 sources are identified with an AGN. On the other hand, among the 36 sources with a single candidate counterpart 10 are identified as stars (2 sure and 8 uncertain), 19 as AGNs (8 sure and 11 uncertain) and 2 with galaxies (since the *WFI* images show an evident extended source as countepart); the other 5 sources remain unclassified, due to unconstrained or conflicting hardness ratio and/or X-ray/optical flux ratio, but in the error-circle of two of them a clear galaxy can be seen in the *WFI* images. Finally, in the case of the 43 X-ray sources with two or more candidate counterparts we propose 11 classifications as stars (10 sure and only 1 uncertain) and 28 classifications as AGNs (27 sure and only 1 uncertain), while for the other 4 sources it is not possible to suggest any classification.

In summary, we classified 21 sources (corresponding to 20% of the total) as stars and 68 sources (65%) as AGNs, while other 2 sources (2%) were identified with galaxies and the remaining 13 sources (13%) remained unclassified.

Table 3.5: *Main characteristics of the 39 brightest sources. The sources are sorted by decreasing count number.* *(*Continued on next page*)*

(1) SRC	(2) NAME	(3) cts	(4) Model	(5) N_H (10^{21} cm^{-2})	(6) Γ/kT (-/keV)	(7) χ^2_ν	(8) D_{XO} (arcsec)	(9) MAG (mag)	(10) OPTICAL FILTER	(11) $\frac{f_X}{f_{opt}}$ ($\log_{10}$)	(12) OPTICAL CLASS	(13) X-RAY SOURCE CLASS
520	XMMUJ121101.5-523030	6464	wabs(pow)	$2.2^{+0.4}_{-0.3}$	$1.97^{+0.12}_{-0.11}$	1.07	2.71	19.68	R	0.39	-	AGN^{a}
338	XMMUJ120942.1-522458	5611	wabs(pow)	$1.1^{+0.3}_{-0.3}$	$1.98^{+0.12}_{-0.11}$	1.15	2.99	19.43	R	0.15	QSO	AGN
241	XMMUJ120858.8-522129	3829	wabs(mekal)	$1.4^{+0.6}_{-0.6}$	$0.62^{+0.02}_{-0.02}$	1.63	3.07	13.71	V	-2.11	-	STAR^{a,c}
508	XMMUJ120857.1-523014	2287	wabs(brem)	$2.9^{+0.9}_{-0.8}$	$0.28^{+0.70}_{-0.54}$	1.81	3.14	16.25	R	-1.55	-	STAR^{a,c}
			wabs(bbody)	$1.0^{+0.9}_{-0.6}$	$0.17^{+0.02}_{-0.02}$	1.72						
480	XMMUJ120908.1-522918	2146	wabs(pow)	$1.2^{+0.5}_{-0.5}$	$1.92^{+0.19}_{-0.16}$	0.90	2.42	19.36	R	-0.06	QSO	AGN
198	XMMUJ120841.6-522026	1976	wabs(pow)	$0.1^{+0.02}_{-0.04}$	$1.85^{+0.22}_{-0.19}$	0.95	3.38	20.14	R	0.46	QSO	AGN^{b}
							3.28	21.71	R	1.10	MS M3-M4	
674	XMMUJ121007.2-523555	1631	wabs(pow)	$0.8^{+0.5}_{-0.5}$	$1.71^{+0.14}_{-0.17}$	1.13	1.83	19.26	R	-0.39	QSO	AGN^{b}
244	XMMUJ120842.5-522128	1603	wabs(pow)	<0.08	$1.66^{+0.20}_{-0.22}$	0.82	3.70	21.97	V	1.22	-	AGN^{a,b}
							3.33	21.02	R	0.75	MS A7-WD	
357	XMMUJ121113.8-522532	1488	wabs(brem)	$4.4^{+1.8}_{-1.5}$	$0.26^{+0.10}_{-0.10}$	1.73	-	-	-	-	-	uncl^{c}
			wabs(bbody)	$2.5^{+1.9}_{-1.4}$	$0.16^{+0.03}_{-0.03}$	1.75	-	-	-	-	-	
471	XMMUJ121057.3-522905	1353	wabs(pow)	$9.4^{+0.4}_{-2.8}$	$2.12^{+0.32}_{-0.33}$	1.48	3.92	20.11	R	-0.10	-	AGN^{a}
			wabs(mekal)	$8.9^{+3.4}_{-2.8}$	$3.63^{+2.06}_{-1.06}$	1.42	3.60	20.42	R	0.03	-	
			wabs(brem)	$7.6^{+2.8}_{-2.0}$	$4.27^{+3.28}_{-1.53}$	1.48					-	
509	XMMUJ120913.8-523023	1319	wabs(pow)	$0.9^{+0.5}_{-0.5}$	$1.97^{+0.17}_{-0.21}$	0.89	2.67	20.11	R	0.00	WD	AGN^{b,c}
			wabs(brem)	$0.3^{+0.4}_{-0.0}$	$4.27^{+2.57}_{-1.24}$	0.96						
426	XMMUJ121000.0-522747	1271	wabs(pow)	$0.1^{+0.6}_{-0.0}$	$1.64^{+0.16}_{-0.18}$	2.15	3.66	15.84	R	-1.92	Sbc-vB2	uncl^{c}
340	XMMUJ120951.1-522525	1131	wabs(pow)	$0.4^{+0.7}_{-0.0}$	$1.79^{+0.21}_{-0.28}$	0.87	-	>23.97	R	>1.24	-	AGN^{a,b}
			wabs(brem)	<0.4	$5.34^{+4.37}_{-2.10}$	0.93	-				-	

Table 3.5: (*Continued on next page*)

(1) SRC	(2) NAME	(3) cts	(4) Model	(5) N_H (10^{21} cm^{-2})	(6) Γ/kT (-/keV)	(7) χ^2_ν	(8) D_{XO} (arcsec)	(9) MAG (mag)	(10) OPTICAL FILTER	(11) $\frac{f_X}{f_{opt}}$ (log$_{10}$)	(12) OPTICAL CLASS	(13) X-RAY SOURCE CLASS
598	XMMUJ120927.4-523326	1128	wabs(pow)	$0.9^{+0.6}_{-0.5}$	$2.07^{+0.16}_{-0.21}$	0.92	3.81	20.17	V	0.00	-	AGN^{a,b}
404	XMMUJ121017.5-522706	1119	wabs(mekal)	$5.3^{+1.1}_{-1.2}$	$0.63^{+0.06}_{-0.06}$	1.39	3.46	15.47	R	-2.51	MS K3-K2	STAR^{b}
158	XMMUJ121018.4-521911	1090	wabs(brem)	$2.8^{+1.5}_{-1.2}$	$0.28^{+0.11}_{-0.08}$	1.38	4.04	16.49	R	-1.82	MS M3	STAR^{b}
490	XMMUJ120935.6-522940	1058	wabs(pow)	$4.5^{+2.6}_{-1.5}$	$2.46^{+0.64}_{-0.45}$	1.09	3.00	22.33	R	0.33	QSO	AGN
			wabs(brem)	$3.0^{+1.9}_{-1.3}$	$2.46^{+1.93}_{-0.84}$	1.10					-	
			wabs(bbody)	$0.2^{+1.9}_{-0.0}$	$0.57^{+0.09}_{-0.09}$	1.29					-	
216	XMMUJ120955.1-522105	1033	wabs(pow)	$1.5^{+0.8}_{-0.9}$	$2.06^{+0.37}_{-0.29}$	1.25	3.39	18.74	R	-0.78	QSO	AGN
							3.58	22.27	R	0.63	MS M2	
585	XMMUJ120906.9-523310	980	wabs(pow)	$1.8^{+0.8}_{-0.8}$	$1.96^{+0.21}_{-0.25}$	1.01	3.79	21.76	R	0.58	QSO	AGN
			wabs(brem)	$1.0^{+0.8}_{-0.5}$	$4.46^{+3.58}_{-1.48}$	1.05	2.53	19.51	R	-0.32	QSO	
141	XMMUJ120945.2-521828	959	wabs(pow)	$0.1^{+0.5}_{-0.0}$	$1.48^{+0.28}_{-0.18}$	1.38	3.46	21.05	R	0.44	QSO	AGN^{b}
688	XMMUJ120959.0-523618	946	wabs(pow)	$2.3^{+1.0}_{-0.9}$	$1.94^{+0.22}_{-0.29}$	0.80	2.18	22.00	V	0.57	-	AGN^{a}
			wabs(brem)	$1.5^{+1.0}_{-0.6}$	$4.69^{+4.41}_{-1.58}$	0.81	3.63	22.53	V	0.79	-	
654	XMMUJ120936.5-523515	888	wabs(pow)	$1.3^{+0.1}_{-0.0}$	$2.08^{+0.69}_{-0.55}$	1.63	3.38	22.66	R	0.89	-	AGN^{a}
							1.51	22.88	R	0.98	-	
433	XMMUJ120850.5-522738	818	wabs(brem)	$2.2^{+0.2}_{-0.1}$	$0.47^{+0.21}_{-0.17}$	1.69	2.27	16.63	R	-1.77	MS K5-M0	STAR^{b}
214	XMMUJ121040.9-522055	785	wabs(pow)	<0.3	$1.92^{+0.24}_{-0.21}$	1.76	-	>23.97	R	>1.39	-	AGN^{a,b}
363	XMMUJ121039.9-522538	773	wabs(mekal)	$1.7^{+1.1}_{-1.4}$	$0.53^{+0.10}_{-0.06}$	2.70	3.06	14.22	R	-2.74	-	STAR^{a,b}
304	XMMUJ121052.9-522354	699	wabs(pow)	$2.4^{+2.6}_{-1.4}$	$1.56^{+0.38}_{-0.28}$	1.41	-	>23.97	R	>1.52	-	AGN^{a}
326	XMMUJ121034.6-522457	694	wabs(pow)	$7.8^{+5.0}_{-3.7}$	$1.30^{+0.30}_{-0.31}$	1.31	-	>23.97	R	>1.44	-	AGN^{a}
			wabs(bbody)	$0.9^{+0.3}_{-0.0}$	$1.26^{+0.24}_{-0.18}$	1.33	-	>23.97	R	>1.40	-	
372	XMMUJ120950.5-522613	618	wabs(bbody)	<0.05	$0.25^{+0.03}_{-0.03}$	1.26	5.43	20.57	R	-0.55	MS K4	STAR^{d}
			wabs(brem)	<0.05	$0.73^{+0.27}_{-0.24}$	1.13	2.59	23.86	U	0.82	-	
386	XMMUJ121043.1-522638	605	?	-	-	-	2.41	18.47	R	-0.96	-	uncl
236	XMMUJ120904.8-522129	551	wabs(pow)	$2.2^{+1.7}_{-1.6}$	$1.89^{+0.66}_{-0.28}$	0.94	3.50	22.42	R	0.65	-	AGN^{a}
			wabs(bbody)	<0.9	$0.61^{+0.13}_{-0.11}$	1.21						

Table 3.5

(1) SRC	(2) NAME	(3) cts	(4) Model	(5) N$_\mathrm{H}$ (10^{21} cm^{-2})	(6) Γ/kT (-/keV)	(7) χ^2_ν	(8) D$_{XO}$ (arcsec)	(9) MAG (mag)	(10) OPTICAL FILTER	(11) $\frac{f_X}{f_{opt}}$ (log$_{10}$)	(12) OPTICAL CLASS	(13) X-RAY SOURCE CLASS
222	XMMUJ121006.3-522122	540	wabs(pow)	$0.5^{+1.5}_{-0.0}$	$2.38^{+0.93}_{-0.51}$	1.06	3.36	20.44	R	-0.50	QSO	AGN^b
			wabs(brem)	<0.7	$1.70^{+1.30}_{-0.73}$	1.04	2.18	19.76	R	-0.77	QSO	
204	XMMUJ120934.1-522034	535	wabs(brem)	$6.4^{+5.6}_{-3.1}$	$4.35^{+8.50}_{-2.53}$	1.56	3.48	21.39	R	0.21	MS F5	uncl^c
			wabs(pow)	$8.9^{+0.8}_{-4.6}$	$2.18^{+1.02}_{-0.37}$	1.53				0.23	-	
			wabs(bbody)	$0.7^{+4.7}_{-0.0}$	$0.77^{+0.18}_{-0.19}$	1.72				0.14	-	
410	XMMUJ120921.0-522700	535	wabs(pow)	$4.6^{+0.5}_{-0.3}$	$2.15^{+0.58}_{-0.69}$	1.54	-	>23.97	R	>0.88	-	AGN^{a,d}
			wabs(bbody)	$0.2^{+0.3}_{-0.0}$	$0.65^{+0.18}_{-0.18}$	1.75	-				-	
121	XMMUJ120901.3-521741	533	?	-	-	-	3.75	21.87	R	0.49	QSO	uncl
106	XMMUJ120955.3-521716	522	wabs(pow)	$4.8^{+0.4}_{-2.4}$	$1.73^{+0.57}_{-0.41}$	1.16	2.95	19.96	R	-0.18	QSO	AGN
							2.13	23.53	R	1.24	-	
263	XMMUJ120928.2-522225	515	?	-	-	-	0.86	22.46	R	0.49	-	uncl
			?				2.19	22.51	R	0.51	QSO	
			?				3.93	22.09	R	0.34	MS M2.5	
			?				3.04	22.14	R	0.36	MS K7-K5	
64	XMMUJ120958.7-521449	512	wabs(pow)	$0.2^{+0.1}_{-0.2}$	$1.84^{+0.79}_{-0.46}$	1.25	1.72	23.46	R	1.26	-	AGN^{a,b}
517	XMMUJ121031.9-523046	508	wabs(pow)	$1.7^{+0.4}_{-0.0}$	$1.78^{+0.86}_{-0.58}$	0.77	-	>23.97	R	>0.73	-	AGN^a
			wabs(bbody)	<1.6	$0.63^{+0.18}_{-0.14}$	0.98	-					
533	XMMUJ121013.2-523123	499	wabs(pow)	$3.4^{+0.3}_{-0.2}$	$2.05^{+0.30}_{-0.44}$	1.43	3.65	20.66	U	-0.18	-	AGN^a
			wabs(bbody)	<1.4	$0.65^{+0.11}_{-0.10}$	1.63	3.28	16.18	R	-2.25	-	

Key to Table - Col.(1): source ID number. Col.(2) catalogue name. Col.(3): source total counts (in the 0.3–8 keV energy range). Col.(4): best–fit emission model(s); the symbol 'uncl' indicates that none of the tested single–component models provided an acceptable fit. Col.(5): best–fit hydrogen column density with the associated 90% confidence errors. Col.(6): best–fit photon–index or plasma temperature (for a power–law or a thermal emission model, respectively) with the associated relevant 90% confidence level error. Col.(7): best–fit reduced chi–square. Col.(8): angular distance between the X–ray source position and its optical candidate counterpart (if any). The most likely optical counterpart are listed first. Col(9): magnitude of the optical candidate counterpart or $R \geq 23.97$ upper limit if no candidate counterpart is found. Col.(10): optical filter; if the optical candidate counterpart has no R-band magnitude the V, B, I and U-band magnitudes in this order are considered. Col.(11): logarithmic values of the X–ray–to–optical flux ratio; the optical flux is based on the magnitudes in Col.(9) while the X–ray flux is based on the best–fit model or, when no model is acceptable, on a power–law spectrum with photon–index $\Gamma = 1.7$ and hydrogen column density $\mathrm{N_H} = 1.3 \times 10^{21}$ cm^{-2}, corresponding to the total galactic column density. Col.(12): suggested classification of the optical candidate counterpart from the *WFI* catalogue. MS indicates a main sequence star, QSO indicates a quasar, WD indicates a white dwarf, Sbc and vB2 indicate a spiral galaxy and a blue compact galaxy respectively. Col.(13): proposed source classification of X–ray source with warning flags: *a* the source classification is likely but not secured by the identification of its optical counterpart: the candidate optical counterpart is unclassified, or poorly classified, or undetected; *b* the source classification is uncertain because the best–fit N_H value is too low for AGNs and too high for stars, *c* the X–ray spectrum is not in agreement either with the magnitude or with the colour-based classification of the candidate optical counterparts, *d* the source X–ray spectrum is not unambigously determined, and/or the spectral parameters have large errors.

Chapter 4

The *Swift* mission

4.1 Science goals of the mission

The *Swift* mission (Gehrels et al., 2004), fruit of an international collaboration involving teams mainly from the USA, the United Kingdom, and Italy, is a multi-wavelength observatory successfully launched on November 20, 2004 (general characteristics are summarized in Table 4.1). The instruments on board *Swift* are the Burst Alert Telescope (BAT), operating in the soft gamma-ray domain, the X-ray Telescope (XRT) and the Ultraviolet/Optical Telescope (UVOT). A schematic view of the three co-aligned instruments on the spacecraft is given in Figure 4.1.

Swift is specifically designed to study the Gamma-ray Bursts (GRBs) and their afterglow. The wide-angle BAT monitors the sky awaiting for a new GRB and, whenever the system on board triggers it, an autonomous rapid spacecraft slew is performed to bring the burst into the narrower XRT and UVOT fields of view. Due to such an autonomy and to the very large BAT FoV (~ 2 sr), *Swift* is able to perform X-ray and UV/optical observations of > 100 bursts per year within 20-70 seconds of a burst detection. The *Swift* nominal lifetime is 5 years with a predicted orbital lifetime of ~ 10 years. The number of GRBs and their relevant afterglows that is predicted to be observed during the mission should be enough to determine their origin and to pioneer their usage as probes of the early universe.

Thanks to the gamma-ray telescope BATSE on board the Compton Gamma-Ray Observatory (*CGRO*), launched on April 5, 1991, GRBs are known to be uniformly distributed over the sky and to appear at the rate of ~ 1 per day, lasting from seconds to a few hours at gamma-ray wavelengths (for a detailed description see for example Piran (2005)). Thus, while waiting for new GRBs, the BAT spends a large fraction of time collecting a huge amount of data on the hard X-ray sky. Indeed, a sensitive all-sky survey in the 15-150 keV energy range will be one of the major outcomes of the *Swift* mission. With an expected limiting flux of ~ 0.2 mCrab at high Galactic latitude and ~ 3 mCrab at low

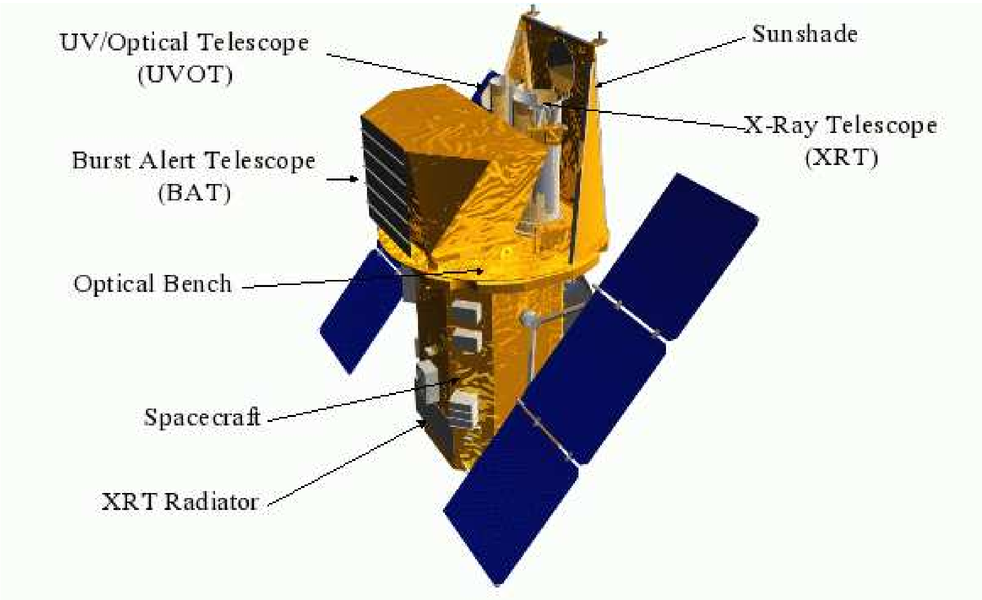

Figure 4.1: *The Swift satellite.*

Table 4.1. *Swift Mission Characteristics (Gehrels et al., 2004)*

Mission Parameter	Value
Slew Rate	50° in < 75 s
Orbit	Low Earth, 600 km altitude
Orbit Duration	96 min
Inclination	22°
Launch Vehicle	Delta 7320-10 with 3 meter fairing
Mass	1450 kg
Power	1040 W
Launch Date	November 20, 2004

Table 4.2. *Burst Alert Telescope Characteristics (Gehrels et al., 2004)*

BAT Parameter	Value
Energy Range	15-150 keV
Energy Resolution	$\sim$ 7 keV
Aperture	Coded mask, random pattern, 50% open
Detection Area	5240 cm^2
Detector Material	CdZnTe (CZT)
Detector Operation	Photon counting
Field of View (FoV)	1.4 sr (half-coded)
Detector Elements	256 modules of 128 elements/module
Detector Element Size	$4 \times 4 \times 2$ mm^3
Coded-Mask Cell Size	$5 \times 5 \times 1$ mm^3 Pb tiles
Telescope PSF	$<$ 20 arcmin
Source Position and Determination	1-4 arcmin
Sensitivity	$\sim 10^{-8}$ erg cm^{-2} s^{-1}
Number of Bursts Detected	$>$ 100 yr^{-1}

Galactic latitude (with a 4-year dataset), the *Swift* survey is expected to be $\sim$ 10 times deeper than the HEAO1 A4 reference all-sky hard X-ray survey (Levine et al., 1984), performed more than 25 years ago. Preliminary results, based on 3 months of data, were published by Markwardt et al. (2005). The non-GRB science also includes a study of Active Galactic Nuclei (AGNs) as well as a monitoring of transient hard X-ray sources (see Gehrels et al. (2004) for a detailed description).

4.2 The Burst Alert Telescope (BAT)

The BAT (Barthelmy et al., 2005) is a highly sensitive, large FoV instrument designed to perform a detailed study of GRBs as well as a hard X-ray all-sky survey. It is a coded-mask telescope (see Caroli et al. (1987) for a detailed description of this kind of instruments) operating in the 15-150 keV energy range, with a possible non-coded response extension up to $\sim$ 200 keV. BAT has a Point Spread Function (PSF) of $\sim$ 20 arcmin and can provide the position of a source with a 1-4 arcmin uncertainty. The parameters of the instrument are summarized in Table 4.2. A schematic view of the BAT is shown in Figure 4.2.

4.2.1 Technical description

The coded aperture mask

Since it is not possible to produce an image in the gamma-ray domain using traditional focusing optics, especially over a large FoV as for the BAT, the only way to create an image is to use the coded-aperture method (see Dicke (1968),

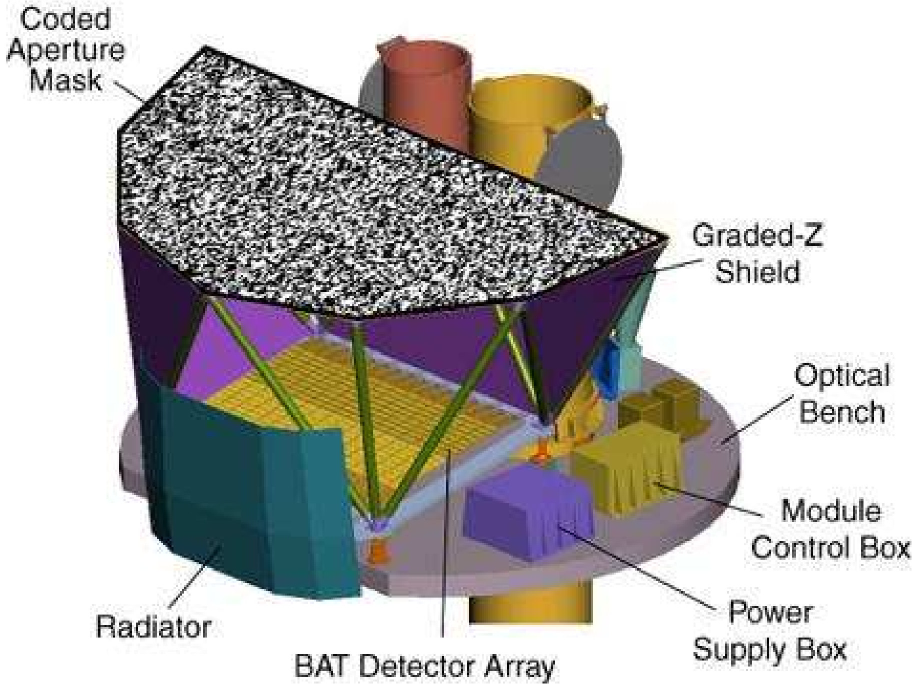

Figure 4.2: *A schematic view of the Burst Alert Telescope. The D-shaped coded mask, the CZT detector array, and the graded-Z shield are visible.*

Skinner et al. (1987); see also Caroli et al. (1987) and references therein for a complete description). Basically, a coded-mask telescope consists of a mask overheading a position sensitive detector. The mask is composed of elements transparent and opaque to the radiation assuming a selected pattern. Given a gamma-ray source illuminating the mask, the portions of the aperture blocked by the opaque elements absorb the gamma-rays, and the not blocked portions allow the rays to pass through. As a result, a shadow of the pattern, which depends on the position of the source, is projected on the detector array below. Starting from the map of illuminated detector pixels and the mask aperture, an image of the source can be reconstructed by a deconvolution process. If many sources are present in the FoV, different shadows overlap on the detector plane obstructing the image reconstruction. Thus, the aperture pattern must be carefully selected in order to allow each distinct source to cast a unique shadow pattern on the detector array. Moreover, when a source is on-axis, the aperture shadow fully illuminates the detector array, and so it is *fully coded*. As the source moves farther off axis, only a portion of the aperture shadow illuminates the detector array. The fractional illumination is called the *partial coding fraction* and obviously imply a sensitivity loss as compared with the on-axis case.

The BAT has a D-shaped coded mask, made of $\sim 54,000$ lead tiles ($5 \times 5 \times 1$ mm) mounted on a 5 cm thick composite honeycomb panel. Such tiles are opaque to radiation in the 15-150 keV energy range and become progressively

Figure 4.3: *Picture of the BAT coded aperture mask before* Swift *launch.*

transparent above 150 keV reducing the coding response. The BAT coded mask is located 1 meter above the CZT detector plane and uses a completely random, 50% open-50% closed pattern (see Figure 4.3). The mask is 2.4 × 1.2 m (considering the D-shape, it is 2.7m^2), which yields a 100° × 60° FoV (half-coded).

The BAT partial coding map is shown in Figure 4.4. It can be seen that only a small region around the centre of the BAT FoV is 100% coded whereas the partially coded region is wider. The BAT FoV with coded fraction greater than 10% is about 2.2 sr (> 50%, 1.5 sr ; > 90%, 0.5 sr).

The detector plane

The BAT detector plane is composed of 32768 pieces of 4 × 4 × 2 mm CdZnTe (CZT), forming a 1.2 × 0.6 m sensitive area. For electronic control, event data handling, and fabrications reasons, these pixels are grouped following a hierarchical structure. Groups of 128 detector elements are assembled into 8 × 16 arrays, each one connected to a different readout electronic circuit. Detector modules, each containing two such arrays, are further grouped by eights forming 16 blocks. For fabrications reasons, there is a gap between two adjacent pixels: it was restricted to be an integer multiple (2 or 3) of the basic pixel dimension, so that the image reconstruction process could easily handle it. Considering that a coded-mask telescope cannot derive the direction of any

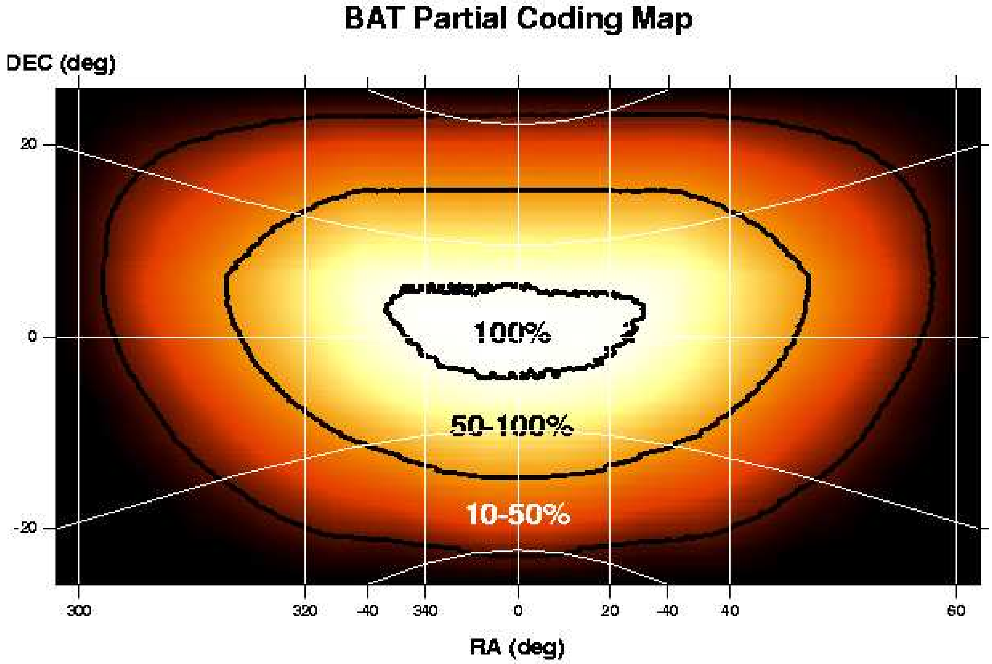

Figure 4.4: *The D-shaped BAT FoV. Fully coded (100%), half-coded (50%) down to the 10% coded fraction contours are indicated.*

photon arriving at the detector, such a hierarchical structure is optimised to allow BAT to tolerate the loss of individual pixels, detector modules, and even whole blocks without losing the ability to detect bursts and determine locations. There is, of course, a loss in burst-detection and the survey sensitivities.

The Fringe Shield

A graded-Z Fringe Shield, composed of Pb, Ta, Sn, and Cu, is located on the side walls between the Mask and the Detector Plane and under the Detector Plane in order to reduce the event rate in the detector plane. Due to its performance, the isotropic cosmic diffuse flux and the anisotropic Earth albedo flux are reduced by 95%.

4.2.2 BAT operating modes

BAT can work in two distinct operating modes: the so-called “Burst mode” and “Survey mode”. Most of the BAT time is spent in Survey mode, waiting for a GRB occurring in the FoV. Events are accumulated in the detector plane and searched by the on board algorithm for increases in the count rate over a range of time scales. If no special triggers are found, all these events are binned into eighty energy bins and integrated over ~ 5 minutes (survey data) because there is not enough on board storage or down-link capacity to send them all to the ground. Instead, when the trigger algorithm is satisfied, the Burst mode is enabled and photon-by-photon data are produced and sent to the ground.

Burst mode

The algorithm on board BAT, which search for a GRB, is composed of two processes. First, it looks for excesses in the detector count rate above the expected background and constant sources count rate. During a 96-minute low Earth orbit, the detected background rates can vary by more than a factor of two. Moreover, the duration of the gamma-ray emission from GRBs ranges from milliseconds to minutes. For such reasons the triggering algorithm was written in order to be able to extrapolate the background and compare it to the measured count rate over a variety of timescales and in several energy bands. If at least one trigger is found, the algorithm switches to the second process. Another independent trigger criterion is implemented to search for slow rising GRBs and transients: it consists in an image analysis of the detected count rate performed every 64 sec. Such images are scanned for point sources which are then cross-checked against an on board catalog. The detection of any new source produce a GRB alert, whereas any known source above a given level initiates the interesting-source response procedure. The second process begins whenever the trigger algorithm detects a count-rate excess in the detector. In this case the data are analysed to discover if this excess is due to a GRB. The system on board extracts source and background data based on the energy range and time intervals flagged by the trigger. Such data are converted to a sky map which is then searched for excesses. If a significant excess is detected in a position that not match any source of the on board catalog, then a GRB is declared. The imaging process is fundamental to confirm the reality of the previous count rate detection. Thus, in order to eliminate false triggers, the trigger threshold was set to an opportune level. Finally, when a GRB alert is produced, the system on board decides if it is worthy to begin a spacecraft slew to point the source, depending on the merit of the burst and the observing constraints (e.g. the Earth limb does not cover a large fraction of the FoV).

When a GRB is declared, several products are constructed, the most significant of these being a dump of all event data included in the trigger time, with a total duration of about 10-15 minutes. Each event is tagged with an associated time of arrival, detector number and energy. This allows event data to be used for the extraction of light curves of all the sources in the FoV with different timescales and energy bands. These data can also be used to extract spectra of a given source. The BAT also produces several products all the time, regardless of whether there is a GRB or not. These are typically various array rates, spacecraft attitudes, housekeeping values, and trigger diagnostics.

Figure 4.5: *Representation of a Detector Plane Histogram (DPH). It is three dimensional in the sense that there are two spatial dimension (that of the detector plane) and one spectral dimension.*

Survey mode

Most of the time is spent by BAT waiting for a GRB occurring in the FoV (Survey mode). Photons interacting with the detector are processed (events) and then are tagged with an associated time of arrival, detector number and energy. Such information is stored on board in a memory buffer which may contain $\sim$ 10 minutes of data (depending on the actual count rate). If the burst trigger algorithm described above fails, the event data from the array are collected on board into Detector Plane Histograms (DPHs). DPHs are three dimensional histograms: for a given buffer set, every cell contains the number of events received in one of the 32768 pixels of the detector plane and in one of 80 energy channels. The energy bin widths are variable from one energy bin to the next, but have remained always the same since the *Swift* launch. Figure 4.5 shows a representation of a survey DPH.

Such histograms are accumulated over a typical 5 minutes time interval and then stacked as independent rows in a “Survey” data file. In some cases the duration of a DPH row can be longer or shorter depending on operational reasons (e.g., telemetry reduction or to get diagnostic information about the instrument). Also, DPH row integration times are truncated whenever the spacecraft begins a slew or enters the South Atlantic Anomaly (SAA). Generally speaking, the survey data cannot be used to search for time variations on

Table 4.3. *X-Ray Telescope Characteristics (Gehrels et al., 2004)*

XRT Parameter	Value
Energy Range	0.2-10 keV
Telescope	JET-X Wolter 1
Detector	E2V CCD-22
Effective Area	110 cm^2 @ 1.5 keV
Detector Operation	Photon counting, integrated imaging, and timing
Field of View (FoV)	23.6×23.6 arcmin
Detection Elements	600×602 pixels
Pixel Scale	2.36 arcsec
Telescope PSF	18 arcsec HPD @ 1.5 keV
Sensitivity	2×10^{-14} erg cm^{-2} s^{-1} (1 mCrab) in 10^4 s

time scales shorter than 5 minutes.

Other useful products are obtained on board, such as the Rate Data and the Maps. The former are lightcurves of the overall detected counts with different time scales, used by the on-board software for trigger searching. Housekeeping maps, useful for BAT analysis, are also produced. Among these, detector enable/disable maps and gain/offset maps are the most important. The former represent those detectors which were automatically disabled because noisy, whereas the latter record the approximate pulse-height-to-energy calibration for each detector. Gain/offset maps, in combination with ground calibration files, are used to produce calibrated event lists and survey files.

Together with auxiliary files (which contain all spacecraft-related information for a given observation), they are the standard basic products for BAT non-GRB science.

4.3 The X-ray Telescope (XRT)

The XRT (Burrows et al., 2005) is designed to measure fluxes, spectra, and lightcurves of GRBs in the 0.2-10 keV energy range. It can locate a typical GRB to 5-arcsec accuracy within 10 seconds of target acquisition and it can observe it beginning 20-70 seconds from burst discovery and continuing for days to weeks. The XRT is a focusing X-ray telescope with a 110 cm^2 effective area, 23 arcmin FoV and 18 arcsec resolution (half-power diameter). Table 4.3 summarizes the XRT parameters.

The XRT uses a grazing incidence Wolter 1 telescope to focus X-rays onto a performant CCD detector. Designed for the EPIC MOS instruments on the XMM-Newton mission, the CCD has an image area of 600×602 pixels (40×40

mm) and a storage region of 600×602 pixels (39×12 mm). The FWHM energy resolution of the CCD decreases from ∼ 190 eV at 10 keV to ∼ 50 eV at 0.1 keV, where below ∼ 0.5 keV the effects of charge trapping and loss to surface states become significant.

The XRT can work in three readout modes in order to cover the dynamic range and rapid variability expected from GRB afterglows. The telescope autonomously selects which mode is the best to use during an observation. The first mode is the "Imaging Mode" which produces an integrated image measuring the total energy deposited per pixel and does not permit spectroscopy. Usually this mode is used to position bright sources up to ∼ 37 Crab. The "Windowed Timing Mode" is selected whenever a high time resolution (2.2 ms) and bright source spectroscopy is required at expenses of the position information. This mode is very useful for sources with flux below ∼ 5 Crab. Finally, "Photon-counting Mode" uses sub-array windows to allow full spectral and spatial information to be obtained for source fluxes ranging from 1 mCrab to 45 mCrab

4.4 The Ultraviolet/Optical Telescope (UVOT)

The UVOT (Roming et al., 2003) is a 30 cm clear aperture Ritchey-Chrétien telescope with a primary f-ratio of f/2.0 increasing to f/12.72 after the secondary. It operates as a photon-counting instrument and carries two redundant detectors. Each detector has a filter wheel which allows low-resolution grism spectra of bright GRBs, and broadband UV/visible photometry. It is mounted in front of the detector carrying the following elements: a blocked position for detector safety; a white light filter; a field expander; two grisms; U, B, and V filters; and three broadband UV filters centred on 190, 220 and 260 nm. The two detectors are CCDs with 384×288 pixels, 256×256 of which are usable for science observations. Each pixel corresponds to 4 × 4 arcsec on the sky, providing a 17 × 17 arcmin FoV. Table 4.4 summarizes the UVOT parameters.

The UVOT can work in six different operating modes: slewing, settling, finding chart, automated targets, pre-planned targets, and safe pointing targets. When a GRB or a new target is triggered, the spacecraft is slewed to allow it to be within the UVOT FoV. During the slew, the UVOT is switched off in order to protect it from bright sources slewing across its FoV and damaging the detector. When the object is within ten arcminutes of the target, the UVOT begins the observation. Since the spacecraft is still settling, the target is moving rapidly across the FoV and the positional accuracy is only known to a few arcmin based on the BAT's centroided position. When the spacecraft is settled with small pointing errors, the UVOT begins a 100 second exposure in the V filter to produce a finding chart with positional accuracy of ∼ 0.3 arcsec. This aids the ground-based observers in localising GRBs. Then, an automated sequence of exposures, which uses a combination of filters, is executed (Au-

Table 4.4. *UltraViolet/Optical Telescope Characteristics (Gehrels et al., 2004)*

UVOT Parameter	Value
Wavelength Range	170-600 nm
Telescope	Modified Ritchey-Chrétien
Aperture	30 cm diameter
F-number	12.7
Detector	Intensified CCD
Detector Operation	Photon counting
Field of View (FoV)	17 × 17 arcmin
Detection Elements	2048 × 2048 pixels
Telescope PSF	0.9 arcsec FWHM @ 350 nm
Colors	6
Sensitivity	B = 24 in white light in 1000 s
Pixel Scale	0.5 arcsec

tomated Targets). When no Automated Targets are produced, observations of planned targets such as follow-up of previous automated targets, targets-of-opportunity, and survey targets begin. When observing constraints do not allow observations of automated or pre-planned targets, the spacecraft points to predetermined locations on the sky that are observationally safe for the UVOT.

The UVOT data can be collected in two modes which can be run contemporaneously: "Event" and "Imaging". The Event mode consists on tagging the arrival time of each photon with a resolution equal to the CCD frame time ($\sim$ 11 ms). In Imaging Mode, photon events are summed into an image for a time period $\leq$ 20 s. The advantage of Imaging Mode is that it minimizes the telemetry requirements when the photon rate is high, but at the expense of timing information.

Chapter 5

Swift/BAT as a bright source monitor

There has been little progress in the hard X–ray surveys during the last 25 years due to a lack of wide-field instruments with good sensitivity and sufficient angular resolution together at a large sky coverage to produce a wide sample of data in order to perform a all-sky survey. The last all-sky hard X–ray survey (Levine et al., 1984) was performed more than 25 years ago with the NASA mission HEAO1 A4. It collected data in the 0.2 keV-10 MeV energy range and obtained a new sky survey in the 13-180 keV energy range. The instrument on board HEAO1 A4 was characterized by a not wide field of view ($3^\circ \times 3^\circ$) and by a low sensitivity of $\sim$ 14 mCrab in the 13-80 keV energy band (Levine et al., 1984). More recently the ESA satellite *INTEGRAL* (Winkler et al., 2003), thanks to the high sensitivity and good imaging capabilities of the hard X–ray instrument (IBIS/ISGRI) on board, performed wide and deep observation in the 15 keV-10 MeV energy range. The IBIS/ISGRI (Ubertini et al., 2003) large field of view ($\sim 29^\circ \times 29^\circ$) and its good angular resolution ($\sim 12'$) was sufficient to resolve most of hard X–ray sources allowed a detailed study of previously unknown sources and the discovery of new ones. More than $\sim$ 400 sources were detected by ISGRI during the first $\sim$ 4 ys of the mission (Bird et al., 2007). Nevertheless, *INTEGRAL* observations are predominately in the galactic plane, thus the high latitude coverage is patchy.

The Burst Alert Telescope (see § 4.2), on board the *Swift* satellite (Gehrels et al., 2004), represents the major technological improvements for the imaging of the hard X–ray sky (for details see Chapter 4). During the survey mode (see § 4.2.2) BAT collect a large sample of data, and thanks to its wide FoV and its pointing strategy, BAT can monitor continuously up to 50-80% of the sky every day. These characteristics (for details, § 4.2) allow BAT to follow the spectral and temporal evolution of many bright X–ray sources in large time windows (even for the entire duration of the mission) and to estimate fundamental physical parameters (as the absolute flux and the spectral index) of the sources to complete the multi-waves studies of them.

After the description of the pipeline to analyse the BAT survey data in section 5.0.1, using the very bright and steady Crab as a reference source, the reliability of the pipeline has been tested in the § 5.1.1. In the § 5.1.2 the study of the 2005, 9-month long outburst of the galactic BH binary GRO J1655–40 has been performed. Such event was also carefully monitored with the narrow field instruments PCA and HEXTE on board the Rossi X-Ray Timing Explorer (*RXTE*), allowing the cross-check of the BAT results with those obtained simultaneously by an independent well calibrated instrument. The spectral analysis is described in § 5.0.1. Finally, BAT and *RXTE* spectral results are compared, thus assessing the performance of the pipeline in order to use the BAT data to monitor the behaviour of a strongly variable source (section 5.1.2).

The complete description of the technical characteristics of the pipeline and of the all results are reported in the paper Senziani et al. (2007).

5.0.1 Pipeline for the analysis of bright source

BAT survey data (§ 4.2.2) can be analysed using the public tools available at the Heasarc-U.S. web site[1] each of which performs a single analysis step required for a coded mask instrument (see section 4.2.1). The wide sky coverage is one of most important and peculiar characteristic of BAT instrument and allows the accumulation of a very large sample of survey data in the *Swift* on–line archive both for the target sources and for the serendipitous source populations randomly located in the filed of view. The data are public but no information about how to build a complete pipeline for the BAT survey data analysis is given either in the on-line guide[2] or in the literature.

In this section a procedure aimed at following the spectral and flux evolution of hard X–ray sources is described. Integrating long periods of observations BAT is characterized by a high sensitivity but this is not the only strength, many X–ray sources have a strong flux variability and sometimes reach a flux threshold to be detected by BAT in a single DPH observation. In this way, without to use a mosaic technique the procedure can run both on a single DPH row –corresponding to the shortest temporal interval for survey data– and on groups of DPHs having a similar pointings. In this section is presented a short description of the technique to perform a time resolved spectroscopy of a bright X–ray source detected with BAT. For each single or many DPH rows can be extract the source spectra within `XSPEC` which are then analysed to estimate the flux in a selected energy range and the model spectral parameters. With this procedure the temporal and spectral hard X–ray source variability for a desired timescale can be monitored.

---

[1] *http://heasarc.gsfc.nasa.gov/cgi-bin/W3Browse/swift.pl*

[2] *http://swift.gsfc.nasa.gov/docs/swift/analysis/bat_swguide_v6_3.pdf*

Data selection and preparation

The pipeline can analyse both single DPH rows (see § 4.2.2) and groups of co-aligned DPH rows in order to provide the light curve and time resolved spectra. Of a selected sky position the data are selected in the desired time interval, with the target inside the BAT field of view. Data, including housekeeping and auxiliary files, may be searched and retrieved through the *Swift* data archive (see above in § 5.0.1).

The energy scale for each detector in each DPH is corrected using gain offset maps. Gain offset files are not supplied for each OBS ID, thus the temporal nearest available file is selected for each observation (the mean time between the file and the next is $\sim$ 3h). The dedicated tool `baterebin` is used to perform the correction. A data quality filtering is performed using the information stored both in housekeeping and attitude files. Data are selected on the base of the pointing stability, the background noise level and the occultation. For example the data for which the star tracker is not locked and the spacecraft is not in pointing mode, the data for which the background noise exceeds the threshold of 18,000 counts s^{-1} in the 14-190 keV energy range and the data for which the angle between the pointing direction and the Earth limb is less than 30 degrees, or the spacecraft is in the South Atlantic Anomaly (SAA) are discarded. The time intervals in which BAT collects data in survey mode (see § 4.2.2) are always terminated when the spacecraft begins a slew to a new target or when entering in the SAA. Time intervals during which the source under study is occulted by the Earth, Moon and Sun may be identified using the dedicated `batoccultgti` tool. Other filters are applied to check the quality of the data. While the DPHs for which data quality is acceptable are identified by checking the appropriate flag stored in each DPH file, allowing observations affected by bad telemetry to be discarded. At the end of this filtering processes $\sim$ 20% of the rows on average are rejected.

Imaging analysis

The coded mask techniques have been widely investigated and used in a variety of experiments to image photon source above $\sim$ 15 keV where the effectiveness of grazing incidence optics breaks down. In coded aperture telescopes the source radiation is spatially modulated by a mask of opaque and transparent elements before being recorded by a position sensitive detector. The data recorded at the detector plane are the superposition of many shadows of the coded mask, cast by each source in the FoV, and of the background signal that is distinguished in physical background and instrumental background. The reconstruction of the sky image is generally based on a correlation procedure between the information recorded at the detector plane and the mask pattern. The image reconstruction goal is to decode this information and obtain the best estimate of the original sources field intensity distribution. The details on the concepts and on the theory of using a coded aperture approach for the imaging analysis are largely described in literature (Groh et al., 1972; Brown, 1974; Cannon & Fenimore, 1980; Skinner et al., 1987; Goldwurm, 1995). Here the principle steps to decode the observed part of the sky and to perform the source detection on the image with the standard Heasarc software are briefly summarized (release 2.7 - June 15, 2007).

During the BAT data analysis is always useful to collapse the physical information, contained in a DPH file, to obtain an histogram. In particular, integrating the DPH information about the collected photons on the time and on the energy range, the Detector Plane Image (DPI) is obtained. Energy selection may be performed "a priori" in order to have the energy resolved DPIs and to add for each detector, the total counts recorded in the desired band. These operations may be performed with the `batbinevt` tool.

A detector mask is generated starting from the map of enabled/disabled detectors stored in the housekeeping files. As for the case of gain offset files, detector masks are not supplied for each observation. They are supposed not to change rapidly, so the nearest available file is used. Hot pixels are then searched for and identified using the special task `bathotpix`. A bad pixel map is obtained, and it is combined with the original map to produce the final detector mask.

Since with a coded aperture telescope the photons incoming from a point source are detected in every points of the detector plane, the single pixel can be illuminated from a large sample of sources and from the diffused background. Thus, the diffused background and the single sources are noise for others objects respectively. The impact of the presence of this noise can be measured and neutralized with a "cleaning" procedure. The `batclean` task creates a fourteen parameters background model, performs a fit on DPI to compute the coefficients afterwards used to estimate the impact of the background noise on the detector plane. At the end of the process a background map is made, which is then subtracted from the input DPI to obtain a background cleaned DPI.

For each cleaned DPI a sky image is produced using the task `batfftimage`. Exploiting the Fast Fourier Transform technique such a tool constructs a sky image by deconvolving the observed detector plane image with the BAT mask aperture map. The result is a background-subtracted image of the sky, including all the sources within the instrument FoV. The tool `batfftimage` can also perform a coded fraction map (see Figure 4.4) which represents the fractional exposure of the sky for BAT.

The dedicated tool `batcelldetect` is used to run a source detection on the sky images in order to produce a catalogue of the sources in the FoV above a fixed signal–to–noise ratio and partially coded fraction thresholds. This task divides the sky image in cells and for each of these fits the point spread function (PSF). If the result of the fit is good, the local fluctuation is considered a "real" source otherwise it is downgraded as an accidental background fluctuation. The catalogue includes sky and image coordinates, signal-to-noise, count rate, coded fraction and other useful pieces of information for each source.

Spectral analysis

An alternative approach without the imaging analysis is the spectral procedure using standard tools. Before extracting a source spectrum from the DPH file, is necessary to assign a weight to each pixel, proportional at the fraction of the detector which is illuminated by the target source, taking into account the contribution of background signal. In order to estimate only the source contribution on the total signal recorded neutralizing the background one, the tool `batmaskwtimg` performs a weight map. `Batbinevt` applies the weight map to a DPH file and the background–subtracted spectrum for a target source is extracted. A dedicated response matrix –including effective area information– for each spectrum is generated using the task `batdrmgen`.

The source signal-to-noise ratio for each spectrum is estimated in order to check the detection level and to discriminate between a spurious detection and a significant one. This is simply done by selecting a suitable spectral range, which has to be optimised on a case by case basis, and checking the source count rate together with its associated error. If the ratio between the count rate and the error is null or negative, the spectrum (and the corresponding DPH group) is discarded. If such a ratio is positive, then further steps are performed.

The hardness ratio is defined as:

$$HR = \frac{CR_H - CR_S}{CR_H + CR_S} \tag{5.1}$$

where CR is the count rate estimated in two contiguous energy bands, the first hard (H), the second soft (S). The hardness ratio provides a qualitative information on the source X–ray spectra. It is not sufficient to obtain robust spectral information but can be an initial guess of the spectral shape and can suggest the different source states, and/or the identification of the presence and relative contribution of different spectral components. The resulting hardness ratio values allow one to choose the spectral model to be used to fit the source spectra, and/or to select an appropriate energy range to perform spectral analysis.

Before running a complex spectral fit, a preliminary fit with a simplified model (reducing, e.g., the number of free spectral parameters) is performed to obtain the source flux with its associated error. The flux/error ratio is used as a criterion to decide if the data quality warrant a more complex spectral model. In particular, a preliminary power law fit with a photon index fixed to -3 is performed and the source flux is evaluated. A flux/error ratio threshold of 4 is used to discriminate between low and high S/N spectra. Spectra with poor S/N are used to set an upper limit to the source emission using the simplified model. An attempt to recover spectral information is made, by summing low S/N spectra extracted from consecutive groups of DPHs, up to a maximum of 10 contiguous spectra. The corresponding response matrices are also combined. The resulting spectra are then analysed through the same steps of the automated pipeline. Spectra with an adequate S/N are studied in detail within `XSPEC`. After spectral fitting, the best spectral parameters, as well as the source refined flux in a given energy band, are computed together with their uncertainties.

5.1 Calibration of the pipeline with Crab and GRO J1655-40

The aim of the pipeline for the analysis of the BAT survey data is to follow the flux time and spectral evolution of a target source exploiting the spectral performance of the BAT instrument. The pipeline described in § 5.0.1 is optimised to the study of a X–ray bright source; a first test on the systematic analysis of a large number of observations of the Crab nebula under different observing conditions was carried out. Since Crab is a very bright and steady reference source, it is the main target to perform the calibration of the pipeline and to study the flux stability in function of the source position in the BAT field of view. The second test is about a detailed study of the 2005, 9-month long outburst of the galactic BH binary GRO J1655–40. Such an event was also carefully monitored with the narrow field instruments PCA and HEXTE on board the Rossi X-Ray Timing Explorer (*RXTE*), allowing the cross-check of the BAT results with those obtained simultaneously by an independent, well calibrated instrument. BAT and *RXTE* spectral results are compared, thus assessing the performance of the pipeline in order to use the BAT data to monitor the behaviour of a strongly variable source.

5.1.1 Calibration with the Crab

To estimate the fluxes of the Crab in the different positions within the BAT field of view corresponding to different mask coded fractions, two approaches are possible using the pipeline: the "imaging approach" is characterized by the sky image of the BAT FoV (in different energy ranges) obtained using the `batfftimage` tool (see § 5.0.1, Imaging analysis) on which the source detection algorithm is performed to extract the rates (cts/s) of the source. The "mask–weighting" allows to avoid the detection step –no differences using the detection coordinates or the nominal position (see below)– and to extract a background-subtracted spectrum of the source and its response matrix. With `XSPEC` the fluxes (erg cm^{-2} s^{-1}) in many energy bands can be estimated as described in the § 5.0.1 (Spectral analysis).

The test on Crab was performed on 365 observations with 4626 DPH rows collected in the 2005 first semester for a total observing time of ~ 1.46 Ms. The Table 5.1 shows the effect of the quality filter on the sample of data, 1014 rows

Detectors not enabled	36
Earth contamination + SAA	121
Star tracker unlocked	264
Pointing unstable	317
High count rate	328
Earth/Moon/Sun source occultation	297

Table 5.1: *Number of DPH rows of the Crab sample rejected after the filtering stage (Senziani et al., 2007).*

	Coded fraction > 0	Coded fraction > 0.1
$< 1 arcmin$	84.8%	90.9%
$< 2 arcmin$	98.6%	99.4%
$< 3 arcmin$	99.9%	100.0%

Table 5.2: *Catalogue and detection coordinates percent difference.*

are rejected ($\sim 20\%$), furthermore 34 rows are lost because no calibrations files are checked.

Using the “imaging approach” for each DPH row, an image of the BAT FoV was produced, and the standard source detection was performed with the tool `batcelldetect` in order to estimate the source count rate in the 10-100 keV energy band. The Crab source detection was performed on all the images adopting a signal to noise ratio threshold of 3.8 and a partially-coded fraction threshold of 0.001 in the tool. The source was detected 1,541 times on 3,600. The target detection coordinates agree well with the known Crab position and the dispersion around the nominal source coordinates is very small, as shown numerically in the Table 5.2.

As shown in the Figure 5.1, it is immediately evident that the Crab count rate is not stable, the “image approach” is not completely efficient over the entire BAT FoV. A deficit of $\sim 20\%$ is apparent for coded fraction below $\sim$ 0.2 (i.e. when the source is between 40-50 and 60 degrees from the pointing direction, corresponding to $\sim 45\%$ of the entire BAT FoV). Thus, over a large fraction of the FoV the count rate estimated by the simple source detection algorithm seems to be biased by systematic effects. Such results are not completely satisfactory for the above purposes.

The “mask–weighting” approach, using the target catalog coordinates in comparison with the detection ones, allows directly to extract the Crab spectra and to obtain the flux and spectral parameters (as the photon indices and normalization) adopting a spectral power–law model fit within `XSPEC`. The flux difference as a function of the offset between the sky catalogue Crab coordinates and those estimated by the detection algorithm is, at most, $\pm 5\%$ as shown in the Figure 5.3.

The trend of the Crab 10-100 keV flux in physical units (erg cm^{-2} s^{-1}) as

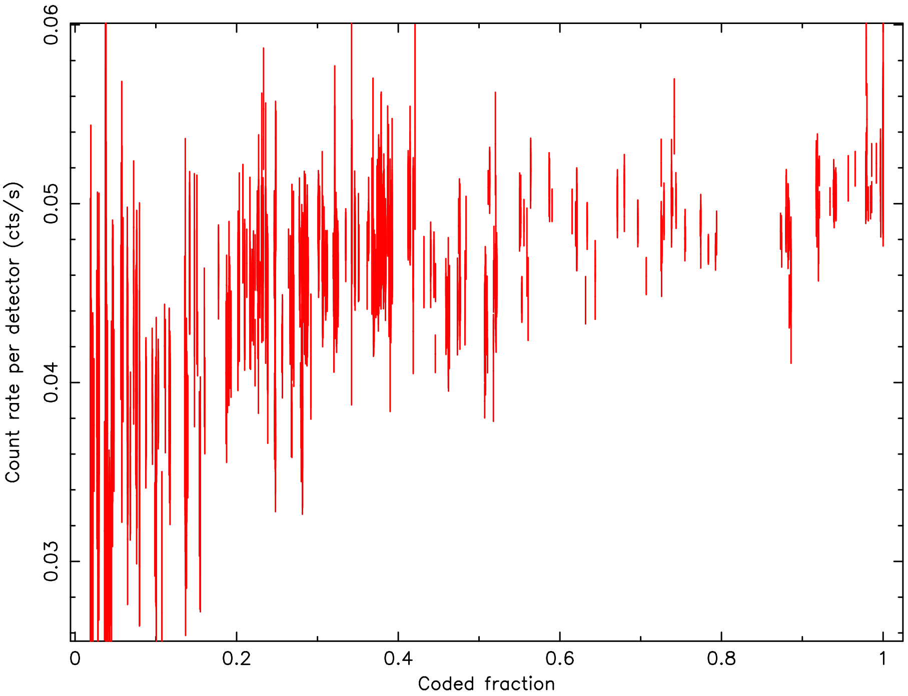

Figure 5.1: *Crab count rate per detector in the 10-100 keV energy band as a function of the coded fraction, as estimated by the source detection technique. Fluxes and error bars are taken from the output list produced by* `batcelldetect` *tool (Senziani et al., 2007).*

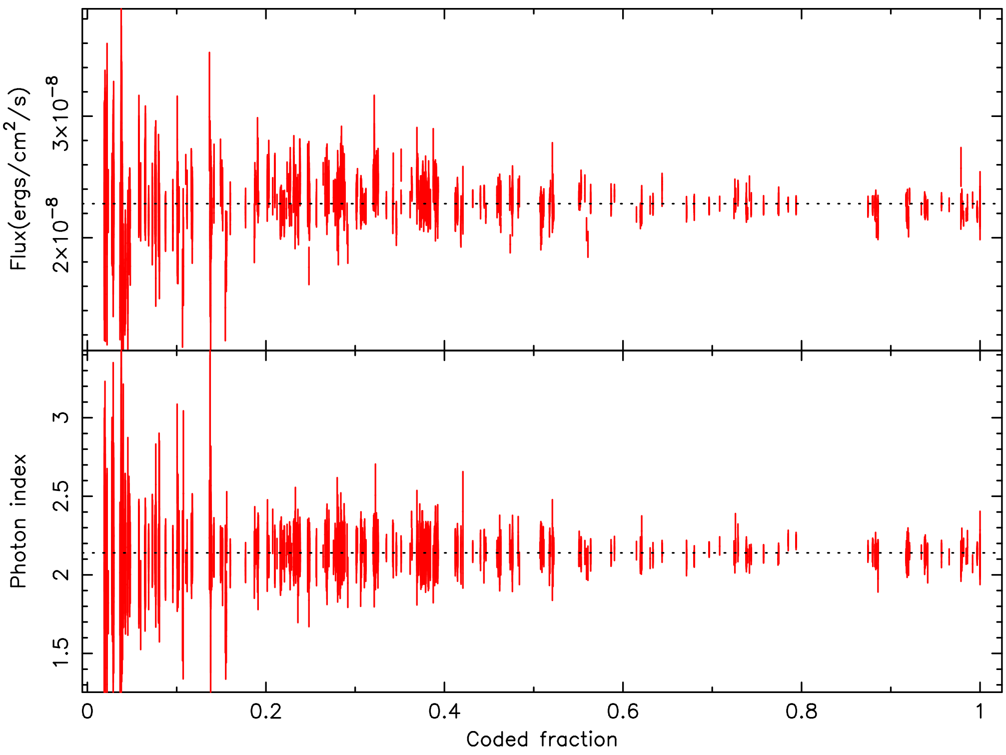

Figure 5.2: *Crab flux in the 10-100 keV energy band (upper panel) and spectral photon index (lower panel) as a function of the coded fraction, as estimated with the mask-weighting technique using celestial Crab coordinates. The horizontal dotted lines represent the best fit to the constant model (see Table 4.4 in Senziani et al. (2007) for details).*

a function of partial coding fraction is shown in Figure 5.2 (upper panel). A similar plot with the values of the photon index is shown in the lower panel of the same figure. Both the flux and the photon index are in good agreement with the values assumed for the BAT instrument calibration [3].

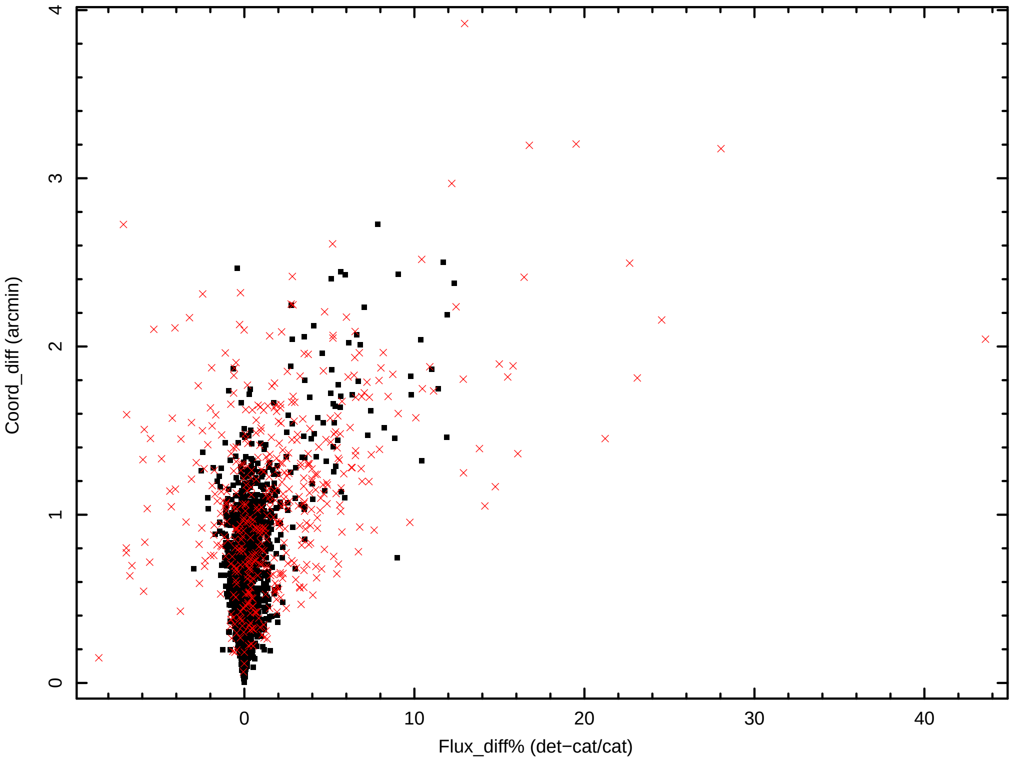

Figure 5.3: *Flux difference using detection coordinates and nominal coordinates as a function of coordinate difference. Black squares represent the rows for which Crab was located at a coded fraction greater than 0.1, whereas red crosses are those for which the coded fraction was smaller than or equal to 0.1 . The use of detection coordinates induces a slight source flux overestimate which can be quantified as* $\sim$ *0.5%.*

If the target source is much less bright of Crab, it is important to merge several DPH rows in order to increase the events statistic and the signal–to–noise ratio of the detection and to reach faint X–ray source flux limits. Since the different DPH files have different pointings and different housekeeping files is very important to quantify how these differences may cause a partial loss in the reconstructed source flux and in which “pointing offset” limits, for different coded fractions, is allowed to merge the DPHs. A simple test shows that no significant losses in the flux are present if the DPH offsets remain in the range of 1-2 arcmin. The number of the stacked DPHs is not wide because the slew of the *Swift* satellite don’t allow to keep steady the pointing parameters, this puts

---

[3] *http://heasarc.nasa.gov/docs/swift/analysis/bat_digest.html*

a bound in the detected limiting fluxes. For this reason a different approach is necessary to study the faint sources.

5.1.2 The stongly-variable source GRO J1655-40

GRO J1655-40 is a black hole binary, fainter than Crab and known to be strongly variable. An interesting activity period of this source was the middle of February of the 2005 when, during Galactic bulge scans, the *RXTE*/PCA instrument (Markwardt & Swank, 2005) detected a violent change of its flux variability corresponding at the begin of the large outburst lasted for more than nine months.

GRO J1655-40, between the 22 January and the 11 November 2005, was in the BAT FoV for an observing exposure time of ~ 2.6 Ms corresponding at a total of 8724 DPHs. After the data screening with the quality filters 2080 DPHs were discarded ($\sim 24\%$, in accord with the Crab data set). Good data were grouped on the base of the pointings difference within 1.5 arcmin and contiguous DPH rows were merged for a maximum exposure time of 1 hour.

An automatic spectral analysis is performed in `XSPEC` (see § 5.0.1), the spectra and response matrices are accumulated in order to fit the data with a non–thermal single component model. After evaluating the source signal-to-noise ratio, 378 spectra with no signal (S/N=0) were rejected, low S/N spectra –with significant below ~ 4-σ level– were used to set an upper limit to the source flux. Contiguous, low-S/N spectra were summed, as well as their response matrices, in an attempt to increase the statistics, and the spectral analysis repeated on such combined spectra. High-S/N spectra were used for a complete spectral fit using a power–law model[4].

The *RXTE* data set is composed of 490 observations, performed between 26 February and 11 November 2005. Each observation has a typical integration time of ~ 1.5 ks, for a total observing time of ~ 664 ks. Only data from the HEXTE instrument (operating in the 20-200 keV energy range) were used for the spectral fits. In addition, public *RXTE* All Sky Monitor (ASM) data collected during the whole GRO J1655-40 outburst were downloaded and a count rate light curve in the 2-10 keV range was extracted.

In Figure 5.4 (top panel) the 9-months light curve (in erg cm^{-2} s^{-1}) of the outburst of GRO J1655-40 extracted by BAT survey data is reported. HEXTE measurements are also shown, to allow for a direct comparison. The light curves extracted from the PCA data (count rate in 3-20 keV, central panel) and from the ASM data (count rate in 2-10 keV, bottom panel) are plotted. Errors are at the $1-\sigma$ level.

Generally, BAT and HEXTE measurements appear to be fully consistent within errors. Considering time windows for which the BAT and HEXTE observations are frequent and close in time, a difference not larger than $\sim$ 10-15% is apparent when the source flux is above 1-2$\times 10^{-9}$ erg cm^{-2}s^{-1}, or

---

[4] `pegpwrlw` in `XSPEC`

$\sim$ 90 mCrab. Generally, a good agreement (within errors) is found when the S/N in BAT spectra is greater than 4. The actual flux yielding such a S/N obviously depends on the position of the target within the FoV. Indeed, in one hour exposures, the $3-\sigma$ sensitivity with such approach is $\sim 10-20$ mCrab for an on-axis source, while it is a factor $\sim$ 10 worse at a coded fraction of 0.2 . Thus, if the target lies within the half-coded region, such approach yields significant spectral measurements (consistent with HEXTE) in the 30-100 keV range down to (5-6)$\times 10^{-10}$ erg cm^{-2}s^{-1}, or $\sim$ 50 mCrab. It is evident from the total light curve that the collect of the BAT data start before the HEXTE one. This is a BAT point of strength, it allows to use not only the pointed observations but in particular the serendipitous data.

The only doubtful point is that no provision was made to take into account and correct the effects of the potentially presence of the other bright sources in FoV which could affect the spectrum of the source of interest. On the other hand, the good results obtained could show that these contamination effects could be negligible. The study of sources fainter than $\sim$ 50 mCrab would require a different and more complex approach. One of these different methods could be to implement in the pipeline the subtraction of the known sources present in the FoV directly by the DPH files in order to improve the sensibility. A second method could be the mosaic technique that is not bound at the pointing offset limits to be able to increase the statistic and to improve the S/N ratio. This approach is described in the Chapter 6.

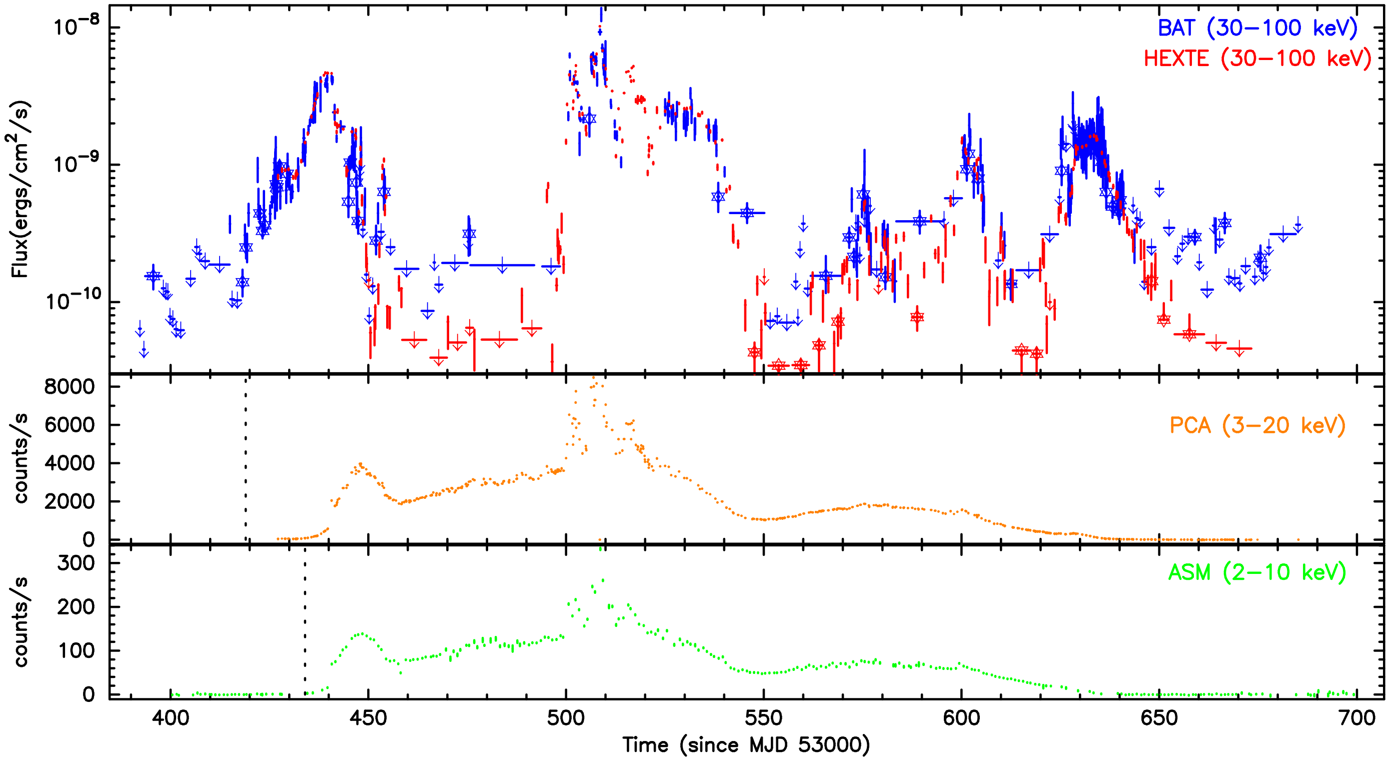

Figure 5.4: *GRO J1655-40 complete 2005 outburst as seen from* Swift*/BAT and* RXTE*/HEXTE (upper panel),* RXTE*/PCA (central panel), and* RXTE*/ASM (lower panel). In the upper panel, stars mark BAT and HEXTE points corresponding to averaged spectra. 3-σ upper limits are also plotted, marked by arrows. Vertical dotted bars in the central and lower panels represent the time of the first detection of the outburst obtained with PCA and ASM respectively (Senziani et al., 2007).*

Chapter 6

Swift/BAT survey data analysis mosaic tools

The thorough analysis of BAT survey data, getting over the misalignment of different pointings, required us to develop four tools, that are thereafter described. In section 6.1 `batfilldb` is described: it extracts information from DPH row data and fills a database. The second is `batbkgmap`, its characteristics are reported in § 6.2: it uses both DPH row data and database checksums for creating detector background maps. The third tool is `batcloseup` described in the section 6.3: it uses DPH row data, checksum and background maps for studying a target object. In the § 6.4 the last software `batsurvey` is considered: it uses all kind of data for studying an extended region of sky. In the following paragraphs these four tools are described in detail.

6.1 `batfilldb`

This tool collects the main information from DPH row data (see § 4.2.2) and put it in a database. Accessing indexes like timestamp or pointing directions is normally very slow since this information is stored in the header of single files. It takes even more time to filter the data using quality constraints. Because of this we decided to analize once for all the row data: in such a way we can then both retrieve data and perform filtering very efficiently.

First of all we designed a database using MYSQL that keeps row and preprocessed data from housekeeping files, headers, and links to the files themselves. The structure of the database follows the row data organization. We have thus tables for observations, DPH files, and DPH rows in a tree structure and a table for gain-offset files. In order to access in a human readable form these data we wrote functions for managing sky distances, combining errors, converting timestamps, and getting pointings with the target in field of view.

As soon as data are available from *Goddard Space Flight Center* (GSFC, NASA), we download them and process with `batfilldb`. Since the directory tree is split in months of data we follow the same procedure filling the database: each month is processed separately. The directory structure is imited in the database and filled with links to useful files, values from file headers and from GTIs. Auxiliary files are then parsed and summarized in few parameters that control the stability of the pointing, the time spent in the *South Atlantic Anomaly* (SAA) or with the startrackers unlocked, the number of detectors turned off, the average rate on the whole detector plane.

`batfilldb` produces an SQL file that can be loaded in a MYSQL database. We actually use many mirror databases, one for each pc, for backup and speed, and 2 mirror copies of the whole archive exported in the *Network File System* (NFS). The data we are saving in the database should be flexible enough to loosen or harden quality constraints in a second phase. For this reason we prefer real parameters to booleans. In any case the size of the database is small enough (less than 1 GB) to be managed, and eventually rebuilt, quite comfortably.

6.2 `batbkgmap`

This tool builds a DPI that accounts for background residuals. Other standard tools like `batmaskwtimg` and `batclean` (§ 5.0.1) can be used to neutralize both resolved and unresolved components of background. Housekeeping files should take into account anomalous detectors and the electronic response of the others. Anyway, the actual response of the detectors may slightly differ from ground and onflight calibration. Furthermore, models for fitting diffuse background are simmetrics although the D shape of the coded mask is not. In order to account for these 2 contributions, we stacked DPIs independently from their pointings.

Swift is on a *Low Earth Orbit* (LEO), thus, if we exclude the transits nearby the SAA, hard X ray background is mainly due to photons with respect to particles. Photon background in this band is produced by X–ray sources; diffuse background is thought to derive from unresolved X–ray objects although this point is still debated. In a coded mask instrument a source may enlighten the whole detector plane, depending on his position in the FoV. The presence of a bright source strongly affects the detection of fainter astronomical objects. Bright hard X–ray sources must then be cleaned from DPI in order to increase the sensibility. Since pointlike and diffuse sources must be subtracted from DPI we must understand how they appear to the detector.

A pointlike source casts the shadow of the coded mask on the detector: this effect can be simulated with `batmaskwtimg`. In order to do this we must know both the flux and the location of the source in relation to the spacecraft, so we must first create images of the sky. Unfortunately there are leaks around the coded mask and regions, nearby the border, that are not completely opaque or transparent. We tried to account for these problems fitting at best the shape of the mask and filtering, after cleaning, hot pixels. There is another problem connected with pointlike sources: the detector elements on border of a detector module are partly illuminated on the side. We couldn't account for this effect with standard tools so we decided to rebalance just the final map, where the cumulative effect is more apparent.

Diffuse background is not correlated with the pattern of the coded mask, thus it appears smooth on the detector. It is not evident how it could be modeled a priori, so we chose to fit directly the DPI. Since pointlike sources can be disentangled from diffuse background we must clean them first: if we don't, the fit is affected and depressions appear around bright hard X–ray sources in the deconvoluted sky image as shown in the Figure 6.1. The standard tool `batclean` performs this fit on a polynomial model that balance independently the borders of detector modules.

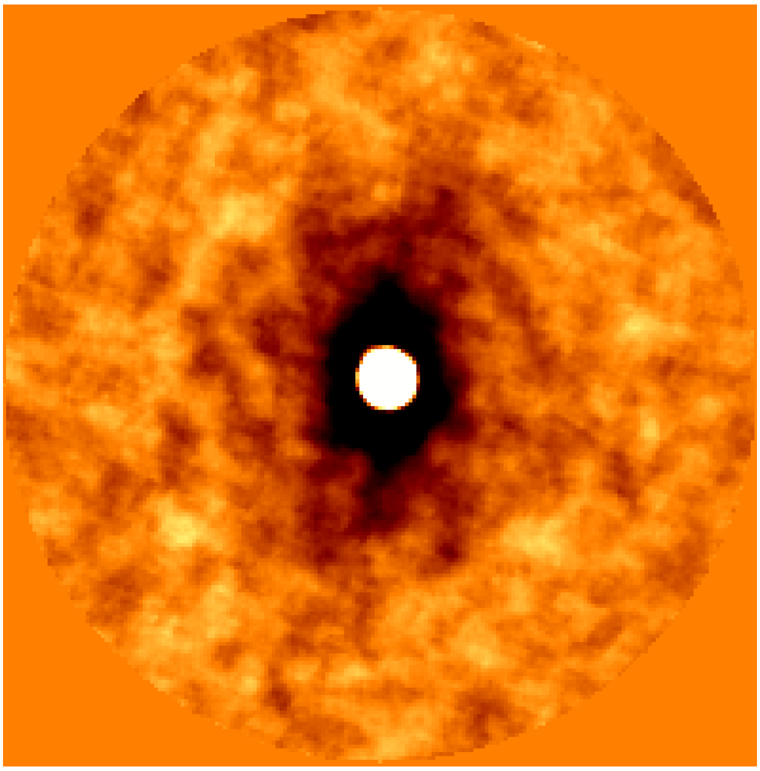

Figure 6.1: *Crab in the 20-100 keV energy range in the period between January 1 2008 amd May 5 2008, for a net exposure time of* $\sim$ *530 ks. It is a deprojected image of radius 5°. The depression around Crab is clearly evident.*

The D shape of the BAT coded mask can't be fit properly: uniform background would project an asymmetric image, while the models provided by `batclean` are all symmetric. The final map obtained stacking all the DPIs should account even for this effect.

BAT detector is an array of CZT crystals, structured in a 3 layers tree structure for electronic control, data handling and fabrication reasons. The response of each detector element has been calibrated on ground and is checked on a regular basis on board. Some housekeeping files report the response of each detector while exposed to an americium crystal and with a simulated electronic impulse. These data can be summarized in 2 files: a detector mask indicating anomalous elements and a gain/offset map reporting the response of the others. Taking into account these corrections the whole detector should have a uniform response. Nevertheless, DPIs show some modulation strongly correlated with electronic hierarchy.

The steps performed by `batbkgmap` are here reported:

- It first extracts from database (§ 6.1) the information about all the DPHs in the selected period, matching the quality constraints.
- DPHs are rebinned in energy according to ground calibration and collapsed in DPIs in a specified energy band with the standard task `baterebin`[1].
- Detector elements are turned off using both onflight masks and statistical analysis of DPIs.
- Detected sources are fit in the sky images and subtracted from DPIs.
- Diffuse background is subtracted fitting a polinomial 14 parameters model in DPIs with the standard task `batclean`[1].
- Detector elements that result noisy after cleaning are turned off, accounting for leaks around the coded mask with the standard task `bathotpix`[1].
- Cleaned DPIs are stacked, considering which elements are turned off.
- Sides of detectors modules are then rebalanced obtaining the final background map.
- Detector elements whose value deviates too much from average are considered noisy and, together with the elements always turned off, constitute the background mask .

We obtained background maps and masks with the task `batbkgmap` processing six months (10906 DPHs) of survey data between January 1 2005 and July 1 2005 for five energy bands (20-100 keV, 20-30 keV, 20-60 keV, 30-60 keV and 60-100 keV).

---

[1] see § 5.0.1 for details

6.3 `batcloseup`

This tool is meant to study in detail a single hard X–ray source from BAT survey data. It first retrieves from the database and the archive all the data for studying the target source. These data are then filtered and analysed until images are worked out. A frame around the target is cut out from these images, deprojected, and combined into a mosaic. Finally, a detection of the target is performed over the mosaicked images and a light curve is generated.

Our goal is to make out the most from BAT survey data: increasing the sensibility with a longer exposure, we can study sources too faint to be detected in single observations. The randomness of the pointing ensure a quite uniform coverage of the sky; this, joined with the large FoV of the instrument, allows us to monitor any source. Depending on the flux of the source and on how well we can reduce the background, we can extract spectral and timing information about the emission, even if *Swift* never pointed to the target in the meanwhile.

6.3.1 Chosing the best data for the purpose

Since we are studying a target for a limited period of time, not all of the data is useful. Furthermore, many factors can lower the quality of BAT survey data: some housekeeping files might be missing or incomplete, the attitude might be unstable or the environment condition particularly bad. Processing useless data means a spare of time; keeping bad data may lead to the deterioration of statistics, and even unreliable results. We need to filter the bulk of the data in order to save time and improve the quality and reliability of our results. Although in recent versions of the software data filtering is split in 2 tools, and preanalysis on row data is left to `batfilldb`, we describe here the ideas behind the whole design.

We must search in the data for the pointings that look at our target; for a coded aperture instrument this operation is not a trivial one and some issues arise. DPHs contain GTIs, so we can crosscheck attitude files and extract pointing information. We can then calculate the position of the target with respect to the pointing and thus determine if it lies inside the BAT field of view. In a coded mask telescope, the position inside the field of view determines how much of the detector plane is illuminated by the target. We want to keep here just the pointings in which the coded fraction is large enough to be worth analysing. Since the D shape of BAT aperture has no central symmetry, we decided to skim first the pointings with the target in FoV and then to restrict our selection. The first operation is realized with a simplified model of the shape of BAT FoV, the second by mean of a lookup partial coding map.

Quality filters are composed of many different checks: we need all housekeeping files to be present; we must avoid observations too much affected by background noise; pointings must be stable and reliable; the detector must be working properly. The first requirement is straightforward, otherwise we couldn't perform the other checks. We recognize observations infected by noise in two ways: the fraction of time spent nearby the SAA and the average rate on the whole detector plane. The steadiness of pointing is determined extracting the average and standard deviation of pointing parameters from housekeeping files while its reliability depends on the locking of the startrackers. Because of calibration or anomalous response some detector elements can be turned off: we keep only the DPH rows where enough elements are working properly for the whole exposure period.

We can configure both kind of filters to be much or less restrictive. We can consider to a great extent BAT pointing to be random, thus a minimum pcode fraction of 0.01 keeps $\frac{2.2}{4\pi} \cong \frac{1}{6}$ of all data, while a value of 0.50 keeps $\frac{1.4}{4\pi} \cong \frac{1}{9}$ of all data, and 0.99 $\frac{0.5}{4\pi} \cong \frac{1}{25}$. These considerations show the enormous importance of serendipitous observations, that constitute the great majority of data for any source. A maximum rate of 18,000[2] counts/s in the 20-100 keV energy band for the whole detector, causes about 1% of the data to be discarded: the same DPH rows correspond to transits around the SAA (Figure 6.2). Stability in the pointing is highly inhomogeneous along the lifetime of the mission; fortunately the low angular resolution of BAT allows a loose constraint with respect to UVOT and XRT. Usually, after a short time from the beginning of DPH, the pointing is stable and a stdev of 3 arcmin on the target filters less than 5% of the data. Along more than 99% of DPH rows at least 18,000 detector elements work properly (Figure 6.3).

6.3.2 Cleaning from noise and background

The DPI obtained collapsing the DPH over the energy channels must be cleaned from background. This operation is very delicate since the effects of cleaning may be apparent only after a great amount of data is stacked. We realize it in two ways: we search for noisy or hot pixels and turn them off; we fit the contribution of background and subtract it from the DPI. In a coded mask instrument sources affect much of the detector; we must identify and clean the contribution from bright sources and, afterwards, from unresolved ones. A statistical analysis on the sky images shows the good effects of cleaning, confirmed by the image we obtain as a mosaic. In order to maintain this improvement while keeping a lumious target, we must reintroduce it at the end of the process directly in the sky image.

Many different approaches have been tried in order to identify and subtract background contribution, but chosing among them is not an easy task. We tried the pipeline suggested for GRB analysis: the cleaning is quite uneffective and image counts don't follow a gaussian profile. When we stack them the regions around sources is depressed and statistics don't improve as expected. Then we modified slightly the standard approach turning off all pixels in the detector for wich the signal to noise ratio is too low. In this way, althought

---

[2] This default threshold is suggested by the Swift/BAT Team (Goddard Flight Center - NASA)

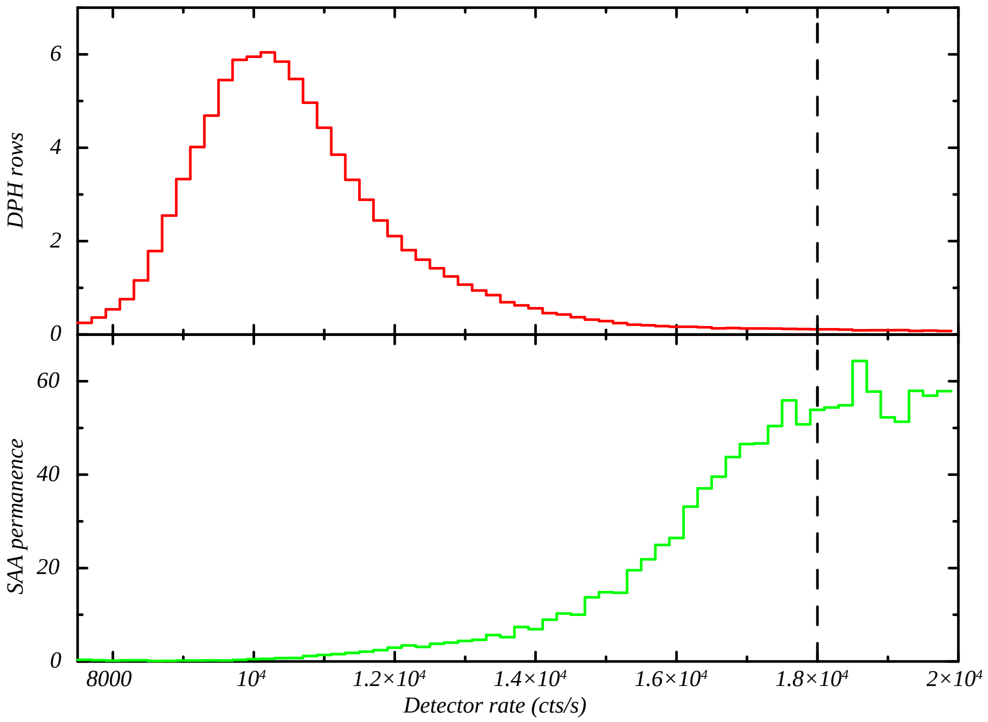

Figure 6.2: *The distribution of DPH rows as a function of detector rates (upper panel). The SAA permanence (%) as a function of detector rates (bottom panel). The dashed line corresponds to the limit of 18,000 cts/s, the DPHs characterized by rates higer than this limit are rejected. Only 6% of the overall time is spent nearby the SAA, concentrated in few DPH rows with an elevate rate.*

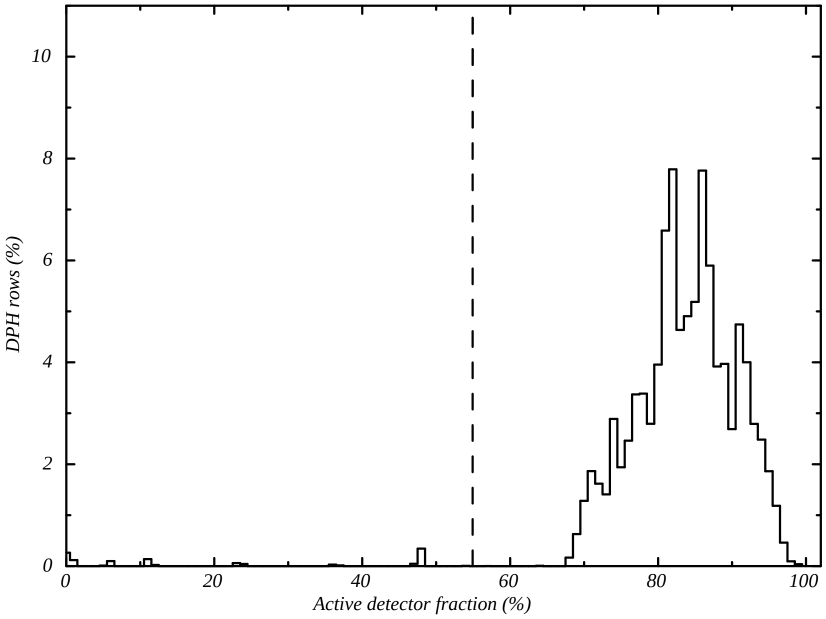

Figure 6.3: *The percentage of DPHs as a function of active detector fraction. The dashed line corresponds to the limit of 18,000 active detectors: DPH rows below this threshold are rejected.*

statistics of the sky image deteriorate, fainter sources emerge. Unfortunately rate values are not conserved and we discard this method as unreliable. We are interested in faint sources, that cannot be seen in single observations, but only on larger integration time.

Our final choice is to turn off pixels according to a detmask, then to fit sources in the sky images and completing the background map fitting the DPI. The detmask we use is obtained merging the one built on board and the one produced by `batbkgmap`, then analysing with `bathotpix` the DPI. With a standard pipeline we extract sky images and detect all the sources; using batmaskwtimg we simulate their effect on the detector. We then fit the detector using the built-in model and, as a further parameter, the map produced by `batbkgmap`. We finally turn off the pixels of the detector with an anomalous signal to noise ratio. This approach is slower than the others but give far better results, in terms of source cleaning and statistics of the final image.

The procedure for modelling sources in the DPI is the same used for `batbkgmap`: here we show how it is implemented. The fit of the sources is performed on images, while they are subtracted from DPIs. Source cleaning is thus composed of cycles; every time new sources may appear and cleaning is refined. The cycle begins by fitting the DPI for background with `batclean`. Then `batfftimage` deconvolves the DPI into an image of the sky with the background map just created. `batcelldetect` performs source detection, saving a catalog that is parsed and skimmed. Finally, the effect of sources on the DPI is simulated with `batmaskwtimg` and subtracted from the DPI. When cleaning is completed, the model of subtracted sources is embodied in the background map

We analyse here the distribution of values in the pixels of DPIs (Figure 6.4) and sky images (Figure 6.5) before and after cleaning. Cleaning acts on DPIs, but our aim is to have better statistics in the final images. We consider first the distribution of pixels in DPIs, disregarding their position in the detector plane. Before cleaning it fits a gaussian centered around a positive value with small bumps in the high tail. After cleaning the gaussian fit improves, reduces its FWHM, and moves the center to 0. We consider now the sky images extracted with `batfftimage` using the default configuration. Since partial coding is not uniform in the image we don't expect a gaussian distribution of pixels. We expect instead to find a distribution that is the convolution of many gaussian with different width. This is exactly what we find and, comparing the statistics, we see that cleaning improves them, reducing the spreading.

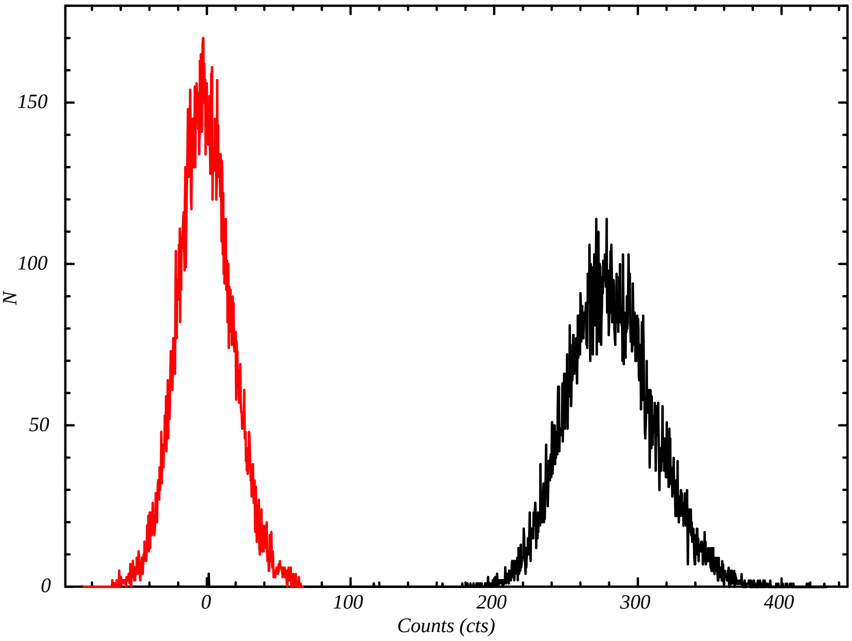

Figure 6.4: *The distribution of DPI counts before (black) and after (red) cleaning for a 1.6 ks DPI. Before cleaning the gaussian fit is rough, while after cleaning improves, is centered in zero and narrows.*

The case in wich the target is bright enough to deteriorate statistics needs a particular care. If we don't clean it from DPI, we obtain a background map that sinks the image as previously described. We tried to reintroduce the target directly in the DPI but it turned out that batfftimage doesn't deconvolve properly a point source. Our choice is then to create a fake source of proper flux, and put it back where it was detected in the sky image (Figure 6.6).

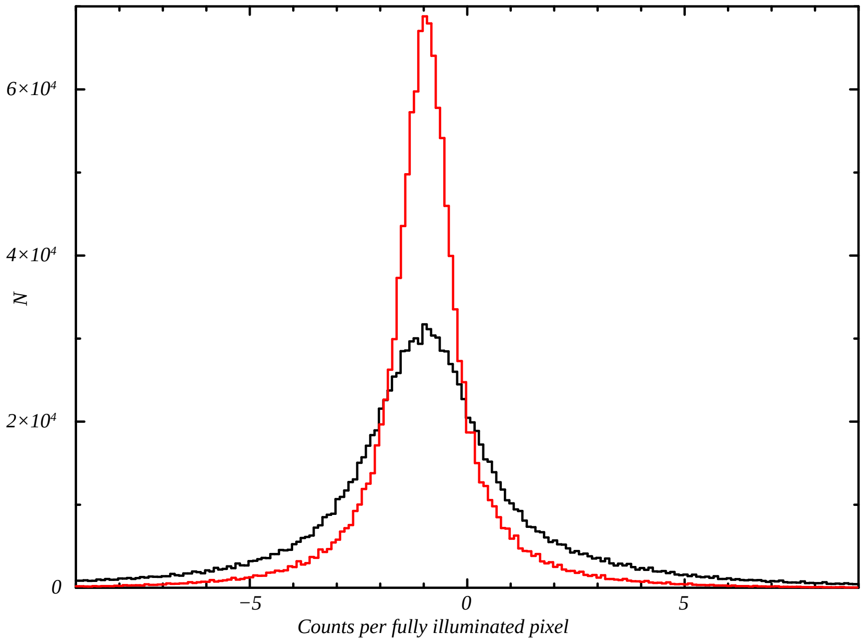

Figure 6.5: *The distribution of counts per fully illuminated pixel from the (same) DPIs of Figure 6.4 of the sky images before (black) and after cleaning (red). The distribution narrows with cleaning.*

We use the PSF shape known from calibration and the parameters used for subtraction from DPI.

6.3.3 Extracting and remapping images

DPIs are properly deconvolved and images are deprojected so that they can be stacked in a mosaic. We first create a set of maps using the proper detmask, background map, and corrections. Then images are deprojected as if the instrument were always pointing to the target: due to the large FoV of BAT non-linear effects must be taken into account. Furthermore, in this operation emerges the quantized nature of images that needs a special care. As a matter of facts images are distorted; we must take into account the effects on the PSF and flux values. We build the effective exposure map which is affected by the amount of coded fraction. All the information needed for the mosaic are conveyed by binary files and FITS maps with counts, exposure, and variance, all corrected by Earth occultation.

We construct with `batfftimage` a sky image by deconvolving the DPI with Fast Fourier Transform algorithms (FFT). Background is taken into account by mean of the mask and the map created in the previous steps. Images are corrected by cosine effect, number of active detectors, FFT losses. Just the inner part of the coded mask is used for deconvolution, while edges, partially opaque, are excluded. At the same time `batfftimage` provides also for the the-

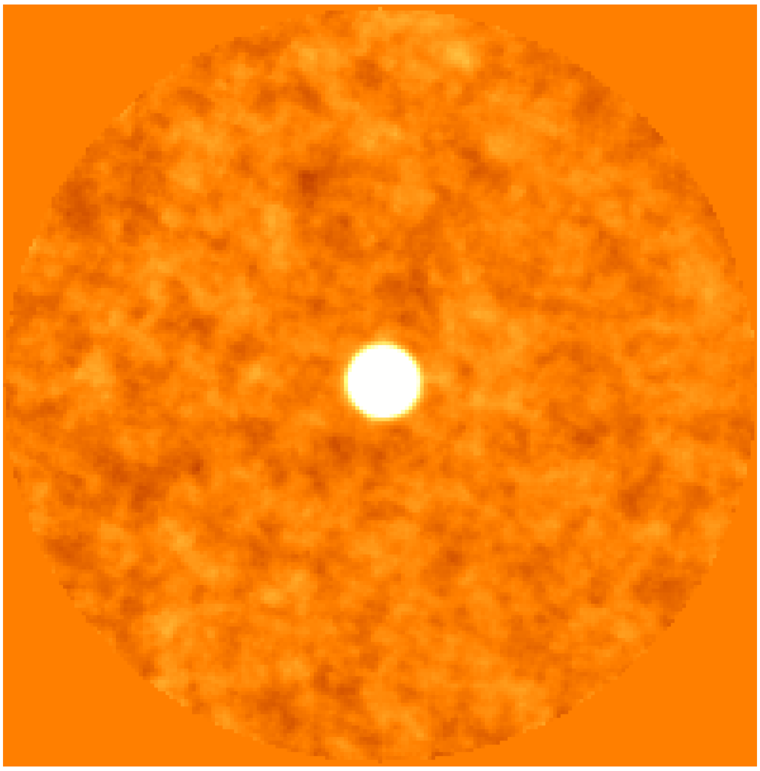

Figure 6.6: *Crab in the 20-100 keV energy range in the period between January 1 2008 and May 5 2008, for a net exposure time of ∼ 530 ks. The frame has radius 5°. Thi image is obtained cleaning the Crab from DPI and putting it back in the sky images.*

oretical variance map, calculated from a Poisson statistic on the detectors. A further correction from partial coding could be applied, similar to devignetting in imaging telescopes. Since we use effective exposure as a weight parameter, we don't apply it, and obtain directly the weighted count map.

We need to change the system of coordinates used by BAT in order to stack images: we call this deprojection. Images of the sky are necessarily deformed: the choice of GSFC is for tangent plane projection, that limit deformation around the center and maintain geodetycs. In this case, every image has a different system of coordinates, according to the direction of pointings. Our target may be far away from the center, in a strongly deformed area. We deproject images in a system of reference centered in the target, with the Nord direction upward. In this way the region around it is almost isometric to the celestial sphere and we can use the standard tools for detection. Since this operation is quite time consuming, we deproject only a circular frame encompassing the target. Deprojected images are thus uniform and can be easily stacked with standard tools. In mathematical terms we must find the function h that maps the region $\mathcal{T}$ around the target in the sky image $\mathcal{S}$ into the frame $\mathcal{F}$:

$$\begin{cases} f: & FoV \subset \mathbb{S}^2 & \longmapsto & \mathcal{S} \subset \mathbb{R}^2 \\ g: & \mathcal{R} \subset \mathbb{S}^2 & \longmapsto & \mathcal{F} \subset \mathbb{R}^2 \end{cases}$$

$$h \doteq g \circ \left(f|_{FoV \cap \mathcal{R}}\right)^{-1} : \mathcal{T} \subset \mathcal{S} \longmapsto \mathcal{F}$$

Images are composed of pixels, each one carrying his value and placement information that must be transferred during deprojection. Let us consider a single pixel; it is small enough to treat the transformations as linear. A squared pixel is thus cast into a quadrilateral that overlaps the array of pixels in the final frame. The value of the original pixel can be conveyed in 3 ways: we can assign the same value to the only pixel where the center of the original is projected; spread the value to all the pixel proportionally to the coverage; use some kernel function to turn a discrete distribution into a continuous one. The first solution is very fast, maintain the fluxes while deprojecting, but cause holes in the final image if oversampling is not enough decreased. The second solution is slower than the first one, values are spread and there are no holes, but some problems arise about distortion of flux. The third solution is the smoothest, but also the slowest, so we decided to discard it. We chose the second solution with similar oversampling in the 2 images: in this way we can use standard tools for detection.

Pixel and metrics are distorted while deprojecting: how does this event affect fluxes and PSF shape ? Tangential plane projection is anisotropic along radial and normal directions: the unit circle is mapped into an ellypse with axes $\cos\vartheta^{-1}$ and $\cos\vartheta^{-2}$ where ϑ is the off axis angle. The BAT PSF is a symmetric gaussian function, whose FWHM ($\sim 22'$) is independent from the position in the sky image. If we treat as linear its transformations, the final PSF will look as an asymmetric gaussian, whose axis are different and not perpendicular. Apart from the shape, since counts are extensive in the sky area, fluxes must be normalized. In particular, since the area is multiplied by $\cos\vartheta^3$, in order to preserve fluxes, we must divide values by the same quantity. If we stack many images coming from different pointings, the PSF averages to a symmetric gaussian while fluxes must be properly recovered.

The effective exposure under wich a spot of the sky is seen depends on the area of detector striked by his radiation. `batfftimage` can provide also for partial coding maps, that assign to every point in the FoV, the exposure time t multiplied by the coded fraction p. Statistical error scales, for a Poisson event, as $\sqrt{N} = \sqrt{A \cdot t \cdot R} \sim p^{\frac{1}{2}} \cdot t^{\frac{1}{2}}$ where R is the flux of photons and A the effective area. In a coded mask instrument every value in the sky image is a combination of Poisson events: the statistics is thus gaussian while its spreading scales in the same way with p and t. Since variance combines linearly, the effective exposure map should be proportional to the variance map. Unfortunately, systematic errors and variability in the effective area prevent exposure and variance map to be strictly proportional.

We pass to the mosaic 3 maps; counts, effective exposure, and count variances. The most of the sources are variable in hard X rays, however, as long as a short period is considered, we can consider their flux to be a constant. If we assume the statistics to be as previously described, the probability for this flux to be R, given counts c_i, is:

$$P\left(\{c_i\}, R\right) = \prod_i \frac{1}{\sqrt{2\pi}\Delta c_i} exp - \frac{\left(A_d \cdot R \cdot p_i \cdot t_i - c_i\right)^2}{2 \cdot \Delta c_i^2} \tag{6.1}$$

where A_d is the effective detector area.

The maximum likelihood is obtained for:

$$R = \frac{1}{A_d} \cdot \frac{\sum\limits_i \frac{p_i \cdot t_i \cdot c_i}{\Delta c_i^2}}{\sum\limits_i \frac{(p_i \cdot t_i)^2}{\Delta c_i^2}} \cong \frac{1}{A_d} \cdot \frac{\sum\limits_i c_i}{\sum\limits_i p_i \cdot t_i} \tag{6.2}$$

As we see, we could approximate results using 2 maps only while we need 3 maps to fully derive the flux.

6.3.4 Building and interpreting a mosaic

We stack images and extract a light curve; we can then analyse the results and calibrate our tool. As a first step we combine deprojected frames into images representing temporal bins. Afterwards, we try to detect the target in each image and collect the results in a light curve. As a calibration test we check that the significance map has average 0 and standard deviation 1. We use the standard deviation of background to derive sensibility and its scaling with exposure time. We finally estimate, from the results obtained with Crab, the systematic error for the whole analysis.

For a good time analysis we must configure properly time binning. If intervals are too short, error bars are too large; if they are too long, information on variability is lost. Furthermore, since the flux is averaged along the bin, in short periods we are more exposed to inhomogeneities. As an example, suppose that a source has periodicity of 1 day, that until noon is in high state, and after noon is in low state. If we use bins of 1 day, we might catch only one of the 2 states and be misled to a superorbital modulation. For longer intervals, the probability that all observations are in the same state falls down to 0, and the source might seem stable. For shorter time intervals, we might find out the period or holes in time coverage of the source. Nevertheless, we may also find out that enormous error bars make the light curve compatible with a constant.

Once images are stacked, we can extract a light curve for the target. Detection is performed using the standard tool `batcelldetect`. The position of detected sources is then cross checked with the coordinates of our target. If none of the sources lies within a configurable number of times the position error from the target, we mark the bin as undetected. In this case we compute the standard deviation of background pixels and set an upper limits to 3 times this value. Results are then collected in a file that can be read as a light curve by qdp. Errors on the X axis correpond to the time bin width while on the Y axis to the errors estimated by `batcelldetect`.

We analize the images to check if they are compatible each other. The first test is a comparison between the variance map and the exposure map. We expect them to be proportional but we see that, although they look similar, this is not true. The variance map shows patterns while exposure map is smooth; furthermore, variance grows more than linearly with the effective exposure. The second test is a statistical analysis of the significativity map, obtained dividing counts by the square root of variance. We expect a normal distribution with central value 0 and variance 1. This lies on 2 assumptions: values are distributed among the pixels as expected for each one of them; both the variance and counts maps are uniform. The latter ansatz can be controlled by a proper choice of the maps while the former is the matter of this test. We obtain a good gaussian fit centered around 0 but the width of the distribution is smaller than 1. This means that variance maps are slightly overestimated with respect to the actual pixel distribution.

These 2 tests show that the theoretical variance map is quite unreliable, at the moment. For this reason we use the effective exposure instead of the counts variance in the formula 6.2 for estimating the flux.

The sensibility of `batcloseup` doesn't scale with time as expected. By definition, it scales instead like the inverse of background pixels standard deviation. As already pointed out, the theoretical variance obtained combining variance maps differs from the actual variance obtained from the mosaicked image. Since our detection is based on the latter we use the distribution of pixels to estimate sensibility. We consider images obtained with different inte-

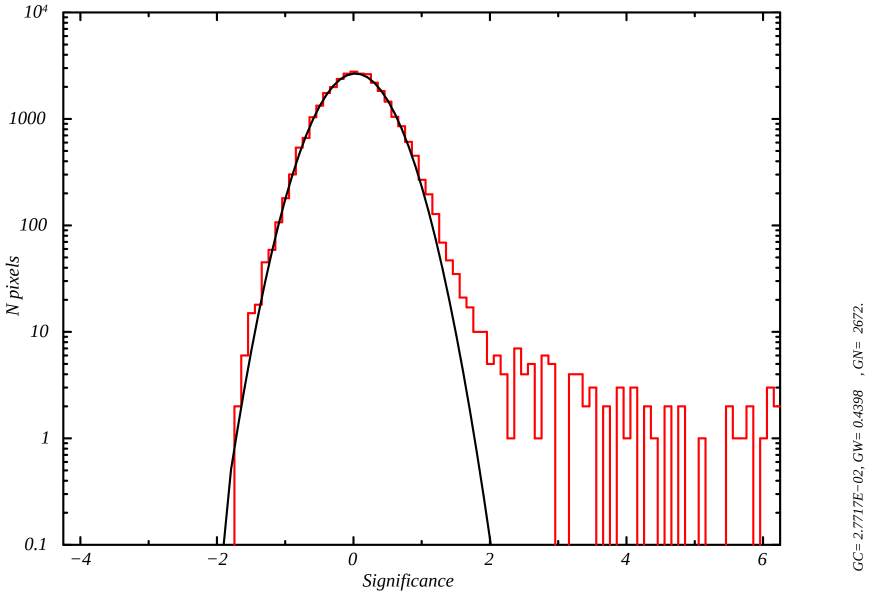

Figure 6.7: *Pixel distribution in the significance map, corresponding to the Crab image of Figure 6.6. The fit with a gaussian function in this semi–logarithmic graph is really good, with a tail due to the source. FWHM is 0.44 while the center around 0; to normalize the width, x axis should be rescaled by a factor 1.34.*

gration times and plot the 3 sigma sensibility. We find that sensibiliy s scales with effective exposure $p \cdot t$ like $s \sim (p \cdot t)^{0.41 \pm 0.05}$ instead of $s \sim (p \cdot t)^{0.5}$ as expected (Markwardt et al., 2005)

We calibrated `batcloseup` on Crab (§ 7.1.1): if we want the light curve to fit properly a constant we must assign a systematic error. We first analysed the light curve extracted from single deprojected frames. Since exposure time is small, error bars are large enough to compensate partially the oscillations. The fit with a constant still returns a χ^2_r larger than 1: error bars are underestimated. If we add a relative sistematic error of 10% we can recover a proper fit. We applied then the same correction to the error bars obtained integrating by months and the fit still works fine. We are now working, trying to reduce sytematics; we consider for this phase 10% to be quite acceptable.

6.4 batsurvey

This tool extracts from BAT survey data a mosaic of an extended region of sky. This tool is composed like `batcloseup` by 2 pipelines, one for analysis and one for mosaic. The first pipeline shows only few differences with respect to the other tool. In particular source cleaning requires a particular care, since all the FoV matters, here. The second pipeline includes frame deprojection and creates just one set of maps. At the end of this process all sources are detected and results are resumed in a catalog.

`batsurvey`, like `batcloseup`, first retrieves and analyses the proper data, then gets to the point of its design. In this case the point is not to dig into the analysis of a single source, but to scan vast regions searching for as many sources as possible. Like in the other tool, the first pipeline is a common ground: we choose a band and a period, and launch the analysis. The second part instead can be run several times, searching for sources in different spots of the vast region we chose. Similarly, we could launch the mosaic in `batcloseup` many times, searching for variability at different time scales. Frame deprojection has thus been moved to the second pipeline, since we must rerun it for every pointing.

The analysis pipeline in `batsurvey` looks similar to the one in `batcloseup` but the lack of a target implies some differences. Data retrieval doesn't care for the pointing direction, since there is no preferred direction marked by a target. This means that, for a similar time window, it must process several times more data than `batcloseup`. Quality constraints are weakened, since the steadiness of pointing degrades off axis. DPI extraction and cleaning are exactly the same for the 2 tools. After background cleaning all the sources not found in a reference catalog are here reintroduced in the sky images. The maps are produced and corrected by occultation as previously described for `batcloseup`. Frame deprojection is moved away from this pipeline.

In `batsurvey` we don't specify a target but a whole catalog of sources we are not interested in. These sources, if detected with enough signal to noise ratio in single images, are not reintroduced in the final images. They might still be present in the mosaic, as the result of stacking of weak signals, but their flux is compromised. The catalog is specified as a FITS file with at least 3 columns: RA_OBJ, DEC_OBJ, NAME. If we don't specify any catalog, all the sources are kept. The procedure for reintroducing the sources in the final image is the same followed for the target in `batcloseup`. We don't have a preferred target here, so we must take care for all of the sources.

The mosaic pipeline first deprojects into a frame all the maps and piles them up into a set of images. Frame deprojection works in the same way as in `batcloseup` but is performed in the second pipeline. Since the images we produced cover all the sky, we can rerun mosaic, pointing in different directions. We still use the tangent plane projection that is faithfull nearby the center but fails far off axis. For this reason, a vast region is better decomposed in smaller parts: to cover the whole sky we need 80 frames of radius 20 deg. Frame deprojection is at the moment the bottleneck of `batsurvey`, we are working toward its optimization. Results from analysis can anyway be exported and mosaic can be performed in parallel on several machines. Image stacking is the same as in `batcloseup`.

The last part of the mosaic pipeline reads the mosaicked maps and detects all the sources therein. This operation is quite straightforward, since the maps are suitable for `batcelldetect`. This standard tool, like in `batcloseup`, is used to perform source detection. The catalog produced by `batcelldetect` is finally cross checked with the same reference catalog used in analysis. In this way, already known sources are expunged from the final catalog. As previously underlined, we can choose to omit the reference catalog and all sources are kept.

Chapter 7

Analysis of X–ray sources with the mosaic technique

7.1 Testing `batcloseup` with the Crab nebula and the Vela pulsar

The aim of `batcloseup`, in the context of BAT survey data analysis, is to detect a faint source and to study its flux and spectral evolution exploiting the mosaic technique (see § 6.3). Since Crab is a very bright and steady source, it is the best target to calibrate the `batcloseup` task and to verify the reliability of its flux reconstruction. In section § 7.1.1 a first test on the systematic analysis of a large number of observations of the Crab nebula is performed using the mosaic technique over one year of data. The second test (§ 7.1.2) is the detection of the faint X–ray source Vela pulsar, from an image obtained with the mosaic technique. We estimate its flux, and compare it with the one reported in literature, verifying at the same time the sensibility and the reliability of `batcloseup`.

7.1.1 Calibration with the bright Crab nebula

We use `batcloseup` in order to analyse the DPHs collected between 2007 January 01 and 2008 January 01.

To estimate the fluxes of the Crab a "imaging approach" is adopted: the source detection algorithm `batcelldetect` (§ 5.0.1) is performed to extract the rates (cts/s/fully illuminated detector on axis) of the Crab on the deprojected (weighting on effective exposure) images of radius 3° portion of the field (in local TAN coordinates) around the target. These deprojected images are obtained from the single pointing sky images of the BAT FoV, cleaned by the diffuse background and by others sources located in the field around the Crab. Two different analysis are considered in order to accumulate two different Crab light curves for five energy bands (20-30 keV, 30-60 keV, 60-100 keV, 20-60 keV, 20-100 keV): in the first case the Crab source detection is performed on all the 2426 deprojected images, in the second case the deprojected images are stacked in order to obtain a monthly light curve.

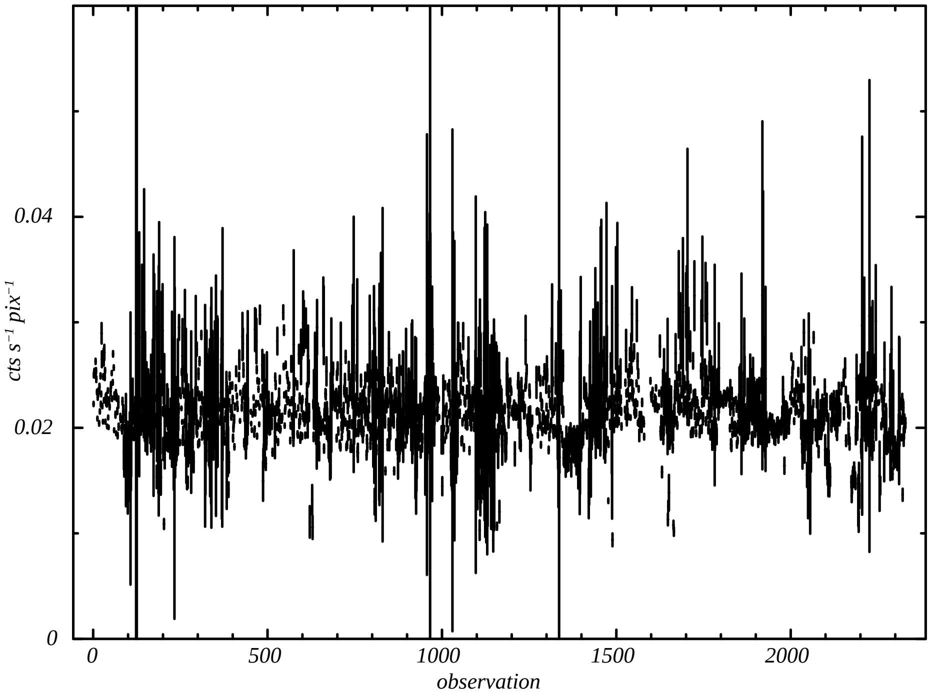

Figure 7.1: *Crab flux with the error calculated by* `batcelldetect` *in the 20-100 keV energy band as a function of the observation collected during the 2007.*

As shown in the Figure 7.1 and in the Figure 7.2, it is immediately evident that the Crab count rate is not stable in the 20-100 keV energy range and the error bars are sub-estimated. The error bars should be greater, in fact, describing data with a constant model, χ_r^2 result too higher. Since such results are not completely satisfactory it is necessary to add an error contribution in order to lead the fluxes stable. If ϵ_0 is the error calculated by `batcelldetect`, the Crab error can be defined as:

$$\epsilon = \epsilon_0 + \alpha\phi \tag{7.1}$$

where ϕ is the Crab flux. Fitting a costant model to data and varying the parameter α for each energy range so that the $\chi_r^2 \sim 1$, the Crab flux becomes stable for α included between the 5-9% both in monthly light curve and the other (single observations) one. This suggests that a systematic error is present; in Figure 7.3 and in the Figure 7.4 are shown the Crab light curves with a systematic error of 10% in order to remain conservative, for these a χ_r^2 of 0.95 and 0.97 respectively is obtained.

In the Crab light curves performed extracting the flux from sky images of the BAT FoV with the same "imaging approach" the trend is stable for the

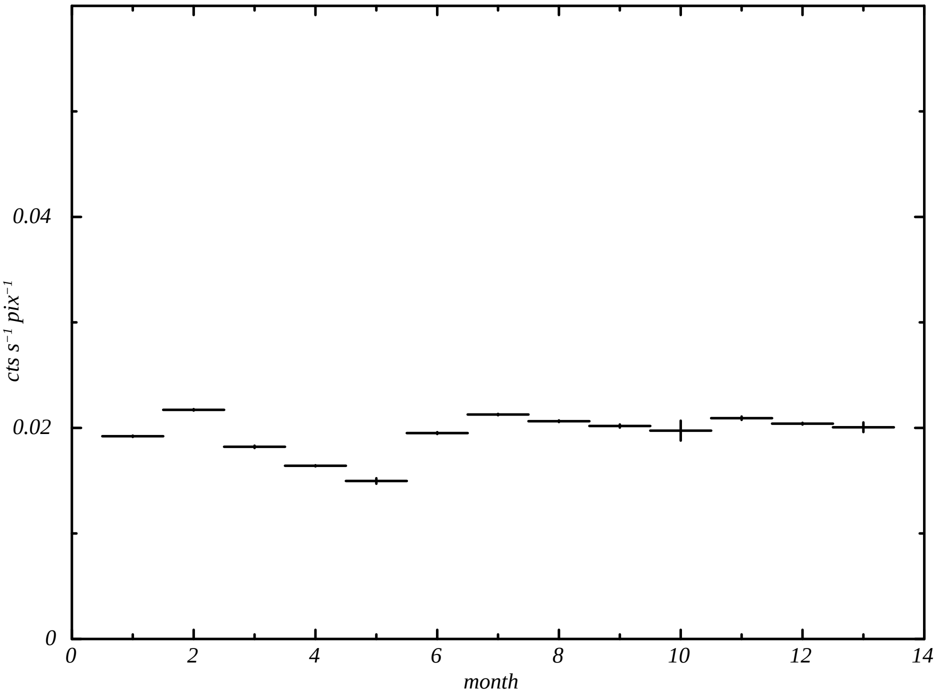

Figure 7.2: *Monthly Crab light curve with the error calculated by* `batcelldetect` *in the 20-100 keV energy range obtained with the 2007 sample of data.*

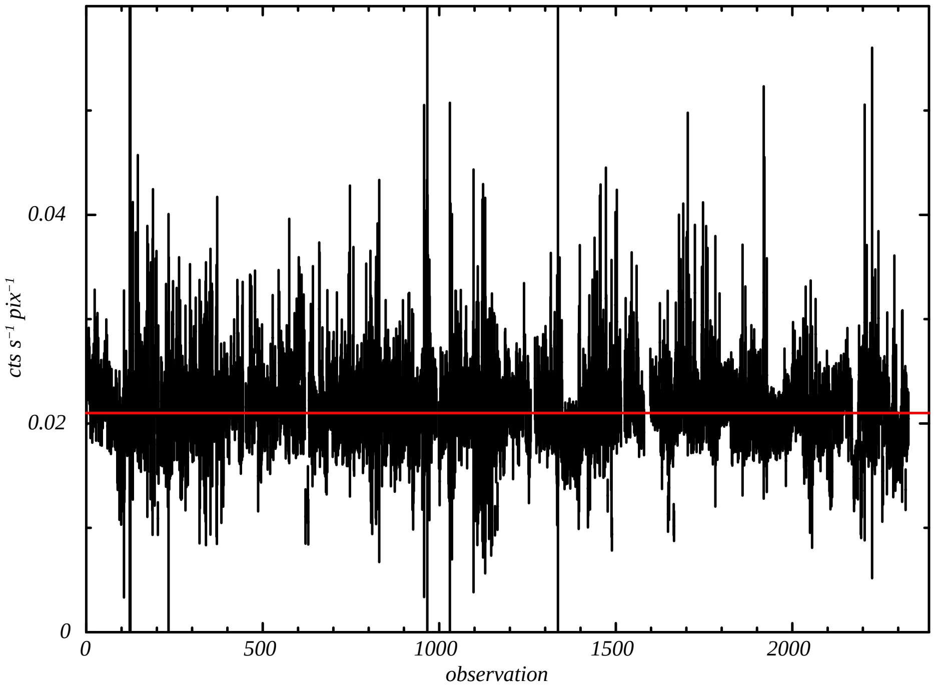

Figure 7.3: *Crab flux with the 10% of statistic error in the 20-100 keV energy band as function of observations collected during the 2007.*

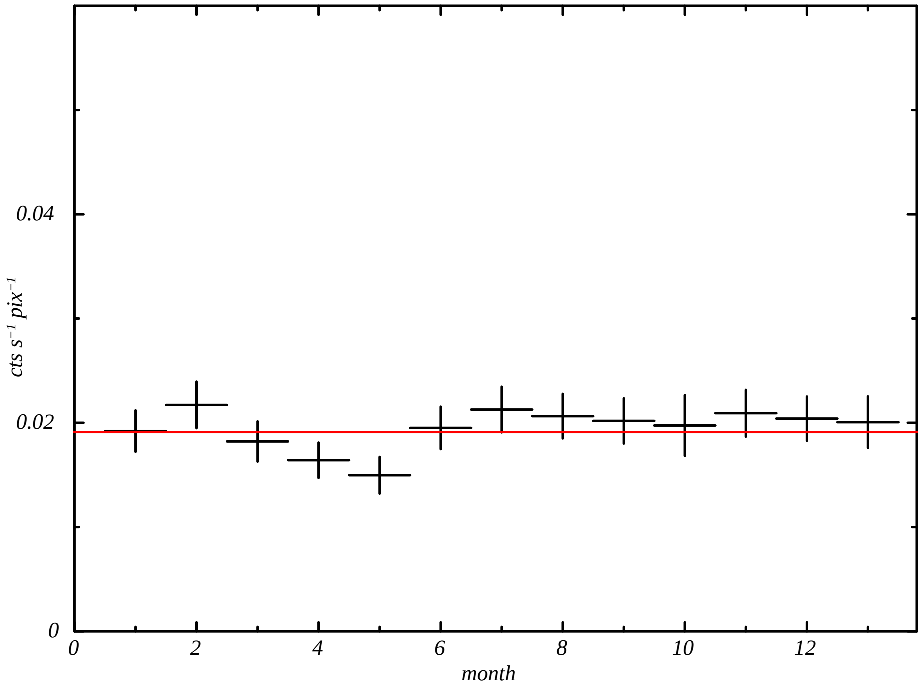

Figure 7.4: *Monthly Crab light curve with the 10% of statistic error in the 20-100 keV energy range obtained with the 2007 sample of data. Describing data with a constant model, the* χ^2_r *is little less of 1.*

DPHs with Crab located at a coded fraction above ~ 0.2 (see § 5.1.1). Also in the case of the Crab light curve based on the sky images the count rate estimated by the simple source detection algorithm seems to be biased by a 5% of systematic effects.

A 10% of systematic error is present performing the source detection on the deprojected images obtained only by the sky images with Crab located at a coded fraction greater than 0.2. This suggests that the systematic error is introduced by the deproject process. A future aim is to reduce this source of error in the deprojected images. At present, the 10% of systematic error has to be added to the flux error in order to obtain correct light curves of sources studied.

7.1.2 Calibration with the faint Vela pulsar

The Vela pulsar is an isolated neutron star in a supernova remnant, emits the radiation from radio to gamma energy range with high luminosity, instead in the hard X–ray band its flux is more faint, ~ 8 mCrab (40-100 keV, Bird et al. (2007)). The sensibility in a single BAT observation is $\sim$ 10-15 mCrab, thus Vela is never detected in single pointings collected in the 2005 January, the period considered to perform the deprojected image reported in Figure 7.5. This source is a good tester to verify the improvement of the sensibility thanks the mosaic approach respect the standard one (see § 5.0.1).

Storing up 233 ks (538 DPHs) of net exposure time in one month, the Figure 7.5 shows clearly the Vela pulsar in the center of the images in the 20-100 keV energy range with a 4-σ detection level.

The count rates of Vela, estimated using `batcelldetect`, were normalized to the Crab count rates in the same energy bands and then converted to flux ($\mathrm{ph \cdot cm^{-2} \cdot s^{-1}}$) assuming for the Crab the canonical power–law spectrum (photon index $\alpha = 2.15$ and normalization of 10 $\mathrm{ph \cdot cm^{-2} \cdot s^{-1} \cdot keV^{-1}}$ @1 keV) and for Vela a power–law spectrum with $\alpha = 2$, averaging the instrument response over the field of view. The Vela flux and the associated error are estimated using this method of $\sim (1.40 \pm 0.15) \cdot 10^{-4}$ $\mathrm{ph \cdot cm^{-2} \cdot s^{-1}}$. At the error has been added the systematic error of 10%.

In order to obtain a flux in mCrab to compare with the flux reported in Bird et al. (2007), the Vela count rates are calibrated using Crab as a reference in the same energy range. The Vela flux measured with this second method is 7.2±0.8 mCrab in which the error of 0.8 mCrab is composed by the statistic and systematic error. This value is in good agreement with the values of 7.1±0.1 mCrab in the 20-40 keV and of 8.1±0.2 mCrab in the 40-100 keV reported in the 3rd IBIS/ISGRI catalog (Bird et al., 2007).

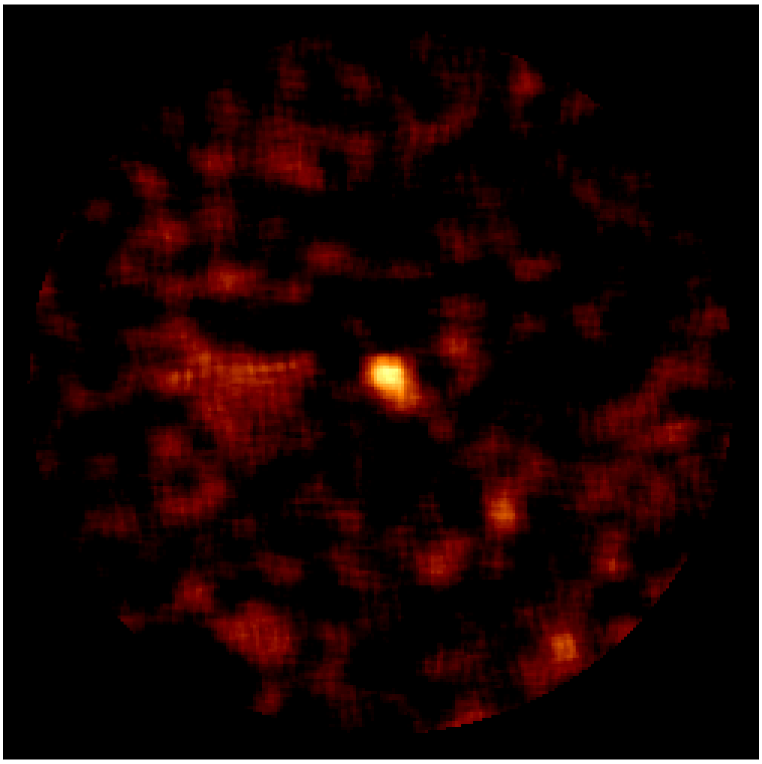

Figure 7.5: *Vela pulsar using one month of survey data (January 2005, 233 ks of net exposure time) in the 20-100 keV energy band. It is a deprojected image of radius 3°.*

Chapter 8

Follow up of the Agile blazars with the mosaic approach

The *AGILE* satellite (Tavani et al., 2008), a mission of the Italian Space Agency (ASI) devoted to high–energy γ-ray astrophysics, is currently the only space mission capable of observing cosmic sources simultaneusly in the energy bands 18-60 kev and 30 MeV-50 GeV. Thanks to the wide FoV, *AGILE* was able to obtain long, almost continous γ-ray coverage of several blazars. We decided to follow up the *AGILE* γ-ray observations of six faint blazars with BAT instrument in order to test our tool `batcloseup` and to give a contribute to the multiwavelength study. The list of targets includes: 3C 454.3, 3C 273, 3C 279, TXS 0716+714, PKS 1510-08, and PKS 2023-07.

8.1 AGNs classification

The classification of AGNs (see § 1.4.5) has been developed rather unsystematically and to date is not completely clear, since many of them have been discovered only recently. In Table 8.1 we summarized a classification scheme of AGNs, considering only two observing parameters: the radio-loudness (the intensity in the radio band) and the optical spectrum (Urry & Padovani, 1995). Two basic classes of active galaxies are the *radio-quiet* and the *radio-loud* ($\sim$ 15-20% of the total), they are divided on basis of the ratio between the radio flux (5 GHz) and the optical one in B band, f_5/f_B: the limit between these two classes is $f_5/f_B = 10$ (Kellermann et al., 1989). Sanders et al. (1989) suggests the hypothesis of a common origin of these two classes of AGNs, thus of their similar optical-UV emission lines and IR-soft X continuum spectra. The radio-quiet and radio-loud objects are distinguished in three groups on the basis of the properties of the optical emission lines.

The objects of type 1 are characterized by broad emission lines, in the active galaxies of type 2 narrow emission lines only can be detected in the optical spectra and the objects of type 0 have faint lines.

Table 8.1: *: AGNs classification.*

Radio-loudness	Properties of the optical emission lines		
	Type 1	Type 2	Type 0
Radio-quiet	Seyfert 1 QSO	Seyfert 2	BAL QSO
Radio-loud	BLRG SSRQ FSRQ	NLRG: FRI FRII	Blazars: BL Lacs FSRQ

- *AGNs of type 1* have an optical spectrum characterized by a bright continuum and by broad emission lines associated to a hot gas, in motion with high velocity (3000-10000 km s^{-1}), located in the inner region ($\sim 10^{16}$ cm from the black hole) of the gravitational potential well near the central black hole (broad line region, see Figure 8.1). Seyfert 1 and quasars galaxies are two examples of radio-quiet type 1 object. Between the radio-loud objects there are the "Broad Line Radio Galaxies" (BLRGs) of low luminosity and the radio-loud quasar. These can be distinguished in "Steep Spectrum Radio Quasar" (SSRQs) and in "Flat Spectrum Radio Quasar" (FSRQs) on the basis of the shape of the radio continuum.

- *AGNs of type 2* have an optical spectrum characterized by a weak continuum and by narrow emission lines. These are associated to a gas cloud that orbits at a distance of $\sim 10^{18-20}$ cm from the central black hole with velocity of 300-500 km s^{-1} (narrow line region, see Figure 8.1) and to the disc of dusts around the nucleus. Seyfert 2 and "Narrow Emission Lines X–ray Galaxies" (NLXGs) are radio-quiet objects of type 2. AGNs radio-loud of type 2 are named "Narrow Line Radio Galaxies" (NLRGs) and are divided by Fanaroff & Riley (1974) in two morphological classes, FRIs and FRIIs. FRIs are radio-galaxies with low luminosity, brighter towards the center, instead FRIIs are characterized by a high luminosity with radio jets collimated.

- *AGNs of type 0* radio-quiet AGNs of type 0 are known as BAL, "Broad Absorption Line" quasars (Turnshek, 1984) and are characterized by broad absorption lines. radio-loud AGNs of type 0 are better known as *blazars* and include two sub-classes, LBL (BL Lac) and FSRQ (Flat Spectrum Radio Quasars) quasars.

8.1.1 Unified model

Although the manifestation of galactic activity may appear diverse, they can be unified within a fairly widely accepted schematic model (Urry & Padovani, 1995; Antonucci & Miller, 1985). Unified models of AGN unite two or more

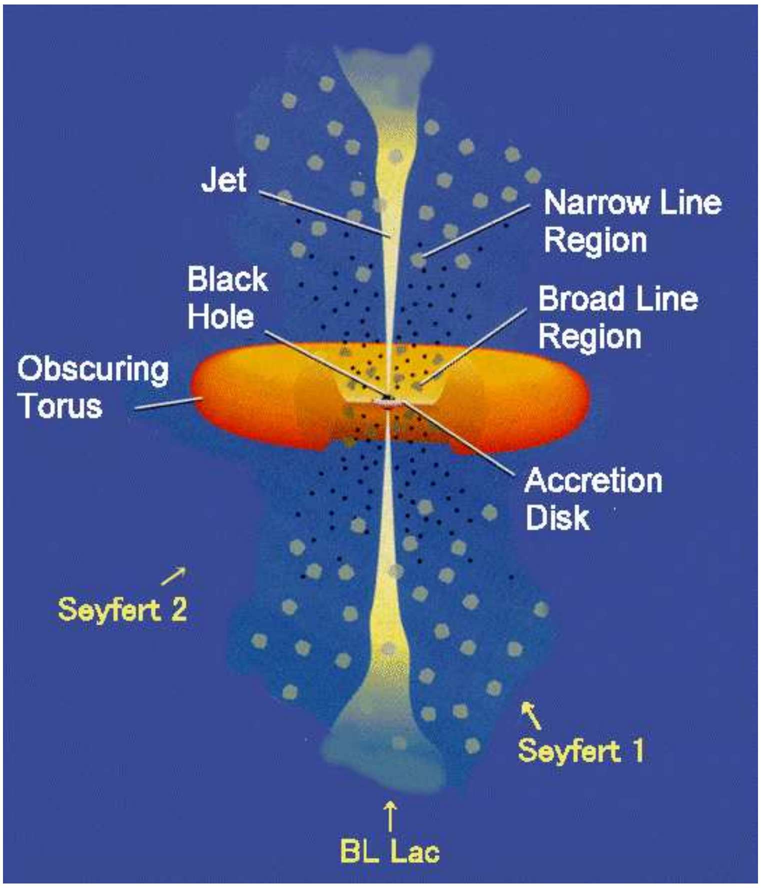

Figure 8.1: *Schematic model of an AGN, consisting of a black hole, accretion disk and jets.*

classes of objects, based on the traditional observational classifications, by proposing that they are really a single type of physical object observed under different conditions.

The currently favoured unified models are “orientation-based unified models” meaning that they propose that the apparent differences between different types of objects arise simply because of their different orientations to the observer. According to this model, most galaxies contain a compact central nucleus, usually supposed to be a black hole, with mass $\sim 10^{7-9}\ M_{\odot}$, surrounded by a disc or ring of hot gas as shown in Figure 8.1. Dissipative processes in the accretion disc transport matter inwards and angular momentum outwards, while causing the accretion disc to heat up. The expected spectrum of an accretion disc around a supermassive black hole peaks in the optical-ultraviolet waveband; in addition, a corona of hot material forms above the accretion disc and can inverse-Compton scatter photons up to X-ray energies. The disc may also give rise to a jet, where some of the energy is converted into perpendicular motions along the rotational axis. For example, at low luminosities the objects to be unified are Seyfert galaxies. The unified models propose that in Seyfert 1s the observer has a direct view of the active nucleus. In Seyfert 2s it is observed through an obscuring structure which prevents a direct view of the optical continuum, broad-line region or (soft) X-ray emission. The standard picture is of a torus of obscuring material surrounding the accretion disc. It must be large enough to obscure the broad-line region but not large enough to obscure the narrow-line region, which is seen in both classes of object. Seyfert 2s are seen through the torus. Outside the torus there is material that can scatter some of the nuclear emission into our line of sight, allowing us to see some optical and X-ray continuum and, in some cases, broad emission lines – which are strongly polarized, showing that they have been scattered and proving that some Seyfert 2s really do contain hidden Seyfert 1s. There is a possibility to see an AGN directly along the jet. It will then appear as a *blazar*, characterized by a rapid and violent variations in brightness and polarization, and by weak or invisible emission lines.

8.1.2 Blazars

Blazars show intense and variable emission across all electromagnetic spectrum from radio to gamma–ray above 100 MeV (Hartman et al., 1999), up to TeV. Variability timescale can be as short as few days, or last few weeks. Blazars spectral energy distributions (SEDs) are typically “double bumped”. A first peak occurrs in IR/optical band in the so–called *red blazars* (including FSRQs and BL Lacs) and at UV/X–rays in the so–called *blue blazars* (including High–energy BL Lacs, HBLs) and it is commonly interpreted as synchrotron radiation from high–energy electrons in a relativistic jet. The second SED bump, which peaks at MeV–GeV energies in red blazars and at TeV energies in blue blazars, is commonly interpreted as inverse Compton scattering (see § 1.3.3) of soft seed photons by relativistic electrons.

Radiation observed from blazars is dominated by the emission from relativistic jets (Blandford & Rees, 1978) which transport energy and momentum to large scales (the length of the jet in gamma and radio is < 1 pc and $\sim$ 100 kpc respectively). The energy content on such scales implies in some jet powers comparable with that which can be produced by the central engine (Rawlings & Saunders, 1991). Thus, only a relatively small fraction of it can be radiatively dissipated on the blazar inner scale. However, we do not know the actual power budget in jets, nor in which form such energy is transported, namely whether it is mostly ordered kinetic energy of the plasma, or Poynting flux (Celotti & Ghisellini, 2008). In principle the observed radiation can set constraints on the minimum jet power and can lead to estimates of relative contribution of particles, radiation and magnetic fields. Currently the models proposed to interpret the emission in blazars fall into two broad classes. The so–called hadronic models invoke the presence of highly relativistic protons, directly emitting via synchrotron or inducing electron–positron ($e^{\pm}$) pair cascades following proton–proton or proton–photon interactions (Mannheim, 1993; Aharonian, 2000; Atoyan & Dermer, 2003; Mücke et al., 2003). The alternative class of models assumes direct emission from relativistic electrons or $e^{\pm}$ pairs, radiating via the synchrotron and inverse Compton mechanism. Different scenarios are mainly characterized by the different nature of the bulk of the seed photons which are Compton scattered. These photons can be produced both locally via synchrotron process (Synchrotron Self-Compton models, SSC, Maraschi et al. (1992)), and outside the jet (External Compton models, EC) by the gas clouds within the broad line region, reprocessing $\sim 10\%$ of the disc luminosity (Sikora et al., 1994, 1997). Other contributions may comprise synchrotron radiation scattered back by free electrons in the BLR and/or around the walls of the jet (mirror models, Ghisellini & Madau (1996)), and radiation directly from the accretion disc (Celotti et al., 2007).

8.2 The blazar 3C 454.3

The AGN 3C 454.3 was discovered at radio wavelengths and its strong variability was studied from radio to the GeV. The estimated redshift identifies it as a distant active galaxy ($z = 0.859$, Giommi et al. (2006)), in particular as a *blazar* (§ 8.1.2). It is one of the brightest ($f_5 \sim$ 10-15 Jy) extragalactic radio sources on the sky and multi-epoch VLBI studies revealed a compact, one–sided core jet structure on the mas scale (Krichbaum et al., 1995; Pauliny-Toth, 1998; Pagels et al., 2004). Strong flux density variability in the radio regime was observed during long–term monitoring campaigns carried out over the last decades (Aller et al., 1997). In spring 2005 a new, exceptionally strong outburst of 3C 454.3 has been reported (Giommi et al., 2006; Pian et al., 2006; Fuhrmann et al., 2006), which triggered subsequent, follow-up observations of the source at radio, IR and optical wavelengths as well as at higher energies (X–ray, gamma–ray, Foschini et al. (2005)). The *Swift* satellite pointed 3C 454.3

on four occasions in April-May 2005, initially as part of an ongoing project to study the X–ray properties of a sample of blazars (Giommi et al., 2006). Because of this exceptionally high state *INTEGRAL* (Ubertini et al., 2003) observed 3C 454.3 as a Target of Opportunity (ToO) between the 15-18 May in the hard–X/gamma–ray band and detected a flux level, assuming a Crab–like spectrum, of $\sim 3{\times}10^{-2}$ ph·cm^{-2}·s^{-1} in the 3-200 keV energy range (Pian et al., 2006). Since the detection of the exceptional 2005 outburst, several monitoring campaigns were carried out to study the source multifrequency behavior (Villata et al., 2006; Raiteri et al., 2006). During the last of these campaigns, 3C 454.3 underwent a new optical brightening in mid July 2007, which triggered observations at all frequencies. In July 2007, Vercellone et al. (2008a) reported the highest γ–ray flare from 3C 454.3. During the period 2007 July 24–30 the average flux was $F_{E>100MeV}$=(280±40)×10^{-8} ph·cm^{-2}·s^{-1}, about a factor of two higher than in 1995.

8.2.1 2005 and 2007 outbursts with the mosaic technique

In November 2007 the *AGILE* satellite began pointing 3C 454.3 at high off–axis angle (about 40°). Nevertheless, in a few days 3C 454.3 was detcted at more than 5-σ (Chen et al., 2007), exhibiting variable activity on a day time–scale (Pucella et al., 2007). Immediately after the source detection, a multiwavelength campaign started. *AGILE* data were collected during two different periods, the first ranging between 2007-11-10 and 2007-11-25 and the second between 2007-11-28 and 2007-12-01, for a total of $\sim$ 592 ks (Vercellone et al. (2008b) in press). *INTEGRAL* data were collected during a dedicated ToO on revolutions 623 ad 624 (between 2007-11-20 and 2007-11-24), for a total of about 300 ks, while *Swift* /XRT data were obtained during several ToO pointings for a total of 10 ks.

We used *Swift*/BAT survey data are analyzed in order to study the hard X–ray emission of 3C 454.3 and to investigate its evolution as a function of time. Two time windows were selected, the first between 2005-04-01 and 2005-09-30 (when intense activity was recorded from the target, Giommi et al. (2006)) for a total of 2,598 DPHs, the second between 2007-06-01 and 2007-12-31 for corresponding 3,707 DPHs. After the data screening with the quality criteria (i.e. background rate, pointing stability, etc. (see § 6.3.1)), 587 DPHs in the 2005 period ($\sim$ 23%) were discarded for a remaining net exposure time of 792 ks. In the 7 month-long time window of 2007 time window 624 DPHs ($\sim$ 24%) were rejected for a remaining net exposure time of 624 ks.

The flux of the source in its high state is of $\sim$ 10 mCrab (for the expression of the BAT sensibility see Markwardt et al. (2005)). At such a flux level, $\sim$ 15 ks of BAT data are required for a 3-σ detection. Pointed observations sum up to 15 ks/month only in two month-long time windows of 2005 and 2007.

A longer exposure time is required to detect the source in its low state. Use of serendipitous BAT data is crucial in order to increase the exposure time and to perform deeper observation of 3C 454.3; this is only possible with the mosaic approach. We analyzed the survey data in the 20-60 keV and 60-100 keV energy bands with the mosaic software `batcloseup` (described in § 6.3) in order to detect 3C 454.3 not only during the higher state but also in the lower state when the source is fainter and it is not detectable in a single pointing.

Exploiting not only the pointed observations but all the data in which 3C 454.3 is in the BAT FoV, the sky images with the blazar located at partially coded fraction (pcode) greater than 0.05 are used to obtained monthly and total 2005/2007 deprojected images (see Figure 8.3). Decreasing the pcode threshold it is possible to increase the exposure time, thus the sensitivity can increase as shown in Figure 8.2. In this example the exposure time increases from 1.5 ks in the first image on the left to 28.7 ks in the last image on the right. However, use of very low pcode data does not improve statistics significantly.

Using no pointed (serendipitous) observations and considering pcode $>$ 0.05, the exposure time is increased by a factor 15-20. In Figure 8.3 the deprojected images integrating all observations between April 1 and Sept 30 2005 and June 1 and December 31 2007 are reported, for net exposure times of 792 and 624 ks respectively. Estimated fluxes of 3C 454.3 in the 20-100 keV are 14.2±0.8 mCrab in 2005 and 5.9±0.6 mCrab in 2007, the high and low state are evident.

The Figure 8.4 shows the long–term *Swift*/BAT monthly light curves of 3C 454.3 in the 20-60 keV (upper panel) and 60-100 keV (bottom panel) energy ranges, during 2005 and 2007 outbursts. The count rates of the blazar were normalized to the Crab count rates in the same energy bands and then converted to flux (ph$\cdot$cm$^{-2}\cdot$s^{-1}) assuming for the Crab the canonical power–law spectrum (photon index $\alpha = 2.15$ and normalization of 10 ph$\cdot$cm$^{-2}\cdot$s$^{-1}\cdot$keV^{-1} @1 keV) and for 3C 454.3 a power–law spectrum with $\alpha = 1.7$, averaging the instrument response over the field of view as described in Appendix A.

In November 2007, during the *AGILE* campaign, BAT data total a net exposure time of $\sim$ 106 ks, for a flux in the 20-60 keV energy band of $(1.07\pm0.19)\times 10^{-3}$ ph$\cdot$cm$^{-2}\cdot$s^{-1}. The *Swift*/BAT flux is in good agreement with the flux derived from the whole *INTEGRAL*/IBIS campaign in the same energy range, $F^{IBIS}_{20-60keV} = 1.02\times10^{-3}$ ph$\cdot$cm$^{-2}\cdot$s^{-1}. In the Figure 8.4 the red line marks the epoch of the giant optical flare 2005 (Fuhrmann et al., 2006; Villata et al., 2006), when the hard X–ray flux was about twice higher than in November 2007.

In conclusion, the task we developed (`batcloseup`) allowed us to exploit BAT serendipitous coverage of the field of 3C 454.3 in order to monitor the hard X–ray behoviour of the blazar during its 2005 and 2007 outbursts. Results have been pubblished in the paper Vercellone et al. (2008b).

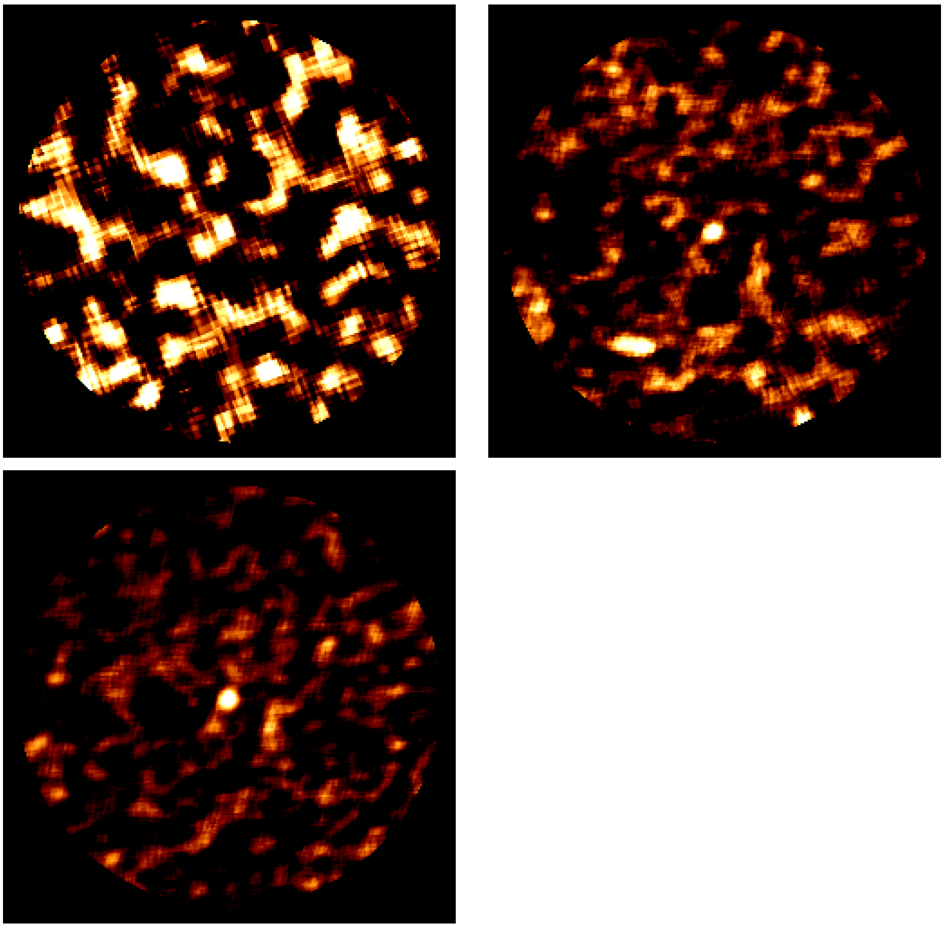

Figure 8.2: *3C 454.3 from 2005 May 08-14 in the band 20-100 keV, using only on–axis observations (0.90 partially coded fraction, exposure time of 1.5 ks, top left), using only observations with pcode > 0.50 (0.50 partially coded fraction, exposure time of 12.0 ks, top right), using only observations with pcode > 0.15 (0.15 partially coded fraction, exposure time of 28.7 ks, bottom left). They are a deprojected images of radius 3°.*

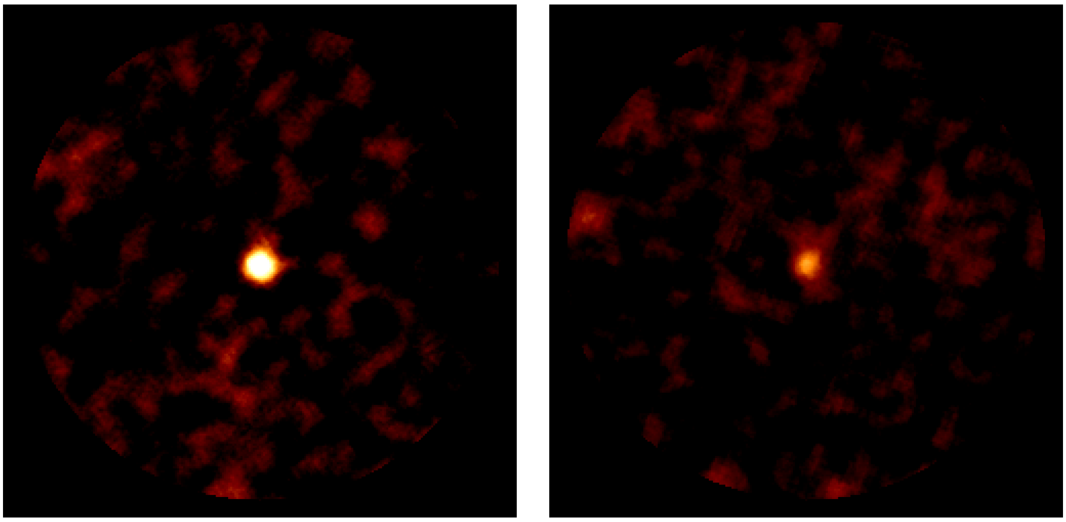

Figure 8.3: *3C 454.3 in the energy band 20-100 keV; all observations between April 1 and September 30 2005 are integrated (on the left). On the right 3C 454.3 in the same energy band integrating all observations between June 1 and December 31 2007. They are a deprojected images of radius 3°.*

8.3 Astrophysical considerations

8.3.1 Models

The most relevant model to explain blazars electromagnetic emission was proposed by (Hartman et al., 2001). Blobs of ultrarelativistic pair ($e^{\pm}$) plasma are supposed to move outward from the central accretion disk along a preexisting straight cylindrical jet structure, with relativistic speed βc and bulk Lorentz factor Γ at an angle θ with respect to the line of sight. Typically, it is assumed that blobs contain a random average magnetic field B' (primed quantities refer to the frame comoving with the relativistic plasma blobs), corresponding to equipartition with the energy density of pairs at the base of the jet, and are characterized by the relativistic Doppler factor δ=[Γ(1-βcosθ)]$^{-1}$. At the time of injection into the jet at height z_i above the accretion disk, the pair plasma is assumed to have an isotropic broken power–law energy density distribution in the comoving frame, with index α. The blobs are spherical in the comoving frame, with radius R', which does not change along the jet. In the blob the most of the dissipation occurs.

As the blob moves out, different emission mechanisms can be invoked to explain the γ-ray emission, the different spectral states, and the spectral energy distribution (SED): in the leptonic scenario, the low–frequency peak is interpreted as synchrotron radiation from high–energy electrons in the relativistic jet, while the high–energy peak can be produced by IC on different *flavors* of seed photons. In the synchrotron self–Compton [SSC] model (Ghis-

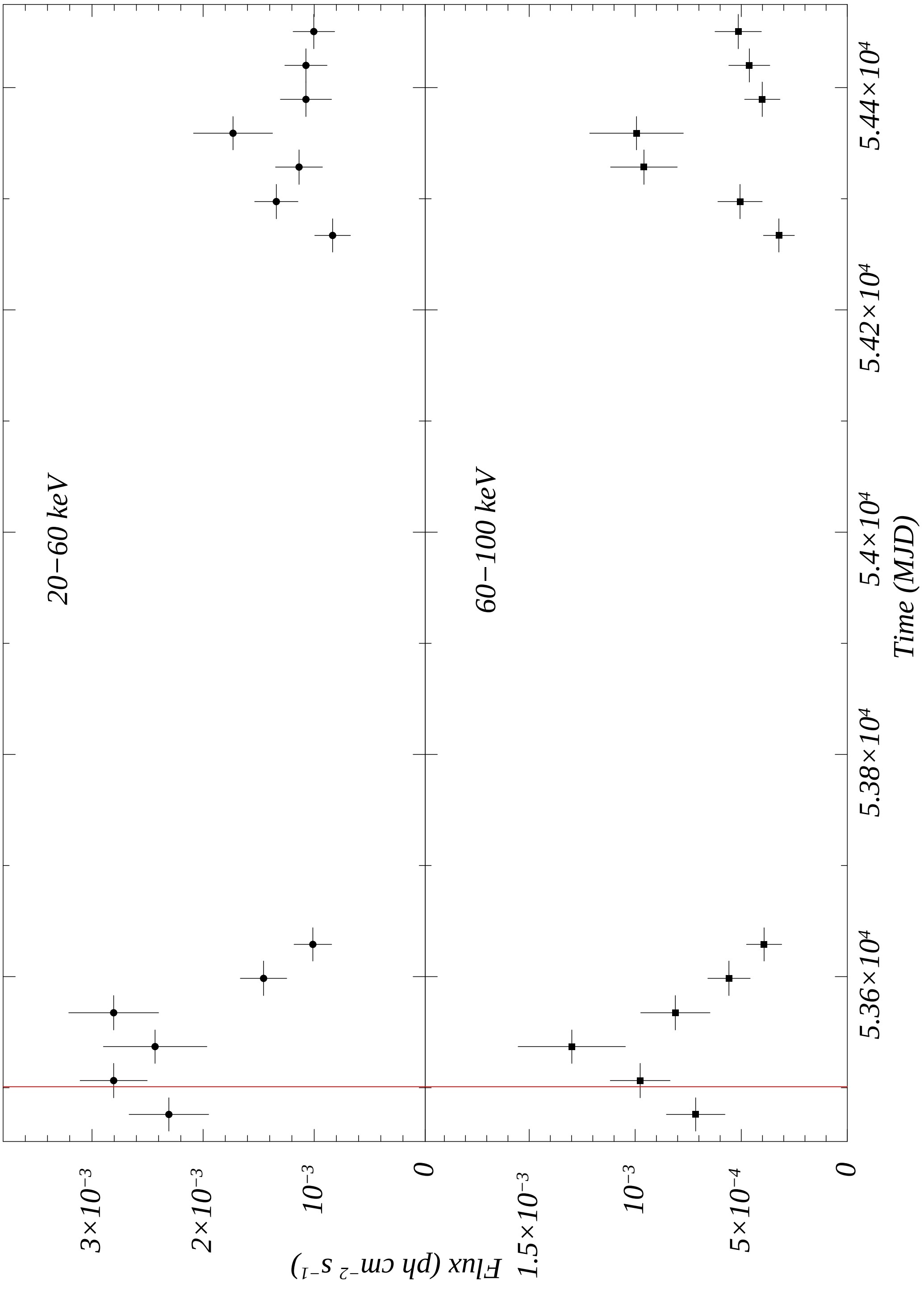

Figure 8.4: *Long–term* Swift*/BAT light curves in the 20-60 keV (upper panel) and 60-100 keV (bottom panel) energy ranges.*

ellini et al., 1985; Bloom & Marscher, 1996), the seed photons come from the jet itself. Alternatively, the seed photons can be those of the accretion disk [external Compton scattering of direct disk radiation, ECD, Dermer et al. (1992)] or those of the broad–line region (BLR) clouds [external Compton scattering from clouds, ECC, Sikora et al. (1994)]. The target seed photons can also be those produced by the infrared (IR) dust torus surrounding the nucleus [external Compton scattering from IR dust, ERC(IR), Sikora et al. (2002)].

A good determination of the overall SED and total observed luminosity of blazars constrain the location in the jet where most of the dissipation occurs. For a given radiation mechanism the modelling of the SED also allows to estimate the power requirements and the physical conditions of this emitting region. The luminosity and SED of the sources appear to be connected, and a spectral sequence in which the energy of two spectral components and the relative intensity decrease with source power seems to characterize blazars, from low–power BL Lacs to powerful FSRQs (Celotti & Ghisellini, 2008). The SED sequence translates into an inverse correlation between the energy of particles emitting at the spectral peaks and the energy density in magnetic and radiation fields (Ghisellini et al., 2002).

In order to study the physical mechanisms that originate high and low states of blazars clearly shown in light curves, simultaneous SEDs during these periods in all energy bands cover a fundamental importance. During the huge multiwavelength flare of 3C 454.3 observed in the spring of 2005 (see Figure 8.4), the optical flux increased by almost two orders of magnitude, while the X–ray flux increased by a factor of ~ 10 with respect to the 2000 level detected by *BeppoSAX* (Tavecchio et al., 2002). Pian et al. (2006) could indeed describe the observed SEDs in 2000 and 2005 with minimal changes in the bolometric luminosity and in the jet power, assuming that the dissipation region (where the most of the radiation is produced) was inside the BLR in 2000, and outside it in the spring of 2005. If the magnetic field is the same in the two epochs, despite the difference in the size of the emitting regions, then the power output is dominated by the inverse Compton scattering of the BLR photons in 2000 (ECC), and by synchrotron and synchrotron self–Compton (SSC) emission in 2005.

Then Katarzyński & Ghisellini (2007) proposed an alternative model, in which the location of the dissipation region varies along the jet, and there is a link between this location, the compactness of the source and the value of the bulk Lorentz factor Γ. The physical bases of this model are as follows:

- The power lost in radiation must be a small fraction of the power of the jet, which has to carry most of the power to the radio lobe regions.
- Therefore the kinetic and Poynting powers of the jet are likely to be conserved, implying that the magnetic field $B' \propto (\Gamma R)^{-1}$, where R is the transverse size of the jet.
- In the internal shock model for blazars the dissipation is due to the

collision of two shells (blobs) moving with different Γ. This introduces a link between the compactness of the source and Γ.

- Even if the dissipation is not due to internal shocks, is possible to have a similar relation between Γ and the compactness if the jet is still accelerating when dissipation occurs.

In the case that the emitting regions with smaller Γ are closer to the black hole, and thus more compact, the magnetic field would be stronger, implying larger synchrotron and SSC luminosity with respect to the EC one. Following these ideas, Katarzyński & Ghisellini (2007) could reproduce the 2000 and 2005 states of 3C 454.3 with a jet of exactly the same power, by assuming different Γ. When dissipation occurs with large Γ the seed external photons are seen to be greatly boosted, while the B'-field is relatively weaker, resulting in an EC-dominated spectrum, where most of the power is emitted in the MeV-GeV band. On the other hand, for smaller Γ, the B'-field is larger, and the external radiation is seen to be less boosted, resulting in a synchrotron and SSC-dominated spectrum, with much less contribution of the EC. It is therefore clear that the main diagnostic of this model is the level of MeV-GeV flux during flares: if both the optical synchrotron emission and the MeV-GeV (EC) emission increase, then this flags a real increase of the jet power, but if the increase of the MeV-GeV flux corresponds to the same (or even to a fainter) optical flux, then this flags an emission episode by a jet of nearly constant power but larger Γ. Vice versa, if the MeV-GeV radiation decrease during an optical flare, this flags a jet of constant power dissipating closer to the black hole and with a smaller Γ. With this approach Ghisellini et al. (2007) found that the 2007 July flare and the state in 2000 can be reproduced by very similar parameters (same radius and bulk Lorentz factors, slightly different magnetic field and shape of the particle distribution), the main difference being the amount of injected power from 7×10^{43} to 3×10^{44} erg s^{-1}. For the two states in 2005, instead, the SED can be reproduced by a more compact source, with a smaller Γ, corresponding to a smaller Doppler factor δ. The magnetic field is greater (15-35 G), and injected power is slightly greater than for the 2007 state.

In order to obtain a fully understanding of blazars it is necessary to accumulate very detailed and simultaneous light curves using all available data from IR to GeV energy bands and it is necessary to accumulate the observed muliwavelength SEDs for each state of blazars. These trends can be verified in the era of simultaneous *GLAST* and *Swift*/BAT observations, able to look for the crucial part of the SED (optical to GeV bands). However, it is possible to anticipate this, for the brightest blazars, using *AGILE* and *Swift*/XRT observations as happened for 3C 454.3 in 2007 July and November flares in order to complete the SED.

8.3.2 3C 454.3 2007 November flare

In this contest, a brief discussion of the modeling of both 3C 454.3 SEDs is presented in this section reporting the results of the *AGILE* multiwavelength campaign (Vercellone et al., 2008b). Figure 8.5 shows the simultaneous light curves acquired during the period 2007 November 6–December 3. Black circles represent *AGILE*/GRID data (30 MeV–50 GeV); red triangles represent *INTEGRAL*/IBIS data (20–200 keV); blue pentagons represent *Swift*/XRT data (0.3–10 keV); cyan–solid and green–open squares represent R-band WEBT and REM (Raiteri et al., 2008) data, respectively. The yellow areas mark the periods P1 and P2 during which we compute the simultaneous spectral energy distributions, and corresponding to higher γ-ray flux levels. We note that during the period P1 the optical flux shows intense variability, reaching a relative maximum on the last day of the γ-ray day-by-day sampling.

Figure 8.6 shows the spectral energy distribution for the period P1, MJD 54417.5–54420.5 (see Figure 8.5). Filled squares represent the *AGILE*/GRID data in the energy range 100–1000 MeV; small filled circles represent *Swift*/XRT data in the energy range 0.3–10 keV (segment 001); open symbols represent radio to UV data taken from Raiteri et al. (2008), corresponding to MJD 54420, when all the WEBT UBVRI bands were available, as well as *Swift*/UVOT data.

Figure 8.7 shows the spectral energy distribution for the period P2, MJD 54423.5–54426.5 (see Figure 8.5). Filled squares represent the *AGILE*/GRID data in the energy range 100–1000 MeV; filled triangles represent *INTEGRAL*/IBIS data in the energy range 17–150 keV (orbits 623+624); small filled circles represent *Swift*/XRT data in the energy range 0.3–10 keV (segments 003, 004, and 005); open symbols represent radio to UV data taken from Raiteri et al. (2008), corresponding to MJD 54425.

The long–term γ-ray activity of 3C 454.3 is one of most interesting discoveries achieved by *AGILE* during its first 6 months of observations. The source was already detected in high state in July 2007 during a 1-week *AGILE* ToO triggered by an intense optical flare detected by the *WEBT*. During that period, the source reached its highest intensity level, with an average γ-ray flux of $F_{\rm E>100\,MeV} = (280 \pm 40) \times 10^{-8}\,\text{photons cm}^{-2}\,\text{s}^{-1}$. In November 2007, 3C 454.3 showed prominent and prolonged γ-ray activity, with flaring episodes on a timescale of a few days and an average γ-ray flux of $F_{\rm E>100\,MeV} = (170 \pm 13) \times 10^{-8}\,\text{photons cm}^{-2}\,\text{s}^{-1}$. This renewed activity triggered observations at different frequencies, allowing us to obtain an almost *simultaneous* SED coverage on 14 decades in energies.

We compared the spectral properties of higher-state periods, P1 and P2, with two lower-state periods, P_low1 and P_low2, chosen of the same duration as P1 and P2 and corresponding to MJD 54414.5–54417.7 and MJD 54420.5–54423.5, respectively. Figure 8.8 shows the *AGILE*/GRID spectra for periods P1 (red square), P2 (green star), P1_low1 (black circle), P2_low2 (blue upside triangle). The July 2007 spectrum is also shown (cyan upside down triangle).

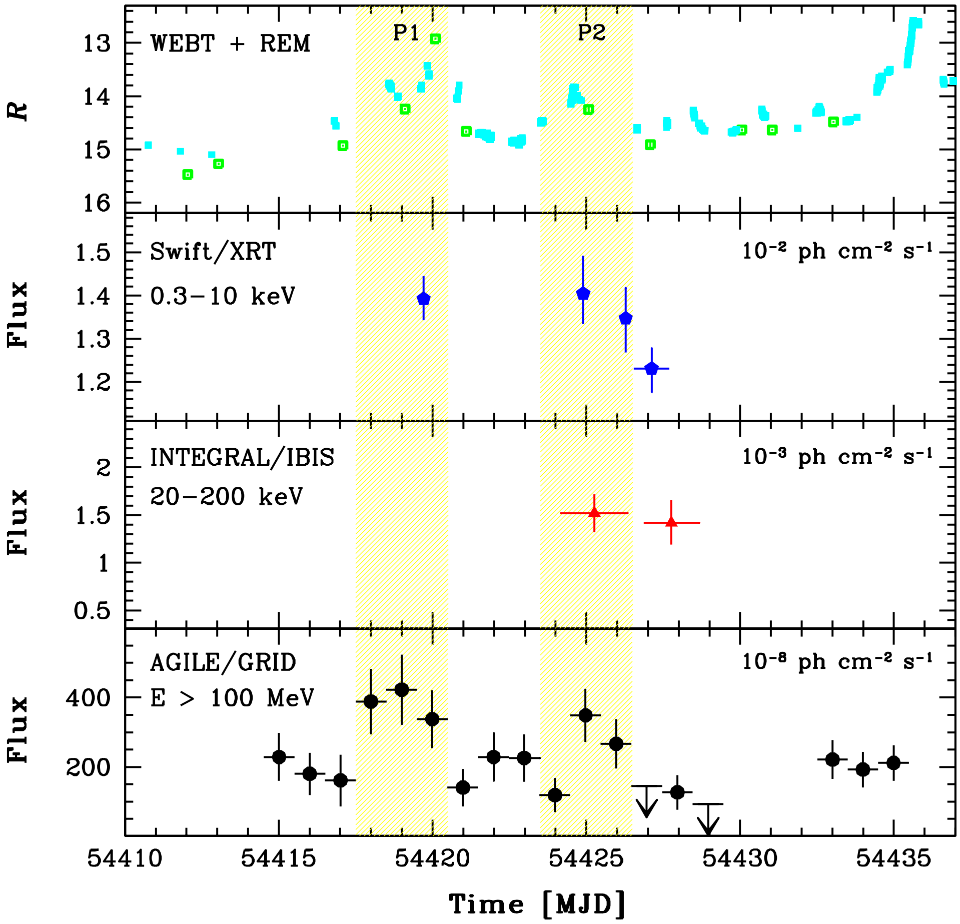

Figure 8.5: *Simultaneous light curves acquired during the period 2007 November 6–December 3. Black circles represent* AGILE*/GRID data (30 MeV–50 GeV); red triangles represent* INTEGRAL*/IBIS data (20–200 keV); blue pentagons represent* Swift*/XRT data (0.3–10 keV); cyan–solid and green–open squares represent R-band WEBT and REM (Raiteri et al., 2008) data, respectively. The yellow areas mark the periods P1 and P2 during which we compute the simultaneous spectral energy distributions.*

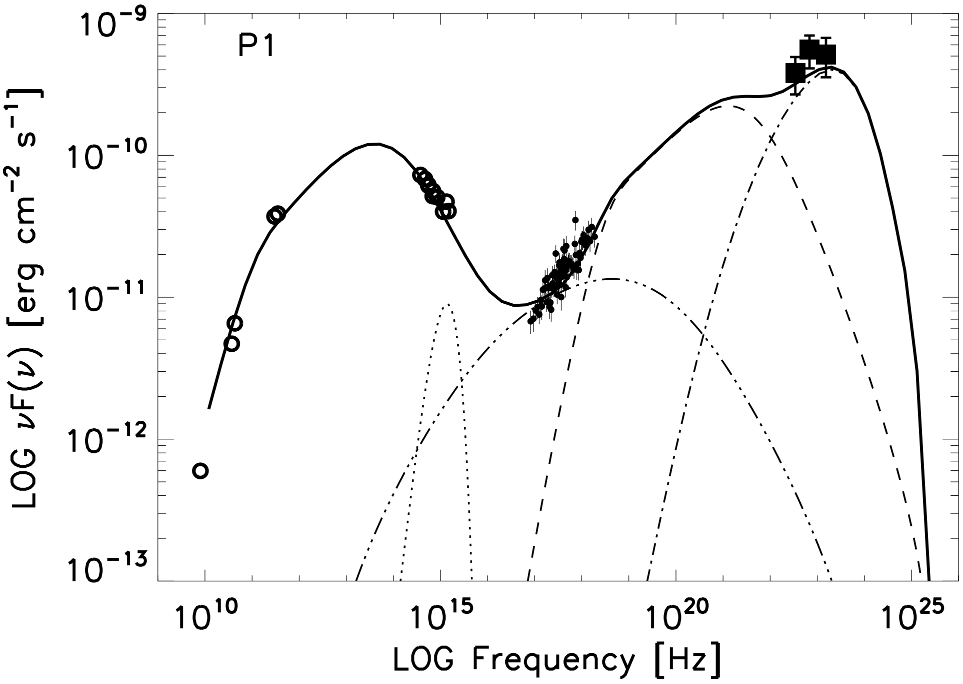

Figure 8.6: *Spectral energy distribution for the period P1, MJD 54417.5–54420.5 (see Figure 8.5). Filled squares represent the* AGILE*/GRID data in the energy range 100–1000 MeV; small filled circles represent* Swift*/XRT data in the energy range 0.3–10 keV (segment 001); open symbols represent radio to UV data taken from Raiteri et al. (2008), corresponding to MJD 54420.The dotted, dashed, dot–dashed, and triple–dot dashed lines represent the accretion disk, the external Compton on the disk radiation, the external Compton on broad line region radiation, and the SSC contributions, respectively.*

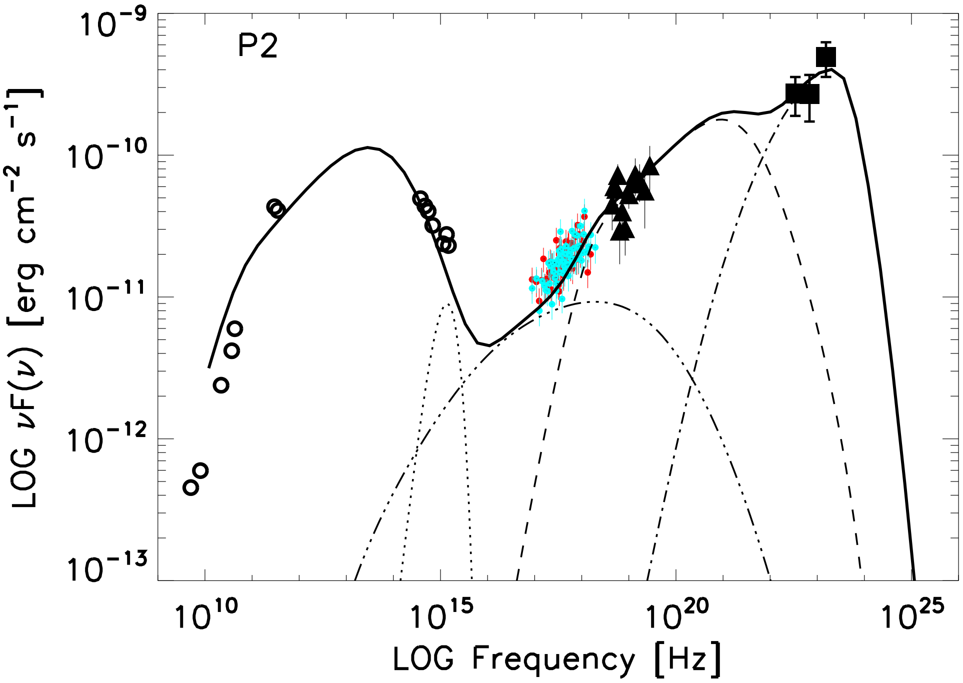

Figure 8.7: *Spectral energy distribution for the period P2, MJD 54423.5–54426.5 (see Figure 8.5). Filled squares represent the* AGILE/*GRID data in the energy range 100–1000 MeV; filled triangles represent* INTEGRAL/*IBIS data in the energy range 20–200 keV (orbits 623+624); small filled circles represent* Swift/*XRT data in the energy range 0.3–10 keV (segments 003, 004, and 005); open symbols represent radio to UV data taken from Raiteri et al. (2008), corresponding to MJD 54425. The dotted, dashed, dot–dashed, and the triple–dot dashed lines represent the accretion disk, the external Compton on the disk radiation, the external Compton on broad line region radiation, and the SSC contributions, respectively.*

Although the statistics accumulated in only 4 days does not allow us to obtain a robust fit of the data, Figure 8.8 shows no clear spectral differences among different source intensity levels.

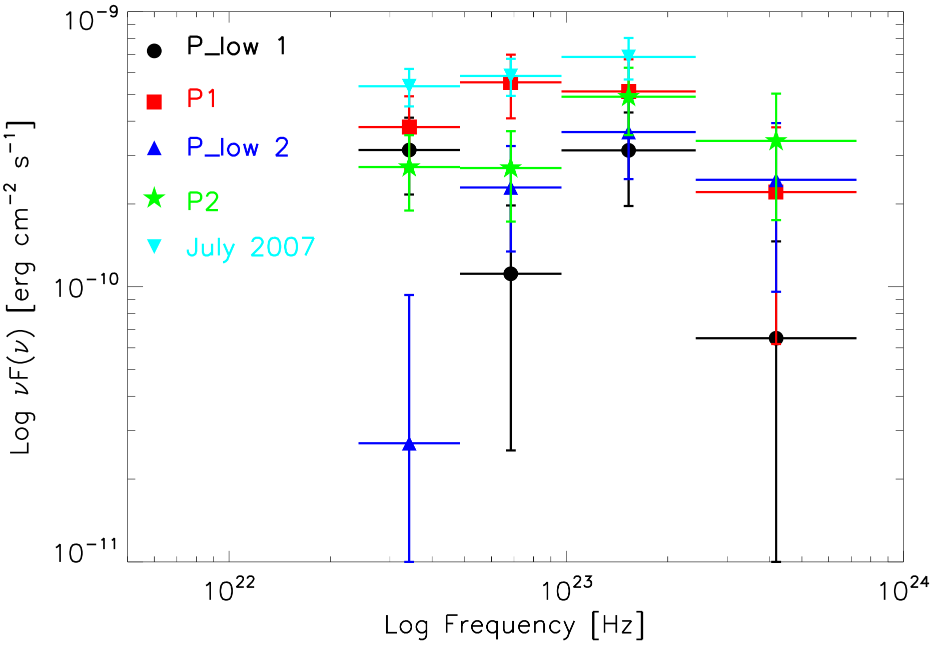

Figure 8.8: AGILE/*GRID spectra for periods P1 (red squares), P2 (green stars), P1_low1 (black circles), P2_low2 (blue upside triangles). The July 2007 spectrum is also shown (cyan upside down triangles)*

Different emission mechanisms reported in § 8.3.1 can describe SEDs shown in Figure 8.6 (P1) and in Figure 8.7 (P2). During intense γ-ray flares, the ECC and ECD processes play a major role and the softness or the hardness of the resulting spectrum is controlled by the dominant component, as illustrated in Hartman et al. (2001) for 3C 279. We fit the SEDs for the P1 and P2 gamma-ray flaring episodes by means of a one-zone leptonic model, considering the contributions from SSC and from external seed photons originating both from the accretion disk and from the BLR. The emission along the jet is assumed to be produced in a spherical blob with comoving radius R by accelerated electrons characterized by a comoving broken power law energy density distribution of the form,

$$n_e(\gamma) = \frac{K\gamma_{\rm b}^{-1}}{(\gamma/\gamma_{\rm b})^{\alpha_{\rm l}} + (\gamma/\gamma_{\rm b})^{\alpha_{\rm h}}}\,, \tag{8.1}$$

where γ is the electron Lorentz factor assumed to vary between $10 < \gamma < 1.5 \times 10^4$, $\alpha_{\rm l}$ and $\alpha_{\rm h}$ are the pre– and post–break electron distribution spectral indices, respectively, and $\gamma_{\rm b}$ is the break energy Lorentz factor. We assume that the blob contains a random average magnetic field B and that it moves with a bulk Lorentz Factor Γ at an angle θ with respect to the line of sight considering the relativistic Doppler factor δ. Our modelling of the 3C 454.3 high-energy emission is based on an Inverse Compton model with two main sources of external target photons: *(1)* an accretion disk characterized by a blackbody spectrum peaking in the UV with a bolometric luminosity L_{d} for a IC-scattering blob at a distance L from the central part of the disk; *(2)* a Broad Line Region with a spectrum peaking in the V band and assumed to reprocess 10% of the irradiating continuum ((Tavecchio & Ghisellini, 2008)). In both Figure 8.6 and 8.7, the dotted, dashed, and dot–dashed lines represent the contributions of the accretion disk blackbody, the external Compton on the disk radiation and the external Compton on the broad line region radiation, respectively. We note that during both the P1 and P2 episodes, the ECD contribution can account for the soft and hard X-ray portion of the spectrum, which show a moderate, if any, time variability. However, we note that the ECD component alone cannot account for the hardness of the γ-ray spectrum. We therefore argue that in the *AGILE* energy band a dominant contribution from ECC seems to provide a better fit of the data during the gamma-ray flaring states P1 and P2. We note, however, that the high energy part of the electron energy distribution appears to be softer during the P2 episode as compared to the electron distribution of the P1 flare.

Results support the idea that the dominant emission mechanism in γ-ray energy band is the inverse Compton scattering of external photons from the BLR clouds scattering off the relativistic electrons in the jet.

8.4 The blazar 3C 273

3C 273 is a radio loud quasar, with a jet showing superluminal motion, discovered at the very beginning of quasar research. Being one of the brightest and nearest ($z = 0.158$, (Soldi et al., 2008)) quasars, 3C 273 was intensively studied at different wavelengths (see Courvoisier (1998) for a review). It shows most of the properties characteristic of blazars, like strong radio emission, a jet, large flux variations and, occasionally, polarisation of the optical emission. In the X–ray band 3C 273 is thought to be quite a unique source since in its X–ray spectrum the blazar–like emission from the pc–scale jet mixes with the nuclear component, which reveals itself through the presence of a large bluebump and so–called "soft excess" below $\sim$ 1 keV. Both are typical for emission from the nuclei of Seyfert galaxies. Synchrotron flares from relativistic jet dominate the radio–to–millimeter energy output and extend up to the infrared and optical domains (Robson et al., 1993; Türler et al., 2000), whereas thermal emission from dust is at least in part responsible for the infrared quiescent continuum (Robson et al., 1983; Türler et al., 2006). When the jet–like contribution is low, the X–ray data can provide an opportunity to study the nuclear component in more details and to test the theoretical models for the emission of 3C 273.

The particularly bright excess in the optical–UV band has been interpreted as a signature of the accretion disc (Shields, 1978).

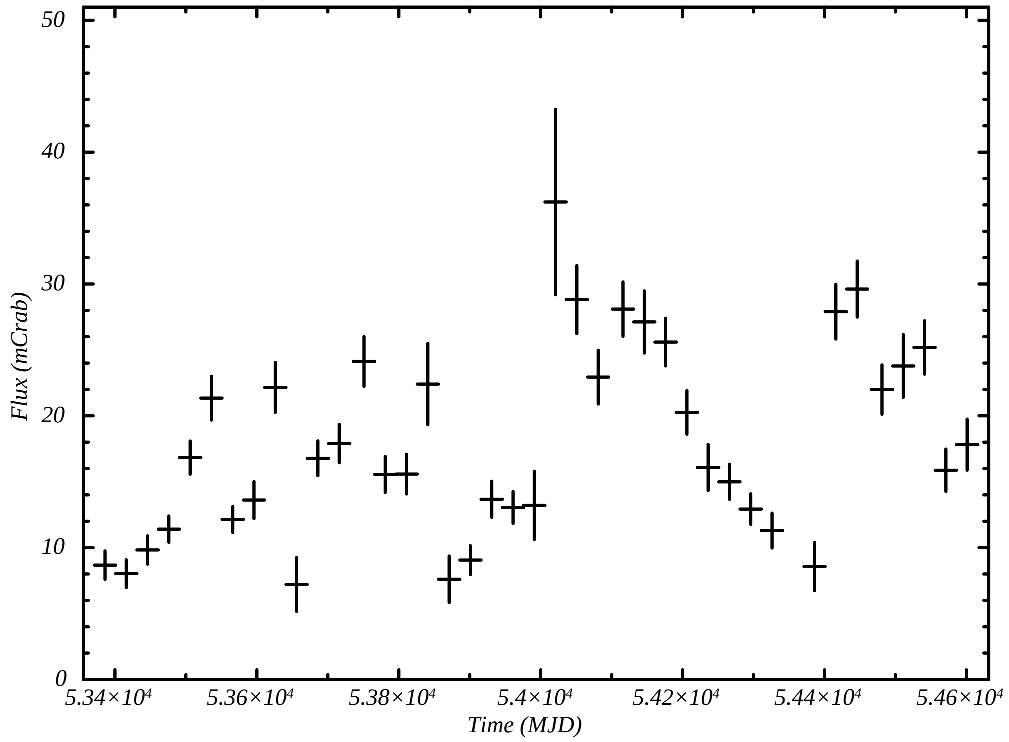

Figure 8.9: *Long–term (3.5 ys)* Swift*/BAT light curve of 3C 273 in the 20-100 keV energy range.*

With the mosaic approach, exploiting all BAT survey data in the archive for a period of 3.5 ys, the monthly light curve of the blazar 3C 273 is performed in the energy range 20-100 keV energy range (Figure 8.9). After the data screening with the quality criteria, 13,486 DPHs from January 1 2005 to May 15 2008, for a net exposure time of $\sim$ 5.3 Ms, are used in order to accumulate the monthly light curve in the 20-100 keV energy band of 3C 273, reported in Figure 8.9. The 3C 273 average flux is $(3.21\pm0.21)\times10^{-3}$ ph$\cdot$cm$^{-2}\cdot$s^{-1}, calculated with the approach described in the Appendix A, considering for 3C 273 a power–law spectrum with a photon index $\alpha = 1.8$.

In order to have spectral information, an analysis of the source is performed in soft and hard energy bands. The Figure 8.10 shows multi–band (20-30 keV bottom panel, 30-60 keV central panel, 60-100 keV upper panel) light curves of 3C 273 during the epoch corresponding to the first year of *AGILE*. Cross–correlating the fluxes reported in the light curves in different energy ranges it possible to investigate the connections between the different emission components, especially concentrating on the origin of the X–ray emission and to obtain spectral informations.

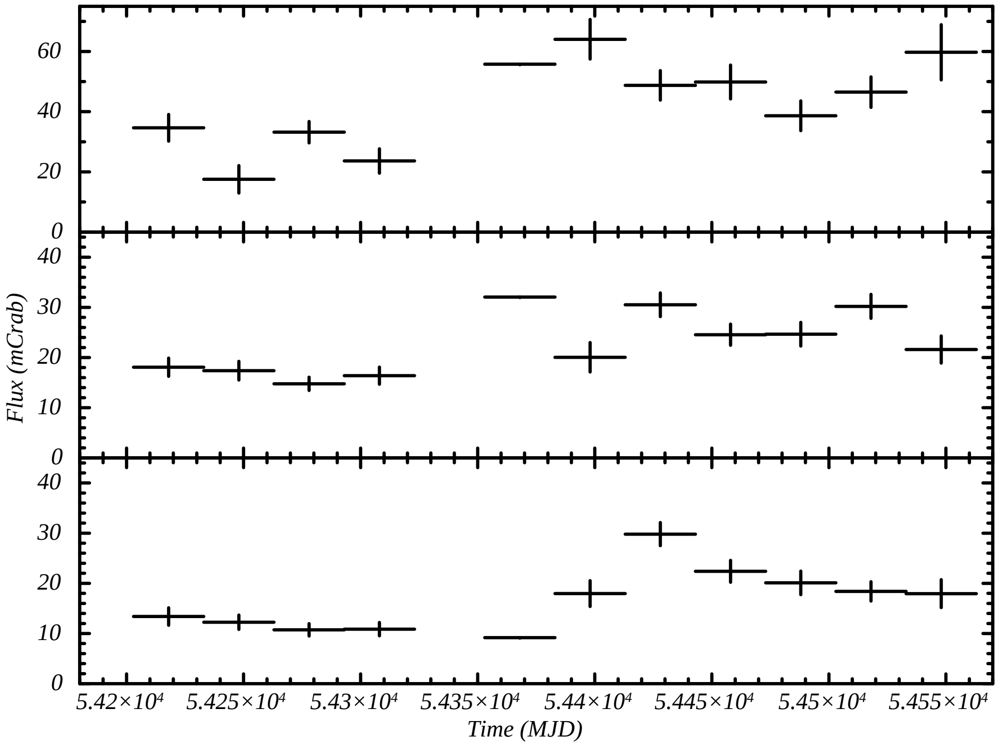

Figure 8.10: *First* AGILE *year* Swift*/BAT light curves of 3C 273 in the 20-30 keV (bottom panel), 30-60 keV (central panel) and 60-100 keV (upper panel) energy ranges.*

8.5 Other blazars: 3C 279, TXS 0716+714, PKS 1510-08, PKS 2023-07

The remaining four blazars of the *AGILE* sample are very faint hard X–ray sources, thus is not possible with the actual version of the software `batcloseup` to obtain a significant detection (up 5-σ level) month by month. All observations, collected in 3.5 ys, have been integrated (see Table 8.2).

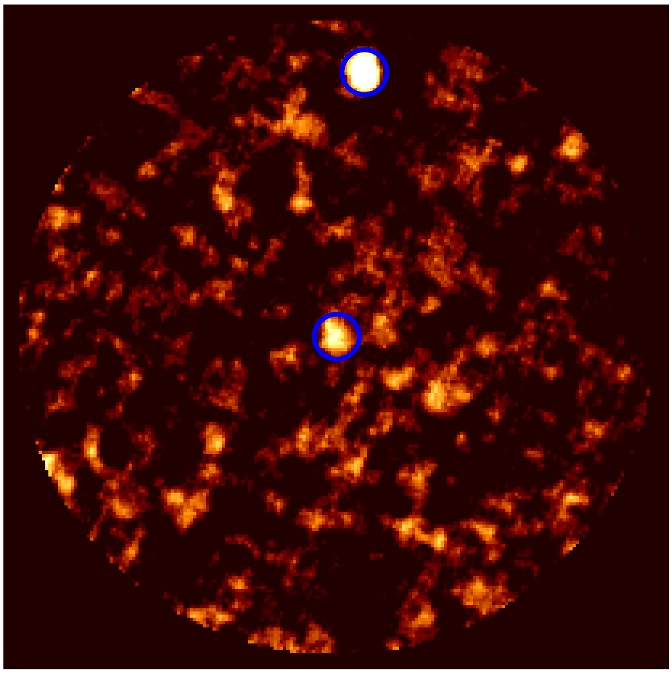

Figure 8.11: *Blazar 3C 279 in the 20-100 keV energy band (in the center of the image). The other source is the Seyfert 1 galaxy NGC 4593. It is a deprojected image of radius 3°.*

In Figure 8.11 the blazar 3C 279 is located in the center of the deprojected image in the 20-100 keV energy band. The net exposure time is 4.9 Ms for a total of 13,751 DPHs analysed and the estimated flux is $\sim 1.37 \pm 0.20$ mCrab. 3C 279 is at the limit of sensibility obtained with the tool `batcloseup` that actually can be fixed at ~ 1 mCrab. In the same $6° \times 6°$ region the Seyfert 1 galaxy NGC 4593 (RA = 198.914, DEC = -5.344, net exposure time of 4.7 Ms) is detected, its flux is $\sim 3.26 \pm 0.31$ mCrab. This source is too faint to be detected in the single observation, thus it is not subtracted and cleaned by sky images of the BAT FoV. Deprojecting sky images in the TAN system of coordinate and adopting the mosaic approach a significant detection is obtained.

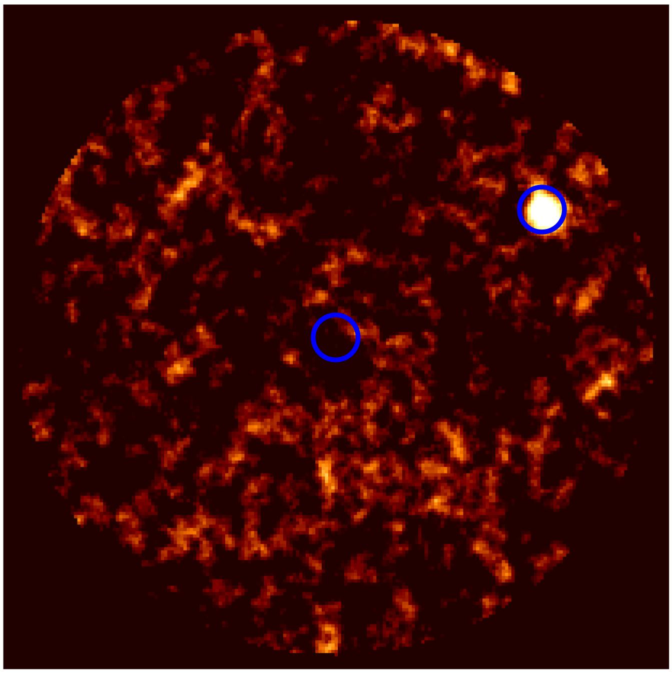

Figure 8.12: *Blazar TXS 0716+714 in the 20-100 keV energy band (in the center of the image). The other source is the Seyfert 1 galaxy IC 450. It is a deprojected image of 6°×6°.*

Analysing 20,043 DPHs and integrating 7.1 Ms of net exposure time the blazar TXS 0716+714 can not be detected in the 20-100 keV energy band as shown in Figure 8.12 (the blue central circle). It was possible to estimate an upper limit for the flux of < 0.74 mCrab. This blazar was detected with a significance of about 8-σ by *AGILE* between September 10 2007 and September 20 2007 as reported in Giuliani et al. (2007). In the same region the Seyfert 1 IC 450 (RA = 103.05, DEC = 74.426, net exposure time of 6.9 Ms) is detected with an estimated flux of $\sim 2.33\pm0.27$ mCrab.

The Figure 8.13 shows the blazar PKS 1510-08, detected by *AGILE* in a first time window between August 27 2007 and August 30 2007 with a detection significance of about 4-σ (Bulgarelli et al., 2007) and in the period started on March 16 2008 (D'Ammando et al., 2008) thanks to a detection significance of $\sim$ 7-σ, displayed by the blue circle; it is at the limit of detection with a flux in the 20-100 keV energy range of $\sim 1.90\pm0.27$ mCrab, for a net integration time of 4.7 Ms (16,868 DPHs analysed). The blazar PKS 2023-07 is not visible in

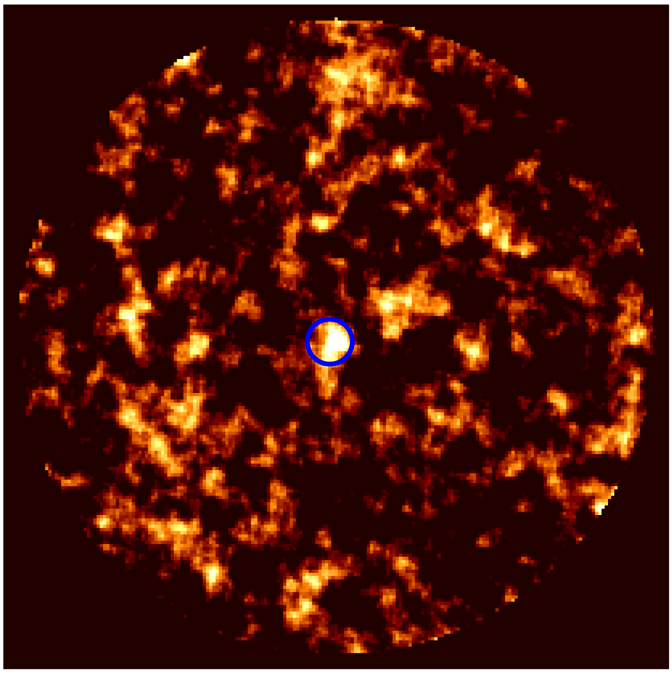

Figure 8.13: *Blazar PKS 1510-08 in the 20-100 keV energy band (in the center of the image). It is a deprojected image of 6°×6°.*

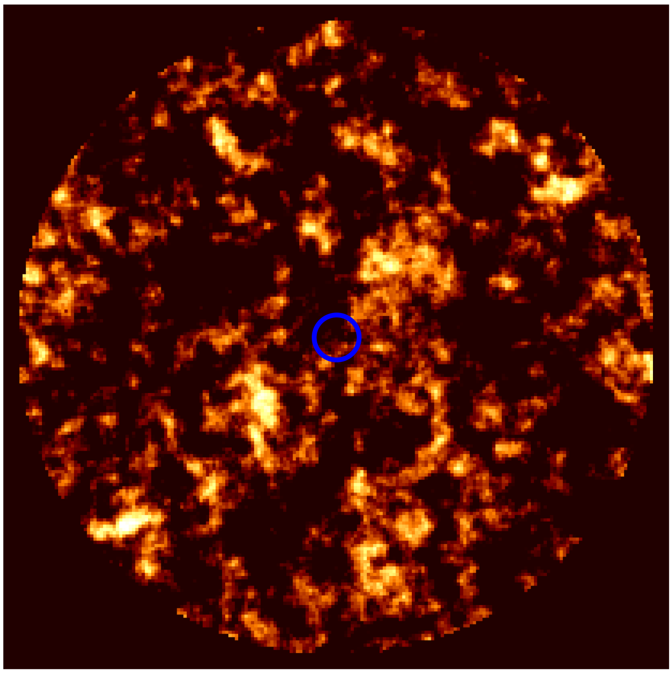

Figure 8.14: *Blazar PKS 2023-07 in the 20-100 keV energy band (in the center of the image). It is a deprojected image of 6°×6°.*

Table 8.2: *: Blazar charachteristics.*

Blazar	Effective exposure	Flux
	Ms	mCrab
3C 279	4.9	1.37±0.20
TXS 0716+714	7.1	< 0.74
PKS 1510-08	4.7	1.90±0.27
PKS 2023-07	4.8	< 0.98

the Figure 8.14 in spite of 14,250 DPHs for a net integration time of 4.8 Ms. The estimated upper limit of the flux is < 0.98 mCrab.

Appendix A

Conversion of fluxes

In this section the procedure to perform the conversion of a generic X–ray source flux from mCrab to the physical "ph·cm^{-2}·s^{-1}" is described, hypothesing that the source is well described by a power–law model and considering the Crab flux in the same energy range. After the flux is measured (§ A.1) and the associated error is calculated (§ A.2), in the § A.3 a possible approach to estimate the source photon index is proposed.

It is possible to consider a generic X–ray source detected in the B energy range with a coded fraction p_i, during the period t. The spectrum is well described by a power–law model in the same energy band with photon index α. The counts rate measured on the detector, normalized for p_i is given by:

$$R(B, \alpha, p_i, t) = \Gamma(B, \alpha, p_i) \cdot \Phi(B, \alpha, t) \tag{A.1}$$

where $\Gamma(\alpha, p_i, B) <$ 5,400 cm^2 is the instrument effective area that can be deduced by the response matrix:

$$\Gamma(B, \alpha, p_i) = \frac{MPR(B, \alpha, p_i)}{F(B, \alpha)} \tag{A.2}$$

where $MPR(B, \alpha, p)$ is the *model predicted rate* and $F(B, \alpha)$ is the *flux* (ph·cm^{-2}·s^{-1}) in `XSPEC`. The ratio between the source counts rate and that estimated for Crab during 6 months integrated time can be computed from the mosaic images:

$$\widetilde{\Phi}_{QDP}(B, t) = \frac{\left\langle \widetilde{R}(B, \alpha, p_i, t) \right\rangle_i}{\left\langle \widetilde{R}_{CRAB}(B, p_i) \right\rangle_i} \tag{A.3}$$

where $\langle ... \rangle_i$ shows that the dependence from p_i is saturated with the mosaic.

A.1 The flux estimate

If the counts rate estimated from mosaic images $\widetilde{R}$ is proportional or equal to the value measured on detector R, we can write:

$$\left\langle \widetilde{R}(B,\alpha,p_i,t) \right\rangle_i = k \cdot \langle \Gamma(B,\alpha,p_i) \rangle_i \cdot \Phi(B,\alpha,t) \tag{A.4}$$

$$\left\langle \widetilde{R}_{CRAB}(B,p_i) \right\rangle_i = k \cdot \langle R_{CRAB}(B,p_i) \rangle_i \tag{A.5}$$

where $R_{CRAB}(B,p_i)$ are the Crab *rates* measured in `XSPEC`, considering 6 months of data ($>$ 5,000 DPH rows) and describing these data with a power–law model with photon index 2.15 and normalization 10 ph$\cdot$cm$^{-2}\cdot$s$^{-1}\cdot$keV^{-1} @1 keV. Therefore:

$$\widetilde{\Phi}_{QDP}(B,t) = \frac{\langle \Gamma(B,\alpha,p_i) \rangle_i}{\langle R_{CRAB}(B,p_i) \rangle_i} \cdot \Phi(B,\alpha,t) \tag{A.6}$$

The symbol $\langle ... \rangle_i$ hides an integral that supposes known the temporal dependence of p_i:

$$\langle F(...,p_i) \rangle_i \equiv \int_0^1 F(...,p_i)\tau(p_i)dp_i \tag{A.7}$$

where $\tau(p_i)$ is the net exposure fraction accumulated in relation to the coded fraction p_i.

If we suppose the distribution p_i to be independent of the integrated period, on condition that is sufficiently long, the dependence both of R_{CRAB} and of Γ by p_i is similar. For this hypothesis:

$$\frac{\langle R_{CRAB}(B,p_i) \rangle_i}{\langle \Gamma(B,\alpha,p_i) \rangle_i} \cong \left\langle \frac{R_{CRAB}(B,p_i)}{\Gamma(B,\alpha,p_i)} \right\rangle_i \tag{A.8}$$

which gives from the (A.6):

$$\Phi(B,\alpha,t) \cong \widetilde{\Phi}_{QDP}(B,t) \cdot \left\langle \frac{R_{CRAB}(B,p_i)}{\Gamma(B,\alpha,p_i)} \right\rangle_i \tag{A.9}$$

As a simple dimensional check, since $[R_{CRAB}(B,p_i)]$ =ph$\cdot$s^{-1}, $\left[\widetilde{\Phi}_{QDP}(B,t)\right] = 1$, $[\Gamma(B,\alpha,p_i)]$ =cm^2, we obtain as expected $[\Phi(B,\alpha,t)]$ =ph$\cdot$ cm$^{-2}\cdot$s^{-1}.

R_{CRAB} is obtained from a large sample of data, while Γ is calculated in `XSPEC` from a narrow sample of values of p_i (655 values) for 61 different values of photon index (α, from 1 to 4 with a bin of 0.05).

In order to calculate R_{CRAB} values for some fixed p_i, corresponding at the target pcode fractions in the observations used to generate the mosaic, the distribution of $R_{CRAB}(B,p_i)$ is described with a model m (5th order polynomial). Since the function $\tau(p_i)$ (eq. A.7) is not known, the selected model m minimize the mean square error on R_{CRAB} in order to give more weight at values p_i more frequent and to simulate the distribution $\tau(p_i)$. It is verified that the distribution of Γ is characterized by a smaller dispersion of values if it is plotted in function of off-axis angles (θ_i) instead of pcode fractions (p_i). In order to obtain the best–fit of the Γ distribution described with ad hoc model, we considered the angles θ_i corresponding to p_i values. With the same principle adopted for the distribution R_{CRAB}, the linear model m' is fitted on the distribution Γ for 61 photon indexes α, sampling the angles θ_i for each p_i values. It is calculated:

$$\left\langle \frac{R_{CRAB}(B,m)}{\Gamma(B,\alpha,m')} \right\rangle_i \cong \frac{1}{N} \cdot \sum_{i=1}^{N} \frac{R_{CRAB}(B,p_i,m)}{\Gamma(B,\alpha,\theta_i,m')} \equiv \mu \qquad \text{(A.10)}$$

This is the flux conversion factor. The dimensional analysis gives $[\mu(B,\alpha)] = ph \cdot cm^{-2} \cdot s^{-1}$. The formula (A.9) can be written in this simple mode:

$$\Phi(B,\alpha,t) \cong \widetilde{\Phi}_{QDP}(B,t) \cdot \mu(B,\alpha) \qquad \text{(A.11)}$$

A.2 Errors analysis

If the equation $(A.9)$ is correct, the $\Phi(B,\alpha,t)$ relative error is composed of the statistical error on $\Phi_{QDP}(B,t)$ ($\epsilon_{QDP}(B,t)$) and systematic error on $\mu(B,\alpha)$ ($\epsilon_{SYS}(B,\alpha)$). Thus the total relative error is the sum of these two contributes, the first $\epsilon_{QDP}(B,t)$ is known from the mosaic, the second $\epsilon_{SYS}(B,\alpha)$ have to be calculated. The $\mu(B,\alpha)$ is calculated for three energy ranges (20-60, 60-100, 20-100 keV) and for all photon indexes α. The systematic error $\epsilon_{SYS}(B,\alpha)$ can be divided in three contributions: the first is due to the approximation of $R_{CRAB}(B,p_i)$ with the model m, the second is bounded by the dependence of the standard deviation of the $\mu(B,\alpha)$ by p_i and the models m, the third one is due to the approximation of $\Gamma(B,\alpha,\vartheta_i)$ with the model m'. The choice of the model m leads to a $\chi^2_r(B,m) > 1$, obtained considering the count rate error $dR_{CRAB}(B,p_i)$ estimated in `XSPEC` The dispersion in values of $R_{CRAB}(B,p_i)$ have to be compared with the intrinsic error $dR_{CRAB}(B,p_i)$. The value of χ^2_r shows that the mean square deviation from the model is higher than the estimated intrinsic error. Thus, it is obtained:

$$\delta R_{CRAB}(B,p_i,m) = \sqrt{\chi^2_r(B,m)} \cdot \frac{dR_{CRAB}(B,p_i)}{R_{CRAB}(B,p_i)} \qquad \text{(A.12)}$$

In order to calculate the average of $\delta R_{CRAB}(B,p_i,m)$, it is necessary introduce the model m'' which describes better $dR_{CRAB}(B,p_i)$:

$$\langle \delta R_{CRAB}(B,m,m'') \rangle_i \cong \frac{1}{N} \cdot \sqrt{\chi^2_r(B,m)} \cdot \sum_{i=1}^{N} \frac{dR_{CRAB}(B,p_i,m'')}{R_{CRAB}(B,p_i,m)} \equiv \sigma' \qquad \text{(A.13)}$$

The second contribute is the standard deviation of the $\mu(B,\alpha)$:

$$\delta\left\langle\frac{R_{CRAB}(B,m)}{\Gamma(B,\alpha,m')}\right\rangle_i \cong \sqrt{\frac{1}{N}\cdot\sum_{i=1}^{N}\left(\frac{R_{CRAB}(B,p_i,m)}{\Gamma(B,\alpha,\theta_i,m')}-\mu(B,\alpha)\right)^2} \equiv \sigma \tag{A.14}$$

The choice of the model m' in order to describe the distribution Γ does not lead to calculate a $\chi_r^2(B,m')$ since the Γ is without error. Nontheless, an estimate can be obtained:

$$\sqrt{\frac{\sum_{i=1}^{N}\frac{[\Gamma(B,\alpha,\theta_i)-\Gamma(B,\alpha,\theta_i,m')]^2}{\Gamma(B,\alpha,\theta_i,m')^2}}{N}} = C = \sqrt{\frac{W-VAR}{N}} \tag{A.15}$$

where $W-VAR$ is the variance measured in `XSPEC`. It is possible to put:

$$\delta\Gamma(B,\alpha,\theta_i,m') = \frac{C}{\Gamma(B,\alpha,\theta_i,m')} \tag{A.16}$$

and to estimate the third contribute calculating the average of $\delta\Gamma(B,\alpha,\theta_i,m')$:

$$\langle\delta\Gamma(B,\alpha,m')\rangle_i \cong \frac{1}{N}\sum_{i=1}^{N}\frac{C}{\Gamma(B,\alpha,\theta_i,m')} \equiv \sigma'' \tag{A.17}$$

The total relative error results:

$$\epsilon_\Phi(B,\alpha,t) = \epsilon_{QDP}(B,t) + \frac{\sigma(B,\alpha,m,m')+\sigma'(B,m,m'')+\sigma''(B,\alpha,m')}{\mu(B,\alpha,m,m')} \tag{A.18}$$

It is possible to combine the equation (A.18) with the (A.11) and to obtain the total error $\Delta\Phi$:

$$\Delta\Phi(B,\alpha,t) = \mu(B,\alpha,m,m')\cdot\Delta\widetilde{\Phi}_{QDP}(B,t) + \widetilde{\Phi}_{QDP}(B,t)\cdot(\sigma(B,\alpha,m,m'+ \tag{A.19}$$

$$+\sigma'(B,m,m'')+\sigma''(B,\alpha,m'))$$

The relative error (i.e. the relative deviation between the Crab count rate measured in `XSPEC` and these estimated from the model m) for each p_i is obtained:

$$\delta S_{CRAB}(B,p_i,m) = \frac{R_{CRAB}(B,p_i)-R_{CRAB}(B,p_i,m)}{R_{CRAB}(B,p_i)} \tag{A.20}$$

In order to verify if the relation (A.13) is correct, a comparison between this relation and the (A.20) is performed. Is verified that the probability distribution, that the relative deviation (A.20) is inferior of the error (A.13), is characterized by a gaussian profile:

$$P\left(\delta S_{CRAB}(B,p_i,m) < n\cdot\frac{1}{N}\sqrt{\chi^2_r(B,m)}\cdot\sum_{i=1}^{N}\frac{dR_{CRAB}(B,p_i,m'')}{R_{CRAB}(B,p_i,m)}\right)\simeq \tag{A.21}$$

$$\simeq erf\left(\frac{n\cdot\sigma}{\sqrt{2}}\right)$$

The trend of the probability distribution is performed changing the confidence level, n, between 1 and 4 with a bin of 0.01 (300 values); in the 20-60 keV energy range, for $n = 1, 2, 3$, the values 0.67, 0.92 and 0.97 are obtained. This test allows to verified that the error definition (A.13) is correct. Likewise, the same approach is used to testing the error definition (A.17), in this case, for $n = 1, 2, 3$, the acceptable values 0.73, 0.92 e 0.99 are estimated.

A.3 Estimate of the source photon index

With this approach it is possible to estimate the flux $\Phi(B,\alpha,t)+\Delta\Phi(B,\alpha,t)$ of a generic source during the period t for each photon indexes α. The source fluxes in two energy ranges B_1 e B_2 (20-60, 60-100 keV) for each α are:

$$\Phi^1(\alpha,t)+\Delta\Phi^1(\alpha,t) \tag{A.22}$$

and

$$\Phi^2(\alpha,t)+\Delta\Phi^2(\alpha,t) \tag{A.23}$$

In the same energy ranges, two fluxes of Crab are measured in `XSPEC` with normalization N =10 h·cm^{-2}·s^{-1}·keV^{-1} @1 keV and photon index α =2.15 fixed:

$$\Phi^1_{CRAB}(\alpha,N) = 0.1990 \tag{A.24}$$

and

$$\Phi^2_{CRAB}(\alpha,N) = 0.0348 \tag{A.25}$$

in unit of $ph\cdot cm^{-2}\cdot s^{-1}$. For each α, two normalizations are calculated thanks to the expressions:

$$N_1(\alpha,t) = 10\cdot\frac{\Phi^1(\alpha,t)}{\Phi^1_{CRAB}(\alpha,N)} \tag{A.26}$$

and

$$N_2(\alpha,t) = 10\cdot\frac{\Phi^2(\alpha,t)}{\Phi^2_{CRAB}(\alpha,N)} \tag{A.27}$$

and the associated errors are obtained:

$$\Delta N_1(\alpha,t) = 10\cdot\frac{\Delta\Phi^1(\alpha,t)}{\Phi^1_{CRAB}(\alpha,N)} \tag{A.28}$$

and

$$\Delta N_2(\alpha, t) = 10 \cdot \frac{\Delta\Phi^2(\alpha, t)}{\Phi^2_{CRAB}(\alpha, N)} \tag{A.29}$$

In this mode, the distributions of normalization in function of photon indexes α, for each energy band B_j and for each period t, are performed.

It is possible to calculate the probability:

$$P\,(\alpha, t) = \int P(N = N_1)P(N = N_2)dN = \tag{A.30}$$

$$= \frac{1}{2\pi\Delta N_1 \Delta N_2} \int exp - \left[\frac{(N - N_1)^2}{2\Delta N_1^2} + \frac{(N - N_2)^2}{2\Delta N_2^2}\right] dN$$

where $N_1 = N_1(\alpha, t)$, $\Delta N_2 = \Delta N_1(\alpha, t)$ and $N_2 = N_2(\alpha, t)$, $\Delta N_2 = \Delta N_2(\alpha, t)$ are the distributions of the normalization and the associated errors for two energy ranges. The idea is to estimate the photon index α that maximizes the probability $P(\alpha, t)$, resolving the integral. Developing the exponential argument the following expression can be obtained:

$$P(\alpha, t) = \frac{exp(-k)}{\sqrt{2\pi(\Delta N_1^2 + \Delta N_2^2)}} \tag{A.31}$$

where

$$k = \frac{(N_1 - N_2)^2}{2(\Delta N_1^2 + \Delta N_2^2)} \tag{A.32}$$

The probability $P(\alpha, t)$ is higher when $(N_1 - N_2)^2$ is minimized, thus when $N_1 = N_2$. Fitting a linear model (i.e. $B_j + A_j\alpha$ e $\Delta B_j + \Delta A_j\alpha$, where j =1,2 is the energy band index) to the distributions during a period t, it is possible to estimate the source photon index α_s for which $N_1 = N_2$. If the error in the soft energy range is negligible respect the hard one and if the terms in α in the linear model are negligible, the α error is:

$$\sigma = \frac{\sqrt{\Delta N_1^2 + \Delta N_2^2}}{|N_1 - N_2|} \approx \frac{\sqrt{\Delta N_2^2}}{|(B_1 - B_2) + (A_1 - A_2)\alpha|} \approx \frac{\sqrt{\Delta B_2^2}}{|(B_1 - B_2)|} \tag{A.33}$$

If the photon index has an error too large to constraint a significant value, the probability that the α_s is included between two value α_1, α_2 can be calculated with the following equation:

$$\int_{\alpha_1}^{\alpha_2} P(\alpha, t)d\alpha = \int_{\alpha_s}^{\alpha_2} P(\alpha, t)d\alpha - \int_{\alpha_s}^{\alpha_1} P(\alpha, t)d\alpha = \frac{1}{|N_1 - N_2|} \cdot \frac{\left[\frac{erf(\alpha_2 - \alpha_s)}{\sigma\cdot\sqrt{2}} - \frac{erf(\alpha_1 - \alpha_s)}{\sigma\cdot\sqrt{2}}\right]}{2} \tag{A.34}$$

Conclusions

This thesis is devoted to serendipitous observations in the X–ray energy range. The work is based on soft X–ray (0.3-12 keV) data collected by the *European Photon Imaging Camera* (*EPIC*) instrument (Turner et al., 2001) onboard the *XMM–Newton* observatory, and on hard X–ray (15-200 keV) data collected by the Burst Alert Telescope (BAT) onboard the *Swift* mission.

XMM–Newton observed the field of the isolated neutron star 1E1207.4-5209 10 times between 2001 and 2005, totalling $\sim$ 450 ks of exposure time. This is possibly the deepest X–ray observation ever performed at middle Galactic latitude ($|b| \simeq 10^\circ$), setting the case for an unprecedented serendipitous survey, sampling both the galactic and the extra–galactic X–ray source population. The high throughput, wide energy range, good angular and spectral resolution of *EPIC*allow to investigate with high sensitivity both the distant population of quasi-stellar objects (QSOs), active galactic nuclei (AGNs), normal galaxies, and the galactic population of stars and X–ray binaries (XRBs).

Swift/BAT, while waiting for new detections of Gamma–ray Bursts, collects a huge amount of data ("Survey data") with good positional and specral information in the 14-200 keV energy range totaling each day a sky coverage of 50-80%. The unique combination of a huge field of view, high sensitivity in the and good angular resolution makes BAT a potentially powerful tool to study the hard X–ray sky. BAT Survey data are immediately released in the public Swift data archive. However, such a large database of serendipitous observations has remained almost unused by the astronomical community because of technical difficulties involved in data analysis. In order to exploit the growing BAT database, we have developed a series of new software tools. First, we have implemented and tested a complete pipeline devoted to study the spectral and flux evolution of bright hard X–ray sources (fluxes $\gtrsim$ 50 mCrab) on a time scale down to the Survey data time resolution (5 minutes). Then, we designed and developed new, ad-hoc tools to optimize background rejection and data stacking (using the mosaic approach). This allows to reach very long integration times and thus to study much fainter sources, down to the $\sim$ 1 mCrab level (using $\sim$ 1 year of data), close to the expected instrument capabilities.

The main results may be summarized as follows:

XMM-Newton middle Galactic latitude deep survey

1. We analysed all the *XMM–Newton* observations of the intermediate–latitude field around 1E1207.4−5209 (10 epochs, for an overall 450 ks exposure time) in order to investigate the properties of the X–ray source population. We detected 144 serendipitous sources in total; 114 of them were detected in the soft energy band (0.5–2 keV), while 87 were detected in the hard energy band (2–10 keV) band, down to limiting fluxes of $\sim 10^{-15}$ erg cm^{-2} sec^{-1} and 4×10^{-15} erg cm^{-2} sec^{-1}, respectively. The lower number of fainter sources detected with respect to that reported in Novara et al. (2006) (see § 3.2.4) mainly affects the log$N$–log$S$ distribution in the soft energy band, which now features a clear flattening at the low flux end (i.e. below $\sim 2.5\times10^{-15}$ erg cm^{-2} sec^{-1}). However, at higher fluxes the log$N$–log$S$ distribution is perfectly consistent with that reported in Novara et al. (2006) and is well above those obtained at high galactic latitudes (Baldi et al., 2002). Therefore we confirm the presence of a non–negligible galactic population component, in addition to the extra–galactic one. In the hard energy band, the log$N$–log$S$ distribution is fully consistent with that reported in Novara et al. (2006) and with those obtained both in the Galactic plane (Ebisawa et al., 2005) and at high Galactic latitude (Baldi et al., 2002), confirming that the distribution is dominated by extra–galactic sources.

2. Thanks to the increased count statistics, we performed a variability and spectral analysis of the 40 brightest sources (0.5-10 keV flux greater than 10^{-14} erg cm^{-2} sec^{-1}, bright source sample). For 10 of them, a large flux variation between the 2002 and 2005 observations has been detected, suggesting that they are transient sources, while for other two sources evidence of variability on short timescales ($\sim$ 0.1 and $\sim$ 10 ks) has been obtained. Moreover, we refined the spectral analysis of the peculiar Seyfert–2 galaxy XMMU J121029.0−522148 discussed in Novara et al. (2006), finding a best–fit redshift value $z = 0.042$, higher than the value 0.032 reported in the literature.

3. We have carried out a complete multi–band (*UBVRI*) optical coverage of the field with the *WFI* of the ESO/MPG 2.2m telescope to search for candidate optical counterparts to the X–ray sources and we found at least a candidate counterpart brighter than $V \sim 24.5$ for 112 of them. By cross–correlating sources with the *2MASS* catalogue, we also obtained a color–based classification for most of them.

   We thus identified 27 of the brightest sources as AGNs and 7 as stars, while we identified 21 of the faintest sources as stars and 70 sources as AGNs or galaxies. Future follow-up investigations will be aimed at confirming the proposed classification of the brightest X–ray sources through multi-object spectroscopy of the candidate counterparts. For the candidate AGNs, radio observations will also be useful to get a better and unambiguous classification.

Exploitation of the BAT Survey database
A) A pipeline to study bright hard X–ray sources.

1. We have created a new, complete pipeline to reduce and analyse BAT survey data. The pipeline, based on public software tools released by the instrument team at the Goddard Space Flight Center, is aimed at extracting good-quality time-resolved spectra and light curves in flux units (erg $\mathrm{cm}^{-2}\mathrm{s}^{-1}$) for a selected source. The "mask wheighting" approach is used, which does not allow to stack different observations unless they are nearly co-aligned.

2. Several tests were performed to calibrate and validate the pipeline (§ 5.0.1). First, we have analysed a large number of observations (~ 7 months) of the steady, very bright Crab nebula (the standard calibration source for almost all high energy observatories). We found that both the flux and photon index values of the spectra are succesfully computed and are very stable as a function of the source location within the BAT FoV. Such results, coupled to the good agreement with the values assumed for the BAT instrument calibration, demonstrate the overall correctness of the approach. The pointing requirements to combine different BAT datasets have been then estimated. The results suggest that significant flux losses ($> 5\%$) may occur, especially for target position at low coded fractions, when stacking different data with a pointing offset larger than 2 arcmin. This sets a limit to the maximum integration time for a given source using this approach to a typical value of 1 hour.

3. We have studied the BH binary GRO J1655-40 during its 2005, 9-months long outburst, to test the results of the pipeline in the case of a fainter, strongly variable source. The outburst was also systematically observed with the well calibrated *RXTE* instruments. This allowed for a robust cross-check of the BAT results. The spectral and flux evolution of the outburst, as independently seen by the two observatories, is in very good agreement: BAT reproduces *RXTE*/HEXTE fluxes within a 10-15% uncertainty, with a 3-σ sensitivity of ~ 20 mCrab for an on-axis source, thus establishing its capabilities to monitor the evolution of relatively bright hard X–ray sources. It is worth noting that the detection of the source activity by *RXTE*/HEXTE and PCA was due to planned observational campaign of the Galactic center region, while BAT serendipitously caught the outburst since the very beginning, simply owing to its good sensitivity over a very large FoV. Had GRO J1655-40 be located outside the galactic bulge region scanned by *RXTE*, its outburst would have been detected by ASM with > 15 day delay with respect to BAT.

We have used the spectra and light curves obtained with Pipeline for GRO J1655-40 to follow its evolution during the rising phase of the 2005 outburst (§ 5.1).

B) An approach to study faint hard X–ray sources

1. The study of hard X–ray sources fainter than $\sim$ 20 mCrab requires integration times significantly longer than 1 hour. Thus, combination of observations collected with different pointing is needed. To this aim, we have designed and developed new, ad-hoc software tools (implemented in `MATLAB`), based on the mosaic technique. With this approach, we can exploit the complete BAT data archive, stacking all the observations in which a given source falls in the BAT field of view. Particular care is required in order to minimize the contamination from bright sources in the BAT FOV, as well as to reduce the impact of diffuse and electronic background effects (see `batcloseup` characteristics reported in § 6.3.2).

2. The new tools have been dubbed `batfilldb`, `batbkgmap`, `batcloseup` and `batsurvey` and were described in Chapter 6.

    - `batfilldb` collects the relevant auxiliary information for each data block and store it in a database in order to maximize the efficiency of the analysis, minimizing the time required to data selection, based on different criteria (e.g. target coordinates, data quality filter, time windows).

      The other three tasks are composed of standard public tools and non–standard products developed in `MATLAB`:

    - `batbkgmap` produces background maps that can describe the diffuse background and border effects connected to electronic noise and to anomalous elements of the detector (§ 6.2). We obtained background maps in 20-100 keV, 20-30 keV, 20-60 keV, 30-60 keV and 60-100 keV energy ranges collecting six months of data (10906 DPHs) between January 1 2005 and July 1 2005. These maps are used by the subsequent tool `batcloseup` (in a selected energy band), adding a further parameter in the built-in model that describes the detector plane during the cleaning operations.
    - `batcloseup` starts from a series of deconvolved sky images of the BAT FoV (each obtained from short, co-aligned observations) and selects and cuts a portion (a frame) with a configurable radius around the target in each image The tool then reprojects such frames and stacks them into a mosaic (§ 6.3.3) until a desired integration time is achieved. Finally, the count rate of the target in the mosaicked image is estimated. A light curve is then generated (§ 6.3.4).

The count rate of the target can then be converted to flux, using an opportune prescription, using the Crab as a reference, assuming a spectral shape for the target and averaging the instrument response on the field of view (Appendix A).

3. We have extensively tested our tools to verify the reliability of results (Chapter 7). First, we have analysed a large number of observations (1 year for a total of 3364 DPH files) of the steady, very bright Crab nebula. We have obtained light curves both on the single observation and on the monthly bin time scale in different energy bands (see § 7.1.1). We found that the flux values extracted with a standard detection algorithm on the mosaicked images is stable into a 10% of systematic error. The work is still in progress in order to reduce systematics. As a second test, we selected a much fainter hard X–ray source: the Vela pulsar. Using one month of BAT data, for a net exposure time of ~ 233 ks, Vela is clearly detected in the mosaicked image. The estimated 20-100 keV count rate of Vela was then converted into flux. We obtained a flux of $\sim (1.40 \pm 0.15) \cdot 10^{-4}$ ph·cm^{-2}·s^{-1} for the Vela pulsar (error includes a systematics of 10%), or of 7.2±0.8 mCrab (error includes systematics). Such a value is in good agreement with the values of 7.1±0.1 mCrab in the 20-40 keV and of 8.1±0.2 mCrab in the 40-100 keV reported in the 3rd IBIS/ISGRI catalog (Bird et al., 2007).

4. As a first application of our tools, we have studied the hard X–ray emission of the six blazars detected by the *AGILE* telescope (Tavani et al., 2008) as high energy γ–ray sources. Results are presented in the Chapter 8. After a first observing window in July 2007, the *AGILE* satellite began a new pointing to 3C 454.3 in 2007 November at high off–axis angle (about 40°) and a multiwavelength follow-up campaign was started. *AGILE* data were collected during two different periods, the first ranging between 2007-11-10 and 2007-11-25 and the second between 2007-11-28 and 2007-12-01, for a total of ~ 592 ks (Vercellone et al., 2008b). We analysed *Swift*/BAT survey data with `batcloseup` in order to study the hard X–ray emission of 3C 454.3 in the 20-60 keV and 60-100 keV energy bands and to investigate its evolutions as a function of time. Taking advantage of the BAT database, we studied the source not only in the AGILE era, but also during an exceptionally strong outburst occurred in 2005 (§ 8.2.1). The November 2007 data set, simultaneous to the *AGILE* campaign, is characterized by a net exposure time of ~ 106 ks for a flux in the 20-60 keV energy band of $(1.07 \pm 0.19) \times 10^{-3}$ ph·cm^{-2}·s^{-1}. The *Swift*/BAT flux is in good agreement with the flux derived from the whole *INTEGRAL*/IBIS campaign in the same energy range and in the same period. We published such results in (Vercellone et al., 2008b).

   Exploiting all BAT survey data in the archive, we generated a 3.5 year long light curve of 3C 273 blazar in the 20-100 keV energy range (see

§ 8.4). The 3C 273 average flux is $(3.21\pm0.21)\times10^{-3}$ ph·cm^{-2}·s^{-1}, calculated with the approach described in the Appendix A, considering for 3C 273 a power–law spectrum with a photon index $\alpha = 1.8$. During the epoch corresponding to the first year of *AGILE*, multi–band (20-30 keV, 30-60 keV, 60-100 keV) light curves of 3C 273 were also extracted.

Finally, we studied the blazars 3C 279, TXS 0716+714, PKS 1510-08, and PKS 2023-07 sby tacking 3.5 ys of data (see § 8.5). A significant detection (> 4-σ) was obtained only for 3C 279 and PKS 1510-08, with a net exposure time of 4.9 Ms and 4.7 Ms respectively, with a flux of (1.37±0.20) mCrab and (1.90±0.27) mCrab.

We developed and validated ad hoc software tools which allow to exploit the very large, serendipitous BAT survey database. Indeed, the results presented in this thesis are only a small sample of the ones which can be obtained by exploiting the BAT survey archive. On the other hand, the amount of data stored in the BAT public archive will grow along the mission lifetime.

Work in the next future will be devoted to improve the performance of our tools, in particular to optimize cleaning of background sources, in order to reduce systematic errors. In parallel, a more extensive and systematic utilisation of our software will be carried out, mining the whole BAT dataset:

- as a first application, we will perform follow up studies of high energy sources detected by the *AGILE* and *GLAST* missions. We will continue and extend our monitoring of γ–ray blazars. Moreover, we will focus on variable, unidentified γ–ray sources at both high Galactic latitude (most likely, blazars) and low Galactic latitude, where a few transient, possibly recurrent high energy γ–ray sources have been singled out, but remained so far unidentified (accreting binary systems?).

- we will study the hard X–ray emission properties of different classes of peculiar galactic and extragalactic sources, for instance Soft Gamma–ray Repeaters (SGRs) and Anomalous X–ray Pulsars (AXPs), i.e. Magnetar candidates. Long term monitoring of Magnetars with mCrab sensitivity could assess variability in the high energy persistent emission for the first time. Discovery of possible correlation with the soft X–ray persistent emission will allow to shed light on the high energy emission physics. As a further example, a particularly interesting (and poorly understood) class is represented by the so-called Supergiant Fast X–ray Transients (SFXTs). It will be possible to assess recurrence times as well as possible periodicities for SFXTs outbursts, so far observed in one source only, which would shed conclusive light on the physics of such sources.

- we aim at producing, as final step, an all sky map by stacking the whole BAT database in order to extract an all sky catalog of sources. Our tools allow to estimate a limiting sensitivity of order 0.8 mCrab for a significant detection of a source at high galactic latitude by stacking 3.5

yr of data. Thus, we expect to produce an all sky survey more than one order of magnitude deeper than HEAO1-A4, the last all-sky hard X–ray source catalog, generated ~ 25 yr ago (Levine et al., 1984).

Bibliography

Abell, G. O. 1958, ApJS, 3, 211

Aharonian, F. A. 2000, New Astronomy, 5, 377

Aller, M. F., Marscher, A. P., Hartman, R. C., Aller, H. D., Aller, M. C., Balonek, T. J., Begelman, M. C., Chiaberge, M., Clements, S. D., Collmar, W., de Francesco, G., Gear, W. K., Georganopoulos, M., Ghisellini, G., Glass, I. S., Gonzalez-Perez, J. N., Heinimaki, P., Herter, M., Hooper, E. J., Hughes, P. A., Johnson, W. N., Katajainen, S., Kidger, M. R., Kraus, A., Lanteri, L., Lawrence, G. F., Lichti, G. G., Lin, Y. C., Madejski, G. M., McNaron-Brown, K., Moore, E. M., Mukherjee, R., Nair, A. D., Nilsson, K., Peila, A., Pierkowski, D. B., Pohl, M., Pursimo, T., Raiteri, C. M., Reich, W., Robson, E. I., Sillanpaa, A., Sikora, M., Smith, A. G., Steppe, H., Stevens, J., Takalo, L. O., Terasranta, H., Tornikoski, M., Valtaoja, E., von Montigny, C., Villata, M., Wagner, S., Wichmann, R., & Witzel, A. 1997, in American Institute of Physics Conference Series, Vol. 410, Proceedings of the Fourth Compton Symposium, ed. C. D. Dermer, M. S. Strickman, & J. D. Kurfess, 1423–+

Antonucci, R. 1993, ARA&A, 31, 473

Antonucci, R. R. J. & Miller, J. S. 1985, ApJ, 297, 621

Aschenbach, B., Briel, U. G., Haberl, F., Braeuninger, H. W., Burkert, W., Oppitz, A., Gondoin, P., & Lumb, D. H. 2000, in Presented at the Society of Photo-Optical Instrumentation Engineers (SPIE) Conference, Vol. 4012, Proc. SPIE Vol. 4012, p. 731-739, X-Ray Optics, Instruments, and Missions III, Joachim E. Truemper; Bernd Aschenbach; Eds., ed. J. E. Truemper & B. Aschenbach, 731–739

Atoyan, A. M. & Dermer, C. D. 2003, ApJ, 586, 79

Baldi, A., Molendi, S., Comastri, A., Fiore, F., Matt, G., & Vignali, C. 2002, ApJ, 564, 190

Barthelmy, S. D., Barbier, L. M., Cummings, J. R., Fenimore, E. E., Gehrels, N., Hullinger, D., Krimm, H. A., Markwardt, C. B., Palmer, D. M., Parsons, A., Sato, G., Suzuki, M., Takahashi, T., Tashiro, M., & Tueller, J. 2005, Space Science Reviews, 120, 143

Bertin, E. & Arnouts, S. 1996, A&AS, 117, 393

Bignami, G. F., Caraveo, P. A., Luca, A. D., & Mereghetti, S. 2003, Nature, 423, 725

Bird, A. J., Malizia, A., Bazzano, A., Barlow, E. J., Bassani, L., Hill, A. B., Bélanger, G., Capitanio, F., Clark, D. J., Dean, A. J., Fiocchi, M., Götz, D., Lebrun, F., Molina, M., Produit, N., Renaud, M., Sguera, V., Stephen, J. B., Terrier, R., Ubertini, P., Walter, R., Winkler, C., & Zurita, J. 2007, ApJS, 170, 175

Blandford, R. D. & Rees, M. J. 1978, in BL Lac Objects, ed. A. M. Wolfe, 328–341

Bloom, S. D. & Marscher, A. P. 1996, ApJ, 461, 657

Brown, C. 1974, Journal of Applied Physics, 45, 1806

Bulgarelli, A., Vercellone, S., Giuliani, A., Chen, A., Mereghetti, S., Pellizzoni, A., Perotti, F., Fornari, F., Fiorini, M., Caraveo, P., Zambra, A., Tavani, M., Pucella, G., D'Ammando, F., Vittorini, V., Costa, E., Feroci, M., Donnarumma, I., Pacciani, L., Monte, E. D., Lazzarotto, F., Soffitta, P., Evangelista, Y., Lapshov, I., Rapisarda, M., Argan, A., Trois, A., Barbiellini, G., Longo, F., Cocco, G. D., Labanti, C., Fuschino, F., Marisaldi, M., Galli, M., Gianotti, F., Trifoglio, M., Picozza, P., Morselli, A., Prest, M., Vallazza, E., Lipari, P., Giommi, P., Pittori, C., Antonelli, L. A., Gasparrini, D., Cutini, S., Verrecchia, F., & Salotti, L. 2007, The Astronomer's Telegram, 1199, 1

Burrows, D. N., Hill, J. E., Nousek, J. A., Kennea, J. A., Wells, A., Osborne, J. P., Abbey, A. F., Beardmore, A., Mukerjee, K., Short, A. D. T., Chincarini, G., Campana, S., Citterio, O., Moretti, A., Pagani, C., Tagliaferri, G., Giommi, P., Capalbi, M., Tamburelli, F., Angelini, L., Cusumano, G., Bräuninger, H. W., Burkert, W., & Hartner, G. D. 2005, Space Science Reviews, 120, 165

Cannon, T. M. & Fenimore, E. E. 1980, Opt. Eng., 19, 283

Caraveo, P. A., De Luca, A., Mereghetti, S., Pellizzoni, A., & Bignami, G. F. 2004, Science, 305, 376

Caroli, E., Stephen, J. B., di Cocco, G., Natalucci, L., & Spizzichino, A. 1987, Space Science Reviews, 45, 349

Carrera, F. J., Ebrero, J., Mateos, S., Ceballos, M. T., Corral, A., Barcons, X., Page, M. J., Rosen, S. R., Watson, M. G., Tedds, J. A., Della Ceca, R., Maccacaro, T., Brunner, H., Freyberg, M., Lamer, G., Bauer, F. E., & Ueda, Y. 2007, A&A, 469, 27

Cassinelli, J. L., Waldron, W., Sanders, W., Harnden, F. R., Rosner, R., & Vaiana, G. S. 1985, ApJ, 250, 677

Celotti, A. & Ghisellini, G. 2008, MNRAS, 385, 283

Celotti, A., Ghisellini, G., & Fabian, A. C. 2007, MNRAS, 375, 417

Chandrasekhar, S. 1931, ApJ, 74, 81

Charles, P. A. & Seward, F. D. 1995, Exploring the X-ray Universe (ISBN 0-521-43712-1, Cambridge University Press)

Chen, A., Vercellone, S., Giuliani, A., Mereghetti, S., Pellizzoni, A., Perotti, F., Fornari, F., Fiorini, M., Caraveo, P., Zambra, A., Bulgarelli, A., Gianotti, F., Trifoglio, M., Cocco, G. D., Labanti, C., Fuschino, F., Marisaldi, M., Galli, M., Tavani, M., Pucella, G., D'Ammando, F., Vittorini, V., Costa, E., Feroci, M., Donnarumma, I., Pacciani, L., Monte, E. D., Lazzarotto, F., Soffitta, P., Evangelista, Y., Lapshov, I., Rapisarda, M., Argan, A., Trois, A., Paris, G. D., Barbiellini, G., Longo, F., Picozza, P., Morselli, A., Prest, M., Vallazza, E., Lipari, P., Zanello, D., Mauri, F., Giommi, P., Pittori, C., Antonelli, L. A., Gasparrini, D., Cutini, S., Verrecchia, F., & Salotti, L. 2007, The Astronomer's Telegram, 1278, 1

Courvoisier, T. J.-L. 1998, A&A Rev., 9, 1

D'Ammando, F., Bulgarelli, A., Vercellone, S., Giuliani, A., Chen, A., Mereghetti, S., Pellizzoni, A., Perotti, F., Fornari, F., Fiorini, M., Caraveo, P., Zambra, A., Gianotti, F., Trifoglio, M., Cocco, G. D., Labanti, C., Fuschino, F., Marisaldi, M., Galli, M., Tavani, M., Pucella, G., Vittorini, V., Costa, E., Feroci, M., Donnarumma, I., Pacciani, L., Monte, E. D., Lazzarotto, F., Soffitta, P., Evangelista, Y., Lapshov, I., Rapisarda, M., Argan, A., Trois, A., Paris, G. D., Barbiellini, G., Longo, F., Vallazza, E., Picozza, P., Morselli, A., Prest, M., Lipari, P., Zanello, D., Mauri, F., Giommi, P., Pittori, C., Gasparrini, D., Cutini, S., Preger, B., Santolamazza, P., Verrecchia, F., & Salotti, L. 2008, The Astronomer's Telegram, 1436, 1

De Luca, A., Caraveo, P. A., Mereghetti, S., Negroni, M., & Bignami, G. F. 2005, ApJ, 623, 1051

De Luca, A., Mereghetti, S., Caraveo, P. A., Moroni, M., Mignani, R. P., & Bignami, G. F. 2004, A&A, 418, 625 den Herder, J. W., Brinkman, A. C., Kahn, S. M., Branduardi-Raymont, G., Thomsen, K., Aarts, H., Audard, M., Bixler, J. V., den Boggende, A. J., Cottam, J., Decker, T., Dubbeldam, L., Erd, C., Goulooze, H., Güdel, M., Guttridge, P., Hailey, C. J., Janabi, K. A., Kaastra, J. S., de Korte, P. A. J., van Leeuwen, B. J., Mauche, C., McCalden, A. J., Mewe, R., Naber, A., Paerels, F. B., Peterson, J. R., Rasmussen, A. P., Rees, K., Sakelliou, I., Sako, M., Spodek, J., Stern, M., Tamura, T., Tandy, J., de Vries, C. P., Welch, S., & Zehnder, A. 2001, A&A, 365, L7

Dermer, C. D., Schlickeiser, R., & Mastichiadis, A. 1992, A&A, 256, L27

Dicke, R. H. 1968, ApJ, 153, L101+

Ebisawa, K., Tsujimoto, M., Paizis, A., Hamaguchi, K., Bamba, A., Cutri, R., Kaneda, H., Maeda, Y., Sato, G., Senda, A., Ueno, M., Yamauchi, S., Beckmann, V., Courvoisier, T. J.-L., Dubath, P., & Nishihara, E. 2005, ApJ, 635, 214

Erben, T., Schirmer, M., Dietrich, J. P., Cordes, O., Haberzettl, L., Hetterscheidt, M., Hildebrandt, H., Schmithuesen, O., Schneider, P., Simon, P., Deul, E., Hook, R. N., Kaiser, N., Radovich, M., Benoist, C., Nonino, M., Olsen, L. F., Prandoni, I., Wichmann, R., Zaggia, S., Bomans, D., Dettmar, R. J., & Miralles, J. M. 2005, Astronomische Nachrichten, 326, 432

Fanaroff, B. L. & Riley, J. M. 1974, MNRAS, 167, 31P

Foschini, L., Di Cocco, G., Malaguti, G., Pian, E., Tagliaferri, G., Ghisellini, G., Maraschi, L., Giommi, P., Gehrels, N., Walter, R., Eckert, D., & A Large Collaboration. 2005, The Astronomer's Telegram, 497, 1

Frank, J., King, A. R., & Raine, D. J. 1992, Accretion powered in astrophysics (ISBN 0521408636, Cambridge University Press, 1992)

Fuhrmann, L., Cucchiara, A., Marchili, N., Tosti, G., Nucciarelli, G., Ciprini, S., Molinari, E., Chincarini, G., Zerbi, F. M., Covino, S., Pian, E., Meurs, E., Testa, V., Vitali, F., Antonelli, L. A., Conconi, P., Cutispoto, G., Malaspina, G., Nicastro, L., Palazzi, E., & Ward, P. 2006, A&A, 445, L1

Gehrels, N., Chincarini, G., Giommi, P., Mason, K. O., Nousek, J. A., Wells, A. A., White, N. E., Barthelmy, S. D., Burrows, D. N., Cominsky, L. R., Hurley, K. C., Marshall, F. E., Mészáros, P., Roming, P. W. A., Angelini, L., Barbier, L. M., Belloni, T., Campana, S., Caraveo, P. A., Chester, M. M., Citterio, O., Cline, T. L., Cropper, M. S., Cummings, J. R., Dean, A. J., Feigelson, E. D., Fenimore, E. E., Frail, D. A., Fruchter, A. S., Garmire, G. P., Gendreau, K., Ghisellini, G., Greiner, J., Hill, J. E., Hunsberger, S. D., Krimm, H. A., Kulkarni, S. R., Kumar, P., Lebrun, F., Lloyd-Ronning, N. M., Markwardt, C. B., Mattson, B. J., Mushotzky, R. F., Norris, J. P., Osborne, J., Paczynski, B., Palmer, D. M., Park, H.-S., Parsons, A. M., Paul, J., Rees, M. J., Reynolds, C. S., Rhoads, J. E., Sasseen, T. P., Schaefer, B. E., Short, A. T., Smale, A. P., Smith, I. A., Stella, L., Tagliaferri, G., Takahashi, T., Tashiro, M., Townsley, L. K., Tueller, J., Turner, M. J. L., Vietri, M., Voges, W., Ward, M. J., Willingale, R., Zerbi, F. M., & Zhang, W. W. 2004, ApJ, 611, 1005

Ghisellini, G., Celotti, A., & Costamante, L. 2002, A&A, 386, 833

Ghisellini, G., Foschini, L., Tavecchio, F., & Pian, E. 2007, MNRAS, 382, L82

Ghisellini, G. & Madau, P. 1996, MNRAS, 280, 67

Ghisellini, G., Maraschi, L., & Treves, A. 1985, A&A, 146, 204

Giommi, P., Blustin, A. J., Capalbi, M., Colafrancesco, S., Cucchiara, A., Fuhrmann, L., Krimm, H. A., Marchili, N., Massaro, E., Perri, M., Tagliaferri, G., Tosti, G., Tramacere, A., Burrows, D. N., Chincarini, G., Falcone, A., Gehrels, N., Kennea, J., & Sambruna, R. 2006, A&A, 456, 911

Giuliani, A., Vercellone, S., Chen, A., Mereghetti, S., Pellizzoni, A., Perotti, F., Fornari, F., Fiorini, M., Caraveo, P., Zambra, A., Bulgarelli, A., Gianotti, F., Trifoglio, M., Cocco, G. D., Labanti, C., Fuschino, F., Marisaldi, M., Galli, M., Tavani, M., Pucella, G., D'Ammando, F., Vittorini, V., Costa, E., Feroci, M., Donnarumma, I., Pacciani, L., Monte, E. D., Lazzarotto, F., Soffitta, P., Evangelista, Y., Lapshov, I., Rapisarda, M., Argan, A., Trois, A., Paris, G. D., Barbiellini, G., Longo, F., Picozza, P., Morselli, A., Prest, M., Vallazza, E., Lipari, P., Zanello, D., Mauri, F., Giommi, P., Pittori, C., Antonelli, L. A., Gasparrini, D., Cutini, S., Verrecchia, F., & Salotti, L. 2007, The Astronomer's Telegram, 1221, 1

Gold, T. 1968, Nature, 218, 731

—. 1969, Nature, 221, 25

Goldwurm, A. 1995, Experimental Astronomy, 6, 9

Green, D. A. 1998, VizieR Online Data Catalog, 7211, 0

Greenstein, G. & Hartke, G. J. 1983, ApJ, 271, 283

Groenewegen, M. A. T., Girardi, L., Hatziminaoglou, E., Benoist, C., Olsen, L. F., da Costa, L., Arnouts, S., Madejsky, R., Mignani, R. P., Rité, C., Sikkema, G., Slijkhuis, R., & Vandame, B. 2002, A&A, 392, 741

Groh, G., Hayat, G. S., & Stroke, G. W. 1972, Appl. Opt., 11, 931

Hartman, R. C., Bertsch, D. L., Bloom, S. D., Chen, A. W., Deines-Jones, P., Esposito, J. A., Fichtel, C. E., Friedlander, D. P., Hunter, S. D., McDonald, L. M., Sreekumar, P., Thompson, D. J., Jones, B. B., Lin, Y. C., Michelson,

P. F., Nolan, P. L., Tompkins, W. F., Kanbach, G., Mayer-Hasselwander, H. A., Mücke, A., Pohl, M., Reimer, O., Kniffen, D. A., Schneid, E. J., von Montigny, C., Mukherjee, R., & Dingus, B. L. 1999, ApJS, 123, 79

Hartman, R. C., Böttcher, M., Aldering, G., Aller, H., Aller, M., Backman, D. E., Balonek, T. J., Bertsch, D. L., Bloom, S. D., Bock, H., Boltwood, P., Carini, M. T., Collmar, W., De Francesco, G., Ferrara, E. C., Freudling, W., Gear, W. K., Hall, P. B., Heidt, J., Hughes, P., Hunter, S. D., Jogee, S., Johnson, W. N., Kanbach, G., Katajainen, S., Kidger, M., Kii, T., Koskimies, M., Kraus, A., Kubo, H., Kurtanidze, O., Lanteri, L., Lawson, A., Lin, Y. C., Lisenfeld, U., Madejski, G., Makino, F., Maraschi, L., Marscher, A. P., McFarland, J. P., McHardy, I., Miller, H. R., Nikolashvili, M., Nilsson, K., Noble, J. C., Nucciarelli, G., Ostorero, L., Pian, E., Pursimo, T., Raiteri, C. M., Reich, W., Rekola, R., Richter, G. M., Robson, E. I., Sadun, A., Savolainen, T., Sillanpää, A., Smale, A., Sobrito, G., Sreekumar, P., Stevens, J. A., Takalo, L. O., Tavecchio, F., Teräsranta, H., Thompson, D. J., Tornikoski, M., Tosti, G., Ungerechts, H., Urry, C. M., Valtaoja, E., Villata, M., Wagner, S. J., Wehrle, A. E., & Wilson, J. W. 2001, ApJ, 553, 683

Hatziminaoglou, E., Groenewegen, M. A. T., da Costa, L., Arnouts, S., Benoist, C., Madejsky, R., Mignani, R., Olsen, L. F., Rite, C., Schirmer, M., Slijkhuis, R., & Vandame, B. 2002a, VizieR Online Data Catalog, 338, 40081

Hatziminaoglou, E., Groenewegen, M. A. T., da Costa, L., Arnouts, S., Benoist, C., Madejsky, R., Mignani, R. P., Olsen, L. F., Rité, C., Schirmer, M., Slijkhuis, R., & Vandame, B. 2002b, A&A, 384, 81

Henrichs, H. F. 1983, Accretion-Driven Stellar X-ray Sources ((eds. W.H.G. Lewin and E.P.J. van den Heuvel. Cambridge and New York: Cambridge University Press, 1992))

Hewish, A., Bell, S. J., Pilkington, J. D., Scott, P. F., & Collins, R. A. 1968, Nature, 217, 709

Ilovaisky, S. 1985, Physica Scripta

Jansen, F., Lumb, D., Altieri, B., Clavel, J., Ehle, M., Erd, C., Gabriel, C., Guainazzi, M., Gondoin, P., Much, R., Munoz, R., Santos, M., Schartel, N., Texier, D., & Vacanti, G. 2001, A&A, 365, L1

Karttunen, H., Kroger, P., Oja, H., Poutanen, M., & Donner, K. J. 2003, Fundamental Astronomy (ISBN 3-540-00179-4, Springer-Verlag (4th Edition))

Kaspi, V. M., Chakrabarty, D., & Steinberger, J. 1999, ApJ, 525, L33

Katarzyński, K. & Ghisellini, G. 2007, A&A, 463, 529

Kellermann, K. I., Sramek, R., Schmidt, M., Shaffer, D. B., & Green, R. 1989, AJ, 98, 1195

King, A. 1995, X-ray Binaries ((eds. W.H.G. Lewin, J. van Paradijs, E.P.J. van den Heuvel. Cambridge University Press, 419))

Krichbaum, T. P., Britzen, S., Standke, K. J., Witzel, A., Schalinski, C. J., & Zensus, J. A. 1995, Proceedings of the National Academy of Science, 92, 11377

Kundt, W. & Schaaf, R. 1993, Ap&SS, 200, 251

La Palombara, N., Mignani, R. P., Hatziminaoglou, E., Schirmer, M., Bignami, G. F., & Caraveo, P. 2006, A&A, 458, 245

Landau, L. 1932, Phys. Z. Sowjetunion, 1, 285

Levine, A. M., Lang, F. L., Lewin, W. H. G., Primini, F. A., Dobson, C. A., Doty, J. P., Hoffman, J. A., Howe, S. K., Scheepmaker, A., Wheaton, W. A., Matteson, J. L., Baity, W. A., Gruber, D. E., Knight, F. K., Nolan, P. L., Pelling, R. M., Rothschild, R. E., & Peterson, L. E. 1984, ApJS, 54, 581

Mannheim, K. 1993, A&A, 269, 67

Manzali, A., De Luca, A., & Caraveo, P. A. 2007, ApJ, 669, 570

Maraschi, L., Ghisellini, G., & Celotti, A. 1992, ApJ, 397, L5

Markwardt, C. B. & Swank, J. H. 2005, The Astronomer's Telegram, 414, 1

Markwardt, C. B., Tueller, J., Skinner, G. K., Gehrels, N., Barthelmy, S. D., & Mushotzky, R. F. 2005, ApJ, 633, L77

Mateos, S., Warwick, R. S., Carrera, F. J., Stewart, G. C., Ebrero, J., Della Ceca, R., Caccianiga, A., Gilli, R., Page, M. J., Treister, E., Tedds, J. A., Watson, M. G., Lamer, G., Saxton, R. D., Brunner, H., & Page, C. G. 2008, ArXiv e-prints

Mereghetti, S., De Luca, A., Caraveo, P. A., Becker, W., Mignani, R., & Bignami, G. F. 2002, ApJ, 581, 1280

Michel, F. C. 1991, S&T, 82, 268

Mücke, A., Protheroe, R. J., Engel, R., Rachen, J. P., & Stanev, T. 2003, Astroparticle Physics, 18, 593

Mushotzky, R. F., Done, C., & Pounds, K. A. 1993, ARA&A, 31, 717

Novara, G., La Palombara, N., Carangelo, N., de Luca, A., Caraveo, P. A., Mignani, R. P., & Bignami, G. F. 2006, A&A, 448, 93

Pacini, F. 1967, Nature, 216, 567

—. 1968, Nature, 219, 145

Pagels, A., Krichbaum, T. P., Graham, D. A., Alef, W., Kadler, M., Kraus, A., Klare, A., Witzel, J. A., Zensus, A., Greve, A., Grewing, M., Booth, R., & Conway, J. 2004, in European VLBI Network on New Developments in VLBI Science and Technology, ed. R. Bachiller, F. Colomer, J.-F. Desmurs, & P. de Vicente, 7–10

Pallavicini, R. 1989, A&A Rev., 1, 177

Pauliny-Toth, I. I. K. 1998, in Astronomical Society of the Pacific Conference Series, Vol. 144, IAU Colloq. 164: Radio Emission from Galactic and Extragalactic Compact Sources, ed. J. A. Zensus, G. B. Taylor, & J. M. Wrobel, 75–+

Petterson, J. A. 1978, ApJ, 224, 625

Pian, E., Foschini, L., Beckmann, V., Soldi, S., Türler, M., Gehrels, N., Ghisellini, G., Giommi, P., Maraschi, L., Pursimo, T., Raiteri, C. M., Tagliaferri, G., Tornikoski, M., Tosti, G., Treves, A., Villata, M., Barr, P., Courvoisier, T. J.-L., di Cocco, G., Hudec, R., Fuhrmann, L., Malaguti, G., Persic, M., Tavecchio, F., & Walter, R. 2006, A&A, 449, L21

Piran, T. 2005, Reviews of Modern Physics, 76, 1143

Pucella, G., Tavani, M., D'Ammando, F., Vittorini, V., Costa, E., Feroci, M., Donnarumma, I., Pacciani, L., Monte, E. D., Lazzarotto, F., Soffitta, P., Evangelista, Y., Lapshov, I., Rapisarda, M., Argan, A., Trois, A., Paris, G. D., Vercellone, S., Chen, A., Giuliani, A., Mereghetti, S., Pellizzoni, A., Perotti, F., Fornari, F., Fiorini, M., Caraveo, P., Zambra, A., Bulgarelli, A., Gianotti, F., Trifoglio, M., Cocco, G. D., Labanti, C., Fuschino, F., Marisaldi, M., Galli, M., Barbiellini, G., Longo, F., Picozza, P., Morselli, A., Prest, M., Vallazza, E., Lipari, P., Zanello, D., Mauri, F., Giommi, P., Pittori, C., Antonelli, L. A., Gasparrini, D., Cutini, S., Verrecchia, F., & Salotti, L. 2007, The Astronomer's Telegram, 1300, 1

Raiteri, C. M., Villata, M., Chen, W. P., Hsiao, W.-S., Kurtanidze, O. M., Nilsson, K., Larionov, V. M., Gurwell, M. A., Agudo, I., Aller, H. D., Aller, M. F., Angelakis, E., Arkharov, A. A., Bach, U., Böttcher, M., Buemi, C. S., Calcidese, P., Charlot, P., D'Ammando, F., Donnarumma, I., Forné, E., Frasca, A., Fuhrmann, L., Gómez, J. L., Hagen-Thorn, V. A., Jorstad, S. G., Kimeridze, G. N., Krichbaum, T. P., Lähteenmäki, A., Lanteri, L., Latev, G., Le Campion, J.-F., Lee, C.-U., Leto, P., Lin, H.-C., Marchili, N., Marilli, E., Marscher, A. P., Nesci, R., Nieppola, E., Nikolashvili, M. G., Ohlert, J., Ovcharov, E., Principe, D., Pursimo, T., Ragozzine, B., Sadun, A. C., Sigua, L. A., Smart, R. L., Strigachev, A., Takalo, L. O., Tavani, M., Thum, C., Tornikoski, M., Trigilio, C., Uckert, K., Umana, G., Valcheva, A., Vercellone, S., Volvach, A., & Wiesemeyer, H. 2008, A&A, 485, L17

Raiteri, C. M., Villata, M., Kadler, M., Ibrahimov, M. A., Kurtanidze, O. M., Larionov, V. M., Tornikoski, M., Boltwood, P., Lee, C.-U., Aller, M. F., Romero, G. E., Aller, H. D., Araudo, A. T., Arkharov, A. A., Bach, U., Barnaby, D., Berdyugin, A., Buemi, C. S., Carini, M. T., Carosati, D., Cellone, S. A., Cool, R., Dolci, M., Efimova, N. V., Fuhrmann, L., Hagen-Thorn, V. A., Holcomb, M., Ilyin, I., Impellizzeri, V., Ivanidze, R. Z., Kapanadze, B. Z., Kerp, J., Konstantinova, T. S., Kovalev, Y. Y., Kovalev, Y. A., Kraus, A., Krichbaum, T. P., Lähteenmäki, A., Lanteri, L., Leto, P., Lindfors, E., Mattox, J. R., Napoleone, N., Nikolashvili, M. G., Nilsson, K., Ohlert, J., Papadakis, I. E., Pasanen, M., Poteet, C., Pursimo, T., Ros, E., Sigua, L. A., Smith, S., Takalo, L. O., Trigilio, C., Tröller, M., Umana, G., Ungerechts, H., Walters, R., Witzel, A., & Xilouris, E. 2006, A&A, 459, 731

Rawlings, S. & Saunders, R. 1991, Nature, 349, 138

Robson, E. I., Gear, W. K., Clegg, P. E., Ade, P. A. R., Smith, M. G., Griffin, M. J., Nolt, I. G., Radostitz, J. V., & Howard, R. J. 1983, Nature, 305, 194

Robson, E. I., Litchfield, S. J., Gear, W. K., Hughes, D. H., Sandell, G., Courvoisier, T. J.-L., Paltani, S., Valtaoja, E., Terasranta, H., Tornikoski, M., Steppe, H., & Wright, M. C. H. 1993, MNRAS, 262, 249

Romani, R. W. 1987, ApJ, 313, 718

Roming, P. W. A., Hunsberger, S. D., Nousek, J. A., Mason, K. O., & Breeveld, A. A. 2003, in Bulletin of the American Astronomical Society, Vol. 35, Bulletin of the American Astronomical Society, 765–+

Rosner, R., Golub, L., & Vaiana, G. S. 1985, ARA&A, 23, 413

Sanders, D. B., Phinney, E. S., Neugebauer, G., Soifer, B. T., & Matthews, K. 1989, ApJ, 347, 29

Senziani, F., Novara, G., de Luca, A., Caraveo, P. A., Belloni, T., & Bignami, G. F. 2007, A&A, 476, 1297

Severgnini, P., Della Ceca, R., Braito, V., Saracco, P., Longhetti, M., Bender, R., Drory, N., Feulner, G., Hopp, U., Mannucci, F., & Maraston, C. 2005, A&A, 431, 87

Shields, G. A. 1978, Nature, 272, 706

Sikora, M., Begelman, M. C., & Rees, M. J. 1994, ApJ, 421, 153

Sikora, M., Błażejowski, M., Moderski, R., & Madejski, G. M. 2002, ApJ, 577, 78

Sikora, M., Madejski, G., Moderski, R., & Poutanen, J. 1997, ApJ, 484, 108

Skinner, G. K., Ponman, T. J., Hammersley, A. P., & Eyles, C. J. 1987, Ap&SS, 136, 337

Soldi, S., Türler, M., Paltani, S., Aller, H. D., Aller, M. F., Burki, G., Chernyakova, M., Lähteenmäki, A., McHardy, I. M., Robson, E. I., Staubert, R., Tornikoski, M., Walter, R., & Courvoisier, T. J.-L. 2008, A&A, 486, 411

Strüder, L., Briel, U., Dennerl, K., Hartmann, R., Kendziorra, E., Meidinger, N., Pfeffermann, E., Reppin, C., Aschenbach, B., Bornemann, W., Bräuninger, H., Burkert, W., Elender, M., Freyberg, M., Haberl, F., Hartner, G., Heuschmann, F., Hippmann, H., Kastelic, E., Kemmer, S., Kettenring, G., Kink, W., Krause, N., Müller, S., Oppitz, A., Pietsch, W., Popp, M., Predehl, P., Read, A., Stephan, K. H., Stötter, D., Trümper, J., Holl, P., Kemmer, J., Soltau, H., Stötter, R., Weber, U., Weichert, U., von Zanthier, C., Carathanassis, D., Lutz, G., Richter, R. H., Solc, P., Böttcher, H., Kuster, M., Staubert, R., Abbey, A., Holland, A., Turner, M., Balasini, M., Bignami, G. F., La Palombara, N., Villa, G., Buttler, W., Gianini, F., Lainé, R., Lumb, D., & Dhez, P. 2001, A&A, 365, L18

Tavani, M., Barbiellini, G., Argan, A., Bulgarelli, A., Caraveo, P., Chen, A., Cocco, V., Costa, E., de Paris, G., Del Monte, E., di Cocco, G., Donnarumma, I., Feroci, M., Fiorini, M., Froysland, T., Fuschino, F., Galli, M., Gianotti, F., Giuliani, A., Evangelista, Y., Labanti, C., Lapshov, I., Lazzarotto, F., Lipari, P., Longo, F., Marisaldi, M., Mastropietro, M., Mauri, F., Mereghetti, S., Morelli, E., Morselli, A., Pacciani, L., Pellizzoni, A., Perotti, F., Picozza, P., Pontoni, C., Porrovecchio, G., Prest, M., Pucella, G., Rapisarda, M., Rossi, E., Rubini, A., Soffitta, P., Trifoglio, M., Trois, A., Vallazza, E., Vercellone, S., Zambra, A., Zanello, D., Giommi, P., Antonelli, A., & Pittori, C. 2008, Nuclear Instruments and Methods in Physics Research A, 588, 52

Tavecchio, F. & Ghisellini, G. 2008, MNRAS, 386, 945

Tavecchio, F., Maraschi, L., Ghisellini, G., Celotti, A., Chiappetti, L., Comastri, A., Fossati, G., Grandi, P., Pian, E., Tagliaferri, G., Treves, A., & Sambruna, R. 2002, ApJ, 575, 137

Türler, M., Chernyakova, M., Courvoisier, T. J.-L., Foellmi, C., Aller, M. F., Aller, H. D., Kraus, A., Krichbaum, T. P., Lähteenmäki, A., Marscher, A., McHardy, I. M., O'Brien, P. T., Page, K. L., Popescu, L., Robson, E. I., Tornikoski, M., & Ungerechts, H. 2006, A&A, 451, L1

Türler, M., Courvoisier, T. J.-L., & Paltani, S. 2000, A&A, 361, 850

Turner, M. J. L., Abbey, A., Arnaud, M., Balasini, M., Barbera, M., Belsole, E., Bennie, P. J., Bernard, J. P., Bignami, G. F., Boer, M., Briel, U., Butler, I., Cara, C., Chabaud, C., Cole, R., Collura, A., Conte, M., Cros, A., Denby, M., Dhez, P., Di Cocco, G., Dowson, J., Ferrando, P., Ghizzardi, S., Gianotti, F., Goodall, C. V., Gretton, L., Griffiths, R. G., Hainaut, O., Hochedez, J. F., Holland, A. D., Jourdain, E., Kendziorra, E., Lagostina, A., Laine, R., La Palombara, N., Lortholary, M., Lumb, D., Marty, P., Molendi, S., Pigot, C., Poindron, E., Pounds, K. A., Reeves, J. N., Reppin, C., Rothenflug, R., Salvetat, P., Sauvageot, J. L., Schmitt, D., Sembay, S., Short, A. D. T., Spragg, J., Stephen, J., Strüder, L., Tiengo, A., Trifoglio, M., Trümper, J., Vercellone, S., Vigroux, L., Villa, G., Ward, M. J., Whitehead, S., & Zonca, E. 2001, A&A, 365, L27

Turnshek, D. A. 1984, ApJ, 280, 51

Ubertini, P., Lebrun, F., Di Cocco, G., Bazzano, A., Bird, A. J., Broenstad, K., Goldwurm, A., La Rosa, G., Labanti, C., Laurent, P., Mirabel, I. F., Quadrini, E. M., Ramsey, B., Reglero, V., Sabau, L., Sacco, B., Staubert, R., Vigroux, L., Weisskopf, M. C., & Zdziarski, A. A. 2003, A&A, 411, L131

Urry, C. M. & Padovani, P. 1995, PASP, 107, 803

Van Paradijs, J. 1998, The Many Faces of Neutron Stars (Kluwer Academic Publishers), 279

Vercellone, S., Chen, A. W., Giuliani, A., Bulgarelli, A., Donnarumma, I., Lapshov, I., Tavani, M., Argan, A., Barbiellini, G., Caraveo, P., Cocco, V., Costa, E., D'Ammando, F., Del Monte, E., De Paris, G., Di Cocco, G., Evangelista, Y., Feroci, M., Fiorini, M., Froysland, T., Fuschino, F., Galli, M., Gianotti, F., Labanti, C., Lazzarotto, F., Lipari, P., Longo, F., Marisaldi, M., Mauri, F., Mereghetti, S., Morselli, A., Pacciani, L., Pellizzoni, A., Perotti, F., Picozza, P., Prest, M., Pucella, G., Rapisarda, M., Soffitta, P., Trifoglio, M., Trois, A., Vallazza, E., Vittorini, V., Zambra, A., Zanello, D., Pittori, C., Verrecchia, F., Gasparrini, D., Cutini, S., Giommi, P., Antonelli, L. A., Colafrancesco, S., & Salotti, L. 2008a, ApJ, 676, L13

Vercellone, S., Chen, A. W., Vittorini, V., Giuliani, A., D'Ammando, F., Tavani, M., Donnarumma, I., Pucella, G., Raiteri, C. M., Villata, M., Chen, W. P., Tosti, G., Impiombato, D., Romano, P., Belfiore, A., De Luca, A., Novara, G., Senziani, F., Bazzano, A., Fiocchi, M. T., Ubertini, P., Ferrari, A., Argan, A., Barbiellini, G., Boffelli, F., Bulgarelli, A., Caraveo, P., Cattaneo, P. W., Cocco, V., Costa, E., Del Monte, E., De Paris, G., Di Cocco, G., Evangelista, Y., Feroci, M., Fiorini, M., Fornari, F., Froysland, T., Fuschino, F., Galli, M., Gianotti, F., Labanti, C., Lapshov, I., Lazzarotto, F., Lipari, P., Longo, F., Marisaldi, M., Mereghetti, S., Morselli, A., Pellizzoni, A., Pacciani, L., Perotti, F., Picozza, P., Prest, M., Rapisarda, M., Rappoldi, A., Soffitta, P., Trifoglio, M., Trois, A., Vallazza, E., Zambra, A., Zanello, D., Pittori, C., Verrecchia, F., Santolamazza, P., Preger, B., Gasparrini, D., Cutini, S., Giommi, P., Colafrancesco, S., & Salotti, L. 2008b, ArXiv e-prints

Vietri, M. 2006, Astrofisica delle alte energie (ISBN 88-339-5773-X, Bollati Boringhieri)

Villata, M., Raiteri, C. M., Balonek, T. J., Aller, M. F., Jorstad, S. G., Kurtanidze, O. M., Nicastro, F., Nilsson, K., Aller, H. D., Arai, A., Arkharov, A., Bach, U., Benítez, E., Berdyugin, A., Buemi, C. S., Böttcher, M., Carosati, D., Casas, R., Caulet, A., Chen, W. P., Chiang, P.-S., Chou, Y., Ciprini, S., Coloma, J. M., di Rico, G., Díaz, C., Efimova, N. V., Forsyth, C., Frasca, A., Fuhrmann, L., Gadway, B., Gupta, S., Hagen-Thorn, V. A., Harvey, J., Heidt, J., Hernandez-Toledo, H., Hroch, F., Hu, C.-P., Hudec, R., Ibrahimov, M. A., Imada, A., Kamata, M., Kato, T., Katsuura, M., Konstantinova, T., Kopatskaya, E., Kotaka, D., Kovalev, Y. Y., Kovalev, Y. A., Krichbaum, T. P., Kubota, K., Kurosaki, M., Lanteri, L., Larionov, V. M., Larionova, L., Laurikainen, E., Lee, C.-U., Leto, P., Lähteenmäki, A., López-Cruz, O., Marilli, E., Marscher, A. P., McHardy, I. M., Mondal, S., Mullan, B., Napoleone, N., Nikolashvili, M. G., Ohlert, J. M., Postnikov, S., Pursimo, T., Ragni, M., Ros, J. A., Sadakane, K., Sadun, A. C., Savolainen, T., Sergeeva, E. A., Sigua, L. A., Sillanpää, A., Sixtova, L., Sumitomo, N., Takalo, L. O., Teräsranta, H., Tornikoski, M., Trigilio, C., Umana, G., Volvach, A., Voss, B., & Wortel, S. 2006, A&A, 453, 817

Visvanathan, N. & van den Bergh, S. 1992, AJ, 103, 1057

Watson, M. G., Schröder, A. C., Fyfe, D., Page, C. G., Lamer, G., Mateos, S., Pye, J., Sakano, M., Rosen, S., Ballet, J., Barcons, X., Barret, D., Boller, T., Brunner, H., Brusa, M., Caccianiga, A., Carrera, F. J., Ceballos, M., Della Ceca, R., Denby, M., Denkinson, G., Dupuy, S., Farrell, S., Fraschetti, F., Freyberg, M. J., Guillout, P., Hambaryan, V., Maccacaro, T., Mathiesen, B., McMahon, R., Michel, L., Motch, C., Osborne, J. P., Page, M., Pakull, M. W., Pietsch, W., Saxton, R., Schwope, A., Severgnini, P., Simpson, M., Sironi, G., Stewart, G., Stewart, I. M., Stobbart, A., Tedds, J., Warwick, R., Webb, N., West, R., Worrall, D., & Yuan, W. 2008, ArXiv e-prints

White, N. E. 1985, A&A Rev., 1, 85

Winkler, C., Courvoisier, T. J.-L., Di Cocco, G., Gehrels, N., Giménez, A., Grebenev, S., Hermsen, W., Mas-Hesse, J. M., Lebrun, F., Lund, N., Palumbo, G. G. C., Paul, J., Roques, J.-P., Schnopper, H., Schönfelder, V., Sunyaev, R., Teegarden, B., Ubertini, P., Vedrenne, G., & Dean, A. J. 2003, A&A, 411, L1

Woods, P. M., Zavlin, V. E., & Pavlov, G. G. 2007, Ap&SS, 308, 239

List of publications

Papers in refereed journals

1. Bode M. F., O'Brien T. J., Osborne J. P., Page K. L., Senziani F., Skinner G. K., Starrfield S., Ness J. U., Drake J. J., Schwarz G., Beardmore A. P., Darnley M. J., Eyres S. P. S., Evans A., Gehrels N., Goad M. R., Jean P., Krautter J. & Novara G.
   Swift Observations of the 2006 Outburst of the Recurrent Nova RS Ophiuchi. I. Early X-Ray Emission from the Shocked Ejecta and Red Giant Wind
   The Astrophysical Journal, Volume 652, November 2006, pp.629-635

2. Senziani F., Novara G., De Luca A., Caraveo P. A., Belloni T., & Bignami G. F.
   Using GRO J1655-40 to test Swift/BAT as a monitor for bright hard X-ray sources
   Astronomy and Astrophysics, Volume 476, December 2007, pp. 1297-1305

3. Vercellone S., Chen A. W., Vittorini V., Giuliani A., D'Ammando F., Tavani M., Donnarumma I., Pucella G., Raiteri C. M., Villata M., Chen W. P., Tosti G., Impiombato D., Romano P., Belfiore A., De Luca A., Novara G., Senziani F., Bazzano A., Fiocchi M. T., Ubertini P., Ferrari A., Argan A., Barbiellini G., Boffelli F., Bulgarelli A., Caraveo P., Cattaneo P. W., Cocco V., Costa E., Del Monte E., De Paris G., Di Cocco G., Evangelista Y., Feroci M., Fiorini M., Fornari F., Froysland T., Fuschino F., Galli M., Gianotti F., Labanti C., Lapshov I., Lazzarotto F., Lipari P., Longo F., Marisaldi M., Mereghetti S., Morselli A., Pellizzoni A., Pacciani L., Perotti F., Picozza P., Prest M., Rapisarda M., Rappoldi A., Soffitta P., Trifoglio M., Trois A., Vallazza E., Zambra A., Zanello D., Pittori C., Verrecchia F., Santolamazza P., Preger B., Gasparrini D., Cutini S., Giommi P., Colafrancesco S. & Salotti L.
   Multiwavelength observations of 3C 454.3. I. The AGILE 2007 November campaign on the "Crazy Diamond"

The Astrophysical Journal (2008), in press, (arXiv:0809.1737)

4. Novara G., La Palombara N., Mignani R.P., Hatziminaoglou E., Schirmer M., De Luca A. & Caraveo P. A.
A deep XMM-Newton Serendipitous Survey of a middle-latitude area. II. New deeper X–ray and optical observations.
Submitted to Astronomy and Astrophysics

Astronomer's Telegrams

5. Israel G. L., Krimm H. A., Rea N., Perez D., Burrows D. N., Beardmore A. P., Campana S., Covino S., Cummings J., De Luca A., Esposito P., Evans P. A., Gotz D., Hill J. E., Holland S. T., Kennea J. A., Markwardt C. B., Novara G., O'Brien P. T., Osborne J. P., Page K. L., Roming P., Sakamoto T., Skinner G. K., & Tiengo A.
Swift detects an X-ray and optical outburst from a Galactic source probably associated with 1RXH J173523.7-354013
The Astronomer's Telegram, #1528 (2008)

Acknowledgements

Desidero ringraziare la Dott.ssa Caraveo per la fiducia e l'aiuto concreto che hanno permesso lo sviluppo di questo lavoro. Un grazie speciale ad Andrea De Luca per il coordinamento del lavoro del gruppo BAT di Pavia, per il suo impegno ampio e costante e il suo continuo incoraggiamento.

Ringrazio di cuore il gruppo di astrofisica di Pavia: Andrea “Mario” Belfiore senza il quale gran parte di questo progetto non sarebbe stato possibile, per il lavoro condiviso, per l'aiuto e soprattutto per i momenti di svago. Fabio “Senzio” Senziani per gli anni di lavoro vissuti insieme tra laurea e dottorato e per l'amicizia duratura.

Tutti gli astrofisici dell'INAF-IASF-Milano, in particolar modo Nicola “Nic” La Palombara per la pazienza e l'amicizia. Ringrazio Roberto Mignani per l'aiuto e per i preziosi consigli.

Gli amici d'ufficio Silvia e Fabrizio per avermi sopportato.

Desidero ringraziare Michele Belotti per la sua amicizia e i suoi suggerimenti nell'utilizzo del LATEX.